Czech Technical University in Prague

Faculty of Biomedical Engineering

Doctoral Thesis

December 2017

Marie Krečmarová

Czech Technical University in Prague
Faculty of Biomedical Engineering
Department of Biomedical Technology

DESIGN AND REALIZATION OF THE PRINCIPLE OF LABEL FREE DETECTION OF DNA MOLECULES USING NV CENTRE QUANTUM ELECTRON TRANSITIONS IN DIAMOND NANOSENSOR

Doctoral Thesis

Marie Krečmarová

Kladno, *December 2017*

Ph.D. Programme: Biomedical and clinical technology
Branch of study: Biomedical and clinical technology

Supervisor: ***Prof. RNDr. Miloš Nesládek, Ph.D., HDR.***
Supervisor-Specialist: ***Dr. Vincent Mortet Ph.D.***

Hereby I declare that this Thesis “Design and realization of the principle of label free detection of DNA molecules using NV centre quantum electron transitions in diamond nanosensor” has been written by me in its entirety as the result of my own original research. I have acknowledged all the sources of information which have been used in the Thesis in compliance with the Methodological Instruction No. 1/2009 - On maintaining ethical principles when working on a university final project.

27. 12. 2018 ……..

Marie Krečmarová

Abstract

DNA diagnostics became indispensable part of biochemical analytic tools today. Further challenges lay in development of sensors which can detect significantly reduced volume of analyte, operate with enhanced sensitivity and analyse larger DNA arrays. In the heart of development of such sensors is search for novel sensing principles that would enable a significant improvement in precision, speed and resolution. It is anticipated that such principles might lead to novel medical diagnosis and genetics with a possibility to detect variety of diseases or gene mutations. Diamond, as wide bandgap semiconductor is an attractive material for developing novel devices for biosensing applications due to its excellent physical and chemical properties. In this doctoral work was devoted to development of novel label free DNA microfluidic biosensor based on quantum sensing principles. We propose a scheme in which so called colour centres in diamond, e.g. a lattice point defects, work as molecular sensors. Our design employs specifically nitrogen vacancy NV centre charge state detection in diamond combining electrochemical detection with NV centre charge state optical readout.

The doctoral thesis is divided as follows. The first part of the work is focused on synthesis of diamond material by plasma enhanced chemical vapour deposition (MW PE CVD). The material engineering was used to define optimal synthesis conditions and consequently electrical, morphology and optical properties of diamond films. Impurity doping and nitrogen vacancy NV point defect engineering was used to design optimal sensor functionality. The NV sensor is then used for detection of molecules carrying electrical charge as DNA molecule combined with electrochemical detection.

The diamond sensing device consists then of highly boron doped diamond serving as electrochemical device covered with ultrathin diamond layer with NV quantum centres acting as charge sensors. The diamond device is covered by polydimethylsiloxane (PDMS) flow cell and transparent conductive indium tin oxide (ITO) coated glass slide and connected to the electronic board. Two independent electrically controlled functions are enabled: the active control of the NV centre charge state by applying a gate voltage and the electrochemical readout. The working and reference electrodes are located on the diamond surface and ITO glass is used as the counter electrode. NV photoluminescence (PL) is detected by confocal microscopy in the microfluidic channel through fabricated micro holes in the gate electrode. The oxygen terminated surface of the undoped diamond layer is electrostatically covered by positively charged cationic polymer polyethylenimine (PEI). PEI tunes the NV centres to NV^0 and NV^+ charge state and low intensity of predominantly NV^0 PL is detected. When negative DNA molecules are electrostatically attracted on the positive PEI molecules, NV PL is recovered, NV centres are switched to NV^- charge state with approximately two times increase of PL intensity. The biochemical reactions in the microfluidic channel are confirmed by electrochemical impedance spectroscopy (EIS).

Acknowledgments

First of all I would like to thank my supervisor Miloš Nesládek for his support, professional guidance and encouragement during my doctoral work. Many thanks for the opportunity to work in his group of Photonics and quantum lab at Hasselt University's Institute for Materials Research (IMO-IMOMEC) in Belgium during my Erasmus scholarship under his supervision.

I would also like to thank my co-supervisor Vincent Mortet, head of the research group of Material for nanosystems and biointerfaces (MNB) at the Institute of physics AV CR for support, and Petr Šittner, head of the Department of Functional Materials at the Institute of Physics, AS CR for the opportunity to work in the laboratories at the Institute of physics AS CR.

I would like to thank my colleagues from the Institute of physics AV CR in Prague from MNB group, especially Andy Taylor, Petr Ashcheulov, Václav Petrák and Lucie Drbohlavová. Many thanks to Vincent Mortet for the fabrication of Ti/Au electrodes on the final diamond device, Ladislav Fekete for AFM microscopy, Jaromír Kopeček for SEM microscopy, Pavel Hubík for electrical Hall effect measurements and Zdeněk Remeš for FTIR spectroscopy, Jan Drahokoupil for GA-XRD measurements.

I would like to thank the colleagues from Photonics and quantum lab group at Hasselt University's Institute for Materials Research Emilie Bourgeois, Michal Gulka, Jaroslav Hrubý, Christopher Freiwald and Takashi Yamamoto. Many thanks to Thijs Vandenryt for the fabrication of the designed microfluidic device and electronic board.

I would like to thank Optima Diamant, spol. s.r.o. in Ostrava, Czech Republic for polishing of the single crystal diamond, David Chvátil from microtron laboratory in Nuclear Physics Institute of the ASCR for electron irradiation of nanocrystalline diamond and Kamatchi Jothiramalingam Sankaran and I-Nan Lin from the Tamkang University in Taiwan for TEM measurements.

Finally, I would like to thank my family, for their support during all my studies.

This work was supported by the EU–FP7 research grant DIADEMS, No. 611143, FWO (Flanders) G.0.943.11.N.10.; the Erasmus Student Mobility Grant; the Czech Republic Ministry of Education, Youth and Sports: Project ID: “Nanointegrace” CZ.1.07/2.3.00/20.0306; the CTU grant SGS14/214/OHK4/3T/17; the Czech Science Foundation (GACR) Grant ID: GAČR 13-31783S and the J.E. Purkyne fellowship awarded by Academy of Sciences of the Czech Republic.

Table of contents

1 Introduction

1.1 Biosensors and their biomedical applications

As quoted from the Reference [1] by McNaught A. D. the "biosensor is a device that uses specific biochemical reactions mediated by isolated enzymes, immunosystems, tissues, organelles or whole cells to detect chemical compounds usually by electrical, thermal or optical signals". Bioreceptors (enzyme, antibody, nucleic acid, lectine, hormone, cell structure or tissue) immobilized on a detection system (transducer) specifically interact with a target in an analyte and specific electrical or optical biosignals at the interface can be detected [1] [2] [3]. Note, that a biosensor can work also without surface functionalization [4].

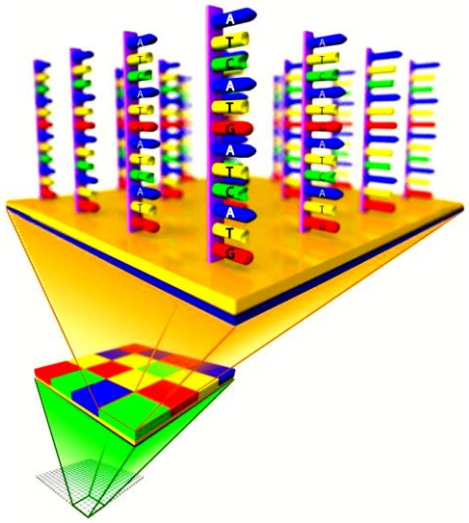

Figure 1. DNA microarrays for identification of specific DNA sequences through the hybridization process. The sensor is divided into many areas and each of them is sensitive for specific DNA sequences [5].

Today the commercially available ex vivo sensors are usually glucose and DNA microarrays. Other types of biosensors are in development [6] [7]. A very small, low cost, and high sensitivity biomedical devices for DNA sensing can bring improvement for diagnostic methods in medical genetics. DNA can be detected by various methods. For example using Polymerase chain reaction (PCR). DNA array can detect millions of specific genes or gene mutations simultaneously with high sensitivity and specificity (Figure 1) [5] [8] [9] [10]. The most commercially available DNA biosensors are based on the colour tagged DNA molecules, while the mainstream in the biomedical research is development of a DNA label free biosensors. Recently microfluidic lab-on-a-chip based DNA biosensors with advantages of fast, sensitive and precise detection brought a high interest. This technique uses small sample volumes (10^{-9} – 10^{-18} l) and brings the benefit of multiple sample detection in parallel [11]. The chip

commonly consists of micro-channels, made of polydimethylsiloxane (PDMS) and several micro valves, mixers and pumps. The DNA detection is performed by electrochemical impedance spectroscopy or cyclic voltammetry [11] [12] [13]. DNA biosensor processing consists of transducer material fabrication, probe preparation, hybridization and data analysis.

1.2 Diamond and its biomedical application for label free DNA detection

Diamond as a wide gap (5.5 eV) material semiconducting or insulating has a unique combination of physical and chemical properties for biosensing applications. The key advantages of diamond are biocompatibility and non-toxicity, which can allow it for in vivo detection [3] [14]. Boron doped diamond is a unique electrochemical material. As an example the diamond shows low electrochemical background current, the largest potential window (> 3V), stability in an electrolyte solution, better than other materials like gold or glassy carbon [6] [15] [16]. Highly conductive electrochemical diamond electrodes can be achieved by boron doping during PE CVD growth [6].

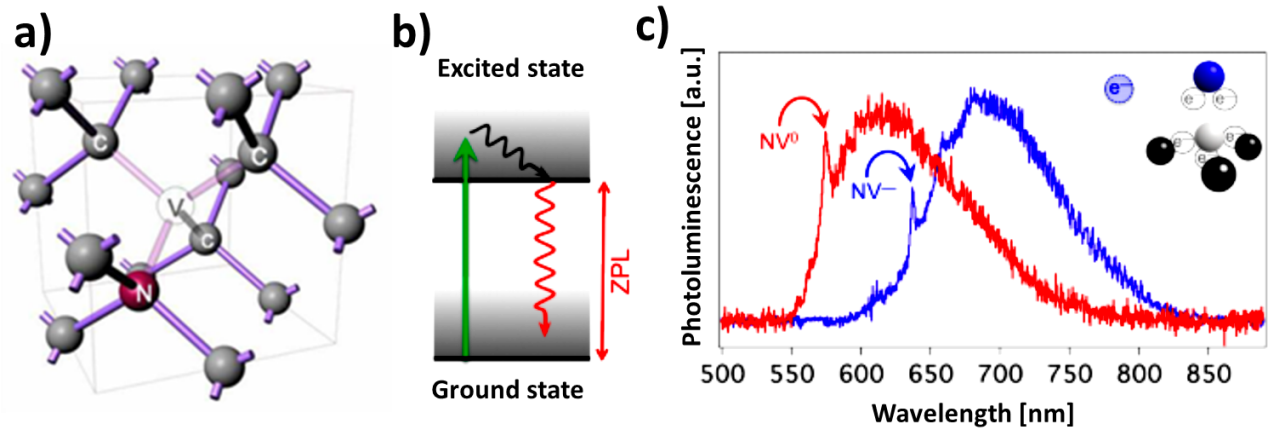

Figure 2. Scheme of the NV centre showing substitutional nitrogen atom lying next to a vacancy in diamond lattice (a) [17], electronic band structure of NV centre showing ground state and excited state (b) and normalized photoluminescence spectra of NV^0 (red) and NV^- (blue) colour centres (c) [18].

The NV centre is a colour defect in diamond, consisting of a substitutional nitrogen atom lying next to a vacancy inside a diamond lattice (Figure 2a). In the Figure 2 its electronic band structure (more detail in the chapter 2.6.2) and photoluminescence (PL) emission spectra for two NV centre charge states are also visible. NV centre can exhibit in neutral NV^- and NV^0 charge state with zero phonon line at 636 nm or 575 nm respectively, or in dark NV^+ charge state without photoluminescence [19] [20] [21]. NV^- charge state centre is a spin triplet (spin 1 centre). Therefore for spin sensing NV^- centre

is preferably required, and the NV^{-}/NV^{0} charge state ratio is demanded to be maximal [19] [22] [23]. The inter conversion of NV^{0} and NV^{-} charge state can be achieved by passive or active manipulation of the Fermi level position. NV centres present close to the diamond surface are sensitive to surface charge changes and can be passively manipulated by surface termination as hydrogen (decrease of NV^{-} formation) or by oxygen and fluorine (increase of NV^{-} formation) [24] [25]. Active control of NV centres charge state can be achieved optically [26] [27] or electrically [21] [28] [29] [30] [31].

These nitrogen vacancy centres can be created by nitrogen implantation and annealing of pure diamond or by nitrogen addition during plasma enhanced chemical vapour deposition (PE CVD) growth [22] [32] followed by irradiation and annealing. NV centres localized close to the diamond surface can be created by low energy ion implantation followed by thermal annealing or by nitrogen doping during PE CVD growth [33] [23] [34] [24] [32].

The NV centre sensitivity, placed close to a specifically terminated diamond surface can be used as a tool for detection of charged molecules, such as DNA [35]. Combination of the exceptional electrochemical properties of boron doped diamond with NV centre sensing is a promising new route for realisation of a novel multifunctional label free diamond DNA sensor.

1.3 Aim of the thesis

The aim of the thesis is to develop novel type of label free DNA microfluidic biosensor based on the NV centre optical detection using electron charge detection method combined with electrochemical readout. In this design the boron doped electrochemical device would allow to set the potential promoting a specific electrochemical reactions, e.g. for example oxidation or reduction, whilst the NV centre can detect by ultrasensitive way the product of such reactions by using the charge detection principle. Alternatively there is potential to combine the proposed device with NV spin sensors, monitoring the changes of the spin environment of ongoing chemical reaction (for example Fe(II) <-> F(III) reaction processes). Additionally the electrochemical sensor can be used for verification of processes of specific molecules such as DNA by working as impedimetric sensor.

To realise such sensor the following aspects have to be realises: Preparation of B doped diamond with optimal B concentration to function as electrochemical sensor. Design of a diamond structure

in which a thin diamond layer with NV centres is deposited on top of the B doped diamond and incorporation of the structure to the electrochemical sensing device.

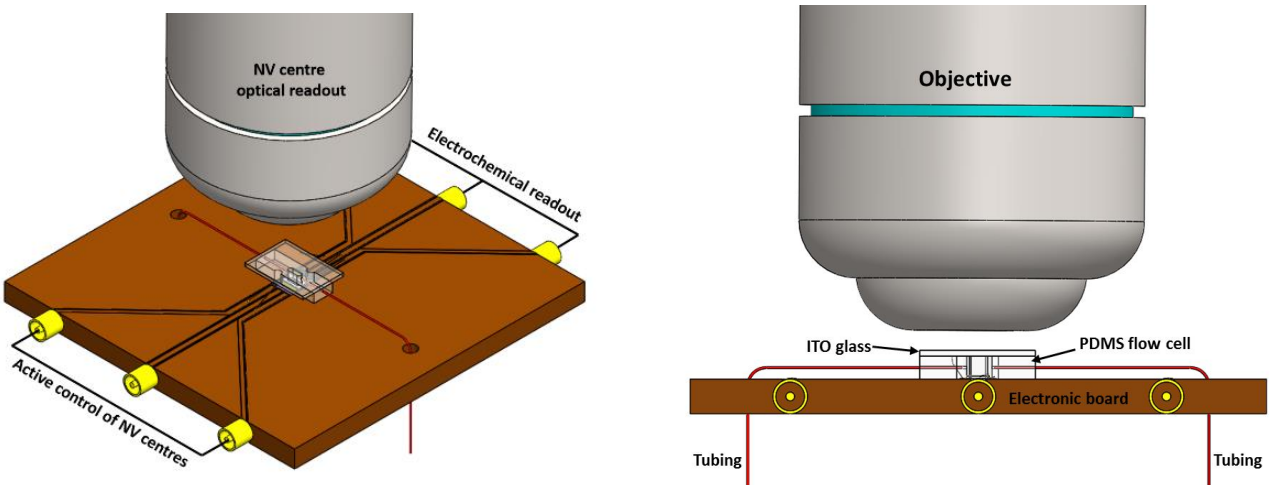

Figure 3. Top (left) and side (right) view of the sensor scheme arrangement including diamond device embedded into the electronic board and covered with flow cell, NV centre photoluminescence is detected by confocal microscopy.

To achieve this following methodological steps were realised:

1. **Study of boron doping** in the conventional microwave (MW) resonance MW PE CVD nanocrystalline (NCD) and single crystal diamond growth to find the best condition for fabrication of the diamond electrode (electrical, optical and morphology properties).

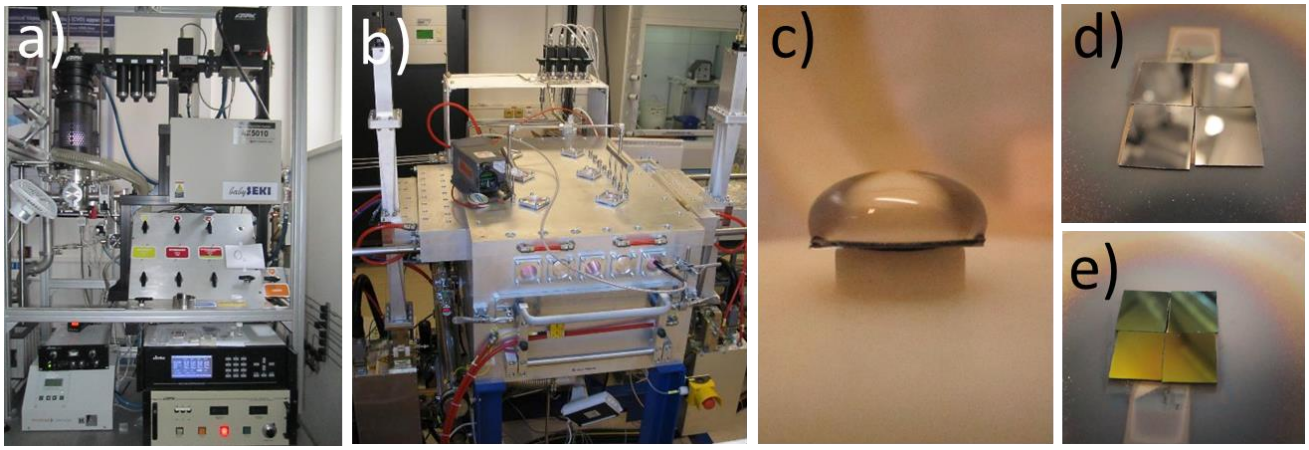

Figure 4. The Seki Technotron AX5010 conventional MW resonance cavity MW PECVD deposition system (a), the large area linear antenna MW PE CVD apparatus (b), seeding pre-nucleation step: detail of a drop of nanodiamond dispersion solution on the silicon substrate (c), seeded silicon substrates before growth (d) and grown nanocrystalline diamond films with 4000 ppm of trimethylboron doping as B precursor (e).

2. **Study of the nitrogen doping** in MW PE CVD NCD and single crystal diamond growth for fabrication of as grown NV centres (morphology and PL properties).

3. **Study of the NV photoluminescence** (PL) in NCD and single crystal diamond as function of concentration of incorporated boron atoms in the film causing PL quenching.

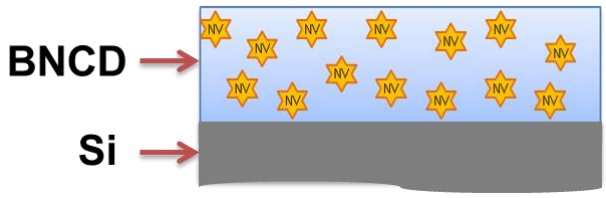

Figure 5. Scheme of the boron doped nanocrystalline diamond (BNCD) film with NV centres grown on Si substrate. NV PL was studied from low to high boron doping concentrations.

4. **Electrochemical impedance spectroscopy (EIS) study** of the BNCD/NCD electrode as function of the NCD film thickness.

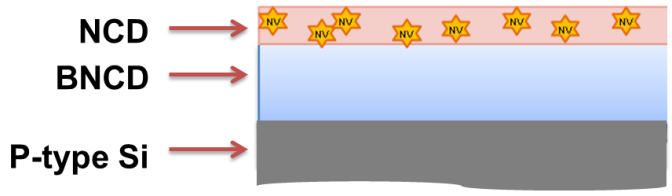

Figure 6. Scheme of undoped NCD diamond film with NV centres grown on BNCD and p-type Si substrate. NV PL was studied as function of the thickness of undoped diamond with NV´s.

5. **Fabrication of the novel label free DNA microfluidic NV centre charge state control diamond sensor.**

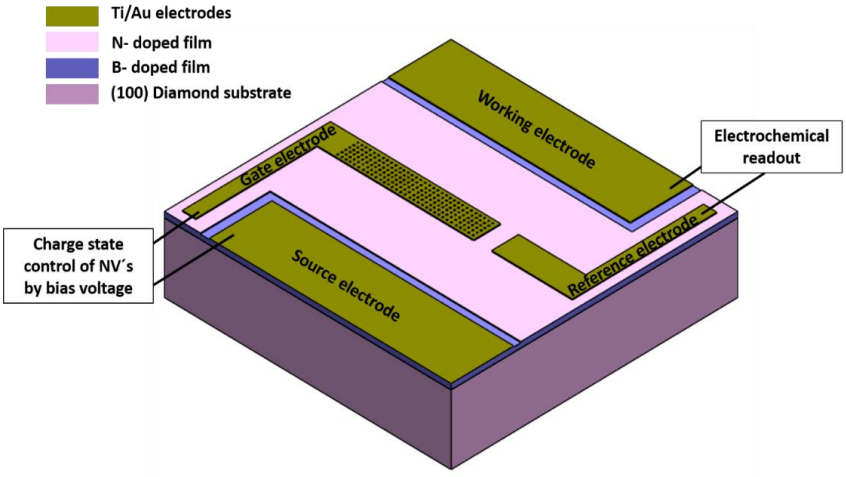

Figure 7. Scheme of the diamond device consisting of high boron doped diamond layer (20 µm), low doped diamond interlayer (100 nm) and NV centre containing film on top (20 nm), which is equipped with electrodes for charge state control and electrochemical readout.

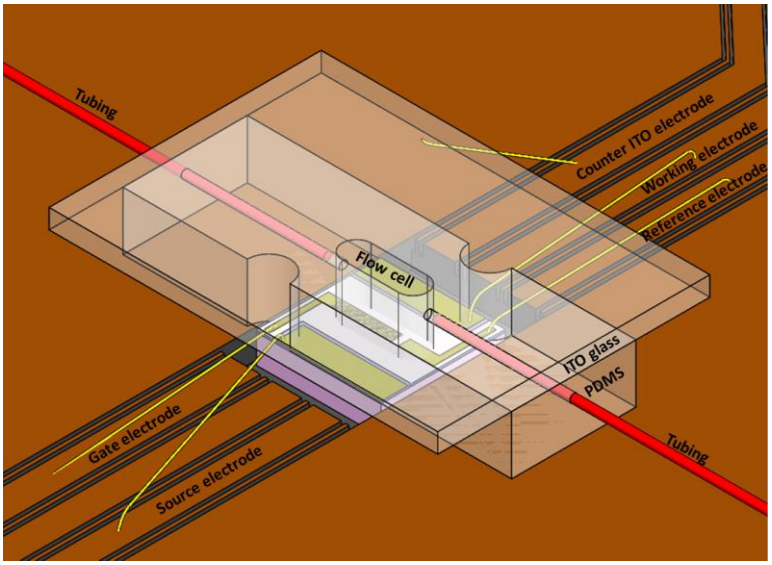

Figure 8. Scheme of the microfluidic system including the diamond device embedded in the electronic board gap and covered with microfluidic PDMS flow cell with ITO coated transparent and conductive glass sheet on top.

6. Study of the passive charge state control of the NV centre with oxygen (O), hydrogen (H) and polyethyleneimine (PEI) surface termination.

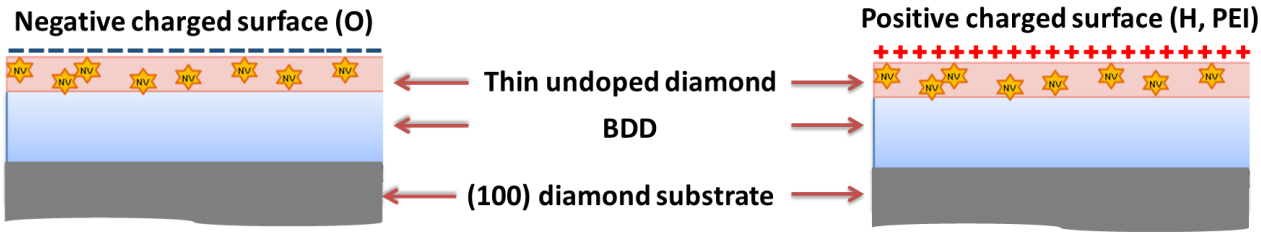

Figure 9. Scheme of the diamond device with negative (O) and positive (H, PEI) surface functionalization affecting close surface NV centres.

7. Study of the active charge state control of the NV centre by applying electric field.

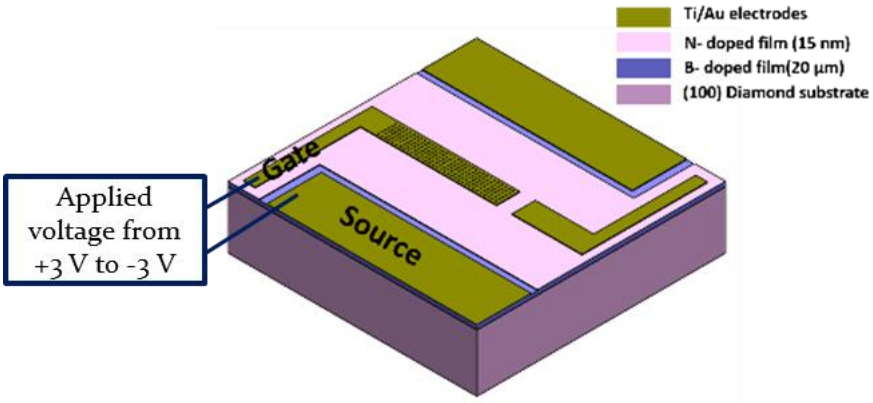

Figure 10. Scheme of the diamond device arrangement for the active NV centre charge state control.

8. **Label free DNA detection by the EIS** (PEI and PEI-DNA functionalized diamond surface).

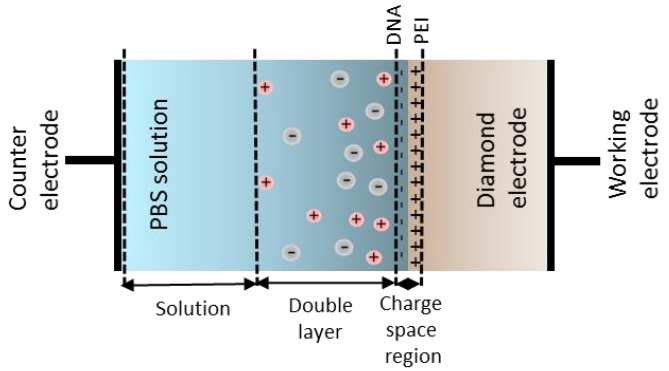

Figure 11. Scheme of the electrochemical system including phosphate buffered saline (PBS) electrolyte between counter electrode (ITO coated glass) and working electrode (BDD) with undoped NV centre containing thin film on top and PEI/DNA bio-functionalized surface.

9. **Label free DNA detection by the NV centre charge state** (PEI and PEI-DNA functionalized diamond surface).

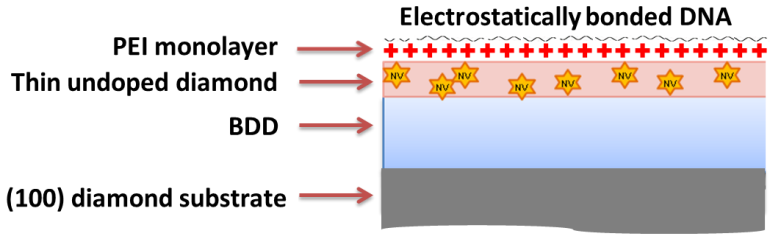

Figure 12. Scheme of the diamond sensing device with covalently bonded negative DNA molecules on the positive (PEI) functionalized diamond surface affecting close surface NV centres.

2 Literature review

2.1 Structure of oligonucleotides

DNA

DNA (Deoxyribonucleic acid) consists of two polynucleotide chains twisted around each other to form a double helix. Orientation of the double helix can be right or left handed. Figure 13a shows its double helix structure, which is composed of alternating sugar and phosphate residues and bases complementary bonded by hydrogen bonds [36].

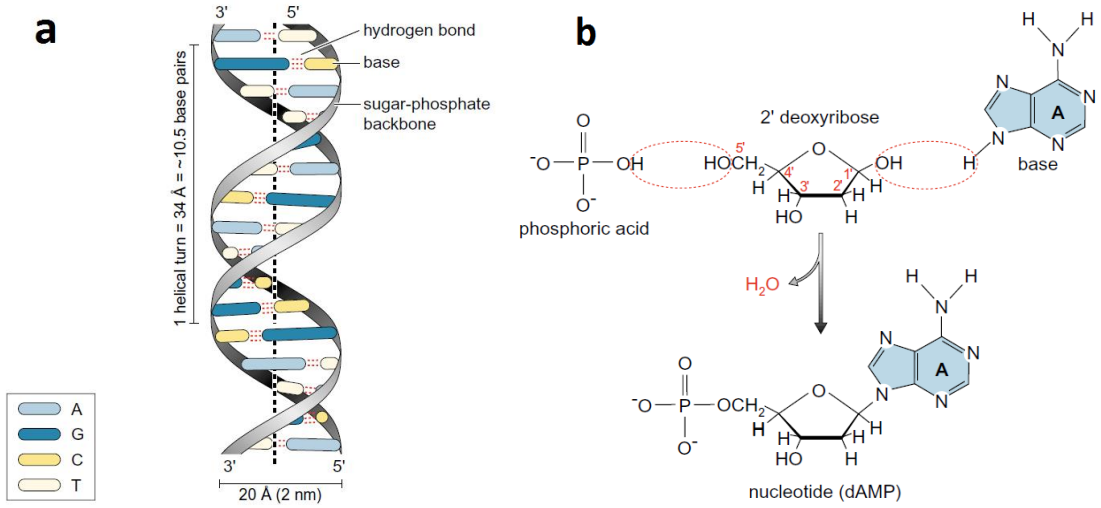

Figure 13. Structure of DNA (a) and nucleotide by removing water (b) [36].

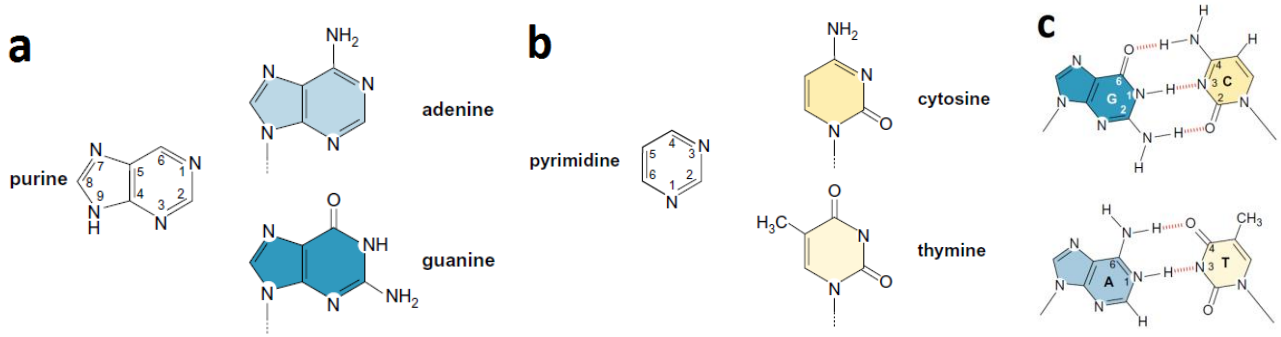

Figure 14. DNA bases: purines (a), pyrimidines (b) and hydrogen bonding between bases (c) [36].

The main component of DNA are nucleotides Nucleotides consist of a phosphate, sugar (2´-deoxyribose) and different bases. The sugar and base are joined by glycosidic bonds and are called nucleoside. By formation of phosphoester bond between the sugar and the phosphoric acid, nucleoside forms a nucleotide. Figure 13b shows structure of nucleotide from nucleotide components by abstraction of water molecule [36].

DNA bases (Figure 14a,b) are divided into two classes, purines (adenine and guanine) and pyrimidines (cytosine and thymine). These bases are connected complementary by hydrogen bonds (Figure 14c). DNA is essential for a genome function. DNA with unique coding sequences ensures genome replication, exact transmission to progeny cells and also for a cooperative molecular interactions forming nucleoprotein complexes [36] [37].

RNA

Ribonucleic acid (RNA) differs from DNA by three factors. RNA consists of only one polynucleotide chain, where the DNA's sugar 2´-deoxyribose is replaced by ribose and base thymine by uracil [36].

In some kinds of RNA as a ribosome, the polynucleotide chain overlaps complementary in some parts and created double helix (Figure 15a). Figure 15b shows the back bone of RNA of alternating phosphate and ribose species. RNA does not provide genetic information except for certain type of viruses. RNA plays an essential role in synthesis of proteins in a form transfer, messenger and ribosomal RNA (tRNA, mRMA and rRNA). RNA also plays a role as an enzyme [36] [38].

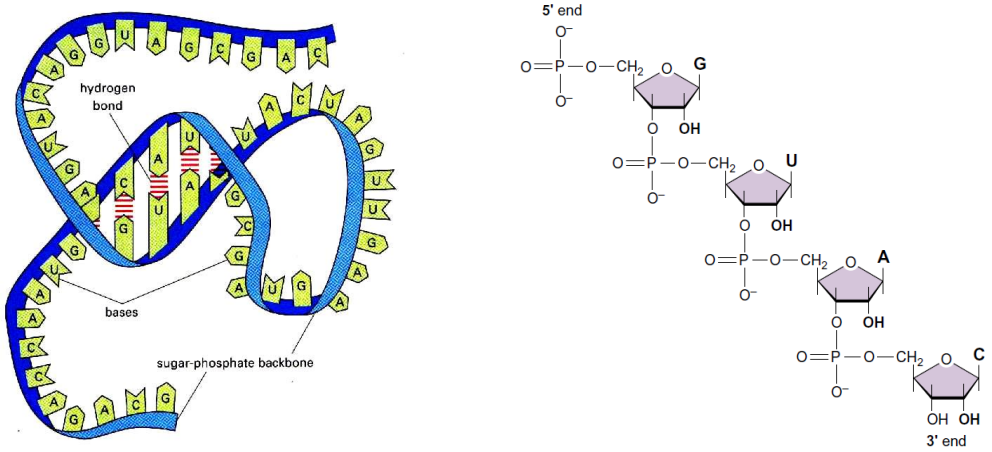

Figure 15. Structure of RNA: overlaps of complementary RNA bases by hydrogen bonds (a) [20] and back bone of RNA of alternating phosphate and ribose species (b) [36].

2.2 Hybridization of DNA

DNA hybridization is an important diagnostic technique in the medicine and molecular biology. Applications of DNA hybridization may be applied in neurology, microbiology, pathology, developmental biology, karyotyping and phylogenetic. In situ hybridization enables to examine macroscopic distribution and cellular localization of DNA and RNA sequences in a heterogeneous cell population. Biosensors based on hybridization are very useful for detection of variety diseases or gene mutations [5] [9] [39]. DNA-RNA hybridization is shown in Figure 16 as an example.

Once a genome has been sequenced, it is possible to synthesise it whole or just a part of it in the automated machines. Synthetic oligonucleotides are designed to be complementary to a known

mRNA sequence from libraries. Synthetic construction process also involves use of plasmid vectors and bacteria [39] [40].

Fundamental objective of hybridization is to identify and quantify nucleic acids in an environment. Oligonucleotides hybridization is based on hydrogen bonding between complimentary sequences of DNA or RNA. Generally, specific DNA sequences, complementary to the DNA or RNA sequences to be detected are bonded on a sensor surface as probes [39] [41].

Four basic types of probes exist: double stranded DNA (dsDNA), single stranded DNA (ssDNA), single stranded complimentary RNA (sscRNA) and synthetic oligonucleotides. By labelling the target molecules it is possible to monitor a hybridization of probes and complementary target molecules. Targets DNA or RNA molecules can be labelled radioactively (^{3}H, ^{32}P, or ^{35}S, but ^{14}C and ^{125}I izotopes) or non-radioactively (biotin, alkaline phosphatase or horseradish peroxidase, hapten and fluorophores) using fluorescent molecules or enzymes for instance [39] [41]. Several parameters as probe construction, temperature, pH, and composition of buffer play a crucial role for detection of hybridization [39] [42].

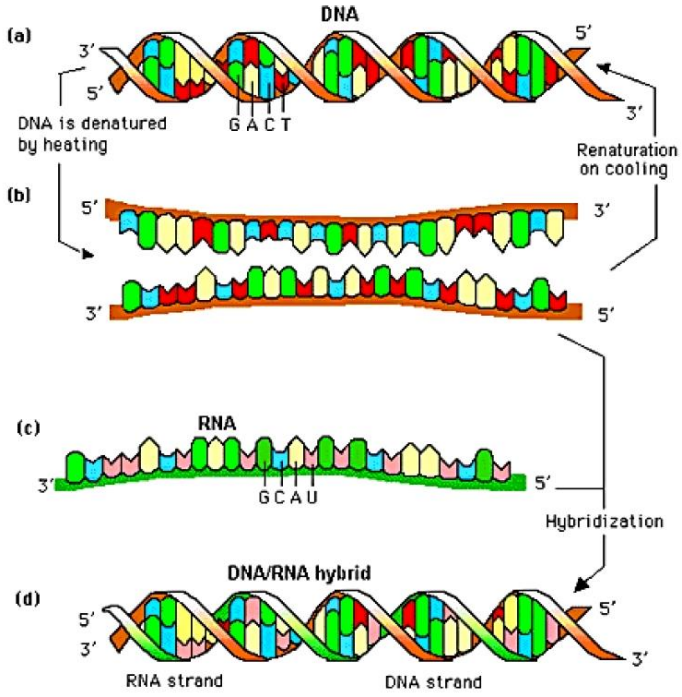

Figure 16. DNA-RNA hybridization. Single-stranded denaturated DNA and RNA molecules are complementary combined into a single molecule of DNA/RNA hybrid [41].

2.3 DNA attachment on the diamond surface

The surface of diamond requires specific surface modification for attachment of biomolecules to serve as biosensos. Because detection of biomolecules is often carried out in a liquid environment, immobilized molecules must be stable to preserve their biological activity and the sensor sensibility. The attachment of molecule to the surface can be achieved either by non-covalent physical adsorption (electrostatic interaction and Van der Waals forces) or covalent bonds (-NH_2, -COOH, -SH, C-C…). For example, a DNA molecule can be directly attached on a functionalized diamond surface or by using linkers [43] [22] [42] [15].

2.3.1 Diamond surface termination

Hydrogen termination

The diamond surface can be hydrogenated by exposure in pure hydrogen plasma. CVD grown diamond surface is naturally hydrogenated after a growth in hydrogen rich plasma. Hydrogen terminated surface is hydrophobic with water contact angles around 90° and higher. Hydrogenated surface of undoped diamond shows p-type surface conductivity when exposed to air and it has already been applied for biosensing applications using electrochemical impedance spectroscopy (EIS) [44] [45]. Hydrogen termination is very stable in air, but it can be removed in a strong oxidizing environment [42] [44]. Hydrogen termination is also used as an initial step for further functionalization. Hydrogen termination is also important for halogenation [46].

Oxygen termination

Oxygen terminated surface can be achieved by exposure to oxygen plasma, ozone treatment or wet chemical oxidation as for instance by a mixture of boiling sulfuric acid (H_2SO_4) and potassium nitrate (KNO_3). Oxygen termination is chemically not well defined and refers to a mixture of different groups (=O, –OH, –COOH, –C–O–C…) on the surface. Oxygenated diamond surface is stable, hydrophilic and electrically insulating [22] [42] [44].

Halogen termination

Halogenation is important for further bio-functionalization. Initial step for halogenation is hydrogen termination of the diamond surface. Then, chlorination and fluorination are obtained by radical reactions using thermal excitation of Cl_2 or F_2/Ar/Ne gas and by ultraviolet photo-excitation in Cl_2 or F_2/H_2 gas [15] [46] [47]. Bromination and chlorination are also achieved by wet-chemical method of

radical substitution reactions [48] [49]. Chlorination is achieved by dipping in chloroform with sulfuryl chloride at 50 °C [50]. Ultraviolet illuminated Chlorinated surface radiation in ammonia (NH_3) leads to amine-modified diamond. Halogenated diamond can react with nucleophilic reagents in substitution reactions leading to amino or acid terminations and linker molecules can be attached on the surface [22] [42].

2.3.2 DNA grafting

Most of the DNA biosensors work on the principle of DNA hybridization. A sensor surface is functionalized with ssDNA probes, which are complementary to a DNA sequence for detection. If the target DNA sequences are present in an analyte, they hybridize with the ss-DNA probes into the ds-DNA molecules.

The choice of suitable functionalization of the diamond surface is important for a stable immobilization of single stranded ss-DNA probes and efficient detection of DNA hybridization. It is necessary to select the optimal surface functionalization with respect to a detection principle. For instance an optical, electrochemical or mass detection principle based biosensors may have different requirements for bio-functionalization [44] [51].

Positioning of DNA probes and their orientation is also critical for the efficiency of the detection. Theoretical DNA density on an ideal hydrogenated (100) diamond is $\sim 3 \cdot 10^{15}$ dangling bonds per area of 1 cm^2 on an ideal, unreconstructed (100) crystal [42]. As a cross-section of a ds-DNA is approximately 4 nm^2, thus a maximum of $2.5 \cdot 10^{13}$ ds-DNA molecules can be attached on a 1 cm^2 surface. However, to preserve the bio-functionality of DNA hybridization a maximum DNA density $\sim 10^{12}$ cm^2 is preferred [42].

Density and orientation of the DNA on the sensor's surface is important for the sensitivity of the biosensor. Attached DNA should have a high density, preferably vertical orientation to the surface, while avoiding steric hindering. For an effective immobilization of DNA probes it is necessary to arrange its placement on a diamond surface with respect to DNA size (diameter ~2.5 nm and length ~25 nm) [42].

There exist several different techniques diamond surface functionalization. Some of them are presented below.

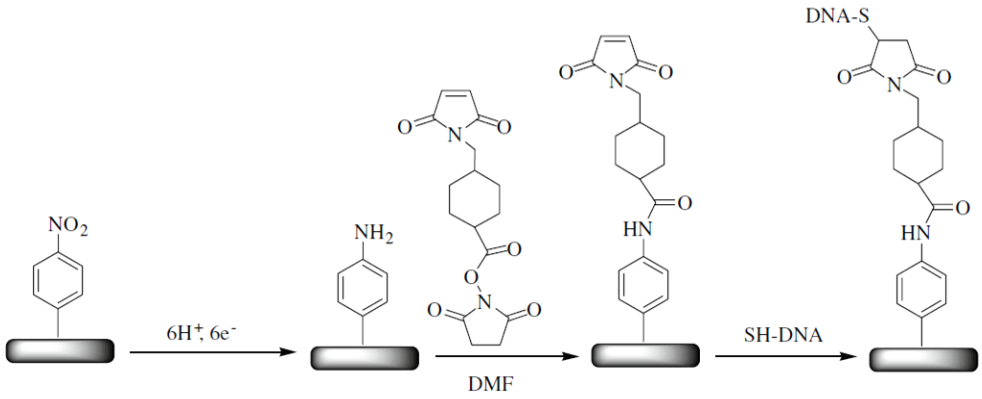

Figure 17. Covalent linking of DNA using a heterobifunctional cross-linker (sulfo-succinimidyl4-(N-maleimidomethyl) cyclohexan-1-carboxylate) to which thiol-modified DNA was linked [44].

DNA probe immobilization can also be achieved by immersion of amine-terminated diamond into a heterobifunctional cross-linker SSMCC (sulfo-succinimidyl 4-(N-maleimidomethyl) cyclohexan-1-carboxylate) to which thiol-modified DNA can be linked (Figure 17) or DNA can be bonded to NH_2 functionalized surface prepared by photochemical or electrochemical reactions (Figure 18) [44].

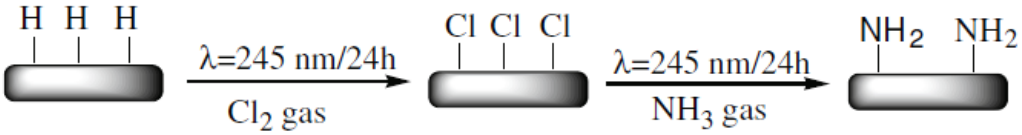

Figure 18. Preparation of an amine-terminated BDD surface in a two steps procedure, consisting on the photochemical irradiation of a hydrogenated surface with chlorine followed with ammonia gas [44].

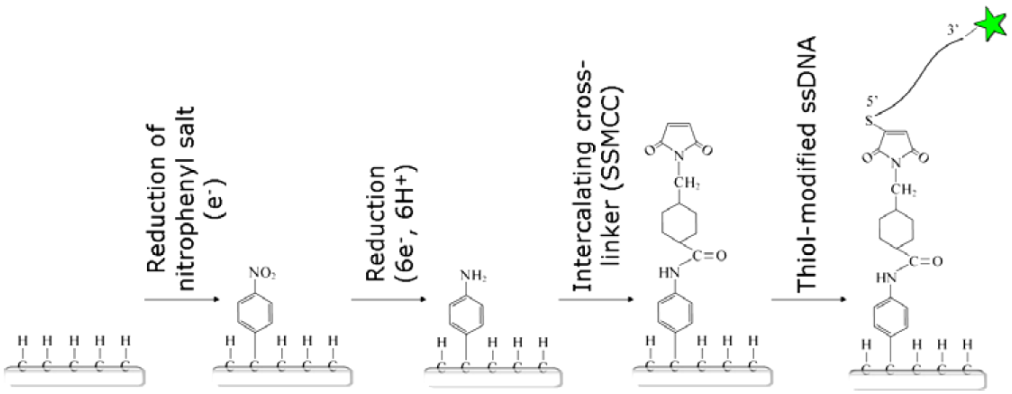

Figure 19. Thiol-modified ss-DNA covalent attachment on hydrogen terminated diamond surface by reduction of nitrophenyl salt using the intercalating crosslinker SSMCC [42].

Covalent attachment of thiol-modified ss-DNA on amino functionalized boron doped diamond surface can also be realized by reduction of nitrophenyl salt at the hydrogenated surface of the diamond using the intercalating cross-linker SSMCC (Figure 19) [42].

Figure 20 shows appropriate functionalization technique for optical as well as electrical DNA detection. Carboxylic acid is attached directly on a hydrogen terminated diamond surface by photo-attachment of 10-undecenoic acid linker (UA). In the second step the zero-length crosslinker 1-ethyl-3-(3-dimethylaminopropyl)-carbodiimide (EDC) is covalently bonded to the ssDNA probe [42].

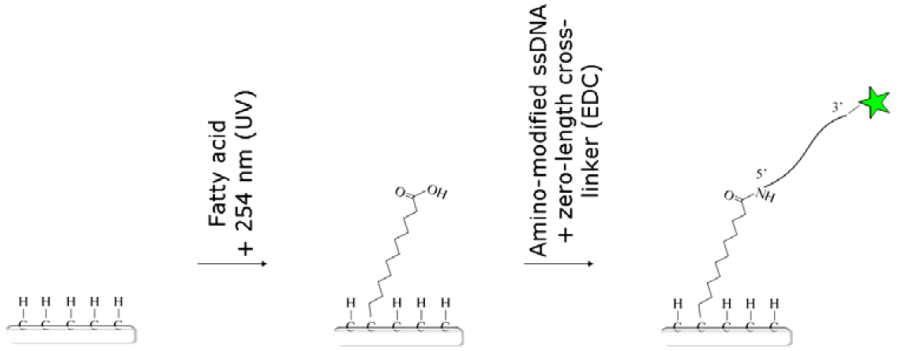

Figure 20. Attachment of 10-undecenoic acid linker molecule and ssDNA probe [42].

Summary of most commonly used diamond surface functionalizations are shown in Figure 21.

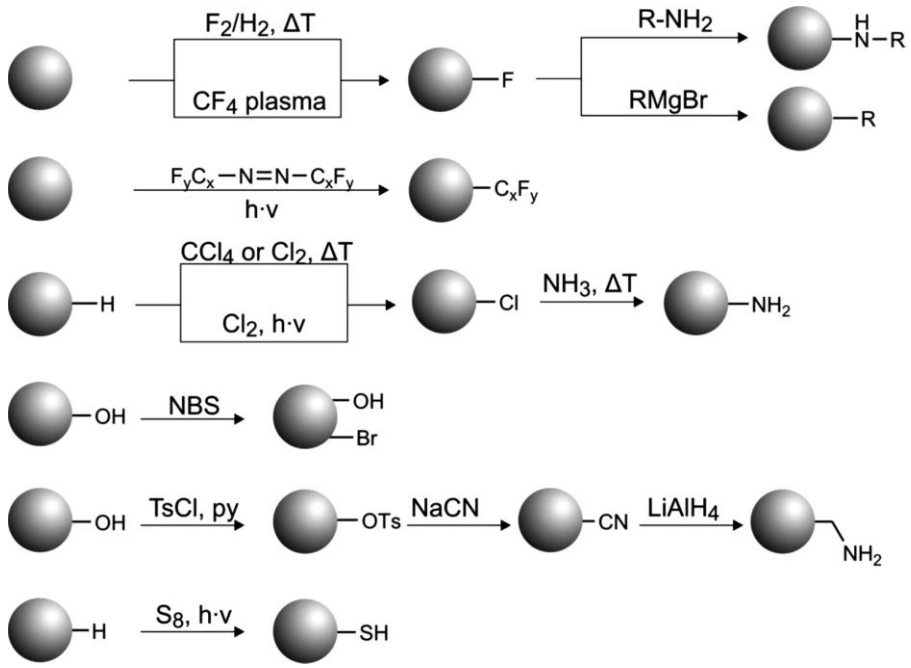

Figure 21. Different surface functionalization routes of nanodiamond particle: halogenation, amination, formation of thiol and nitrile groups. (Icons for ND that do not show specific termination symbolize the possibility to start with different materials) [46].

2.4 Techniques for DNA detection

2.4.1 Electrochemical detection methods

Electrochemical readout is a very suitable technique for DNA detection, because DNA reaction usually results in an electrical signal as current, potential or charge accumulation [16] [52]. The output signal can originate for instance from conductive properties of a medium between electrodes, impedance and field-effect, which uses transistor technology to measure current as a result of a potentiometric effect at a gate electrode [2] [53]. Depending of a bio-functionalized interface and electrode's material, different electrochemical measuring configurations are used. Some of the typically used methods are listed further below.

Typical electrochemical DNA sensor consists of an electrode, capture probe and reporter probe (the capture and reporter probes can be combined), which are specific to the target DNA Boron doped diamond is a perfect material for a working electrode. A captured DNA probe is often immobilized onto a functionalized solid surface through a linker molecule and a complementary targeted DNA flowing in a buffer solution. A reporter probe is a molecule that generates the electrochemical signal in response to the hybridization process. Hybridization response can be based on several reactions as a change of probe structure or diffusion of a redox indicator ($[Fe(CN)_6]^{3-/4-}$) [16] [53].

Voltammetric measurements

The basic principle of voltammetry is based on an application of a time dependent potential excitation signal to the working electrode, which results to a change of its potential relatively to the fixed potential of the reference electrode and output current. Several measurement methods exist and they can be divided into linear, pulse or cyclic voltammetry [54] [55].

Cyclic voltammetry

Cyclic voltammetry (CV) is one of the most common electrochemical detection techniques based on scanning in both directions (positive and negative). The voltage is measured between the reference electrode and the working electrode, the current is measured between the working electrode and the counter electrode. Measured current is plotted vs. voltage in the so called voltammogram (Figure 22). Increase of the voltage in positive values results in increase of the current until the oxidation

potential of the analyte is reached, then the current decreases. Reversible scanning in negative voltage direction results in a decrease of the current to the reduction potential, and then the current again increases [2] [54].

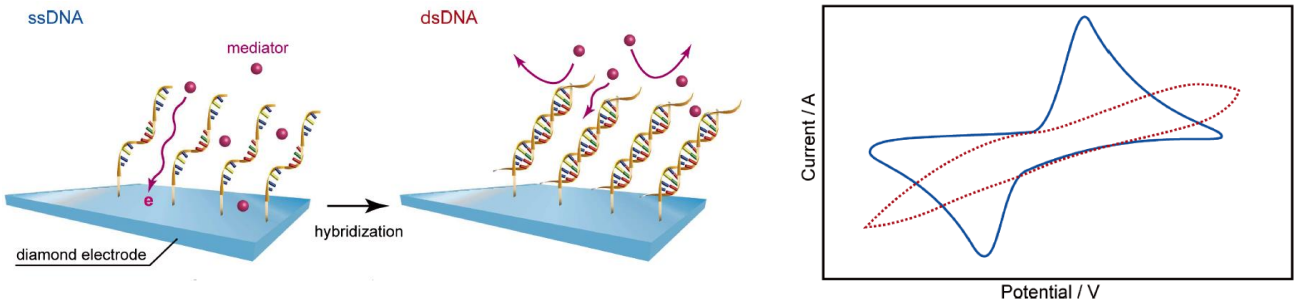

Figure 22. (Left) Scheme of DNA sensing on diamond electrodes using negatively charged redox mediator molecules. (Right) Diffusion of redox mediators toward the diamond electrode results in a peak shaped voltammogram (solid line). The inhibition of redox mediator's diffusion due to DNA hybridization leads to a decrease in the peak currents and a broader peak splitting (dotted line) [16].

Figure 22 shows example of the change of cyclic voltammogram induced by the diffusion of negatively charged redox mediator before and after DNA hybridization. Diffusion of redox mediators toward the diamond electrode results in a peak shaped voltammogram. The inhibition of redox mediator's diffusion due to DNA hybridization leads to a decrease in the peak currents and a broader peak splitting [16].

Differential pulse voltammetry

The electrochemical configuration for differential pulse voltammetry (DPV) is usually the same as in a standard voltammetry with few differences. The applied potential is pulsed instead of continuous. Current is measured immediately before the pulse application and at the end of the pulse. The difference between the two currents is monitored [54] [55]. Martin Bartosika et al. studied differential pulse voltammetry electrochemical hybridization detection based on streptavidin modified magnetic beads. Biotinylated DNA capture probes were complementary attached with microRNA labelled by Os(VI)bipy [56].

Impedance measurements

Electrochemical impedance spectroscopy (EIS) for DNA sensing is based on change of bio-interface impedance of bio-functionalized working electrode, where both real and imaginary components of impedance (electrical resistance and reactance) are characterized. EIS can study any intrinsic material property or any process, which induces a change of conductivity/resistivity or capacitivity of an electrochemical system [2].

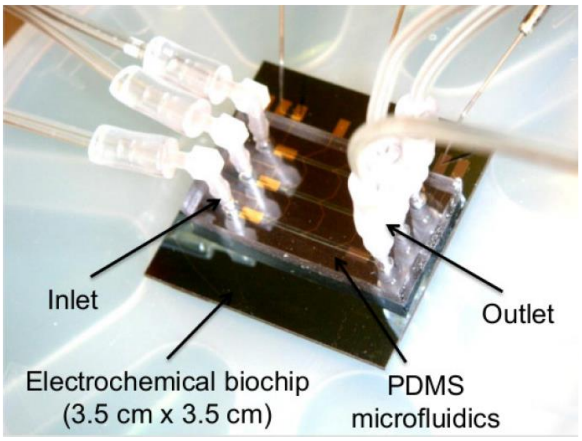

Figure 23. Photo of the electrochemical microfluidic chip for DNA hybridization detection [12]

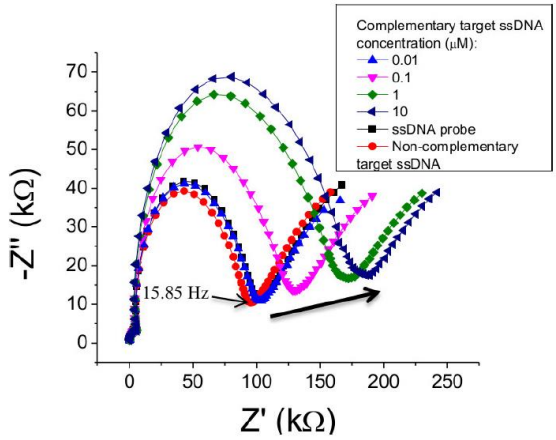

Figure 24. Nyquist plot of the hybridization reaction with different concentration of target ssDNA probes [12].

Hadar Ben-Yoav et al. constructed a microfluidic electrochemical chip for DNA hybridization detection. In the Figure 23 is shown the photo of the chip and in the Figure 24 the Nyquist plot as a response to the different concentrations of ssDNA target probes [12].

Electrolyte-diamond-insulator-semiconductor (EDIS) sensors

Insulating diamond deposited on top of boron doped diamond can be used as a capacitive field-effect sensor (electrolyte-diamond-insulator-semiconductor - EDIS). It is possible to even detect uncharged biomolecules using this technique [42].

M. H. Abouzar et al. realized label-free electrical detection of charged multilayers with an EDIS sensor using the ConCap response to the signal changes as a function of polyelectrolyte layer number. Adsorption of negatively charged poly (sodium 4-styrene sulfonate) (PSS) molecules decrease the potential, whereas the adsorption of the positively charged poly allylamine hydrochloride (PAH) molecules increases the potential [57].

Electrolyte-gated field effect transistors (FET)

A. Blin et al. studied electrolyte-gated field effect transistors (FET) for label-free detection of DNA hybridization with micro-spots. Figure 25 shows the FET array measurement configuration. DNA probes are immobilized onto the two regions P1 and P2 of gate oxide surfaces. Each of the regions consists of several individual transistors. The surface of the device is covered by a KCl solution and an Ag/AgCl is used as a reference electrode. Specific hybridization induced shifts in the FET threshold voltages of a few mV [58].

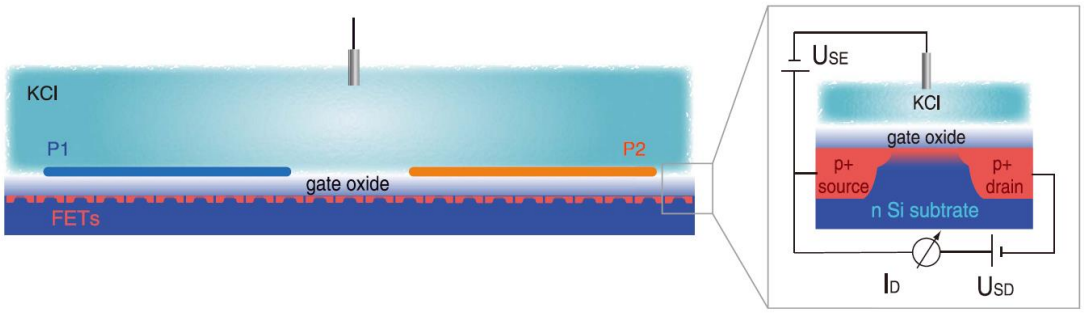

Figure 25. The FET array configuration. On the left is cross sectional view of an FET array with two regions for probes attachment on the oxide surface P1 and P2 with several individual transistors (red underneath the gate oxide), covered by KCl solution and an Ag/AgCl reference electrode. On the right is scheme of an individual transistor and its electrical circuits [58].

2.4.2 Optical detection methods

The most common optical method to detect hybridization of oligonucleotides is based on fluorescence. Fluorescence detection is a frequently used technique in laboratories [42]. A very sensitive optical biosensor called gene-chip microarray based on fluorescence and containing thousands of unique probe sequences is commercially available from the provider The Affymetrix GeneChip (Figure 26a). This device allows the parallel investigation of many of genes [8]. This detection of large number of gene sequences is more suitable for laboratories than for clinical diagnostic [52] [10].

In addition to commonly used fluorescence detection, other optical biosensors based on different detections exists. For instance, Ying Ma et al. developed the amplified resonance light scattering detection of DNA hybridization using nucleic acid–based polycyclic aromatic hydrocarbons (naphthalene, pyrene, fluoranthene, anthracene, and phenanthrene) as a probe [59]. Surface Plasmon Resonance (SPR) is another method for detection of DNA hybridization based on a change of refractive index of a thin metal film [52].

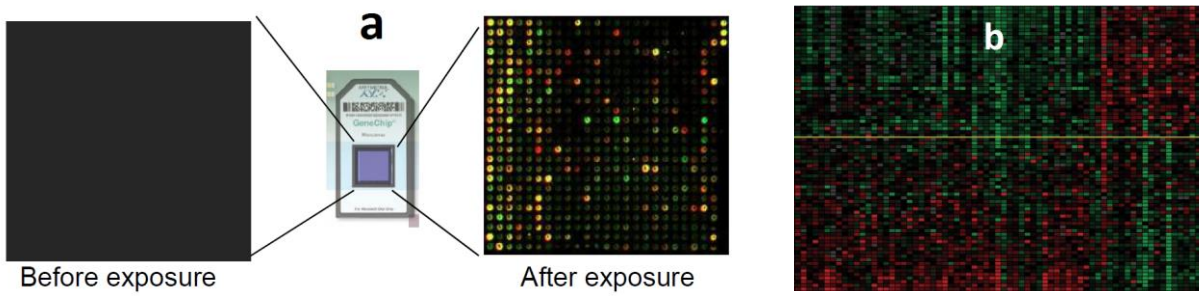

Figure 26. DNA gene-chip microarray: Affymetrix fluorescent gene-chip before and after hybridization [8] (a); hybridization data, where each row represents a tumor tissue from a patient and each column a gene [5] (b).

2.5 Diamond properties for biomedical application

Biocompatibility makes diamond useful for many in vivo and in vitro biomedical applications. Extreme hardness, Young's modulus and low coefficient of friction are suitable properties for diamond coating of implants in tribology or coronary stents [60] [61] [62]. Diamond coating of typical implantable materials such as titanium or stainless steel can improve their biocompatibility, corrosion resistance and deduce their cytotoxicity [62] [63].

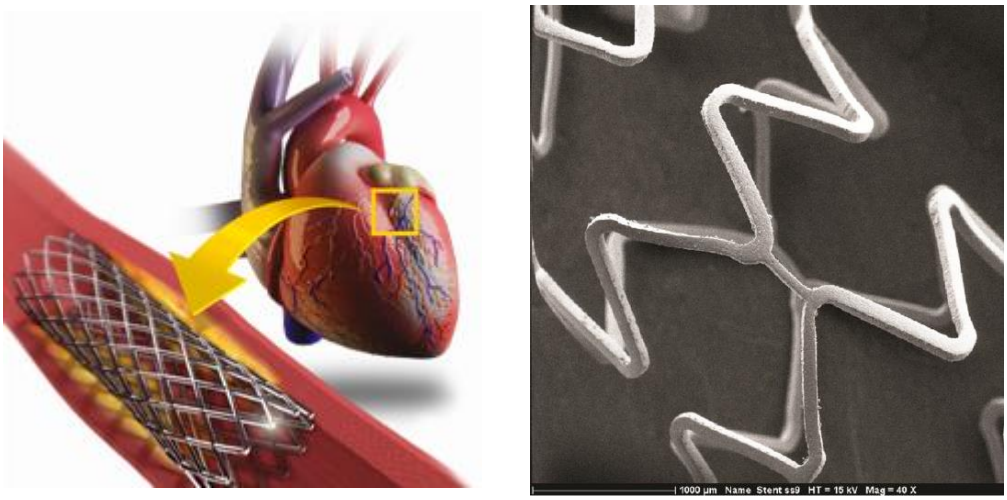

Figure 27. Picture of a metal coronary stent inserted in a coronary artery to restore blood flow, which is reduced or completely stopped by a blockage [64] (left) and nenocrystalline diamond coated coronary stent imaging by scanning electron microscopy: magnified 40x [62].

Diamond was found to be extremely biocompatible to living cells [65]. Diamond surface was also determined to be highly resistant to the adhesion of blood platelets and cells, which allows diamond use for a contact with human's blood [66]. New low pressure and large area diamond chemical vapour deposition systems are promising for industrial coating, including 3D biomedical objects like

prosthesis for instance [67]. Electrical properties such as high resistivity or metallic like conductivity with boron or phosphorus doping, high thermal conductivity and chemical inertness are excellent properties for electrochemistry and bioelectronic devices [52] [6]. Fluorescence, non-toxicity and easy biolabelling of nanodiamonds are promising properties for bioimaging or drug delivery [14] [61].

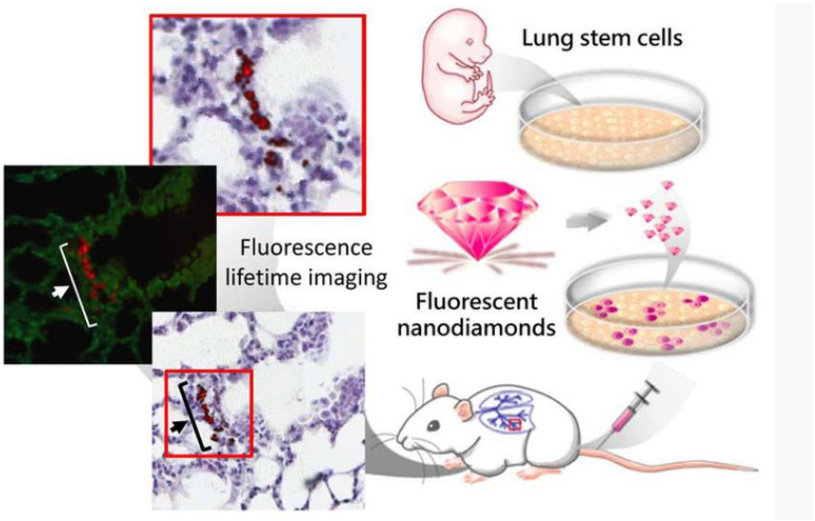

Figure 28. Fluorescent nanodiamonds with NV centres for stem cell tracking [68].

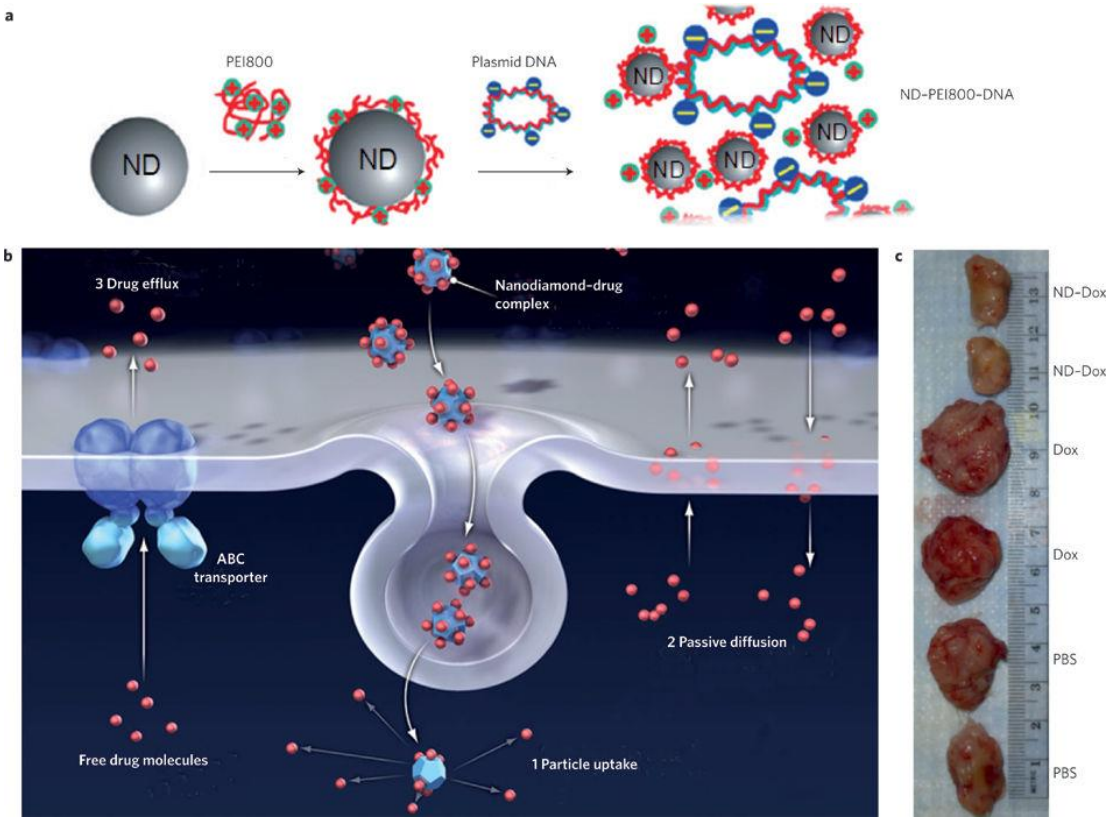

Figure 29. Nanodiamonds for drug delivery [59].

2.5.1 Synthetic diamond

Diamond is made of carbon, where carbon atoms are arranged in a crystal diamond lattice structure with strong covalent sp^3 bonding between the carbon atoms. Diamond has excellent properties such as high hardness, thermal conductivity, optical properties and biocompatibility for biomedical implants and devices. Other allotropes of carbon are graphite and amorphous carbon with different physical properties. Graphite is characterized by sp^2 carbon bonds and its high electrical conductivity and low hardness. The properties of amorphous carbon (a-C) films depending on the ratio of sp^2 to sp^3 hybridized bonds. If in a-C there are more represented sp^3 hybridized bonds, this material is called as tetrahedral amorphous carbon for more occurrence of sp^2 bonds diamond-like carbon.

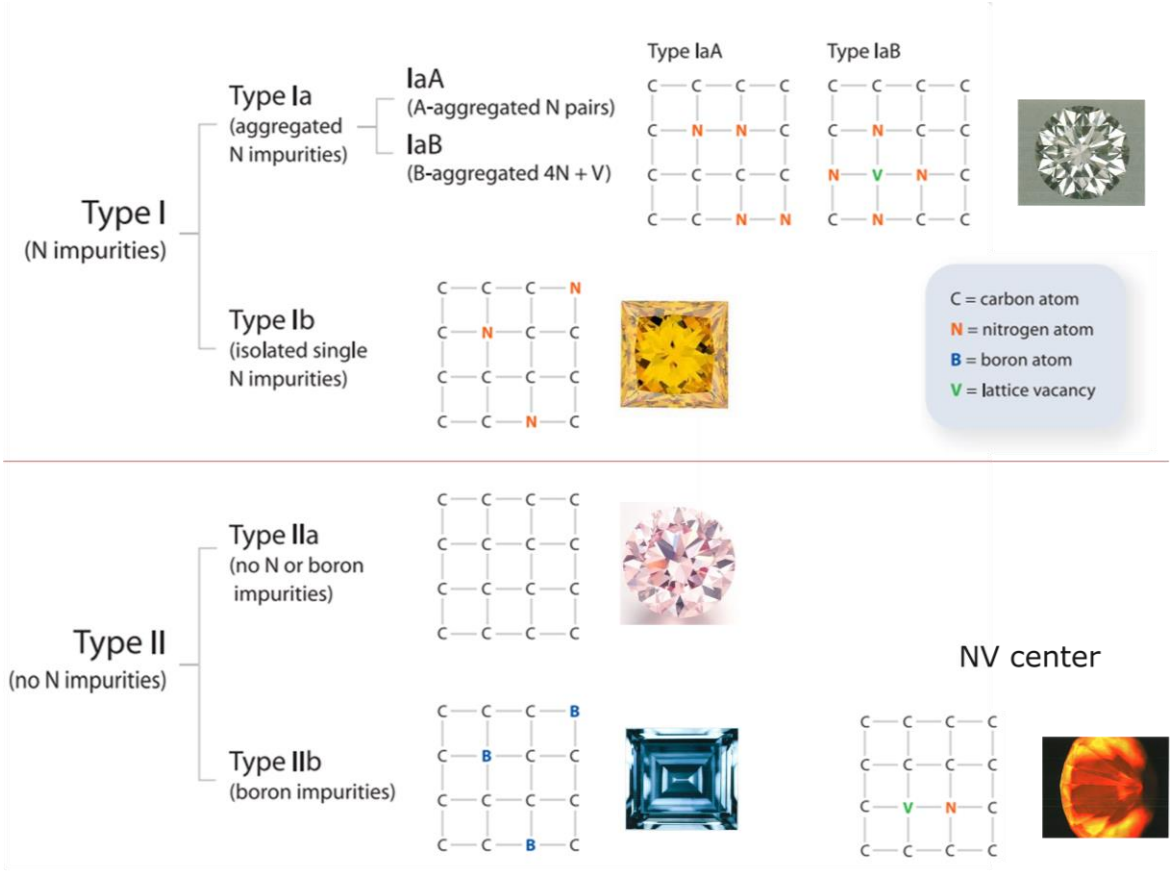

Figure 30. Classification system of diamond [69].

Pure diamond is made of only from carbon atoms arranged in the cubic lattice by covalent C-C bonds. Real diamonds do not consist only of carbon atoms, some impurities such as nitrogen and boron or another atoms or elements can be present in the lattice. Figure 30 shows the diamond type classification system, which divides diamonds into categories based on the presence or absence of certain

nitrogen and boron impurities and the ways in which they are arranged in the lattice. I type diamonds are divided into type Ia (subgroups IaA and IaB) and type Ib, where both subgroups contain nitrogen with a different arrangement in the diamond lattice. Type Ia is composed of nitrogen aggregates whereas type Ib with isolated nitrogen impurities. Type II diamonds are also divided into types IIa and IIb. Type IIa is pure diamond without boron or nitrogen impurities. Type IIb consists of diamond with boron impurities that provides a blue colour and characteristic electrical properties [69].

Synthetic large diamond can be created by a two different processes HPHT (high pressure high temperature) synthesis and low pressure chemical vapour deposition (CVD). HPHT synthesis follows natural conditions for diamond formation, the technique is based on applying high pressure (around 6 GPa) and high temperature (up to 1700 K) on a carbon source (higher temperature) and seed crystal (lower temperature) [70].

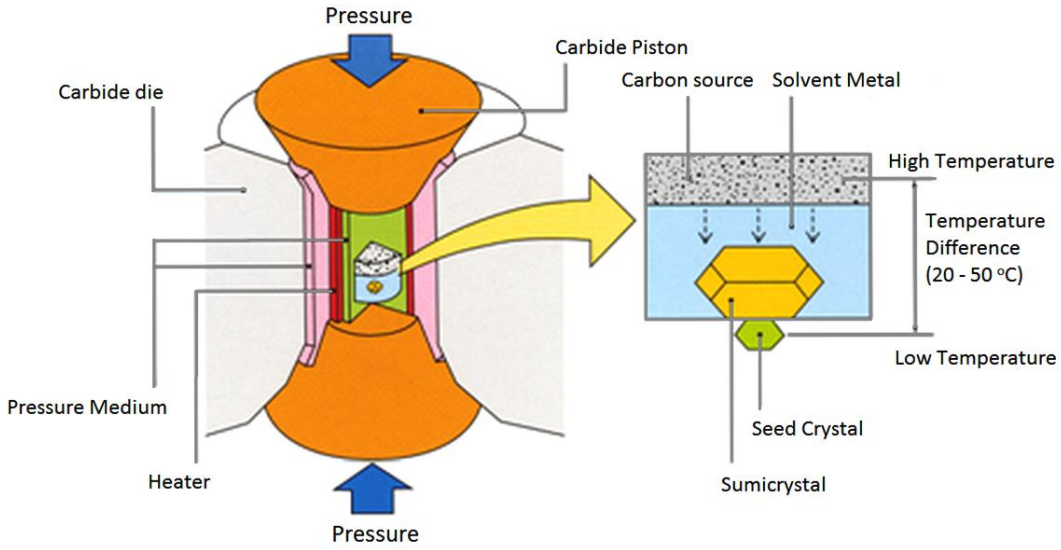

Figure 31. Schematic setup of a “Belt” apparatus for the production of HPHT synthetic diamonds [71].

Low pressure CVD diamond synthesis is based on dissociation of precursors (typically 99 % H_2 and 1 % CH_4) by microwaves, arc discharges or laser beams, leading to the deposition of diamond films on diamond substrates or diamond seeds. Several growth CVD techniques exist as for instance hot filament CVD (HF CVD), combustion CVD (C CVD), plasma enhanced CVD (PE CVD) and others. Principle of the low pressure PE CVD technique is described in the chapter 3.1.

2.5.2 Different form of diamond

Diamonds exist in different forms: bulk crystals, thin films as well as nanodiamonds that will be described in this chapter. Thin films exist with various crystal sizes, morphology and sp^2 bonded carbon concentration. For each form exists a typical synthesising method [22] [45].

Single crystal diamond

Synthetic single crystal diamond is fabricated by high pressure high temperature (HPHT) method or CVD growth (see Chapter 3.1). High quality synthetic single crystal diamond has similar or even better properties than natural diamond. The crystals can be of various form or size from nanometers to few milimeters. HPHT crystals are used as substrates for CVD homo epitaxial diamond growth [72] [73] [74].

The smallest diamonds: Nanodiamonds

Nanodiamond is diamond with a size in nm range. Nanodiamond (ND) small particles of ~ 5 nm in size (Figure 32b) were first prepared by detonation synthesis such as with trinitrotoluene (TNT) and hexogen [75]. Similar small sized particles can be obtained by laser ablation [76]. High-pressure high-temperature synthesis also produces variable sized nanodiamond particles with a minimum size of 30 nm (Microdiamant AG). Nanodiamond particles larger size than 20 nm can also be produced by abrasion of large crystal (Figure 32c) or jet milling [60] [22]. Diamondoid, classifying in nanodiamonds, is cage-like saturated ringed hydrocarbons with a diamond-like structure. It can be synthetized by petroleum purification. Adamantane is the simplest diamondoid molecule (Figure 32a) [77].

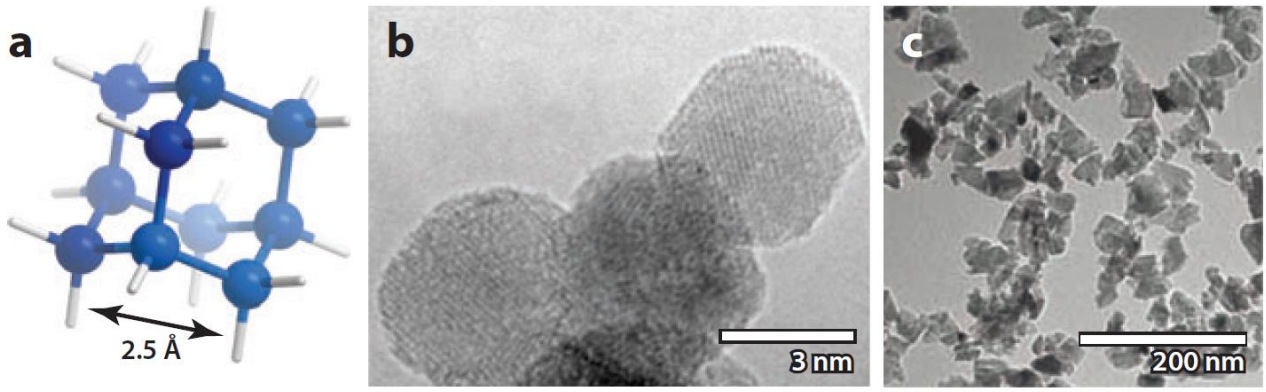

Figure 32. Nanodiamonds: Adamante (a), detonation diamond (b) and nanodiamond particles produced by abrasion of larger crystals [22].

Diamond films

Different forms of diamond films can be distinguished by crystal size, and content of sp^2 bonded carbon. Ultra-nanocrystalline diamond (UNCD) films consists of re-nucleated diamond grains with size around 5 nm surrounded by sp^2 bonded carbon (Figure 33a). UNCD films are prepared in argon rich plasma-enhanced chemical vapour deposition (PE CVD). Nanocrystalline diamond films (NCD) has crystal size usually below 100 nm grown from diamond seeds and contain less sp^2 on crystal boundaries than UNCD (Figure 33b) and there are of columnar structure. NCD films are usually prepared by PECVD in hydrogen rich plasma [60] [78]. Polycrystalline diamond (PCD) films are similar to NCD but with larger crystal size [15]. Single crystal homoepitaxial film (Figure 33c) is a pure diamond in sp^3 form and usually is prepared by PE CVD in hydrogen rich plasma [72] [73] [79].

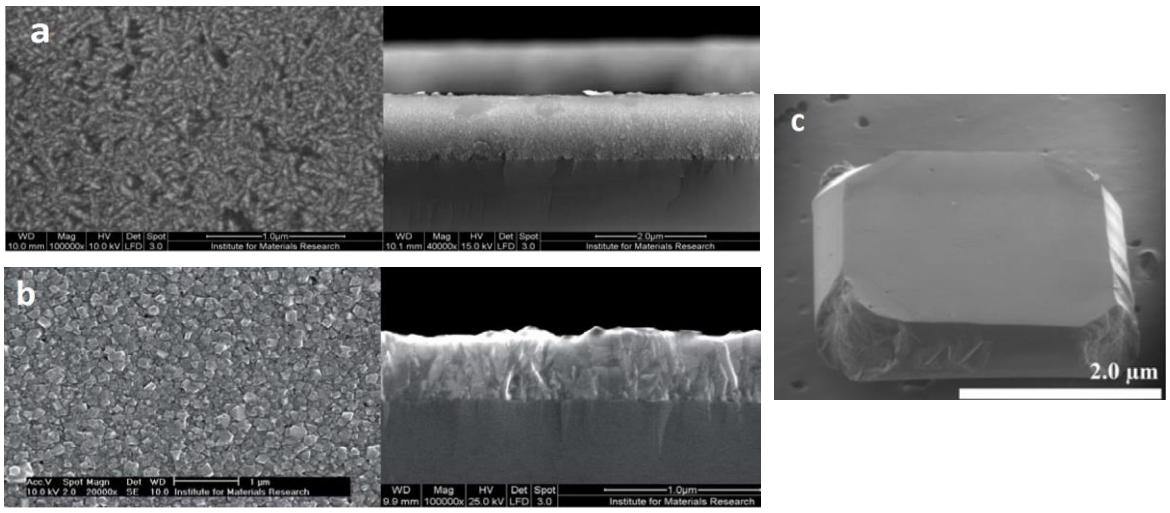

Figure 33. Top view (on the left) and cross section (on the right) of ultra nano-crystalline diamond film on silicon (a), Top view (on the left) and cross section (on the right) of nano-crystalline diamond film on silicon (b) [78], CVD grown single crystal sample removed from its HPHT substrate by laser cutting (c) [15].

2.5.3 Electronic properties of diamond

Semiconducting, metallic and insulating diamond all play an important role in electronic biosensors. Pure diamond is a good insulator. Nevertheless, the surface of undoped diamond can be made conductive by hydrogen termination and it can be used for biosensors. Conductivity of CVD diamond is achieved by addition of a dopant during growth [6]. Doped diamond can be of n or p type.

Conductivity of n-type is obtained by phosphorus or nitrogen doping. On the other hand, the p-type of conductivity is achieved by boron doping, which will be given more attention in this paper. Metallic like diamond conductivity can be obtained by a very large incorporation of B-dopant in the diamond lattice. Metallic like behaviour has also been obtained in highly nitrogen doped ultra-nanocrystalline diamond layers, however in this case the conductivity was caused by pi-bonded carbons. Those UNCD layers grow with strong re-nucleation that results in a small grain sizes and larger grain boundary with conductive sp^2 bonded carbon and nitrogen incorporation probably close to diamond grains [42] [60].

Carriers' mobility in intrinsic diamond is very high. Measurements determined drift mobility at room temperature of 4500 $cm^2/V{\cdot}s$ (electrons) and 3800 $cm^2/V{\cdot}s$ (holes) for single crystal diamond, and 1800 $cm^2/V{\cdot}s$ (electrons) and 1000 $cm^2/V{\cdot}s$ (holes) for polycrystalline diamond [80] [81]. Figure 34 shows experimental and calculated data of carrier mobility and resistivity as function of effective boron doping level for single crystal diamond and polycrystalline diamond [82].

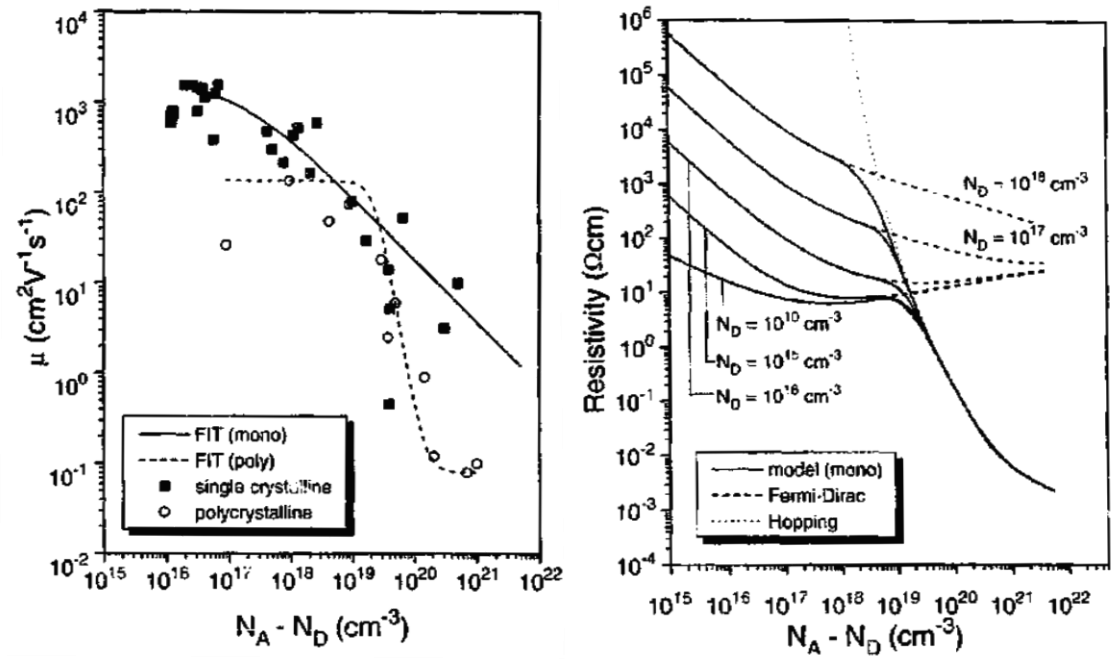

Figure 34. Mobility (left) and resistivity (right) as function of doping concentration for single crystal diamond and polycrystalline diamond [82].

Diamond with boron concentration levels below $3{\cdot}10^{18}$ cm^{-3} exhibits clear extended state transport. Boron concentrations between $3{\cdot}10^{18}$ cm^{-3} and $2{\cdot}10^{20}$ cm^{-3} show thermal activated hopping transport and finally metallic transport at higher boron concentrations than 2 to $-5{\cdot}10^{20}$ cm^{-3} [60] [78].

2.5.4 Optical diamond properties

Refractive index of the diamond depends on a wavelength of an incident radiation, for 589 nm wavelength it is ~2.42. Type IIa diamonds are transparent from UV to far IR with one of the widest optical band gap of around 5.5 eV. Diamond type I and IIb absorb in wide range of energy from UV to IR with typical absorption energies depending on the defects in crystal lattice such as impurities, dislocations, vacancies, and complexes which create new vibration and electronic energy levels within the band gap [42] [69].

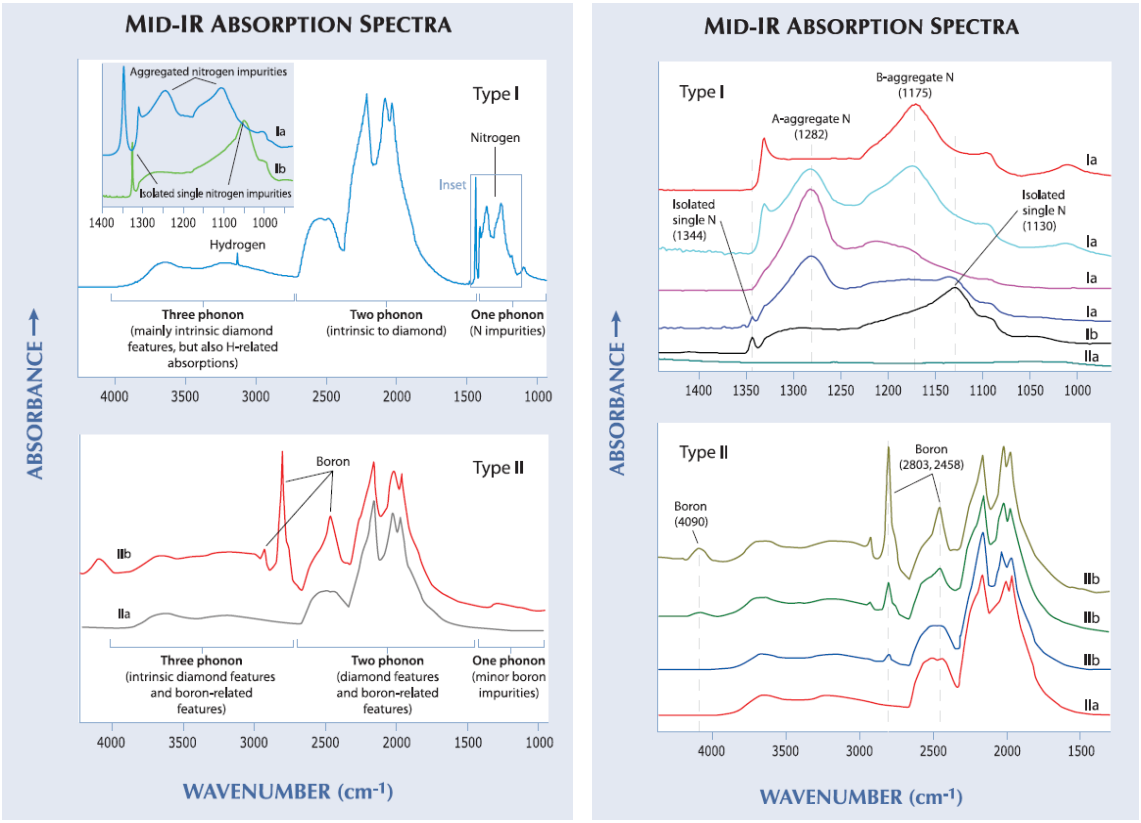

Figure 35. FTIR mid-IR absorption spectra of diamond type I and II, related to three phonon regions for diamond type I (on the left up) and type II (on the left down) (a) and determination of nitrogen impurities in diamond type I (on the right up) and boron absorption intensity peaks depending on boron concentration in IIb diamond type (on the right down) (b) [69].

Although diamond is transparent, there are some absorption bands in mid-IR range (4000 – 400 cm^{-1}) with specific absorption peaks from which the type of diamond can be determined by Fourier transform infrared spectroscopy (FTIR). Figure 35a shows mid-IR absorption FTIR spectra of diamond type I and II divided in to the three absorption phonon regions. In the one-phonon region (~1332 to ~400 $cm^{-1)}$ are nitrogen impurities related to I type of diamond. The two-phonon (2665 to

~1332 cm^{-1}) and three-phonon (~4000 to 2665 cm^{-1}) regions contain common features for all types of diamond caused by vibration of carbon-carbon bonds of the diamond lattice and easily detected absorption peaks belonging boron impurities in IIb diamond type. Configuration of nitrogen atoms in diamond lattice and estimation of boron concentration can be established from IR absorbance spectra (see Figure 35b) [69].

Diamond type I and II can be also distinguished using the property of short-wave UV transparency. Type I diamonds absorb short-wave UV radiation (~254 nm), but type II diamonds allow such wavelengths to pass through (see Figure 36). This absorption property of I diamond type can be used for diamond based UV detectors [42] [69].

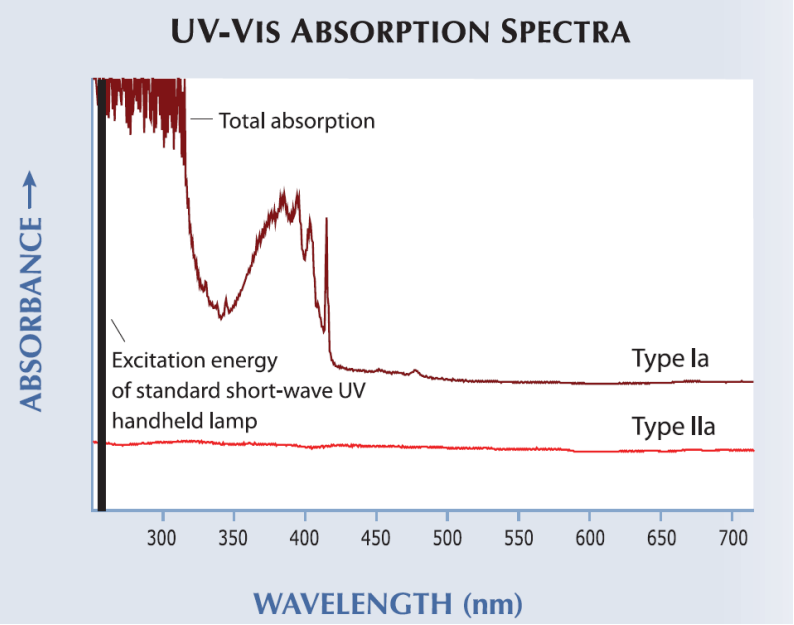

Figure 36. FTIR UV-Vis absorption spectra of diamond type I and II [69].

The transparency of the diamond does not depend solely on its impurities. The transparency of a diamond is also affected by so called colour centre defects or by defects of the crystal lattice as dislocations [6] [60] [83]. Grain size and sp^2 bonded carbon on grain boundaries of other types of diamonds with a different morphology such as ultra-nanocrystalline, nanocrystalline or polycrystalline diamond strongly affect the optical properties. The ultra-nanocrystalline diamond films consist of renucleated diamond nano-crystals with high amount of sp^2 bonded carbon which gives to these films high electrical conductivity and absorption. Nanocrystalline and polycrystalline diamond with large grains are mostly transparent. Higher the grain size and the thickness, means higher layer transparency [6] [60].

2.6 NV colour centres in diamond

Pure diamond is transparent in the visible region. Observed colours in the diamond are caused by defects in the crystal lattice such as impurities, dislocations, vacancies, and complexes leading to the electronic energy levels creation within the band gap. Diamond is an unique crystal material as it is the only material with around 500 photo stable colour centres with absorption or emission from the UV to the near infrared [19] [20] [22]. Nitrogen is the most common impurity in diamond and it can be found in several forms of impurities: N3 defect consists of three nitrogen atoms surrounding a vacancy with an emission line at 415 nm, H3 is an uncharged defect $(N\text{-}V\text{-}N)^0$ consisting of two nitrogen atoms separated by a vacancy with an emission line at 503.2 nm, 3H is a negatively charged V^- vacancy in the diamond lattice with an emission line at 503.5 nm, GR1 is a single, uncharged vacancy in the diamond lattice with an emission line at 741 nm and H2 is a negatively charged defect $(N\text{-}V\text{-}N)^-$ that consists of two nitrogen atoms separated by a vacancy with an emission line at 986 nm [69]. Finally, nitrogen vacancy (NV) centres are the most studied colour centres within a diamond with a high potential in biomedical applications as fluorescence biomarkers or biosensors.

NV centres consist of a substitutional nitrogen atom lying next to a vacancy in the diamond lattice and it occurs in two charge states neutral NV^0 with the zero phonon line at 575 nm and negative NV^- charge states with the zero phonon line at 637 nm [19] [20]. Fluorescence and magnetic properties of NV centres are very promising for biosensing and biolabelling [14] [22]. NV colour centre is extremely bright and a single centre can be seen at room temperature.

2.6.1 Electronic structure of the NV centres

Figure 37 shows scheme of the NV^0 and NV^- centre in the diamond lattice. The electronic structure of the NV^0 centre includes 5 electrons (Figure 37 and 41). Two are provided by the nitrogen atom, and another three are dangling bonds from the three carbon atoms surrounding the vacancy. The NV^0 centre exhibit Zero phonon line at 575 nm. The negative charged NV^- centre is created by a capture of a sixth electron from the lattice (typically nitrogen donors). Electron density for the lowest unoccupied molecular orbital (LUMO), which is mostly localized on three carbon atoms near the vacancy in a vertical plane to the main NV axis. In the case of the highest occupied molecular orbital (HOMO) electron the density is higher around the nitrogen atom [20]. The NV^- Zero phonon line at 637 nm is

the HOMO/LUMO energy gap resulting in a relatively high dipole moment, a rapid spontaneous emission rate (12 ns) and pronounced Stark shift [20] [22] [84].

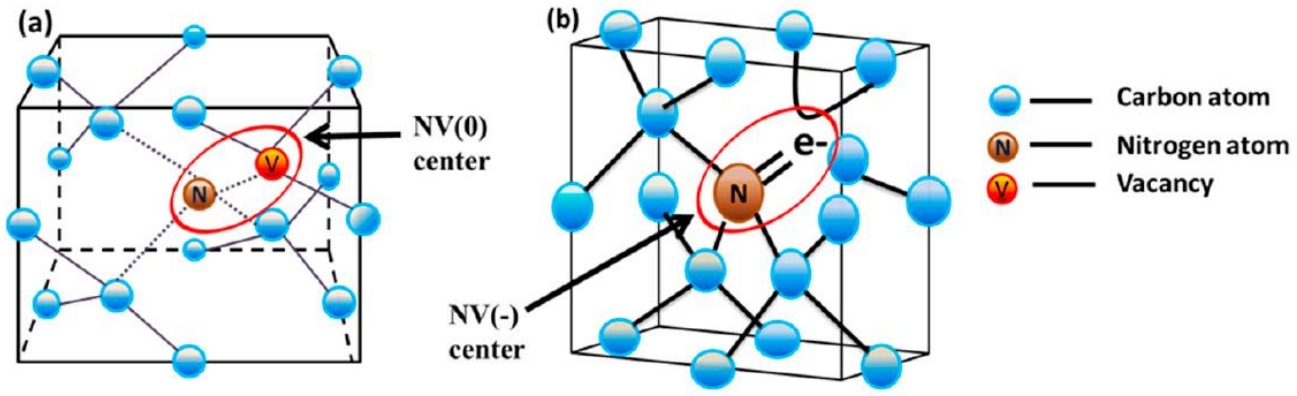

Figure 37. Scheme of the neutral charged NV^0 centre (a) negatively charged NV^- centre (b) [18].

2.6.2 Optical and spin properties of the NV centres

The two charge states of the NV centres are identified by their zero phonon luminescence lines (ZPL) at 575 for NV^o and 637 nm for NV^-. Note that only a few percent of the photons are emitted into the zero phonon line, very broad emission appears in vibrational side bands between 630 and 800 nm (see figure 38) that limits the use of the NV centres for many applications [19] [22].

Figure 39 shows a simple energy-level diagram of the NV^- centre. The radiative lifetime of the excited state is approximately in the range of 10- 25 ns depending on the NV charge state [22].

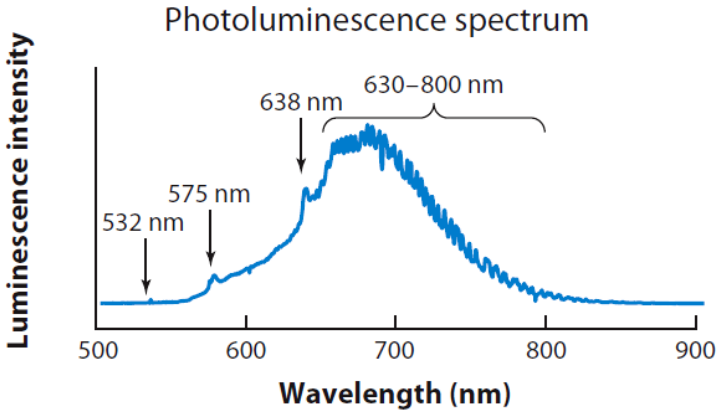

Figure 38. Photoluminescence spectrum excited with 532 nm laser of NV^0 (575 nm) and NV^- (638 nm) with NV^- vibrational side bands (630–800 nm) [22].

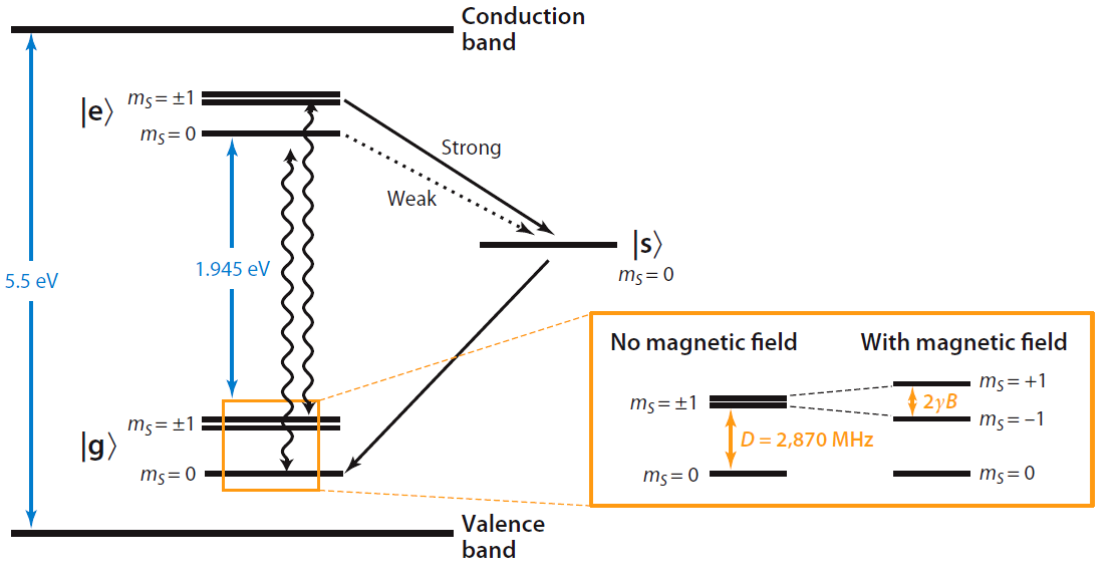

Figure 39. Energy-level diagram of NV^-. **Ig>** denotes the electronic ground state, **Ie>** the electronic excited state, and **Is>** the metastable singlet state. The wiggly arrows indicate the radiative transition, and the black arrows indicate strong and weak nonradiative decay via the singlet state. (Inset) The three spin sublevels with $m_S = 0$ and $m_S = \pm 1$ at zero and nonzero magnetic field B. D is the zero-field splitting and $2\gamma B$ is the Zeeman splitting, where γ is the electron gyromagnetic ratio. By convention, the lower energy transition is associated with $m_s = -1$ [22].

The NV^- centre spin property (spin tripled S = 1) is used in electron paramagnetic resonance (EPR) detection techniques by using a combination of magnetic field and microwave pulse. The ground and excited states are spin triplet (S = 1) are further split into three spin sublevels (0, +1, -1). The difference between this 0 and +- 1 spin sublevels (called zero-field splitting) is D = 2.87 GHz for the ground state and D = 1.42 GHz for the excited state. If the external magnetic field is applied, a Zeeman splitting occurs resulting in a split and shift of the magnetic $m_S = \pm 1$ levels in opposite directions and degeneracy between $m_S = \pm 1$ is lifted (see Figure 39) [22] [85].

Optically detected magnetic resonance (ODMR) is a combination of electron paramagnetic resonance (EPR) and luminescence. Spin-dependent luminescence can be performed using electron EPR experiments on a single electron spin by using microwave energy. Fluorescence intensity is measured as a function of microwave frequency. Figure 40 shows ODMR detection of single NV^- centre with and without external magnetic field [22] [23].

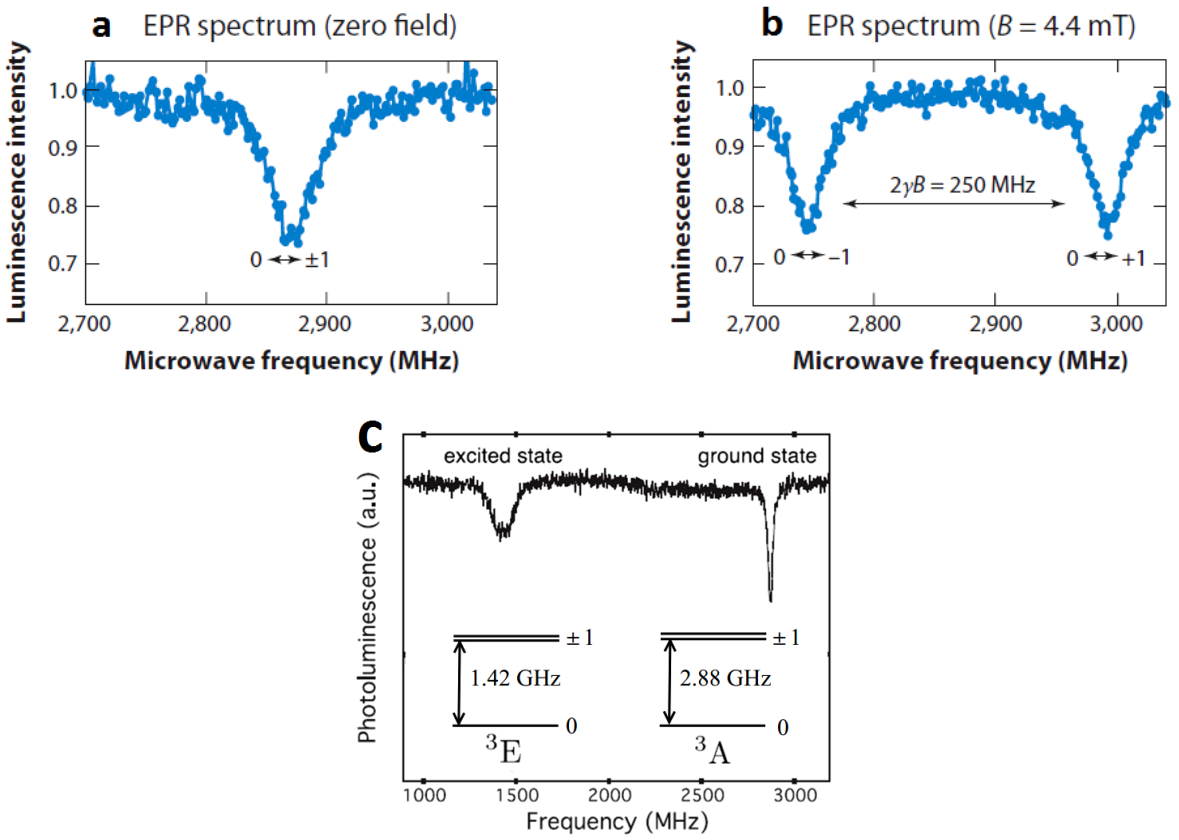

Figure 40. Electron paramagnetic resonance (EPR) spectrum of a single NV centre at zero (a) and nonzero (b) magnetic field, recorded using the ODMR technique [22]; room temperature ODMR spectra of a single NV^- center at ground state (zero magnetic field) and excited state (non zero magnetic field) (c) [86].

2.6.3 Charge state control of the NV centres

The electrons in the NV^- centre with specific spin properties can be used for quantum spin manipulations, important for magnetic field sensing. Because of this is preferred NV^- charge state and thus the ratio of NV^-/NV^0 is required to be maximal [19] [22] [32]. However the NV charge state can be used for sensing of the electric field in the close vicinity of NV centre [87].

Charge state NV detection of biomolecules carrying a charge is based on switching of the close surface NV luminescence between NV^0 (575 nm) and NV^- (638 nm) as a response on the diamond surface charge termination by a manipulation of the Fermi level position. Positive surface termination tunes the Fermi level position below NV^- transition level to NV^0 or even non-photoluminescent NV^+ charge state (lose electron), while negative surface termination above the NV^- transition level to NV^- (receive electron), and related PL is detected [19] [24] [88]. The inter conversion of NV^0 and NV^- charge state

can be manipulated passively by the diamond surface termination [88] [24] or actively by optical [26] [27] or electrical [21] [28] [29] [30] [31] control (Figure 41).

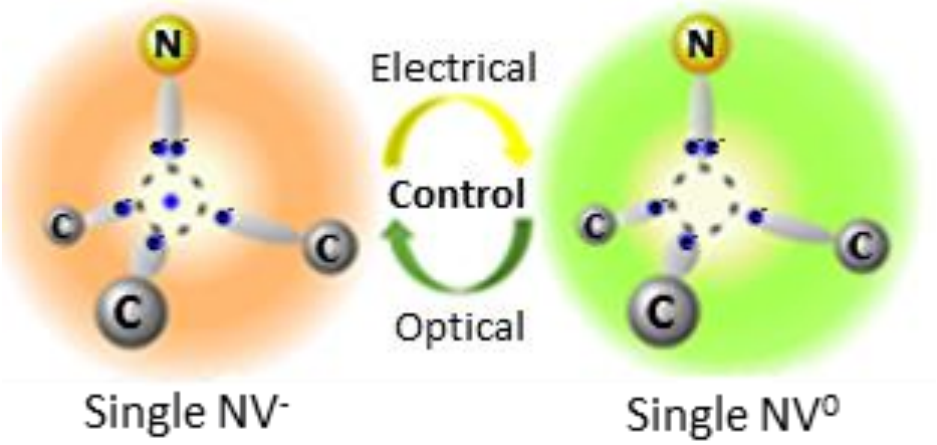

Figure 41. The inter conversion of NV^0 (5 electrons) and NV^- (6 electrons) charge state by optical or electrical control [89].

2.6.3.1 Passive control of NV charge state

Passive control of the NV centre charge state is realized by the Fermi level control due to dopants and impurities in the diamond lattice. NV^0 to NV^- conversion can be also locally controlled by the position of the Fermi level close to the diamond surface by the diamond surface termination. Hydrogen terminated surface acts as an electron acceptor resulting in more preferable NV^0 charge state, whereas oxygen and fluorine surface termination act as electron donors causing more preferable NV^- charge state and can modify the density of charged state NV centres near the surface [24] [32] [88].

The most commonly used dopants occurring close to NV centres also passively affect charge state of NV centres, boron acceptors lead to increase of NV^0 state, whereas phosphorus donors lead to increase of NV^- state [90].

Another impurity affecting the charge state of the NV centre is substitutional nitrogen donor (N_s) in the diamond lattice. If the NV^0 centre is close to the N_s, the extra electron from the nitrogen donor N_s can be transferred to the NV^0 and thus create the NV^- centre [19] [91]. K. Ohashi et al. [32] studied effect of nitrogen concentration on NV centres in 5 nm thin diamond layer grown on a (001) single crystal diamond substrate. Figure 42 shows the schematics of the energy band bending near the surface for low and highly nitrogen doped layer. When the nitrogen concentration is large, the Fermi level is pushed closer to the conduction band to be situated partially above the NV^- level, allowing the NV centres here to become negatively charged [32].

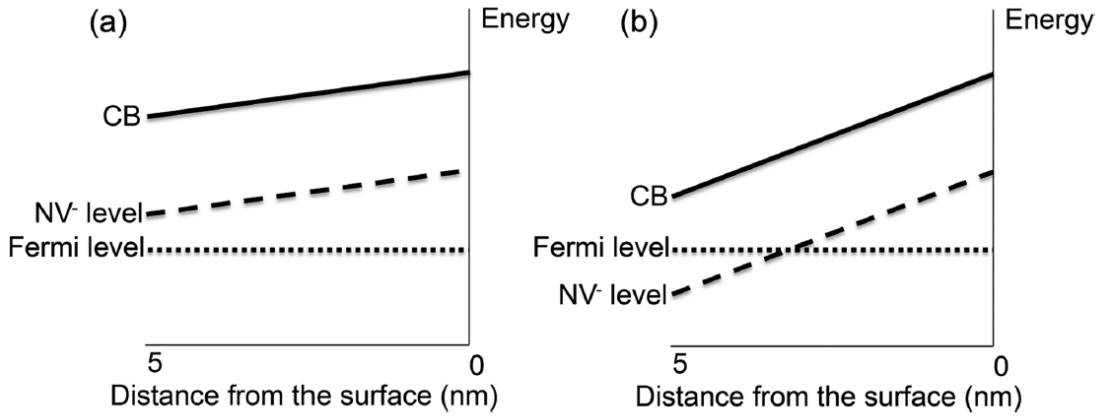

Figure 42. Schematics of the energy band bending near the surface. (a) In case of low nitrogen concentration in the top 5 nm layer, the Fermi level remains far away from the conduction band (CB) resulting in a low concentration of NV^- centres. (b) When the nitrogen concentration in the top 5 nm film is large, the Fermi level is pushed closer to CB to be situated partially above the NV^- level, allowing the NV centres here to become negatively charged [32].

2.6.3.2 Active control

Active control of NV centres charge state can be achieved optically [17, 18] or electrically [19-22]. Internal conversion between NV^- and NV^0 charge state can be controlled optically by using different laser power and wavelengths [26] [27]. Another possibility of the active NV centre charge state control is by applying of an external electric field, which shifts the NV centre transition Fermi level. By applying different voltages the NV centres can be switched between NV^-, NV^0 and NV^+ charge states. For the active electrical control of the NV centre charge state were recently used devices with p-i-n junction [92], Schottky junctions [21] [29], gate structures [30] were recently used. NV centre charge state can be manipulated also in the electrochemical cell by the application of the electrochemical potential [31].

2.6.4 Fabrication of the NV centres

There are three main methods to engineer NV centres in diamond. First technique is based on irradiation to create vacancies defects of nitrogen containing diamond using electron, proton, helium or neutron beam. Second method is based on nitrogen implantation into the pure diamond type IIa. Irradiated diamond is further annealed to promote migration of vacancies towards to substitutional nitrogen and the creation of NV centres [19] [93] [80]. However irradiation methods (e^-, p^+, n^0...) do

not allow a precise control of NV centres position and density [19]. Lower yield of nitrogen implantation method could be caused by limited amount of vacancies created around implanted nitrogen atoms. The nitrogen implantation may also cause a damage of the surrounding NV^- centre, leading to inferred spin and optical properties. Those disadvantages may be solved by a third possible method to produce NV centres. This technique is based on CVD growth of as grown NV centres without the damage by nitrogen beam and therefore may lead to the better properties of NV centres [32] [91]. The third technique can be eventually combined with the first technique to enhance NV density by irradiation and annealing.

Nitrogen is a natural substitutional donor defect (N_S) in diamond. N_S is incorporated into the lattice in the form N_S^0 and create C-N bond, which is 25 – 30 % longer than C-C bond and has 1.7 eV deep donor ionization energy. Despite N_S defects are immobile in the lattice; vacancies can diffuse through the lattice and create NV centres during the diamond growth. Another possibility is to grow NV centre as the unit. However unwanted defects NVH^0 and NVH^- can be created during CVD growth, therefore growth conditions must be optimized for synthesis of NV centres [91] [94] [95] [96].

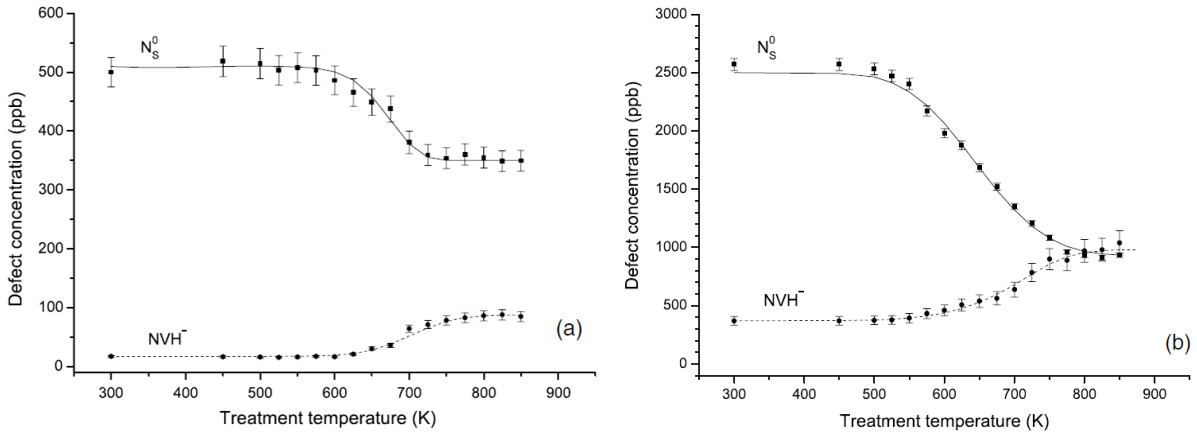

Figure 43. Concentrations of N_S^0 and NVH^- defects in two single crystal diamond (100) samples grown with different conditions, were measured at room temperature by EPR as a function of isochronal (8 min) annealing temperature in dark. Before the first annealing the samples were illuminated with unfiltered light from a 200 W HgXe arc lamp for 5 min. [96].

Figure 43 shows creation of N_S^0 and NVH^- as function of growth temperature in (100) single crystal diamond. Probability of NVH^- creation increases and conversely N_S^0 decreases with growth temperature [96]. Thermal treatment at temperatures well below the growth temperature and ultraviolet irradiation can change concentrations of $N_S^{0/+}$, $NV^{0/-}$ and $NVH^{0/-}$ and thus the diamond's optical absorption [91].

3 Materials and methods

3.1 CVD growth of diamond

Basic principle of plasma enhanced chemical vapour deposition (PE CVD) growth is shown in Figure 44. It is based on dissociation of precursors (typically 99 % H_2 and 1 % CH_4) by hot filaments, microwaves, arc discharges or laser beams, leading to the deposition of diamond films on substrates [7] [60] [97].

Low pressure CVD diamond synthesis is complicated by the allotropic nature of carbon, because graphite is thermodynamically stable crystalline phase of carbon at low pressure low temperature conditions. From this reason graphite phase needs to be simultaneously etched by atomic hydrogen atoms (carbon source gas is diluted with hydrogen gas) [6].

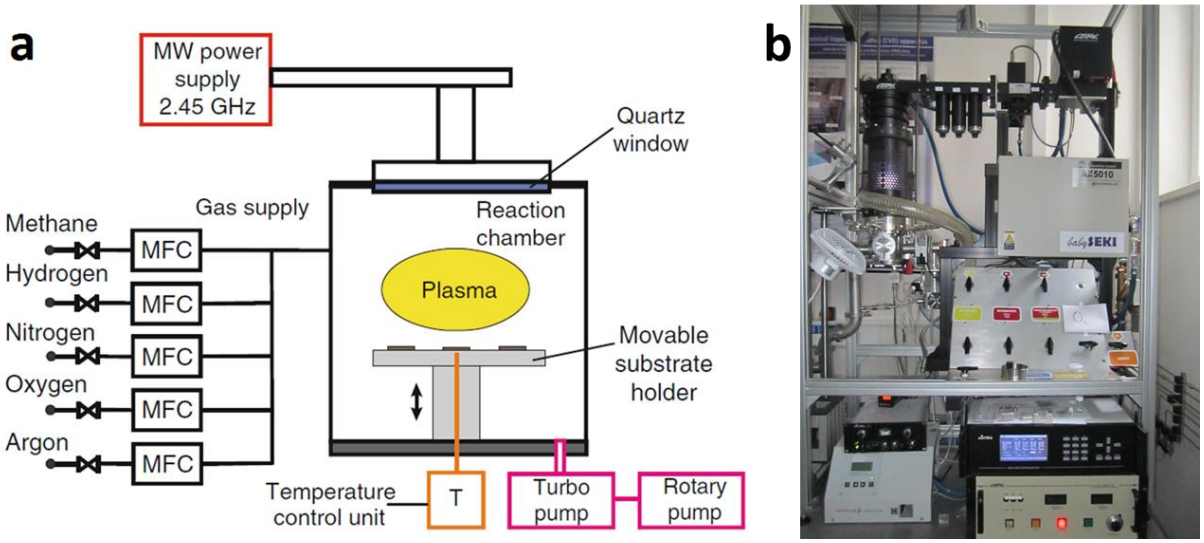

Figure 44. MW PECVD deposition system: scheme of the system [7] and Seki Technotron AX5010 system presenting in the Institute of Physic in Prague used for the diamond growth in this work (b).

Properties of CVD diamond films depend of growth parameters: substrate temperature (250 – 1100 °C), gas pressure (15 - 150 mbar), excitation power (0.5 - 3 kW in case of microwave excitation) and gas chemistry (concentration of H_2, CH_4, O_2, N_2, TMB...) [7] [60] [97]. Substrate is immersed in plasma with high concentration of atomic hydrogen atoms and low concentration of carbon radicals (CH_x). This reactive medium can be created by microwave plasma or by hot filament techniques. Figure 44a shows scheme of MW PE CVD deposition system and Figure 44b Seki Technotron AX5010

system at the Institute of Physics in Prague which was used for the boron doped diamond growth in this work.

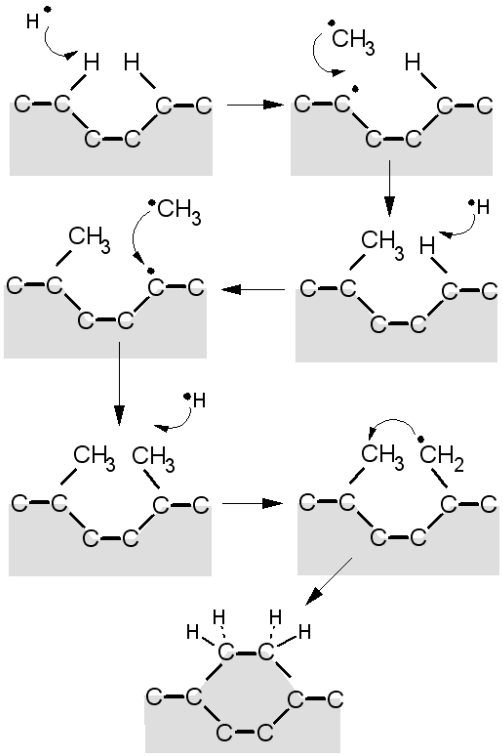

Figure 45. Standard growth model for CVD diamond [98].

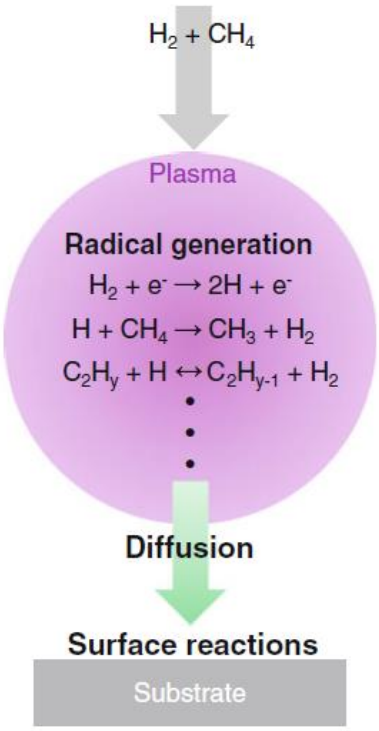

Figure 46. Scheme of CVD diamond growth [79].

Figure 45 and 46 shows the schematic diagrams of CVD diamond growth. Hydrogen atoms react with the diamond surfaces to open the structure to form a dangling bond and to promote radical attachment and stabilise the diamond surface against transformation to graphite. The process of H abstraction, dangling bond creation, and CH_3 addition is to occur on neighbouring sites integrating added carbons into the lattice and finally form a diamond thin film [7] [60] [97] [98].

In case of homoepitaxial single crystal diamond growth, (e.g. using diamond crystal as a seed), by the above process a single crystal diamond grow.

Nevertheless, diamond can also be deposited on non-diamond substrates like silicon, fused silica, metals or even high temperature polymers [62] [97] [99]. However, the diamond nucleation is very difficult because of the diamond surface energy, therefore a substrate's surface treatment before deposition is required to generate nanoscopic residua of sp^3 carbon on diamond surface to initiate an enhanced diamond nucleation. Several kinds nucleation processes exist: mechanical abrasion, bias enhanced nucleation, ultrasonic seeding with various nucleation density. The most used simple and efficient seeding method is based on the recently developed homogenous substrate coverage with

colloidal nanodiamond particles solution by spin coating or dip coating [6] [60]. Individual diamond nanoparticles or seeds grow three dimensionally until they coalesce to form a continuous film (see Figure 47). Quality of deposited films depends on growth conditions and plasma chemistry [60] [97].

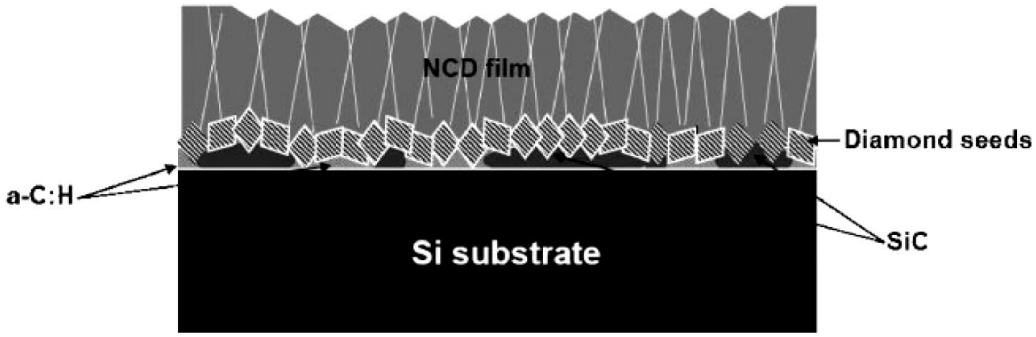

Figure 47. Example scheme of nucleation of NCD film [97].

3.2 Surface morphology characterization

3.2.1 Atomic force microscopy

Atomic force microscopy (AFM) technique visualises surface of the hard, solid or biological 3D objects with up to ~ nm resolution. Cantilever with a very sharp probe tip (usually Si) scans the sample surface by piezo elements. The horizontal deflection of the cantilever is measured by laser beam. Due to the small forces between the probe and the surface ranging from 10^{-11} to 10^{-6} N is this technique non-destructive. AFM works in scanning non-contact, contact or tapping regimes. Non-contact regime operates with probe tip distance from 10 to 100 nm above the sample surface and attractive Van der Waals, electrostatic, magnetic or capillary forces may be detected. This technique requires ultra-high vacuum and lower resolution is obtained. The advantage of this technique is a higher lifetime of the cantilever tip. Reduction of the probe distance up to angstroms during the contact mode allows a higher resolution (less than a nm). The disadvantage of this technique is a possible damage of a soft samples and a lower lifetime of the probe tip. Another regime is the tapping mode, where cantilever vibrates on or close to its resonant frequency on the sample surface. This technique also measures softer materials with high resolution [100] [101].

3.2.2 Scanning electron microscopy

Scanning electron microscopy (SEM) is a widely used technique to visualize surface topography with high resolution. Not only surface topography, but also a chemical material composition, its fluorescent properties and a magnetic domain formation is possible to be studied by SEM [102]. It consists of an electron gun, condenser lens and objective lens, scanning coil and secondary electron detector components. SEM operates under a vacuum of ~ 10^{-2} – 10^{-4} Pa [103]. The electron gun emits electrons, which are accelerated and focused on the the studied surface of a material and scanned across. Basically there are several possible types of interaction of high energy electrons with the sample surface as reflection, absorption leading to back scattered or secondary emitted electrons. Secondary electrons have low energy and only those generated on top of the surface are detected, whereas deeper emitted secondary electrons are absorbed by the studied material. Therefore surface topography study is based on secondary electron detection, which are very sensitive to surface of a material [102] [103] [104].

3.3 Structure and optical characterization

3.3.1 Raman spectroscopy

Raman spectroscopy is a non-destructive technique and can analyse solids, gasses or liquids. Raman spectroscopy system consists of an excitation source (laser), sample illumination system and light collection optics, wavelength selector (filter or spectrophotometer) and detector (photodiode array, charge-coupled device - CCD or Photomultiplier Tubes - PMT). Basic principle of Raman spectroscopy is based on non-elastic scattered monochromatic light. Monochromatic light source, usually laser, is absorbed by molecules and then reemitted with a different frequency – the Raman effect. In reality only fractional detected light originates from the Raman effect (typically a few photons from million). The most of detected light is at same frequency as the incoming light based on Rayleigh elastic scattering. The monochromatic light beam interacting with studied material excites molecules and transforms them into oscillating electrical dipoles vibrating with a characteristic frequency. Excited molecules can emit light at some frequency, this interaction is called Rayleigh elastic scattering. Excited Raman active molecules from a basic vibrational state relaxes at a lower energy than incident light – Stokes shift. Whereas if the Raman active molecule already occurs at the excited vibrational state, by the interaction of the light the molecule returns to the basic vibrational state by emitting light at a

higher energy than incident light – Anti-stokes shift [105] [106] [107]. Raman analysis provides information about diamond quality by calculation of the Diamond quality factor representing ratio of sp^3 and sp^2 related carbon peaks.

3.3.2 Confocal microscopy

The confocal microscopy is a high contrast visualization technique widely used in biology and biomedical sciences. In contrast with classical microscopy which gives information from higher sample volume, confocal microscopy provides a sharp image from a single focal plane, due to placement of a pinhole between studied sample and detector. By scanning of the planes through the sample it is possible to obtain 3D reconstruction [108] [109] [110].

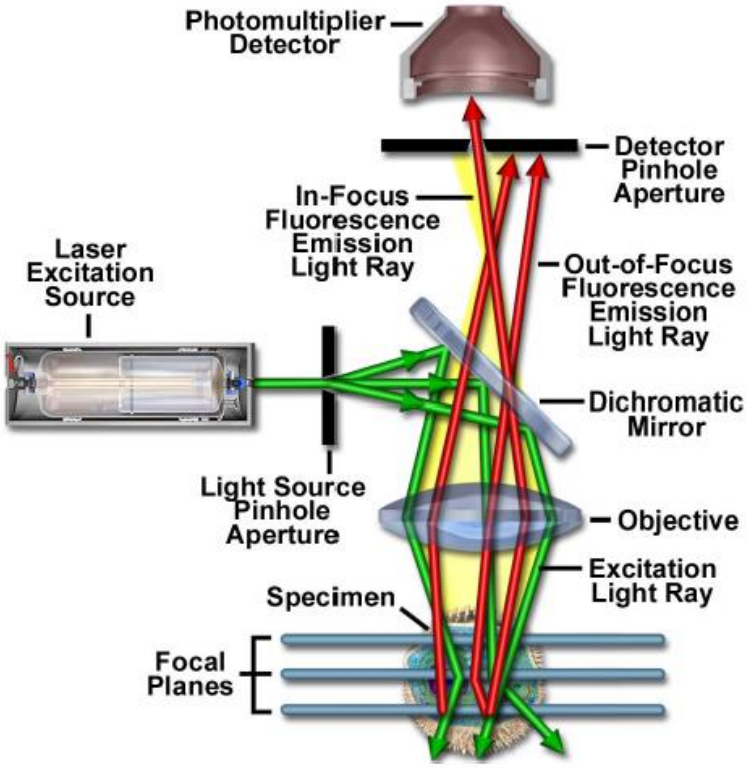

Figure 48. Scheme of the basic principle of laser scanning confocal microscope [108]

The basic principle of the laser scanning confocal microscope is shown in Figure 48. Coherent light emitted from the laser excitation source passes through the light source pinhole aperture, then is reflected by the dichromatic mirror, passes by the objective and is scanned across the specimen in the defined focal plane. Secondary emitted fluorescence from points at same focal plane then pass

back through the dichromatic mirror and it is focused as a confocal point by the detector pinhole aperture situated in front of the photomultiplier detector [108].

3.4 Hall effect electrical characterization

The electrical resistivity and Hall coefficients are very important parameters for the characterization of semiconductor or metallic devices. Van der Pauw geometry of electrodes is a very popular technique and describes how to calculate resistivity and Hall coefficient. Carrier density and mobility can be directly calculated from the Hall coefficient [111] [112]. The Hall effect is based on the flow of current density in the presence of a perpendicular applied magnetic field through studied electrically conducting material. By the effect of Lorentz force charge carriers are moved to one side of the sample and generates an electric field perpendicular to both the current density and the applied magnetic field [112].

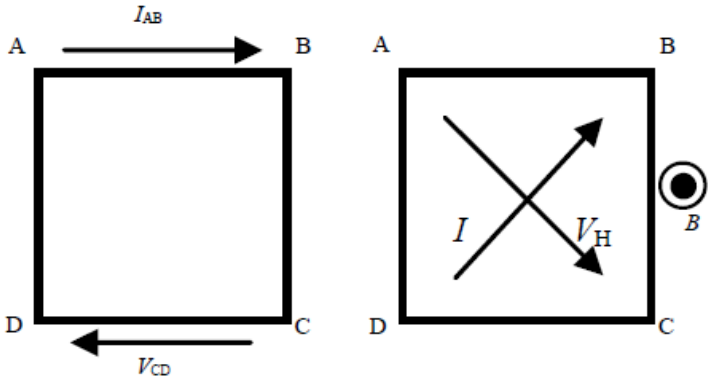

Figure 49. Scheme of resistivity (left) and Hall effect measurements (right) by the Van der Pauw method [113].

Figure 49 shows scheme of the Van der Pauw electrode configuration for the measurement of resistivity and Hall coefficient. In case of resistivity measurements there voltage applied to one side of sample to provide flow current I_{AB} and voltage V_{CD} in the other side is measured. From the measured values then is calculated the resistivity ρ [113]

$$\rho = \frac{\pi d}{ln2} \cdot \frac{\left(\frac{V_{CD}}{I_{AB}} + \frac{V_{DA}}{I_{BC}}\right)}{2} \cdot f, \quad (1)$$

Where f is the correction function.

For the Hall effect measurements the voltage is applied diagonally between the corner contacts and the current *I* flowing between them is measured. With the applied parallel magnetic field *B* in direction of sample thickness *d* is measured change in voltage V_H, between opposite diagonal corner contacts. The hall coefficient R_H is then calculated [113]:

$$R_{\mathrm{H}} = \frac{V_{\mathrm{H}} d}{IB}. \tag{2}$$

Carrier density η is calculated [113]:

$$\eta = \frac{1}{R_{\mathrm{H}} e}, \tag{3}$$

Where *e* is elementary charge.

Carrier mobility μ is calculated [113]:

$$\mu = \frac{R_{\mathrm{H}}}{\rho}. \tag{4}$$

3.5 Electrochemical impedance spectroscopy characterization

The electrochemical impedance spectroscopy (EIS) is a powerful technique for electrochemical sensing or biosensing applications. The electrochemical impedance spectroscopy is a frequency response on the electrochemical reaction in the electrode-electrolyte interface. Electrochemical sensing requires a reference electrode, a counter (auxiliary) electrode and a working electrode (sensing or redox electrode). The reference electrode (Ag/AgCl) brings a known and stable potential in a fixed distance from the reaction. The working electrode with bio-functionalized surface provides a response signal on the biochemical reaction. The counter (auxiliary) electrode mediates transfer of a current to the working electrode [2] [54]. A small amplitude of AC voltage (to avoid a system nonlinearity) is applied and the response of the current is measured. From the input and output signal the impedance (resistance, capacitance and inductance) is determined of the electrochemical system separately for each measured frequency. Different frequencies are applied due to different AC responses of electrochemical processes in the system as an electron and ion transport, gas and solid phase transport or heterogeneous reactions [114] [115].

The flowing current as a response to the electrochemical reaction shows in general the faradaic as well as the non-faradaic character. The non-faradaic current is caused by charging of the double layer capacitance C_d. Figure 50 shows the scheme and equivalent electronic circuit of the electrified sensor interface by an applied voltage. The positively charged oxidants (red) diffuses to the negatively charged electrode, where are reduced by acceptation of the electron (blue). IHP and OHP are the inner and outer Helmholtz planes. The area between vertical dotted lines is represent by an equivalent electronic Randles circuit where C_d is the double layer capacitance, R_p is the polarization resistance, W is the Warburg resistance and R_s is the solution resistance. R_s presents the high frequency component, whereas W, C_d and R_p represent the low frequency component. Measured data as a response to the interface changes can be represented by Nyquist plot (plotted real versus imaginary part of impedance) or bode plot (plotted absolute impedance and phase shift with the frequency response on a logarithmic frequency scale) [115] [116].

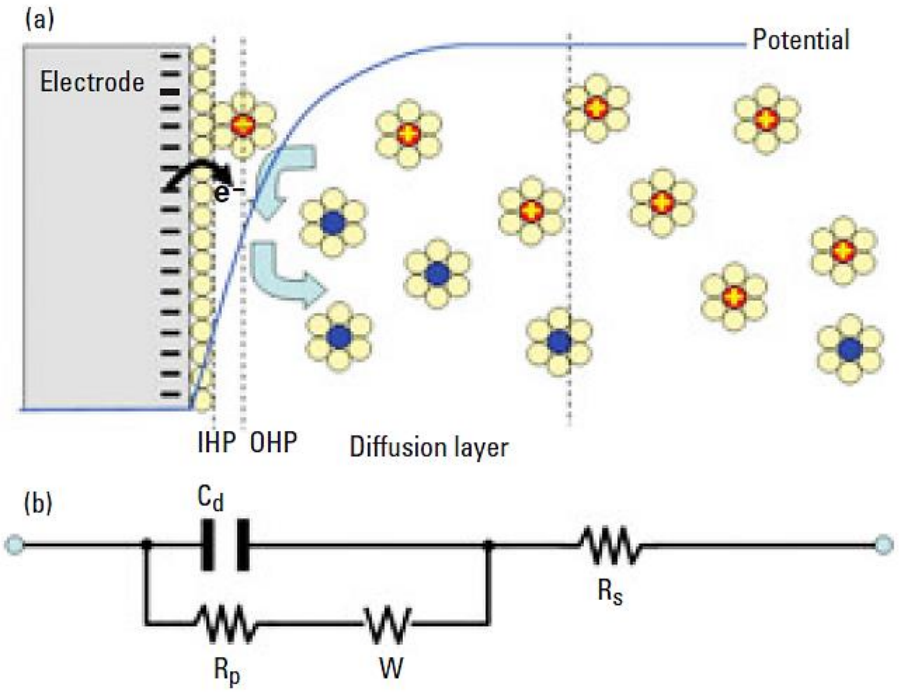

Figure 50. (a) Interface of the electrochemical sensor and (b) its equivalent electronic Randles circuit representing the interface area between vertical dotted lines [116].

4 Results and discussions

The first part of the work (Chapter 4.1 - 4.3) is focused on synthesis of diamond material by MW PE CVD. Material engineering was used to define optimal synthesis conditions and consequently electrical, morphology and optical properties. Due to the relatively high purchase price of high quality single crystal diamond substrates, firstly we studied boron and nitrogen doping with nanocrystalline diamond form to define optimal sensor functionality and then afterwards these experiments were applied to homoepitaxial diamond growth for fabrication of the biosensor device. The nanocrystalline diamond growth was investigated in two PE CVD systems. Firstly the conventional cavity MW PE CVD system (Figure 51) with sample surface area of 5 × 5 cm and operating growth temperatures between 700 – 900 °C and higher growth rates was used. Secondly we used a linear antenna (LA) MW PE CVD system (Figure 67) allowing large area growth (30 × 30 cm) at low temperatures (< 300 °C), with an advantage of diamond coating of 3D substrates and diamond growth on low melting point substrates. The best observed results from were applied for construction of the homoepitaxial diamond biosensor device. Chapter 4.3 deals with synthesis of highly boron doped diamond single crystal diamond layer with very flat surface and thin film with NV centres on top of it.

The chapter 4.4 is dedicated to the investigation of NV PL in the fabricated nanocrystalline diamond samples. Firstly was studied an enhancement of NV PL by a high energy electron irradiation followed by a thermal annealing. For the functionality of the diamond biosensor, which consists of thin sensing diamond film with NV centres deposited on boron doped diamond electrode, we studied NV photoluminescence in order to obtain knowledge about thickness dependence and boron concentration influence on the NV PL.

Because the NV charge state diamond biosensor is combined with an electrochemical device, the electrochemical impedance spectroscopy was carried out for a purpose to find an optimal thickness range of the undoped diamond (with NV centres) grown on the boron doped nanocrystalline electrode were top (Chapter 4.5).

The last chapters deals with the realization and verification of the biomolecular sensor based on operation of colour centres in diamond integrated to a microfluidic biosensor. The single crystal diamond device consists of highly boron doped diamond electrode capped with a thin (15 nm) NV centres containing layer. The device is then covered by polydimethylsiloxane flow cell and transparent indium tin oxide coated glass slide (see Chapter 4.6). First we set the charge state occupation of NV

centre by diamond surface functionalization (Chapter 4.7) and then also by applying a bias voltage between source and gate electrode (Chapter 4.8). The NV sensor is then used for detection of molecules carrying electrical charge as DNA molecule for label free charge control (Chapter 4.10) combined with electrochemical detection (Chapter 4.9).

4.1 Study of MW PE CVD nanocrystalline diamond growth

4.1.1 Experimental details

The diamond films were grown (by Marie Krečmarová) using the Seki Technotron AX5010 cavity based MW PE CVD deposition system (Figure 51) at the Institute of physic Academy of science in Prague, Czech Republic (IoP ASCR) on different substrates (Si, SiO_2, corning glass), with different growth conditions and plasma chemistry. The specific growth conditions are given for each experiment separately. The substrate temperature was monitored by a dual-wavelength Williamson Pro pyrometer.

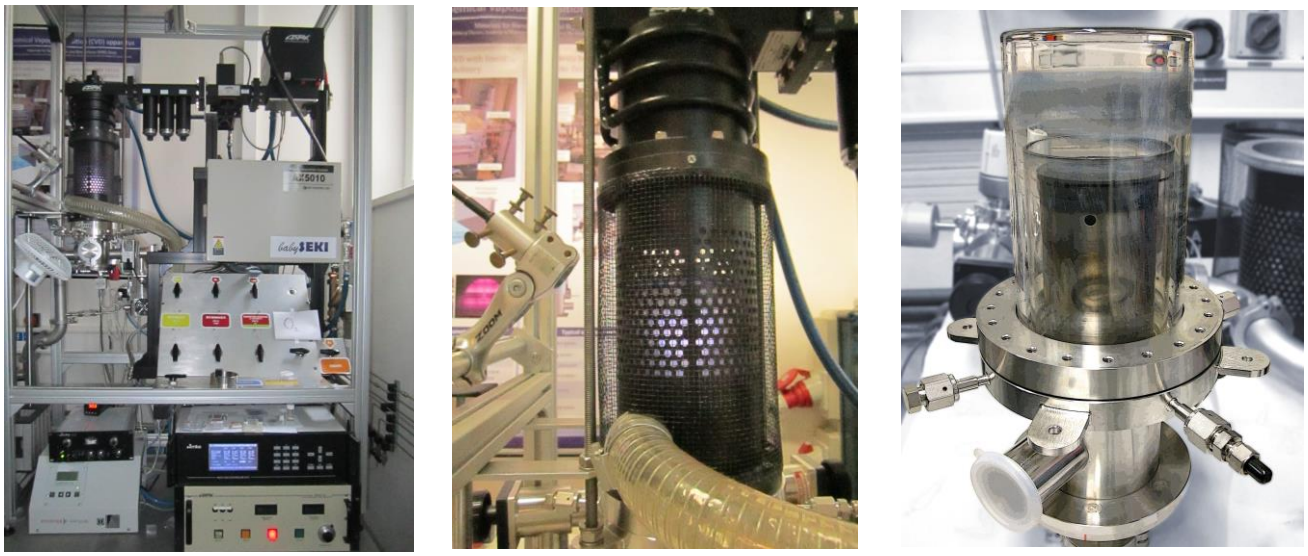

Figure 51. Seki Technotron AX5010 MW PECVD deposition system (left), the cavity with oxygen plasma and pyrometer (middle) and the unmounted cavity (right).

Substrates were cleaned in alcohol and deionized water in two ultrasonic baths and then seeded with nanodiamond colloidal dispersion (NanoAmando®) from the NanoCarbon Research Institute Ltd by spin coating (Figure 52) to enhance monolayer of the nanodiamond particle seeds (by Marie Krečmarová). The attraction of the nanodiamond seeds is caused by a different zeta potential of the nanodiamond particles and substrate surface.

The surface morphology, roughness and grain size were characterized at the IoP ASCR using an optical microscopy (by Marie Krečmarová), atomic force microscopy (AFM) in semi contact mode NTEGRA-Prima (by Dr. Ladislav Fekete) and a scanning electron microscopy (SEM) FEI Quanta 200 FEG-SEM (Dr. Aleš Jäger). The thickness of the deposited diamond film was measured by AFM as a step difference between diamond surface and non-seeded substrate (by Dr. Ladislav Fekete), optical reflectance interferometry assuming the index of refraction of the layers (by Marie Krečmarová), and profilometry (by Marie Krečmarová). The diamond sp^3/sp^2 carbon concentration (e.g. quality factor) and the diamond grain size were determined from Raman spectroscopy measurements using the Renishaw InVia system at IoP ASCR with excitation wavelengths of 488 nm at room temperature (by Marie Krečmarová). The average diamond grain size was determined from the full width and half maximum of fitted diamond Raman peak using Lorentzian function. The diamond quality factor, i.e. sp^3/sp^2 phase ratio was calculated from fitted areas of diamond (sp^3) and amorphous carbon (sp^2) Raman peaks using a Lorentzian function (by Marie Krečmarová).

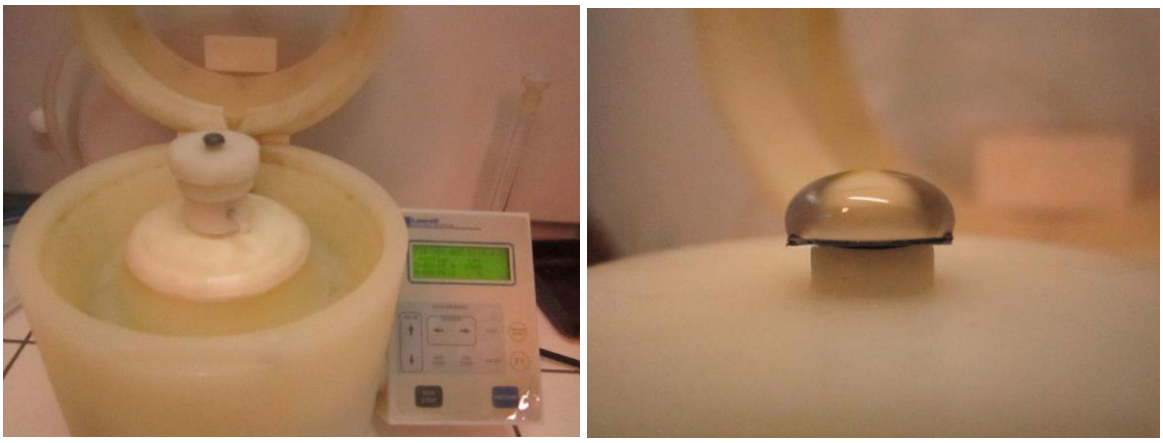

Figure 52. The spin coating mechanism to enhance nucleation density for nanocrystalline diamond growth (left) and detail of a drop of nanodiamond dispersion solution on the silicon substrate (right).

The Nicolet, model Nexus spectrometer Fourier transform infrared (FTIR) spectroscopy at IoP ASCR was used to measure transmittance of deposited layers in the mid infrared region (by Dr. Zdeněk Remeš and Marie Krečmarová). Transmittance spectra of the layers were subtracted from a Si substrate background. The NV centre photoluminescence was measured using a Renishaw InVia Raman Microscope at IoP ASCR, with a 514 nm excitation laser and laser power of 25 mW at room as well as liquid nitrogen temperature (by Marie Krečmarová). The photoluminescence spectra were normalized to sp^3 diamond peak. Photoluminescence measurements were performed also by using the non-commercial confocal microscope with excitation wavelength at 532 nm and laser power of 20 mW

(by Dr. Michal Gulka), which was built at the Faculty of Biomedical Engineering of Czech Technical University in Kladno (FBMI CVUT).

Resistivity, carrier density and mobility of the layers were determined by the van der Pauw method (by Dr. Pavel Hubík - Hall and Marie Krečmarová - 4p resistivity) at the IoP ASCR. Ti/Au (20 nm/80 nm) ohmic contacts were prepared by the metal evaporation through a mask followed by annealing. The current was supplied by a Keithley 6221 current sources; the voltage was measured by two Keithley 6514 electrometers (input resistance ~10^{15} Ω), the differential analog output signal of them was recorded by a Keithley 2182A nanovoltmeter.

4.1.2 Effect of methane concentration

To synthetize good quality diamond films by the MW PE CVD technique, several parameters play an important role, such as a microwave power, working pressure, temperature and a plasma chemistry. This chapter is devoted to the optimisation of methane concentration in the gas phase for the diamond growth. Diamond films were grown at the IoP ASCR on fused silica substrates. Growth conditions were 1 kW microwave power, 50 mbar working pressure, average substrate temperature of 700 °C and methane concentration of 0.1 – 1.5 %.

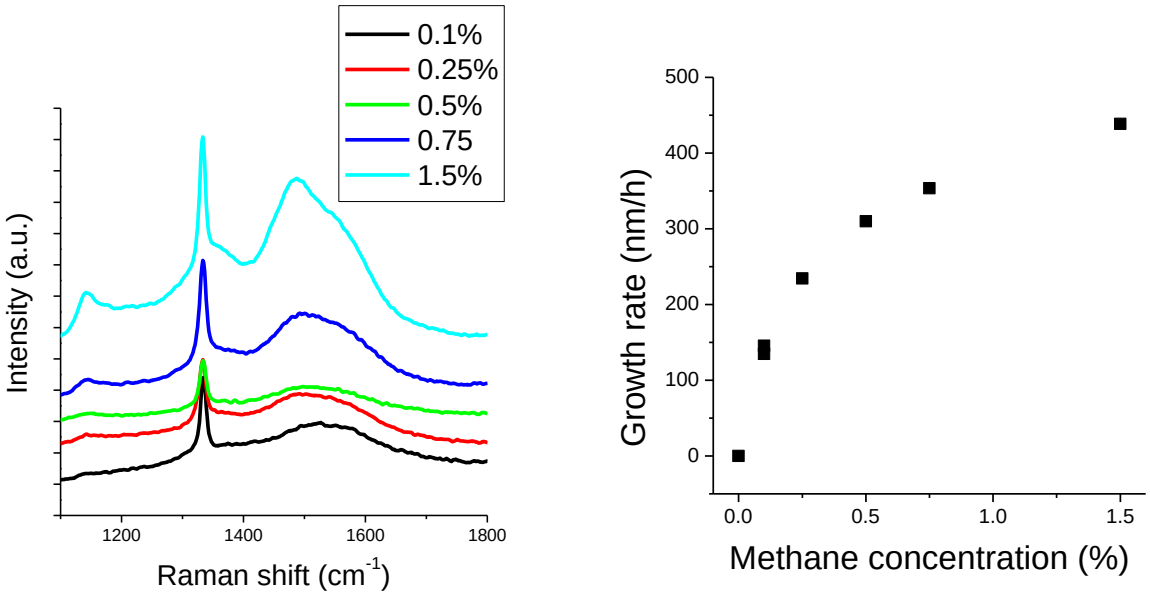

Figure 53. Raman spectra with excitation wavelength of 488nm (on the left) and growth rate (on the right) of nanocrystalline diamond growth films with different methane concentration on fused silica substrates.

Raman spectra in Figure 53 left shows increase of sp^2 carbon peak at 1550 cm^{-1} and transpolyacetylene [117] related peaks at 1140 and 1484 cm^{-1} with methane concentration. Based on the literature

[117] and our experiments (next chapter), unwanted transpolyacetylene can be partially removed by thermal annealing at a high temperature of 900 °C. On the other hand increase of the methane concentration brings a higher growth rate (Figure 53 right). Further higher methane concentration leads to saturation of the growth rate [118].

Conclusions

The increase of the methane concentration creates higher amount of unwanted transpolyacetylene and in general higher sp^2 content. Growth rate increases with methane concentration up to 1.5 %. For boron and nitrogen doping studies were chosen methane concentrations of 0.5 and 1 %.

4.1.3 Nanocrystalline diamond boron doping study

In this experiment boron doping was studied in nanocrystalline diamond to set the best electrical, optical and material properties for further fabrication of the single crystal boron doped electrode for the electrochemical NV centre charge state biosensor (see Chapter 4.3). The BNCD electrodes were also used for an optimization of the biosensor functionality (see Chapter 4.5) in an electrochemical system (BNCD/NCD).

Diamond films were grown on corning glass, fused silica and both side polished (100) oriented silicon substrates at the IoP ASCR with 0.5 and 1 % methane concentration and with using trimethylboron (TMB) as a boron precursor. The chamber reactor was cleaned before experiment by thermal annealing and oxygen plasma.

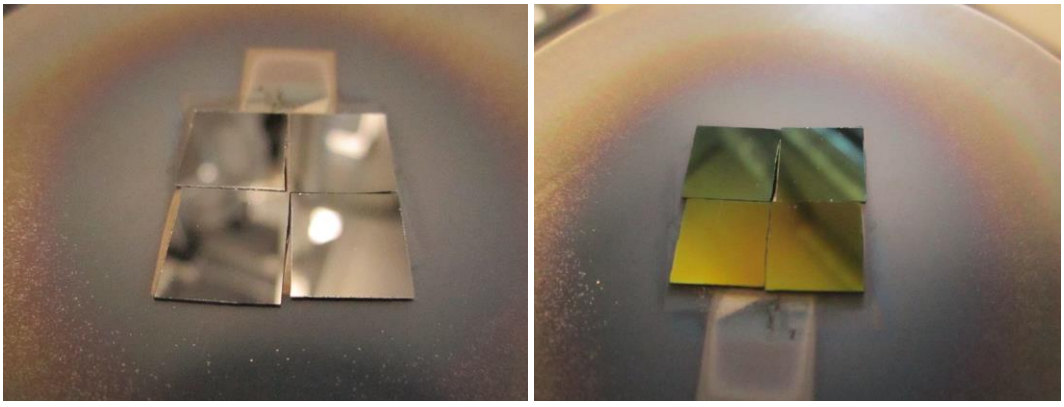

Figure 54. Seeded silicon substrates before growth (left) and grown nanocrystalline diamond films with 0.5% methane and 4000 ppm of TMB doping (right).

First series of layers were grown with 1 % methane concentrations, later with 0.5 % concentration and therefore evolution of chamber boron background and impurities occurred with time. TMB doping from 0 to 4000 ppm B/C concentration was used. Due to the chamber boron background, some boron atoms were incorporated into the layers even if no TMB was added into the gas mixctutre. The growth conditions for 0.5 % and 1 % methane concentration were: 1 kW MW power (for 1% CH_4) and 1.15 kW (for 0.5% CH_4), 50 mbar pressure, average substrate temperature of 700 °C and various TMB doping concentrations (0 – 4000 ppm). The microwave power was increased for 0.5 % methane series to obtain a higher growth temperature around 700 °C. Figure 54 shows photographs of the series with 0.5 % methane concentration before and after growth with 4000 ppm of the TMB doping.

4.1.3.1 Optical properties and morphology

The optical properties of nanocrystalline diamond films grown on from one side of a both side polished Si substrate with 133 - 1000 ppm of TMB and 1 % methane concentration were studied. Figure 55 shows transmission FTIR spectra of the deposited nanocrystalline diamond films. Transmittance spectra of the layers were subtracted from a Si substrate background. FTIR spectra shows the peak around 1280 cm^{-1} that might be attributed to the boron induced phonon band [119], which is shifted to lower wavenumbers with increasing the boron doping level. Higher TMB doping leads to higher optical absorption of the layer.

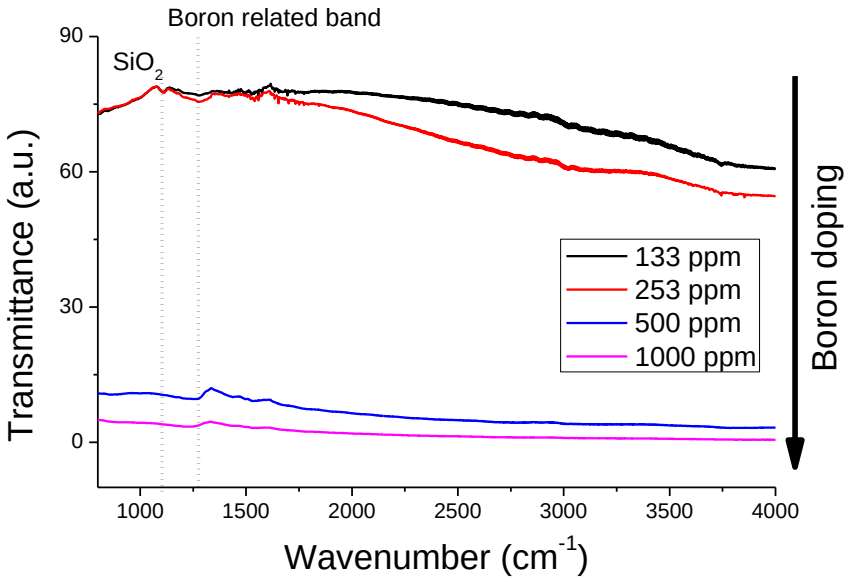

Figure 55. FTIR spectra of deposited nanocrystalline diamond films on both side polished silicon substrate grown with 1 % CH_4 and different TMB concentrations.

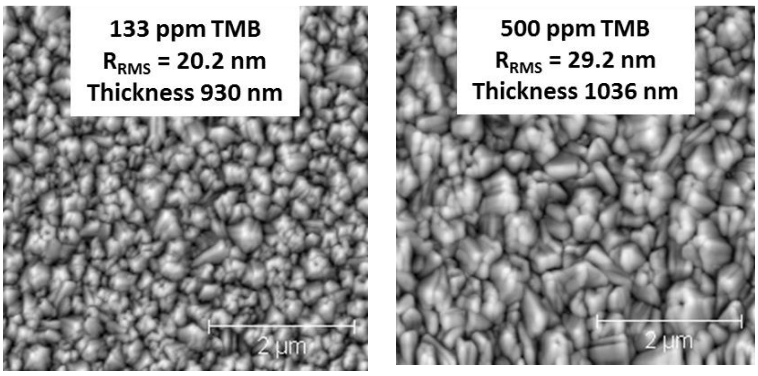

Figure 56. Local contras AFM surface morphology images of grown nanocrystalline diamond films with 133 ppm of TMB (on the left) and 500 ppm (on the right).

Figure 57 shows the growth rate comparison for 0.5 % and 1 % of methane as function of the TMB concentration. In case of 0.5 % methane the growth rate slightly decrease with TMB concentration, whereas for 1 % methane concentration the growth rate increases up to 1000 ppm of TMB and decreases at higher TMB concentration.

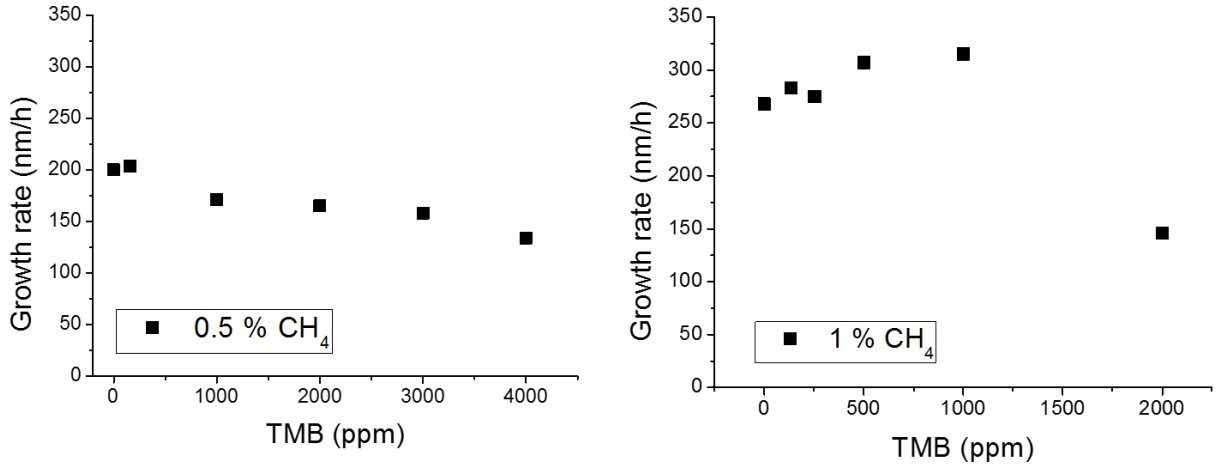

Figure 57. Deposition growth rate as function of TMB doping concentration for 0.5 % methane (left) and 1 % methane (right) concentrations.

The Raman spectra of deposited layers on fused silica substrates with 0.5 % methane and different TMB concentrations is shown in Figure 58. The Raman spectra shows a shift of the diamond peak from 1323 cm^{-1} (0 and 160 ppm of TMB) to 1297 cm^{-1} at higher boron concentrations. The diamond peak for diamond film with addition of 0 ppm of TMB is shifted from 1332 cm^{-1}, due to the presence of chamber boron background and thus boron incorporation into the grown film. The peak observed at 460 cm^{-1} (higher TMB doping: 1000 – 4000 ppm of TMB) and 489 cm^{-1} (0 and 160 ppm of TMB) is the attributed band of B-B boron dimers [120]. Observed peaks at 958 cm^{-1} in highly boron doped layers (1000 – 4000 ppm of TMB) may be attributed to the localized mode of boron in the diamond

[121]. Disordered D band is located at 1347 cm^{-1} and graphitic G band at 1551 cm^{-1}. Transpolyacetylene (Trans $(CH)_n$) [117] related peaks at 1142 cm^{-1} and 1482 cm^{-1} are visible at low TMB doped films. Worse quality of low doped films in comparison with 1 % methane (Figure 59) series is due to the dirtier chamber as the 0.5 % methane series were grown later. However the transpolyacetylene peaks disappear after thermal annealing at 900 °C (Figure 58 down).

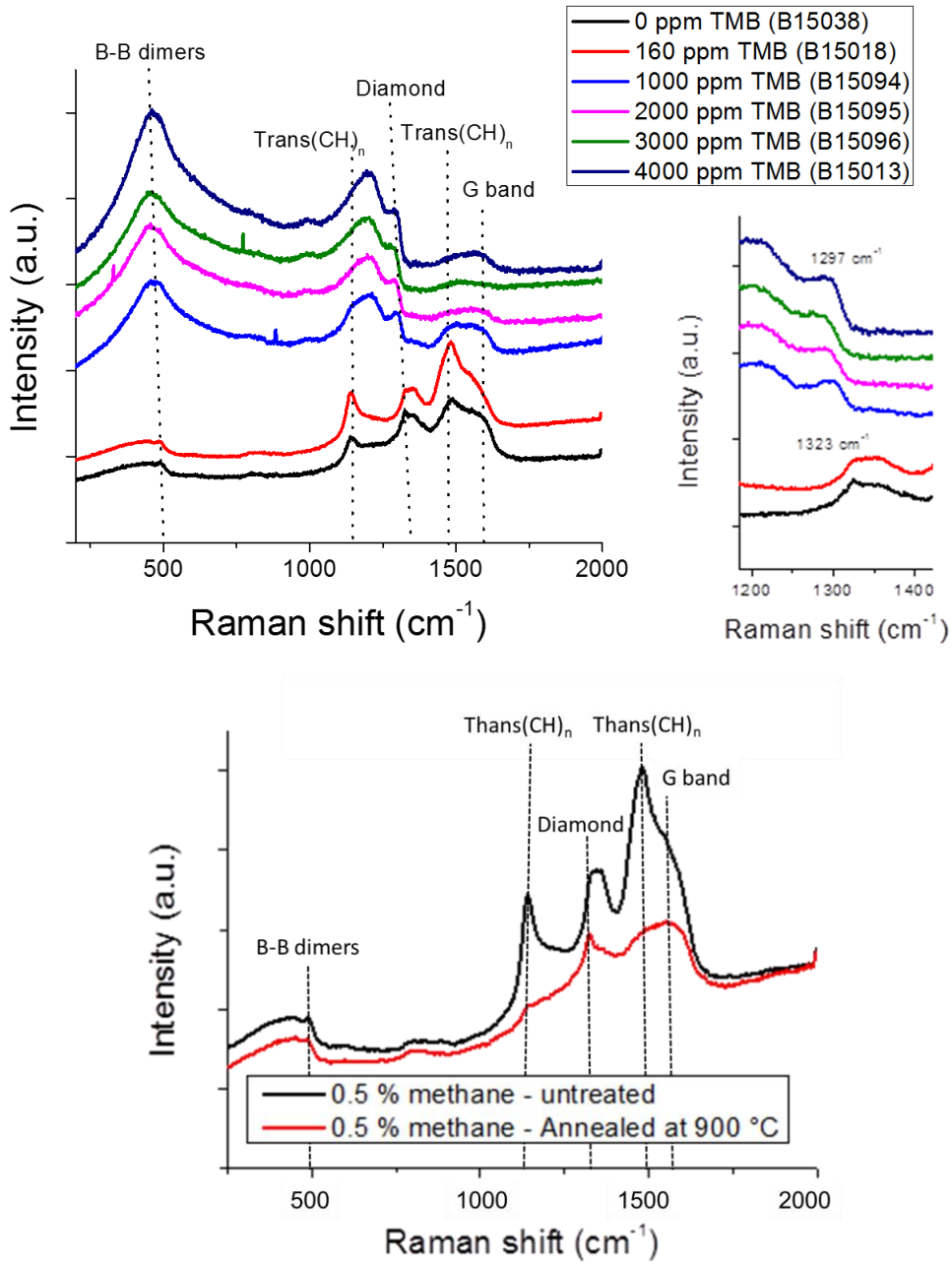

Figure 58. Raman spectra of nanocrystalline diamond layers grown on fused silica at 0.5 % methane and various boron concentrations (upper left), shift of diamond peak with increasing boron concentration (upper right), and removal of transpolyacetylene by thermal annealing at 900 °C for sample with low 160 ppm boron addition (down).

Figure 59 represents the Raman spectra of nanocrystalline diamond films grown on corning glass and fused silica substrates with 1 % methane and different TMB concentrations. The diamond peak is shifted from 1333 cm^{-1} to 1297 cm^{-1} at higher boron concentrations. Disordered D band is located at 1361 cm^{-1} and graphitic G band at 1555 cm^{-1}. Trans $(CH)_n$ related peaks at 1145 cm^{-1} and 1484 cm^{-1} [117] are presented at low TMB concentrations. B-B boron dimers related peak at 489 cm^{-1} [120] raises with TMB doping starting at 253 ppm of TMB due to higher incorporation of boron. Localized mode of boron peak [121] at 992 cm^{-1} was found in highly boron doped films.

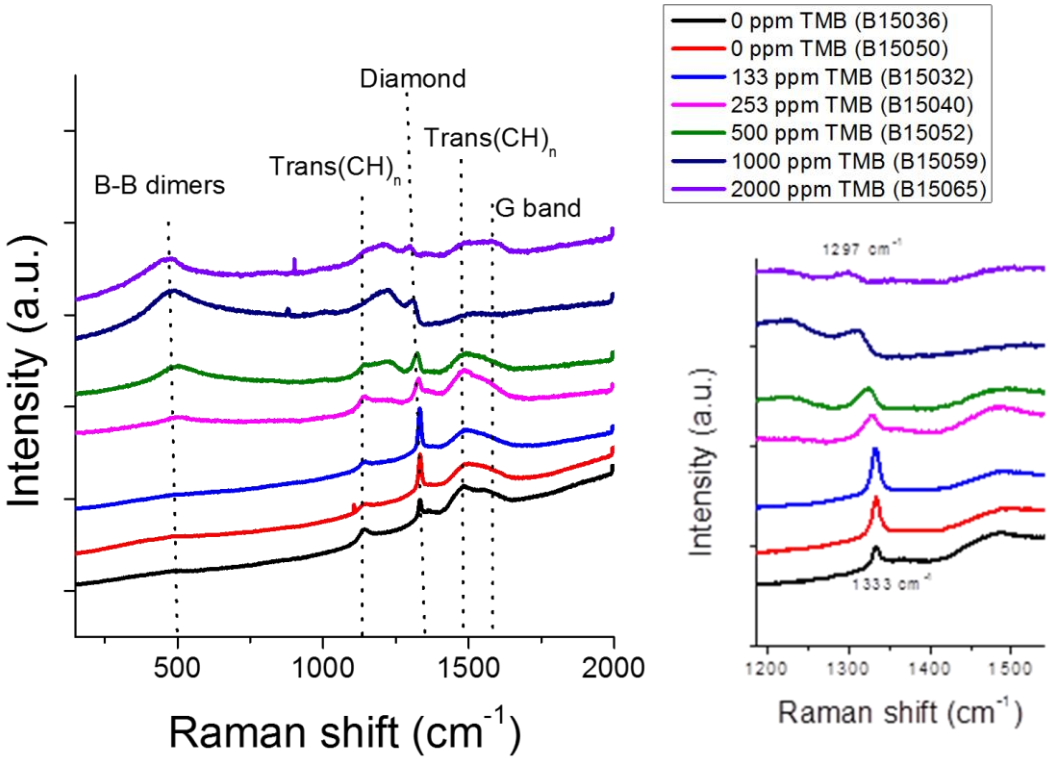

Figure 59. Raman spectra of nanocrystalline diamond layers grown on corning glass and fused silica substrates at 1 % methane and various boron concentrations (left), and shift of diamond peak with increasing boron concentration (right).

4.1.3.2 Electrical properties

The electrical properties of grown nanocrystalline diamond layers on fused silica and corning glass are shown in Table 1. Noted, that samples without any TMB addition into the working gasses were grown just with a residual chamber boron background. The electrical properties of the films obtained from Hall effect measurement by the Van der Pauw technique are plotted in the Figure 60.

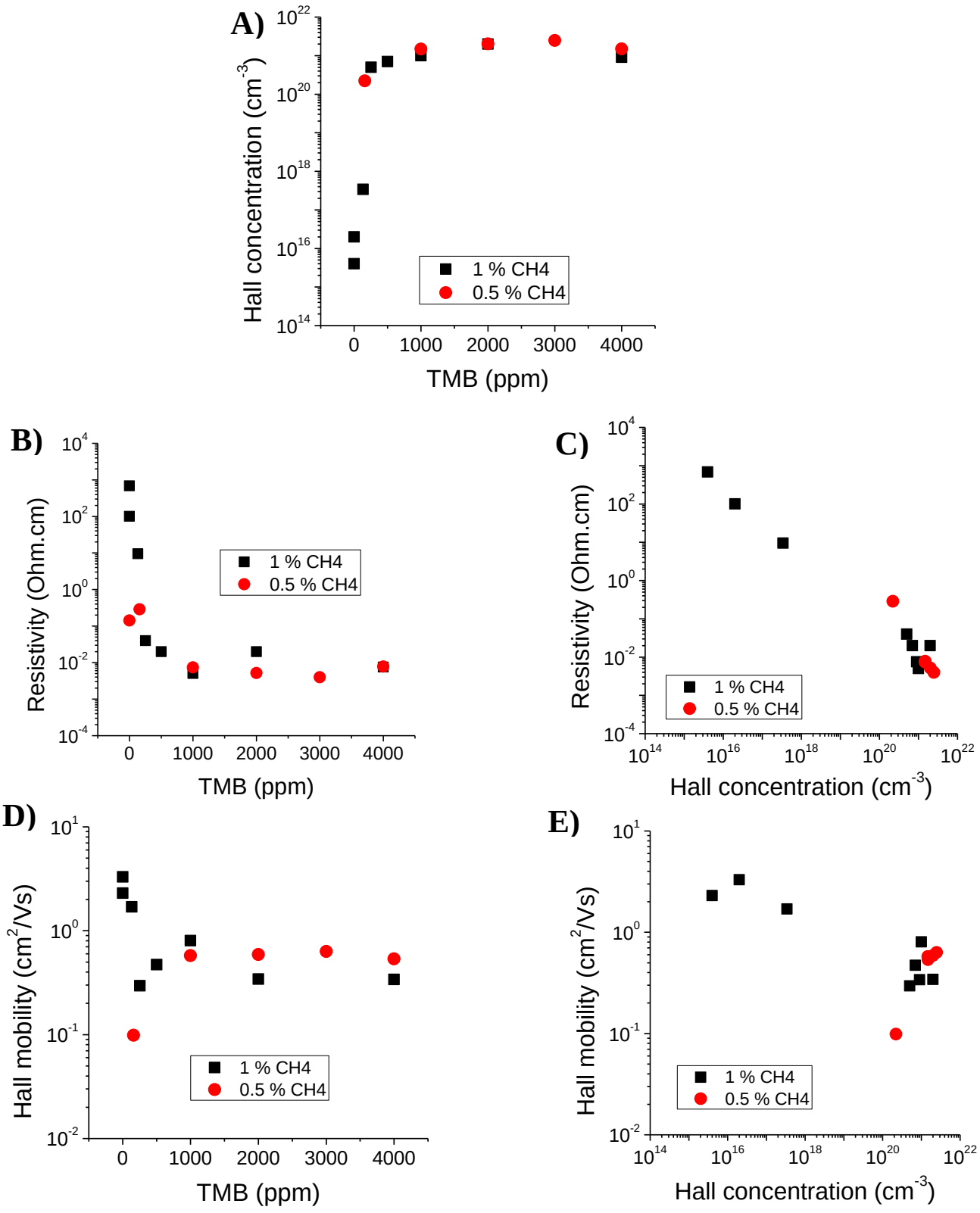

Figure 60. Electrical properties of boron doped films deposited with 0.5 % and 1 % methane concentration at room temperature: Hall concentration as function of TMB concentration (A), Resistivity as function of TMB concentration (B) and Hall concentration (C), Hall mobility as function of TMB concentration (D) and Hall concentration (E).

Higher boron doping than 133 ppm of TMB reaches the semiconductive/metallic transition region with Hall holes mobility higher than 1e20 cm^{-3}. Resistivity and Hall mobility decreases with boron doping. Higher boron doping than 1000 ppm does not induce any improvement of conductivity.

Figure 61 shows temperature variable Hall effects measurements of boron doped nanocrystalline diamond films grown with 1 % methane concentration. Hall holes concentration, mobility and resistivity seem to be stable with temperature at higher boron doping than 253 ppm of TMB. Lower boron doping of 133 ppm TMB leads to a change of electrical properties with temperature.

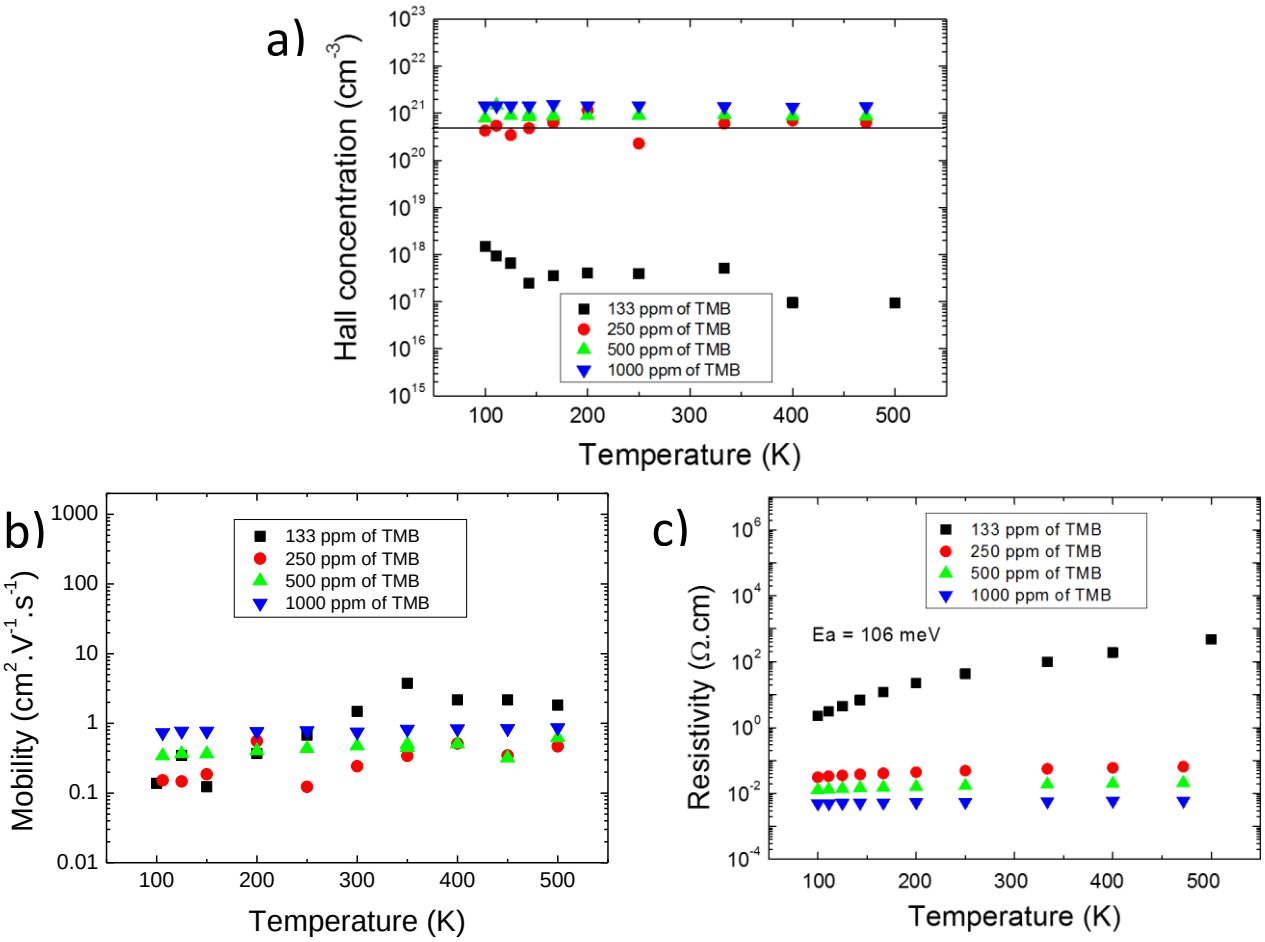

Figure 61. Temperature variable Hall effects measurement of boron doped nanocrystalline diamond films grown with 1 % methane concentration: Hall concentration with marked black line identifying transition between semiconducting and metallic regions (A), mobility (B) and resistivity (C) as function of temperature.

Conclusion

The nanocrystalline diamond layers were deposited with various boron concentrations from semiconducting to metallic conduction regions. The electrical, optical and morphology properties of

variously boron doped nanocrystalline diamond layers were studied. Higher methane concentration leads to improvement of growth rate, excellent boron incorporation was achieved. The higher concentrations of TMB result in improvement of a growth rate and lead to a larger grain size. The presence of the incorporated boron atoms were confirmed using the FTIR and Raman spectroscopy by occurence of boron related phonon bands at measured spectas. Boron doping of 160 ppm of TMB and higher reaches the semiconductive/metallic transition region with hole concentrations higher than 1e20 cm^{-3}. Resistivity and Hall mobility decreases with boron doping for high B concentrations. Specifically, higher boron doping than 1000 ppm does not induce any improvement of conductivity. Higher boron doping (250 - 1000 ppm of TMB) shows stable electrical properties with temperature. Low boron doping (133 ppm of TMB) leads to a change of electrical properties with temperature.

Table 1. Electrical properties of boron doped nanocrystalline diamond films.

Sam-ple ID	CH_4 (%)	TMB (ppm)	Substrate	Thickness (nm)	Growth rate (nm/hod)	Resistivity (Ohm·cm)	Hall conc. (cm^{-3})	Hall mobility (cm^2/Vs)
1	0.5	0	Fused silica	200	200	1.4E-01	N.A.	N.A.
2	0.5	160	Fused silica	197	204	2.9E-01	2.2E+20	9.9E-02
3	0.5	1000	Fused silica	256	171	7.3E-03	1.5E+21	5.8E-01
4	0.5	2000	Fused silica	248	165	5.2E-03	2.0E+21	5.9E-01
5	0.5	3000	Fused silica	316	158	4.0E-03	2.5E+21	6.3E-01
6	0.5	4000	Fused silica	275	134	7.8E-03	1.5E+21	5.4E-01
7	1	0	Corning glass	268	268	6.9E+02	4.0E+15	2.3E+00
8	1	0	Corning glass	694	347	1.0E+02	2.0E+16	3.3E+00
9	1	133	Corning glass	930	283	9.5E+00	3,4e17	1.7E+00
10	1	253	Corning glass	825	275	4.0E-02	5.0E+20	3.0E-01
11	1	500	Corning glass	1036	307	2.0E-02	7.0E+20	4.7E-01
12	1	1000	Corning glass	1258	315	5.0E-03	1.0E+21	8.0E-01
13	1	2000	Fused silica	182	146	2.0E-02	2.0E+21	3.4E-01
14	1	4000	Fused silica	~450	~150	7.5E-03	9.0E+20	3.4E-01

4.1.4 Nanocrystalline diamond nitrogen doping study

This chapter deals with nitrogen doping and its effect on material properties and NV centre fabrication in nanocrystalline diamond using the conventional MW resonance cavity based MW PE CVD growth. This experiment was published in the Proceeding *Instruments and methods for biology and medicine 2014* [122]. The nitrogen doping was investigated also with the large area and low temperature LA MW PE CVD growth (Chapter 4.2).

Nitrogen doped nanocrystalline diamond films were grown on (100) oriented crystalline silicon substrates at the IoP ASCR. The growth conditions were as follow: 1 kW microwave power, 50 - 100 mbar pressure with 300 sccm total gases flow, average substrate temperature of 700 °C, and deposition time 2 and 5 hours. The gas phase compositions during depositions were as follow: 1% methane concentration in hydrogen and variable N_2 concentration (0, 0.07%, 0.17%, 0.25%, 0.5%, 0.75%, 1% and 1.5 %) [122].

4.1.4.1 Morphology study

Diamond quality factor is calculated as a ratio sp^3 and sp^2 phase, concretely as $(sp^3 \cdot 75/((sp^3 \cdot 75)+sp^2) \cdot 100)$ [%] from measured Raman spectra. Figure 62a shows variation Raman diamond quality factor, average crystal size and growth rate of the nanocrystalline diamond layers as function of the N_2 concentration in gases mixture. Growth rate rises with addition of N_2 and saturate to maximum for N_2 concentration above 0.5 %. The Raman spectra of deposited layers are shown in Figure 62b. Bellow N_2 concentration of 0.17 %, spectra shows narrow and intense diamond Raman peak in comparison to sp^2 peaks, i.e. D band (1356 cm^{-1}) and G band (1544cm^{-1}). Transpolyacetylene (Trans $(CH)_n$) peaks [117] located at 1140 cm^{-1} and 1481 cm^{-1} are significant for N_2 concentration above 0.17 %. High nitrogen concentration results in an increase of sp^2 bonded carbon content (see Figure 62) and decrease of the crystal size (see Figure 62a and Figure 63c,d) due to high diamond re-nucleation rate in N_2 enriched gas phase [122].

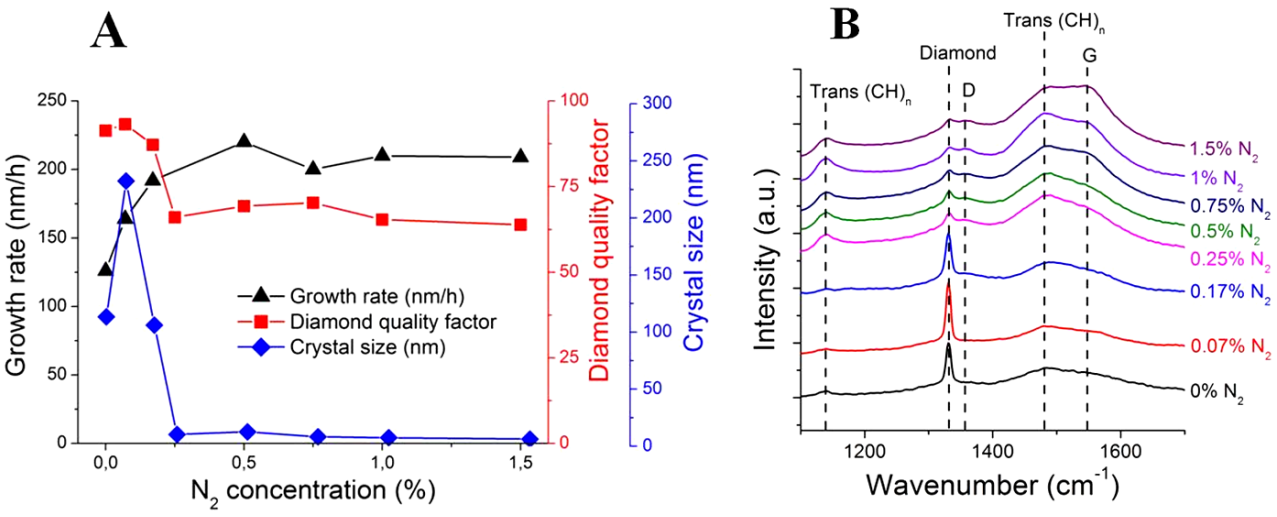

Figure 62. Growth rate, Diamond quality factor (sp^3/sp^2 ratio), average crystal size of nitrogen doped nanocrystalline diamond films (a); Raman spectra as function of N_2 concentration in the gas mixture (b) [122].

AFM images show a dramatic change of surface morphology induced by N_2 addition in Figure 44. Without addition of nitrogen, the layers consist of randomly oriented diamond crystals with clearly distinguishable edges and facets (Figure 63a). The addition of a low amount of nitrogen (0.07 %) results in the growth of larger diamond crystals with sharp edges and squared facets characteristic of (100) oriented crystals (Figure 63b). A dramatic change of morphology is observed for N_2 concentration above 0.25 % (see Figure 63c,d). The sharp-edged crystals structure is replaced by an irregular shape and small crystals with ~10 nm grain size around. RMS roughness decreases with increasing nitrogen concentration from maximum RMS of 54 nm (0.07 %) to minimum of 15 nm (1.5 %). The average diamond grain size determined from the Raman spectra analysis of different layers are shown in Figure 62a. The maximum crystal size of ~230 nm is observed for the N_2 concentration of 0.07 %. The crystal size then decreases to the minimum of 6 nm for the N_2 concentration of 0.25% and higher. These results are consistent with AFM results. Correspondingly, the highest diamond quality factors are observed at low N_2 concentrations (< 0.2 %). Then, it decreases suddenly at higher N_2 concentrations (≥ 0.25 %) as the grain size drop and the re-nucleation rate increases (see Figure 62a) [122].

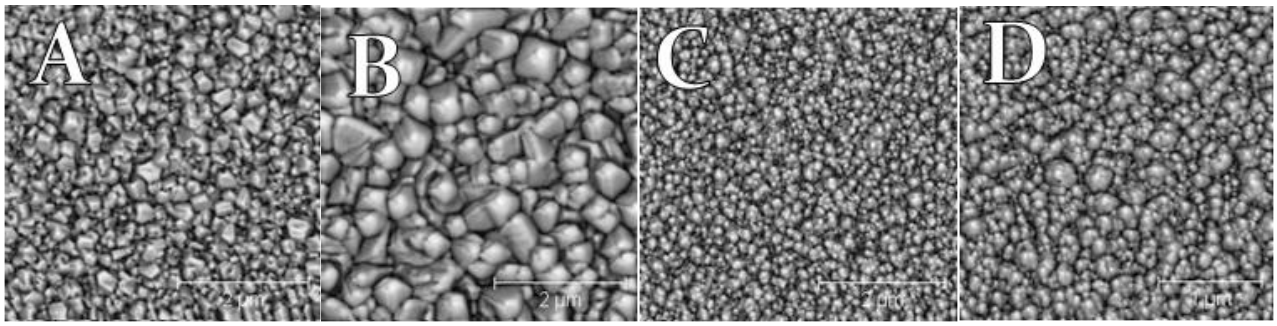

Figure 63. AFM local contrast images of grown films with various concentrations of N_2 in the gas phase: 0 % (a), 0.07 % (b), 0.25 % (c) and 1.5 %.

4.1.4.2 NV centre creation

Figure 64a shows the photoluminescence spectra of the diamond thin films as function of the N_2 concentration in a gas phase measured at room temperature and liquid nitrogen temperature. The NV^0 centre's zero phonon line photoluminescence is clearly observed at minimum N_2 concentration of 0.07 % in gas phase. The synthesis of as grown nanocrystalline diamond layers with NV photoluminescent centres at 0.07 % N_2 concentration in a gas phase is further confirmed by photoluminescence measurements at liquid nitrogen temperature (see Figure 64b). Both NV^0 and NV^- centres' zero phonon line photoluminescence are clearly observed together with their phonon side bands. The

absence of NV^- centre at room temperature photoluminescence measurement and negligible NV^- centre photoluminescence at liquid nitrogen temperature is probably caused by the presence of boron background contamination in deposition system, which might quench NV^- centre photoluminescence [90]. The Hall effect measurements using the van der Pauw technique confirmed the presence of acceptor conductivity in deposited diamond films, certainly due to boron incorporation, at concentration approximately of 10^{17} cm^{-3}. As the N_2 concentration rise, we observe quenching of NV photoluminescence. This quenching is attributed to the increase of sp^2 bonded carbon content, in another word the decrease of diamond quality factor in the nanocrystalline diamond layers.

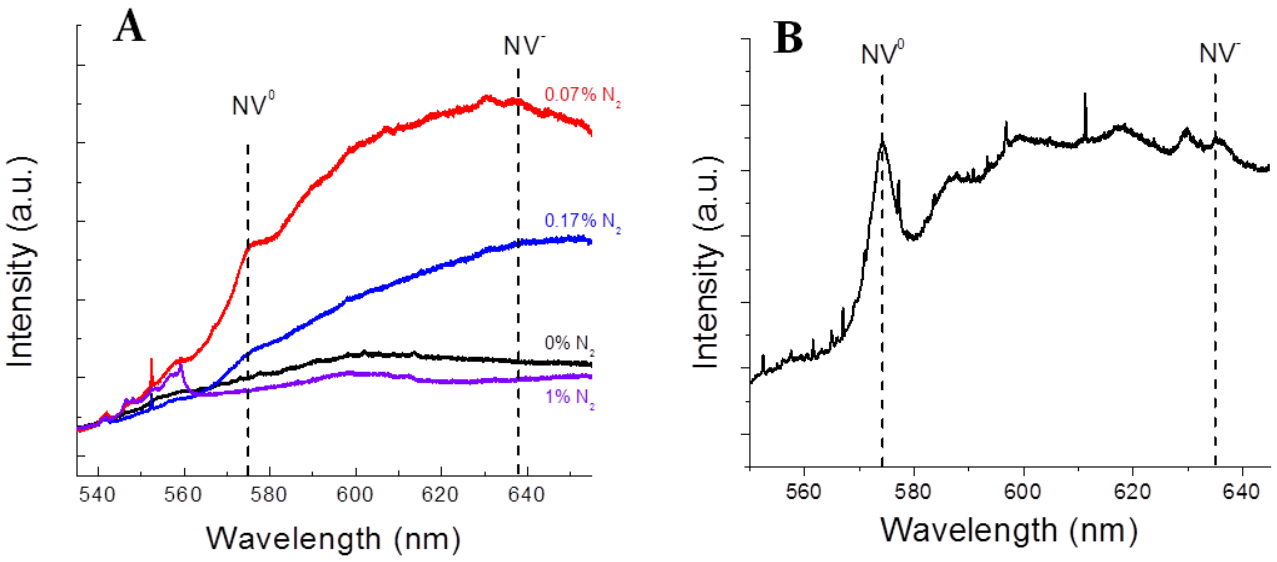

Figure 64. Photoluminescence spectra of grown films with 514 nm excitation wavelength: as function of different N_2 addition in a gas phase measured at room temperature (a), and with 0.07 % concentration of N_2 in the gas phase measured at liquid nitrogen temperature (b) [122].

The minimum nitrogen concentration of 0.07 % in working gas has been determined as the most suitable for creation of NV centres. The effect of working pressure on morphology, on NV photoluminescence and growth rate using this concentration was also studied. Figure 65 shows AFM surface morphology images as function of working pressure. As the pressure rise to 100 mbar, the growth rate is twice higher in comparison of 50 mbar (Figure 66b) and the morphology changes to form large and sharp polycrystalline diamond grains (Figure 65) [122]. Confocal microscope photoluminescence spectra in Figure 66a indicates NV^0 photoluminescence for both spectra (50 and 100 mbar) and negligible for NV^- [122].

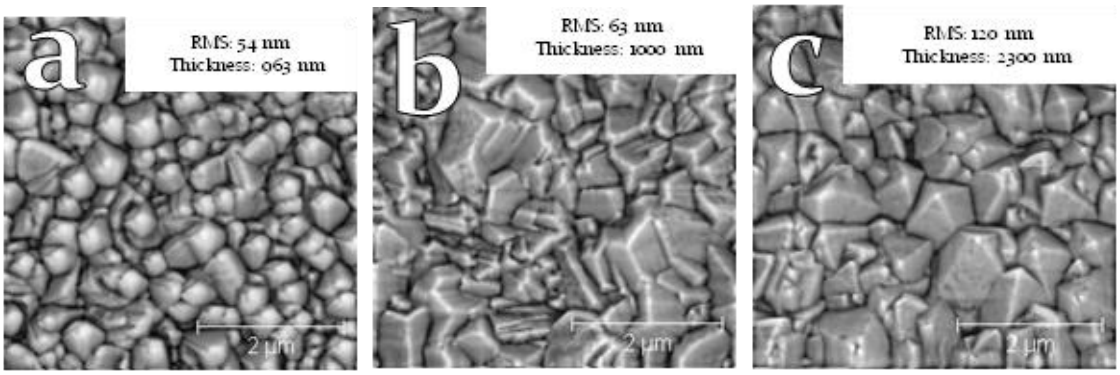

Figure 65. AFM local contrast images representing an effect of a working pressure on diamond morphology with using 0.07 % N_2 doping concentration: 50 mbar (a), 75 mbar (b) and 100 mbar.

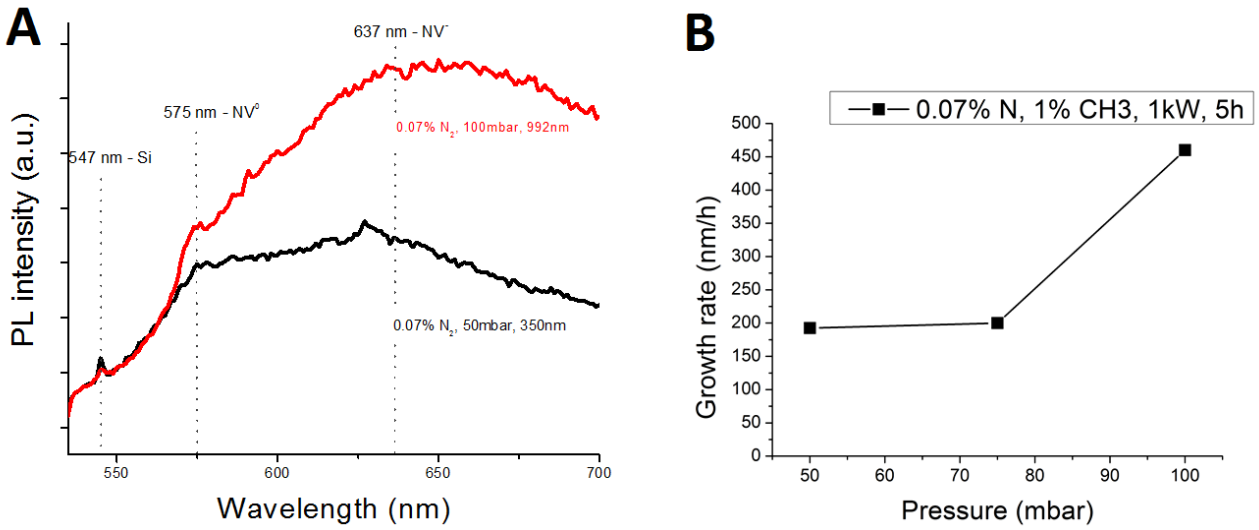

Figure 66. Effect of a working pressure with using 0.07 % N_2 doping concentration on NV photoluminescence measured with confocal microscope with excitation wavelength of 532 nm (a), and growth rate (b).

Conclusions

The growth rate increases with the N_2 concentration and with the working pressure. At high nitrogen concentrations, the surface morphology of deposited thin films changes dramatically due to re-nucleation and resulting in production of small crystals together with high sp^2 bonded carbon fraction that results into the quenching of photoluminescence. Optimal deposition conditions for creation of NV centres have been found using the lowest nitrogen concentration in the gas phase. Observed small NV^- photoluminescence is probably due to the presence of unwanted boron incorporation into the layer.

4.2 Study of large area linear antenna MW PE CVD nanocrystalline diamond growth

Conventional MW resonance MW PE CVD systems used to deposit diamond layers are limited by the size of growth area. The large area diamond growth is important for biomedical application such as for 3D diamond coating of medical implants, which can increase its biocompatibility. Another advantage is the diamond growth at low temperatures (below 300 °C) on biomedical material as plastics. This issue was overcome by the development of microwave plasma enhanced chemical vapour deposition apparatus with linear antenna delivery system (LA MW PE CVD).

The main difference from the conventional MW resonance MW PE CVD system is, that the LA MW PE CVD growth is based on cold surface wave plasma allowing growth at low temperatures. The LA MW PE CVD system uses besides of CH_4 also CO_2 as carbon precursor, and above that oxygen atoms helps hydrogen atoms to etch of sp^2 phase during the growth. Growth rate during the LA MW PE CVD growth can be accelerated by using pulsed plasma increasing density of atomic hydrogen atoms and higher sp^2 phase etching.

In part of the work we studied the effect of nitrogen addition in the gas phase with continual MW plasma on low pressure and low temperature NCD growth and NV centre creation using the linear antenna MW PE CVD apparatus. Some of the results were published at *Physica Status Solidi* A, 211 (2014) 10, 2296–2301 [123].

4.2.1 Experimental details

The diamond films were grown on (100) oriented silicon and corning glass substrates using the Linear antenna (LA MW PE CVD) system (Figure 67) at the IoP AS CR (by Andy Taylor and Marie Krečmarová). Substrates were seeded with a nanodiamond dispersion (NanoAmando®) from NanoCarbon Research Institute Ltd by spin coating (by Marie Krečmarová). On the Si substrates the diamond seeds adhesion was promoted by freshly oxidizing the surface. Oxidized Si surface has a negative zeta potential that matches NanoAmando® ND particles that have a positive zeta potential. This process resulted in homogenous coverage of substrates with a nucleation density of approximately $4 \cdot 10^{10}$ cm^2 as measured by atomic force microscopy. Diamond layers were grown at low pressure of 0.32 mbar, low temperatures of 250 °C and 520 °C, microwave power of 2x3 kW in hydrogen rich

plasma with 5% CH_4, 3% CO_2 and different N_2 concentrations from 0 – 10 % in the gas phase and duration of 8 hours. Substrate temperature was measured by a dual wavelength Williamson Pro pyrometer [123].

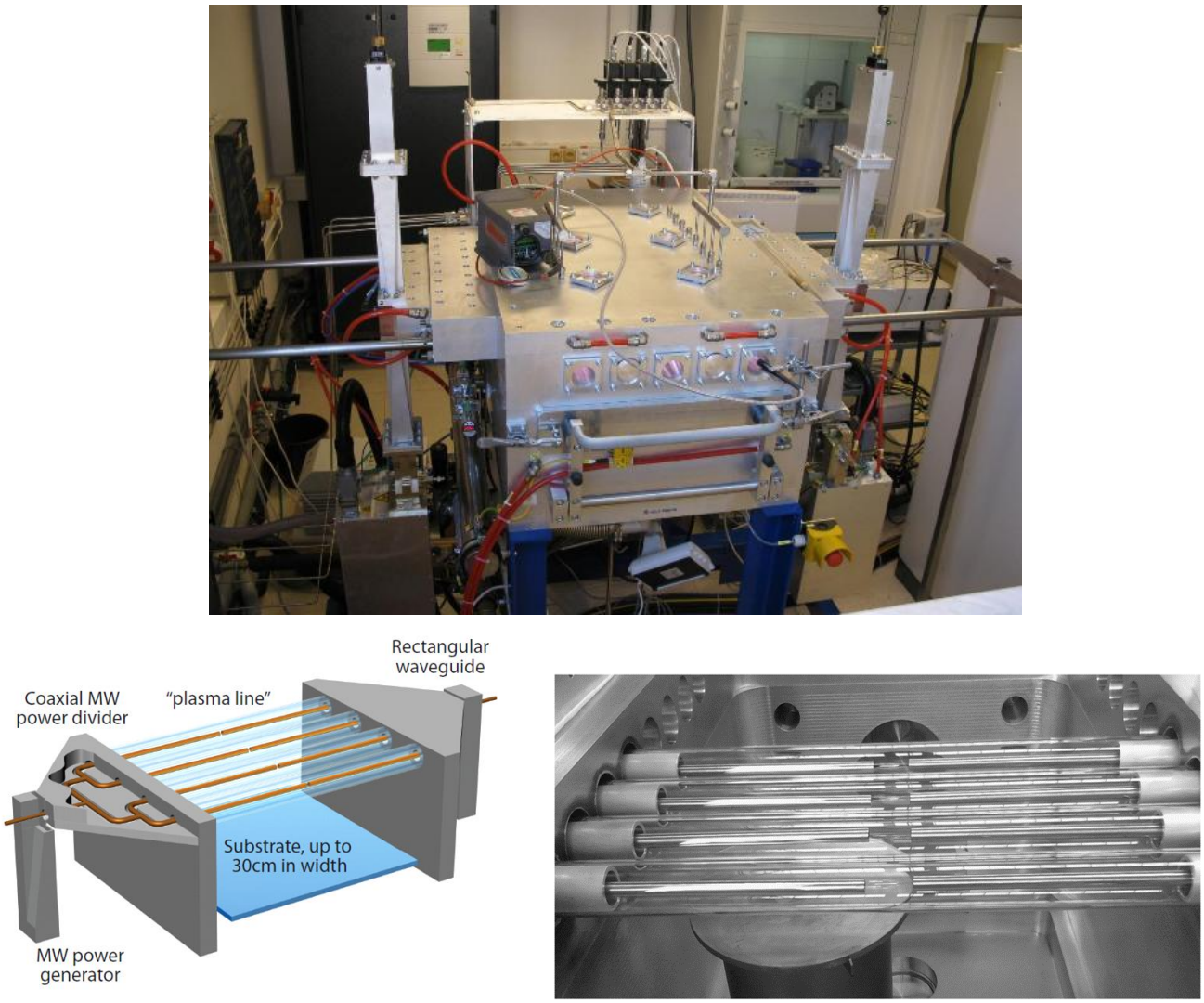

Figure 67. Photograph of the Linear antenna MW PE CVD apparatus (top), scheme (down left) and photograph (down right) of the Linear antenna delivery system.

Surface morphology was measured by a field emission scanning electron microscope (SEM) FEI Quanta 3D FEG (by Dr. Aleš Jäger) and atomic force microscopy (by Dr. Ladislav Fekete) in semi contact mode using NTEGRA-Prima a microscope (AFM) at the IoP AS CR. AFM was used to determined surface roughness, film's thickness and surface grain size in addition to surface morphology. Surface grain's sizes were evaluated from high-resolution images [1024x1024 pixels^2] using an autocorrelation algorithm described in [124]. The shape of the lateral grain size distribution was fitted with the

Gamma distribution. X-ray diffraction (GA-XRD) in grazing incidence (3°) was used to determine layers crystalline structure and its grain size (by Dr. Jan Drahokoupil) using an X´Pert Pro PANalytical diffractometer with CoKα radiation with parabolic mirror in the primary beam and a parallel plate collimator in the diffracted beam and a proportional detector) at the IoP AS CR.

Raman spectroscopy using a Renishaw InVia system was carried out (by Marie Krečmarová) at room temperature with excitation wave-lengths of 325 nm (5 mW) nm and 488 nm (25 mW) to determine diamond quality (sp^3/sp^2 ratio) and to calculate the size of film grains from the zone-centre phonon Raman peak) at the IoP AS CR. For diamond quality factor calculations the diamond carbon (sp^3) and amorphous carbon (sp^2) peaks in the Raman spectra with excitation wavelength at 488 nm were fitted using a Lorentzian function, sp^3/sp^2 ratio was established by areas under the fitted curves of peaks. For investigation of grain sizes, the zone-centre phonon Raman peak was fitted using a Lorentzian function to determine the full width at half maximum (FWHM) of the zone-centre phonon Raman peak which depends of the grain size. The NV centre photoluminescence was measured (by Marie Krečmarová) using a Renishaw InVia Raman Microscope) at the IoP AS CR with a 514 nm excitation laser and laser power of 25 mW at liquid nitrogen temperature. The spectra are normalised to sp^3 carbon peak [123].

Nitrogen distribution was determined by Thermal Neutron Depth Profiling (TNDP), a nondestructive technique used to determined ^{14}N concentration depth profiles at the Nuclear Physics Institute, Academy of Sciences (NPI ASCR) of the Czech Republic (by Dr. Jiří Vacík). The measurement was performed at the TNDP facility of the CANAM infrastructure at NPI ASCR Řež. Energy spectra were evaluated off-line by the new TNDP code [125], where the depth profile was determined on the channel-by-channel basis. The plan-view microstructure of the samples was examined using transmission electron microscopy (TEM; Jeol-2100F operated at 200 kV) at the Tamkang University in Taiwan (group of prof. I-Nan Lin, by Dr. Kamatchi Jothiramalingam Sankaran). Conventional polishing procedure was used, which include hand polishing to thin the samples down to around 200 microns followed by ion milling until a small perforation in the centre of the sample [123].

4.2.2 Nanocrystalline diamond nitrogen doping study in the LA MW PE CVD system

Investigation of the nitrogen doping using the conventional MW resonance cavity based MW PE CVD (in the Chapter 4.1.4) brings important results for the sensor functionality, that just a minimum nitrogen concentration in the gas phase is effective for the best formation of the NV centres and also for material properties (e.g. high sp^3 and low sp^2 carbon phase) of diamond film. Nevertheless, the LA MW PE CVD allows growth of large area, with possibility of a commercial use, and as well as growth at low temperatures (< 300 °C) important for low melting point materials as polymers. For these attractive reasons, the nitrogen doping was studied also in the LA MW PE CVD apparatus with the main focus on material properties and the NV centre formations in nanocrystalline diamond films.

4.2.2.1 Study of morphology and NV photoluminescence

Figure 68a shows variation of the growth rate and calculated diamond quality factor as sp^3/sp^2 carbon ratio with N_2 addition. The growth rate increases at lower N_2 concentrations with maximum growth rate for 2.4 % N_2 and decreases at higher concentration. The decreasing deposition rate is attributed to diamond etching at high N_2 concentration [123]. Coalescence of the diamond grains disappears and isolated grains are formed at 7 %. No growth is observed at 10 % N_2. The diamond quality factor, which corresponds to diamond to carbon and non-diamond carbon (sp^3/sp^2) peaks ratio decreases with a small addition of N_2 into the gas phase (0.5 % of N_2) [123] and then increases up to 4.8 % N_2.

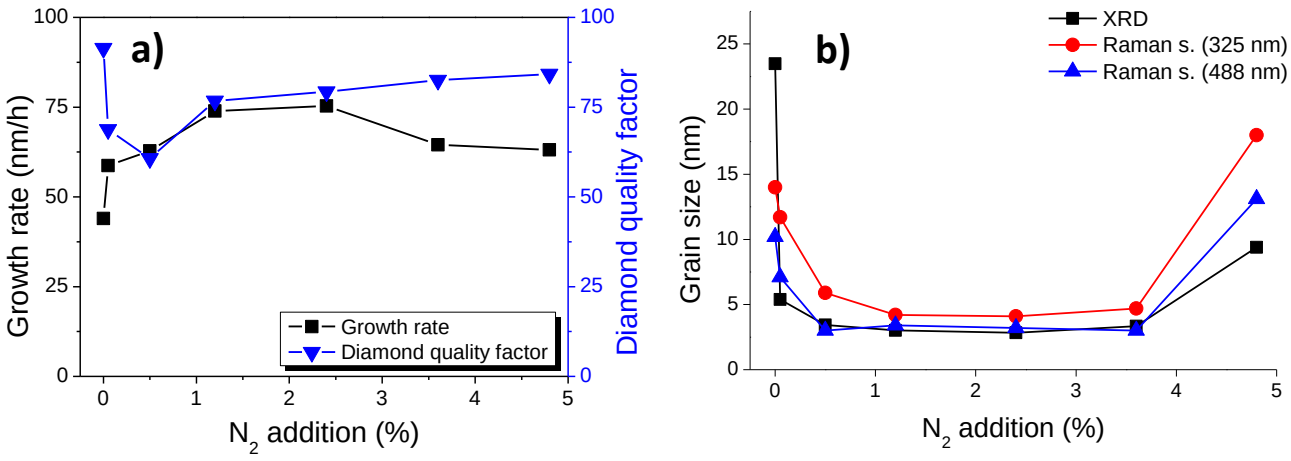

Figure 68. Variation of the growth rate and calculated diamond quality factor as sp^3/sp^2 carbon ratio (a) and diamond grain size calculated from Raman spectra and GA-XRD diagrams (b) in deposited diamond films as a function of nitrogen concentration in the gas phase [123].

GA-XRD analyses of deposited diamond films show characteristic crystalline (111), (220) and (311) diamond diffraction peaks (in Figure 69a for 4.8 % of N_2). Average diamond crystallite size was calculated from the (111) diffraction peak using TOPAS program and is reported as a function of N_2 concentration in the gas phase in Figure 68b. The average grain sizes were also calculated from full width at half maximum (FWHM) of diamond Raman peak. The calculated average grain size by both techniques are consistent. The diamond grain size decreases to ~3 nm with N_2 addition from 0.05 % to 3.6 % N_2 [123]. The grain size increases for 4.8 % N_2 concentration.

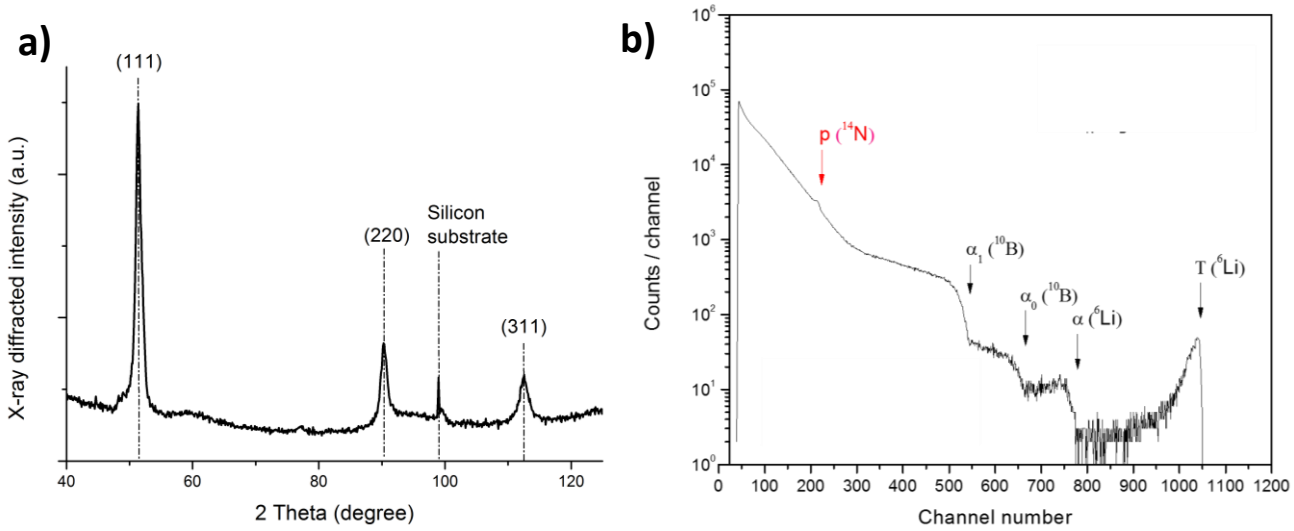

Figure 69. GA-XRD spectra of the diamond film grown with 4.8 % N_2 concentration (a) and TNDP graph of deposited diamond film with 2.4 % concentration of N_2 into the gas phase (b).

TNDP graph of the deposited diamond films with 2.4 % N_2 addition into the gas phase observed in the depth profiles ^{14}N nitrogen atoms concentration of $1.3 \cdot 10^{18}$ cm^{-2} and ^{10}B boron atoms concentration of $5.1 \cdot 10^{15}$ cm^{-2} (Figure 69b). The boron contamination is certainly due to the reactor contamination by previous boron doped depositions despite thorough chamber cleaning [123].

Raman spectra measured with excitation wavelength of 488 nm are shown in Figure 70a. These spectra clearly show the zone-centre phonon diamond Raman peak. The amorphous carbon, graphitic G and D bands are also observed. Addition of N_2 into the gas phase increases sp^2 bonded carbon content in the layers with the highest sp^3/sp^2 ratio being observed for 2.4 % nitrogen concentration in the gas phase [123]. For higher N_2 concentration than 4.8% the sp^3/sp^2 ratio improves, probably due to the N_2 plasma etching of the sp^2 phase around the grain boundaries.

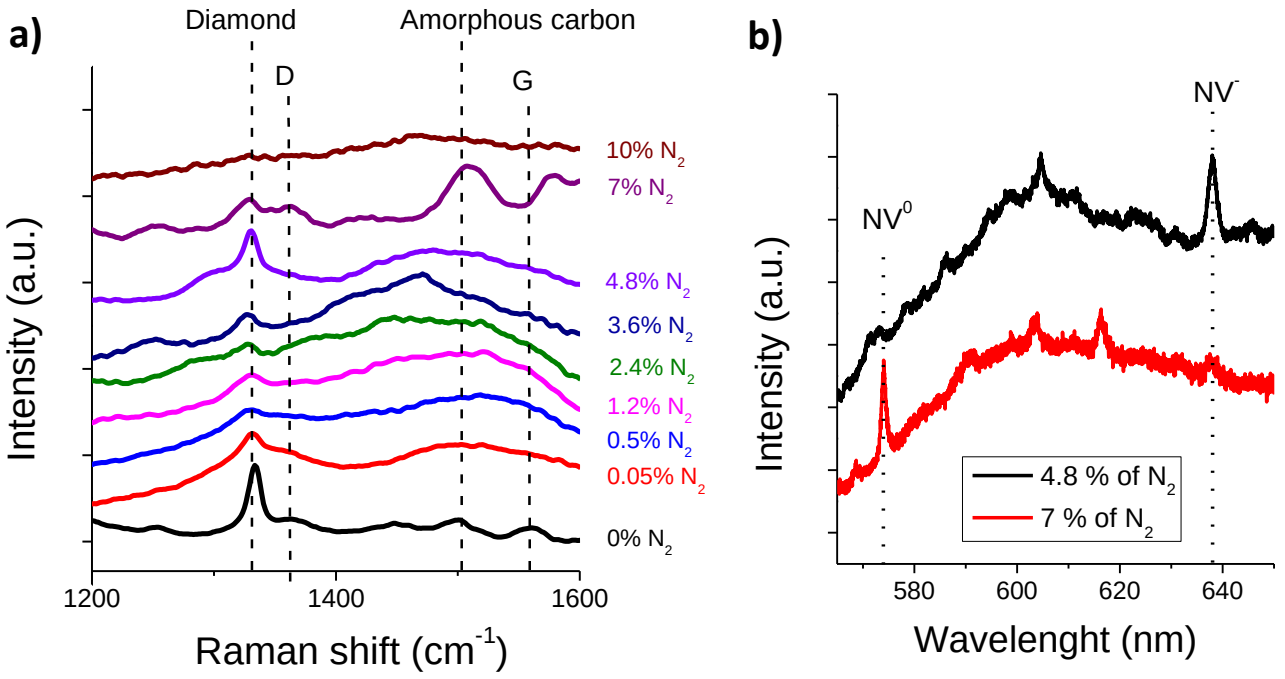

Figure 70. Raman spectra of the grown diamond thin films at different N_2 addition in a gas phase measured with excitation wavelength of 488 nm [123] (a) and NV photoluminescence spectra of the diamond films with 4.8 % and 7 % concentration of N_2 with excitation wavelength of 514 nm (b).

Photoluminescence measurements were also carried out on all deposited samples (Figure 70b). However, despite the presence of nitrogen as measured by TNDP, NV photoluminescence was detected only in case of samples doped with 4.8 % and 7 % of N_2. The absence of detectable NV centres photoluminescence at lower N_2 concentrations is due to sensitivity of commercial confocal setup but it might also be associated to quenching NV photoluminescence via non-radiative channels related to the sp^2 grain boundary defects. The NV photoluminescence spectra for 4.8 % and 7 % of N_2 concentration exhibit NV^0 or NV^- peak with different intensity. It could also be caused due to the B contamination that might affect the Fermi level.

SEM results of the diamond layers show a dramatic change of surface morphology induced by the N_2 doping in Figure 71. Without any addition of N_2 (Figure 71a), the film consists of randomly oriented diamond crystals with clearly distinguishable edges and facets. With an addition of a tiny amount of nitrogen (0.05 % of N_2) into the gas mixture, the sharp-edged crystals structure is replaced by a random structure with coarsened grains (not shown). Further N_2 addition (0.5 % of N_2) leads to even more profound surface relief change as seen in Figure 71b. Small crystals start to build randomly oriented elongated agglomerates with lengths up to several hundreds of nanometres. This same morphology is observed for diamond layers grown with higher nitrogen concentration and it is similar the

morphology of nitrogen doped N-UNCD grown in Ar rich plasma shown in Figure 71d and very different from (100) faceting that is often observed with N_2 addition in hydrogen rich plasmas. This might be explained by either the lower deposition temperature or lower plasma power density during diamond growth [123].

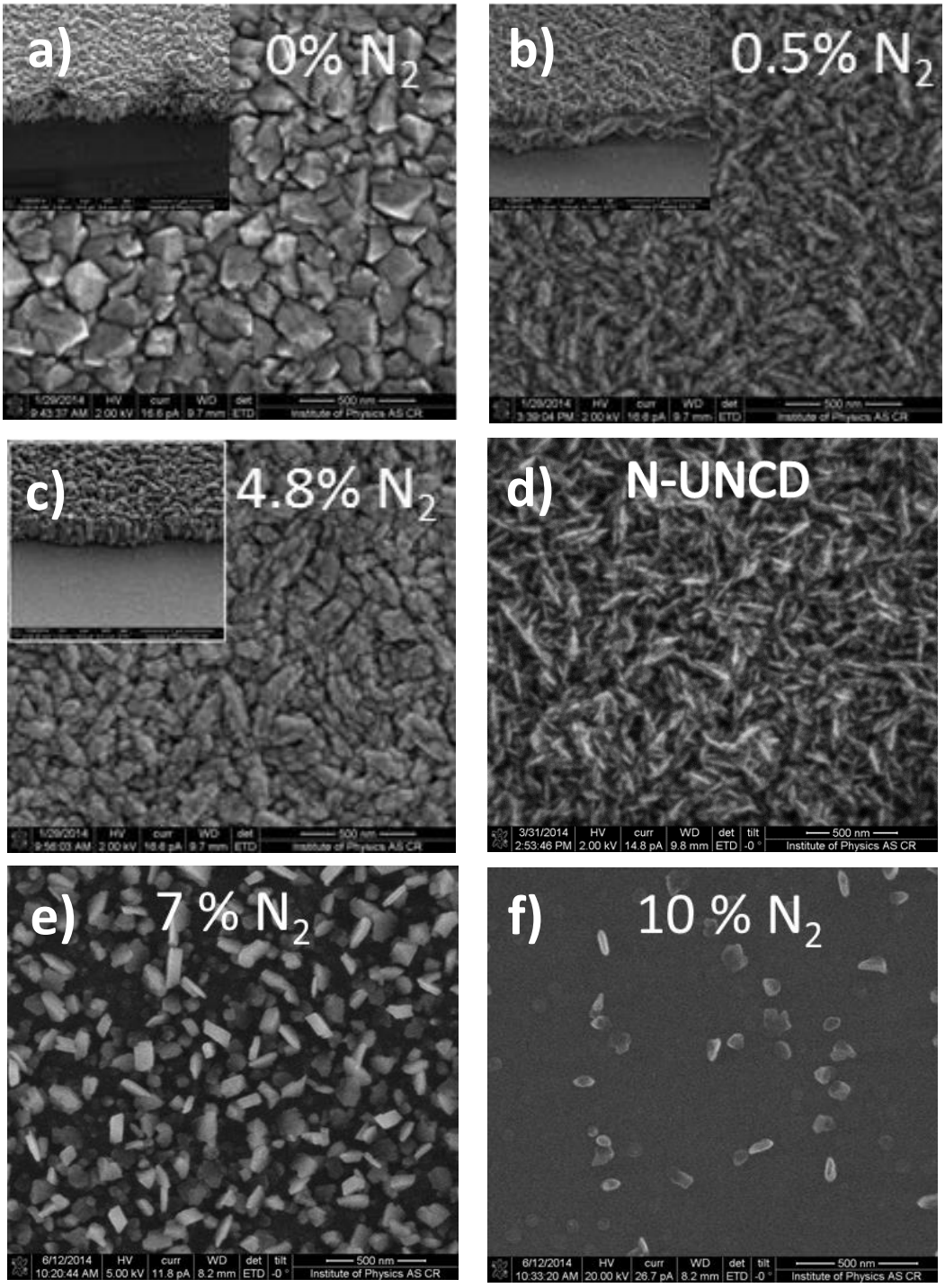

Figure 71. Top and cross view SEM images of diamond layers with concentrations of N_2: 0 % (a), 0.5 % (b), 4.8 % (c); top view SEM images of diamond layers with 7 % (e) and 10 % (f) N_2 concentrations; and morphology comparison of nitrogen doped UNCD film grown from Ar-rich plasma (d) [123].

By the N_2 addition of 4.8 %, the crystals became larger with more symmetric shapes (Figure 71c). Higher N_2 concentrations lead to formation of separated grains and diamond etching occurs (Figure 71e,f). For the highest N_2 concentration of 10 % is not observed the diamond film growth (Figure 71f).

Van der Pauw technique was used to determine electrical properties of studied diamond films. In contrast to nitrogen doped ultra-nanocrystalline diamond (N-UNCD) with specific metallic-like grain boundaries of graphite encasing diamond grains, none of our films show high conductivity but in contrast they showed high resistivity. All grown diamond films exhibit resistivity above ~10^8 Ω·cm. This high resistivity is likely due to the fact that only a small amount of graphitic phase is present around individual grain, as con-firmed by Raman spectroscopy [123].

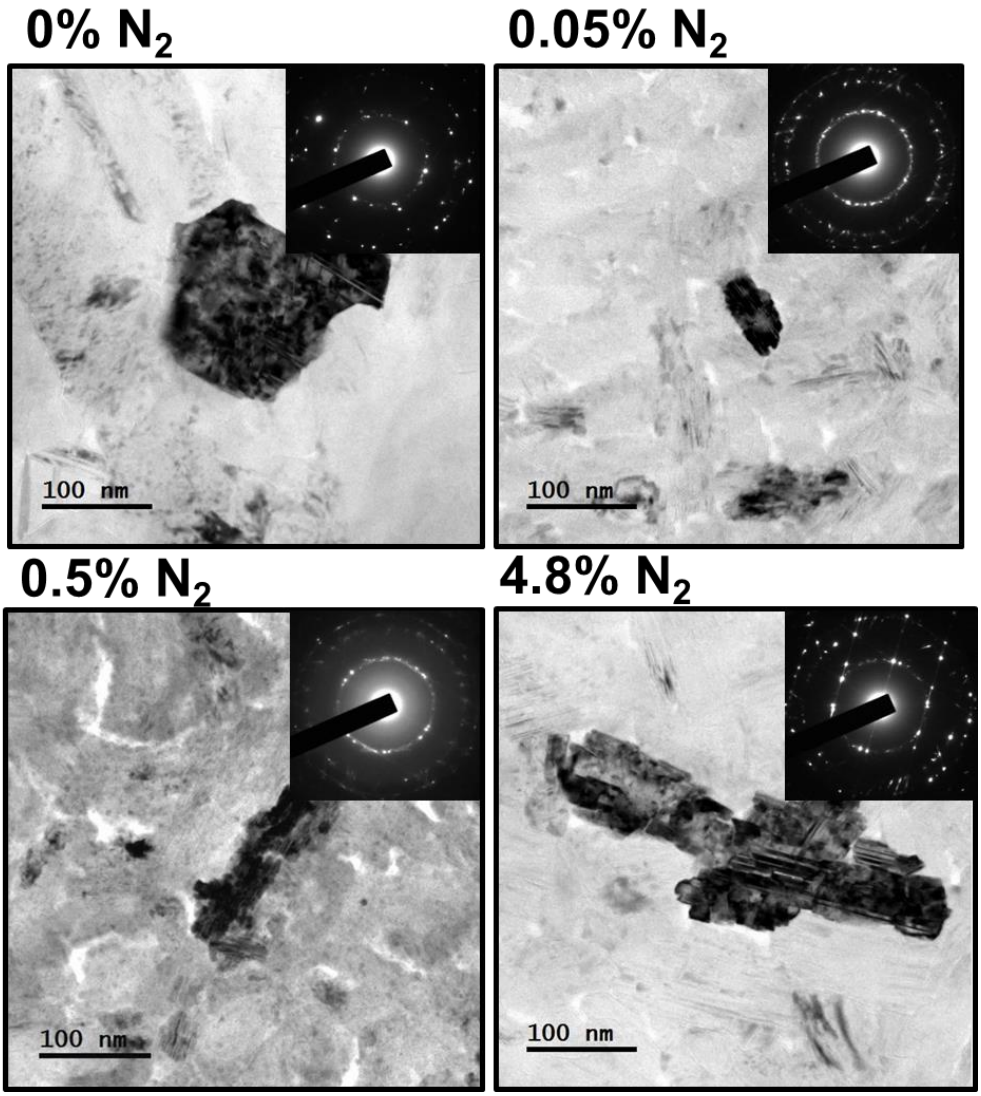

Figure 72. Top view TEM BF images of deposited diamond films with N_2 concentration from 0 % to 4.8 % [123].

In order to have a better understanding of diamond layers crystalline structure, TEM characterisations were carried out. Bright field (BF) HRTEM shown in Figure 72 indicates that the sample with 0 % N_2 concentration shows large grains formation, sample with the 0.05 % of N_2 contains uniformly large diamond grains (~100 nm in size), sample with the 0.5 % of N_2 contains large diamond aggregates of larger size (~200 nm) [123] and sample with the 4.8 % of N_2 contains large clusters with branches.

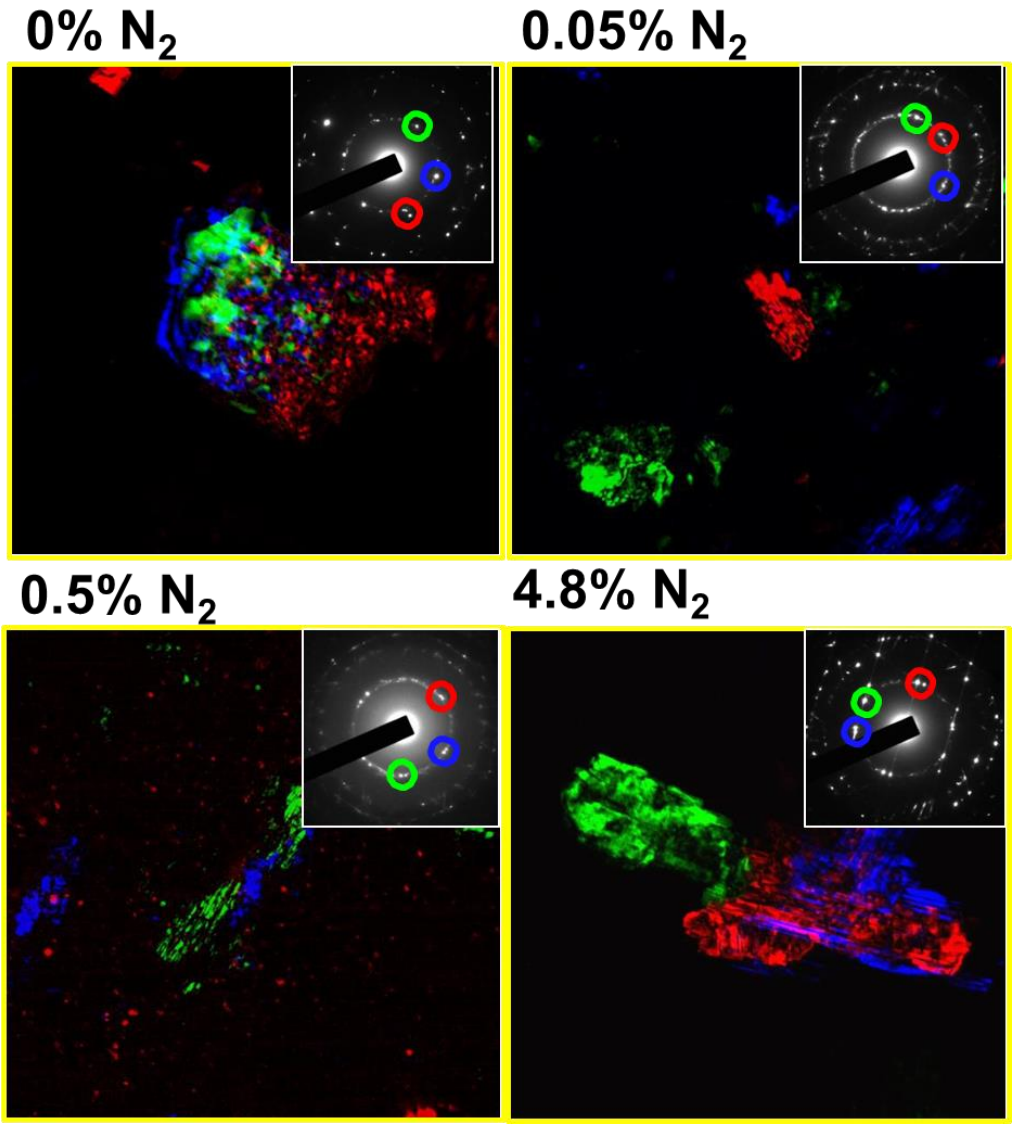

Figure 73. Top view TEM c-DF images of deposited diamond films with N_2 concentration from 0 % to 4.8 % [123].

The distribution of the diamond grains is more clearly illustrated as the composted dark field (c-DF) images shown in Figure 73. Detailed HRTEM microstructure of the diamond grains are revealed in the Figure 74 showing a micrograph and the associated Fourier transformed diffractogram (FT_O). Sample with 0 % N_2 exhibits predominantly with diamond phase. More sp^2 bonded carbon was observed with

N_2 doping. Micrographs with the associated Fourier transformed diffractogram show that the grains has a diamond structure, containing a large proportion of planar defects, which are implied by the streaks and systematic row of diffraction spots in the FT_o image (region 1, FT_1). This large quantity of defects can explain the observed decrease in diamond grain size determined from GA-XRD and Raman measurements. In contrast, TEM structure image corresponding to the region adjacent to the diamond grain, region 2, indicated that this region contains abundant nano-sized sp^2-bonded clusters. The FT image (FT_2) indicated clearly that these nano-sized clusters are graphite phase (0.05 % of N_2) and amorphous carbon phase (0.5 % and 4.8 % of N_2), which is implied by the presence of a large diffuse diffraction ring in the centre of the FT image [123].

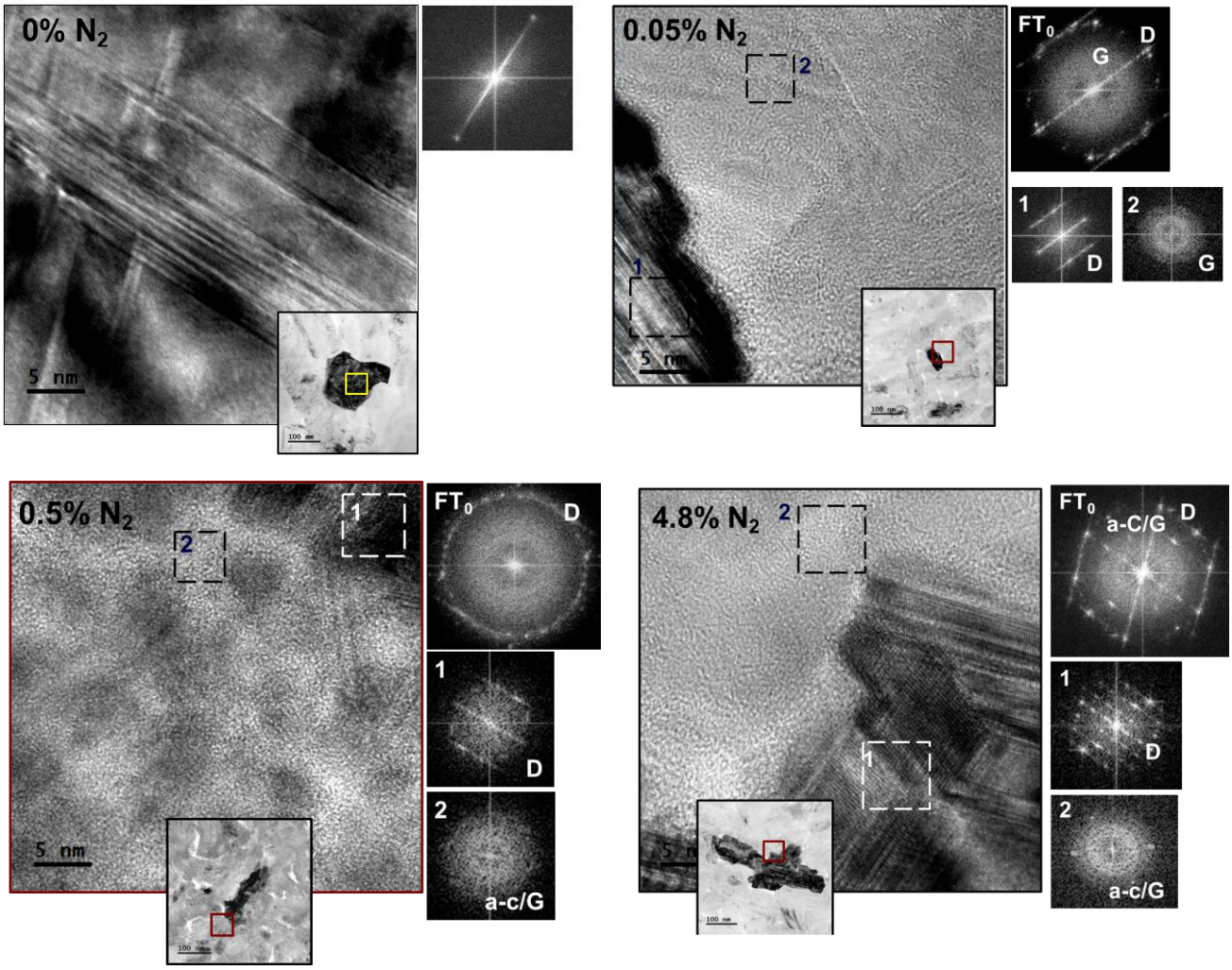

Figure 74. Detailed HRTEM microstructures of the diamond grains with the associated Fourier transformed diffractogram (FT_O) for the selected areas 1 and 2 of the films with N_2 concentration from 0 % to 4.8 % [123].

Sample with 0.5 % of N_2 contains large diamond aggregates of larger size (~200 nm) surrounded by small grains (Figure 73). Figure 74 clearly indicated the presence of the (111)dia, (220)dia and (311)dia

diffraction rings in the region 1, implying that the materials in this region are mostly diamond. HR TEM structure image in Figure 74 shows the enlarged micrograph of the region nearby the large ag-aggregates, indicating that these regions contain abundant small diamond clusters about 5 nm in size, which is similar to those found in UNCD films grown by CH_4/Ar plasma. However, the boundaries between the ultra-small grains are wider and contain amorphous carbon. Typical ultra-small diamond grains and grain boundaries are high-lighted by regions 1 and 2, respectively, and the FT images FT_1 and FT_2, respectively [123].

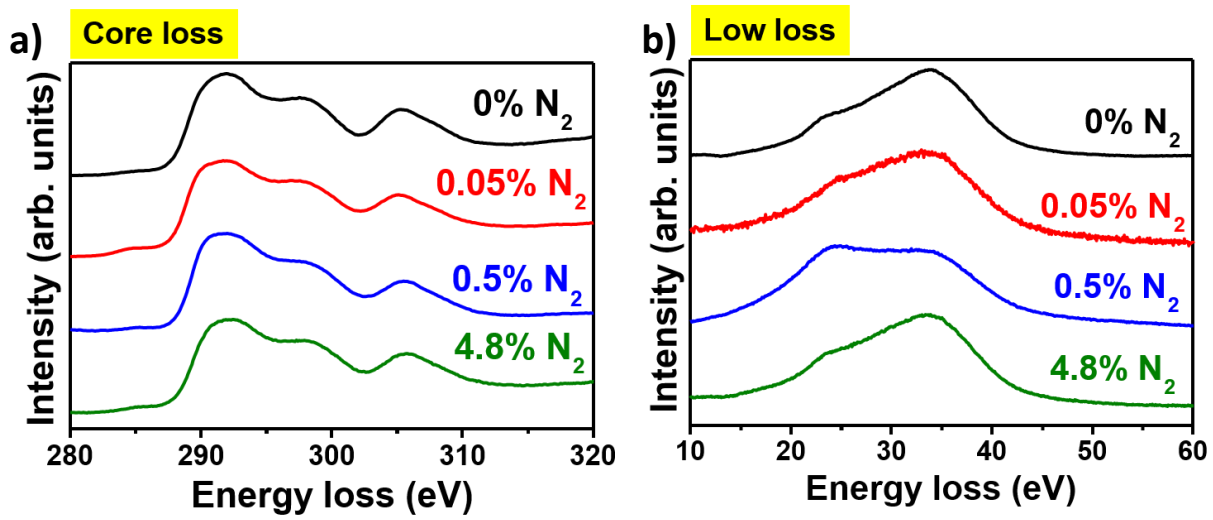

Figure 75. Carbon edge core-loss (a) and plasmon-loss EELS spectra (b) of deposited diamond films with films 0.05 % and 0.5 % concentra-tion of N_2 [123].

The core-loss EELS in Figure 75a, corresponding to the areas shown in Figure 74, indicates the presence of diamond σ*-band near 289.5 eV with a deep valley near 302 eV, confirming that the region was predominated with the sp^3-bonded carbon and some sp^2-bonded carbon (π-band near 284.5 eV), which is presumably contributed by the grain boundary phases. The plasmon loss EELS for samples with 0 %, 0.05 % and 4.8 % N_2 concentrations (Figure 75b) shows a s4-peak at 32 eV corresponding the bulk plasma of the nano-sized diamond cluster, with a shoulder near s2-23 eV corresponding to the surface plasma of the diamond clusters, further confirming that the materials are mostly diamond. The plasmon loss EELS for sample with 0.5 % of N_2 concentration shows a single peak near s1-peak near 22 eV, besides the s2 and s4 peaks, indicating that this region contains some amorphous carbon, mainly around the grain boundaries [123].

Conclusions

The addition of nitrogen increases deposition rate to a maximum at [N_2] = 2.6 % and then decreases it, due to enhanced etching. A tiny addition of N_2 dramatically changes also surface morphology from well facetted diamond crystals to UNCD like morphology without NV photoluminescence. In contrary to UNCD prepared from Ar rich plasmas, Raman spectra exhibits clear diamond peaks in addition to graphitic Raman peaks. GA-XRD results and Raman spectra analysis indicate growth of diamond grains of average size of ~ 3 nm. TEM characterizations show large and randomly oriented elongated diamond aggregates with a large proportion of planar defects and the presence of 5 nm grains nearby the larger grains [123]. Higher nitrogen addition [N_2] ≥ 4.8 % leads to strong diamond etching, resulting in significant decrease of deposition rate, reduction of nucleation density, formation of isolated facetted diamond grains and NV luminescence.

Despite of the advantages of the LA MW PE CVD growth, nitrogen doping at low concentration leads to significant reduction of the diamond quality and re-nucleation occurs. The NV PL was observed only at higher nitrogen concentration in the gas phase with diamond etching and not homogenous diamond film coverage. In conclusion growth conditions used in the experiment are not suitable for the NV centre formation. In contrary, diamond growth by the conventional MW resonance cavity based MW PE CVD system achieved at low nitrogen concentration in the gas phase results to efficient formation of the NV centres and also good material properties (high sp^3/sp^2 carbon ratio) of diamond film.

4.2.2.2 Low temperature growth

In the previous chapter was consider that the N_2 addition into the gas phase plays an important role on the diamond morphology. The diamond films were grown at same condition as in previous chapter except of ultra low temperature of 250 °C at which we attempted to grow the NCD. The lower temperature diamond growth would allow coating of the biomedical materials with lower melting point such as polymers without its degradation and in purpose to increase its biocompatibility.

Figure 76 shows SEM surface images of the low temperature grown films without addition of N_2 and with 2.4 % addition of N_2 into the gas phase. The film grown without N_2 addition exhibits of amorphous carbon film with higher R_{RMS} roughness of 73 nm. Nitrogen addition of 2.4 % dramatically improves the quality showing some crystal structure. The AFM data (Figure 77) are consistent with the

AFM results. AFM surface image for 0 % N_2 concentration is noisy due to the lower stability of the measurement. The Raman spectra (Figure 78) confirmed the improvement of the film quality with nitrogen addition. With nitrogen addition is visible a clear diamond peak shifted probably due to the invented boron incorporation, whereas in the spectra for 0 % nitrogen addition is visible broad amorphous carbon peak.

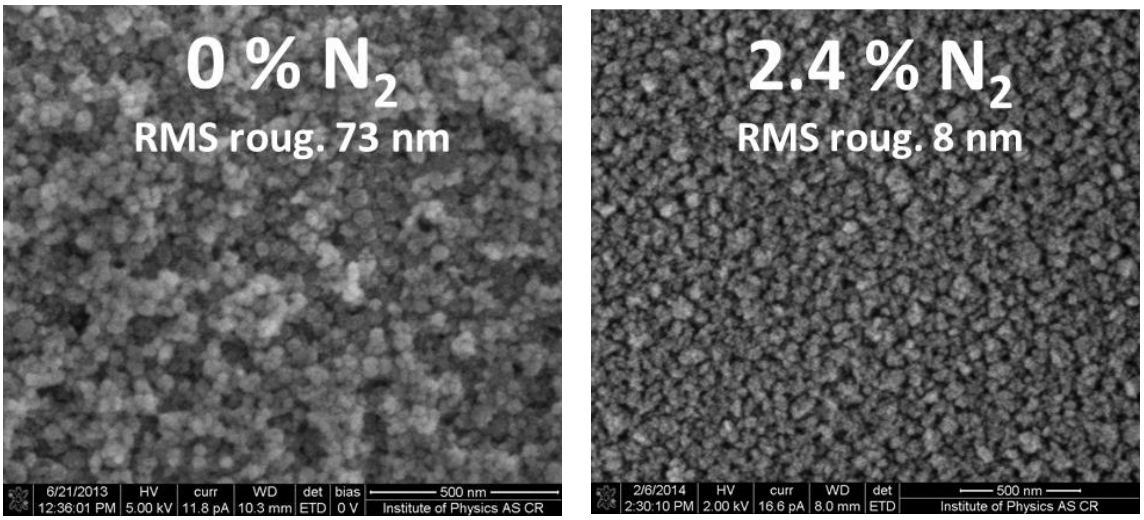

Figure 76. SEM surface images of the diamond films grown with 0 % and 2.4 % of N_2 addition into the gas phase.

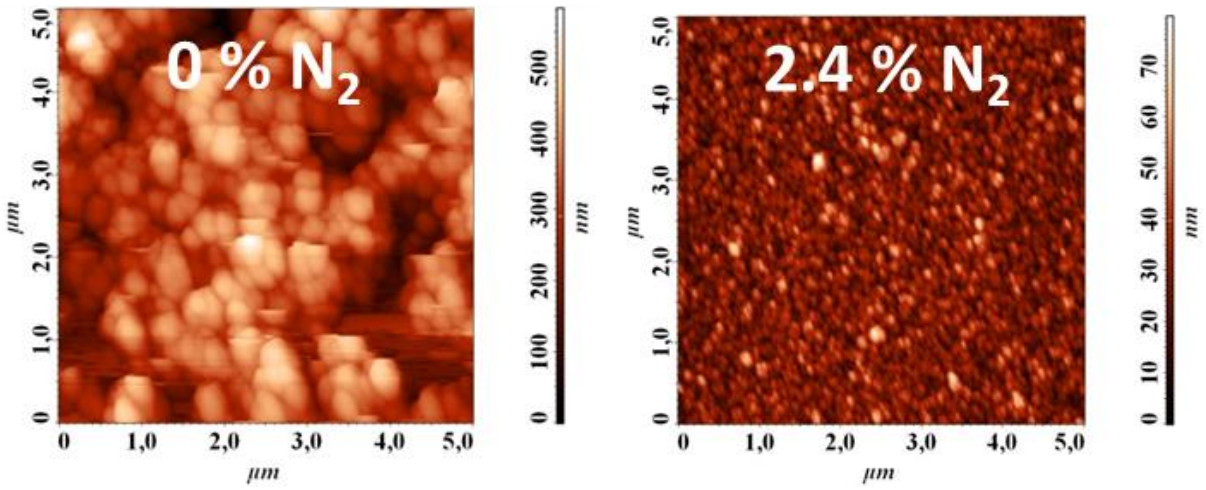

Figure 77. AFM surface images of the diamond films grown with 0 % (unstable measurement) and 2.4 % of N_2 addition into the gas phase.

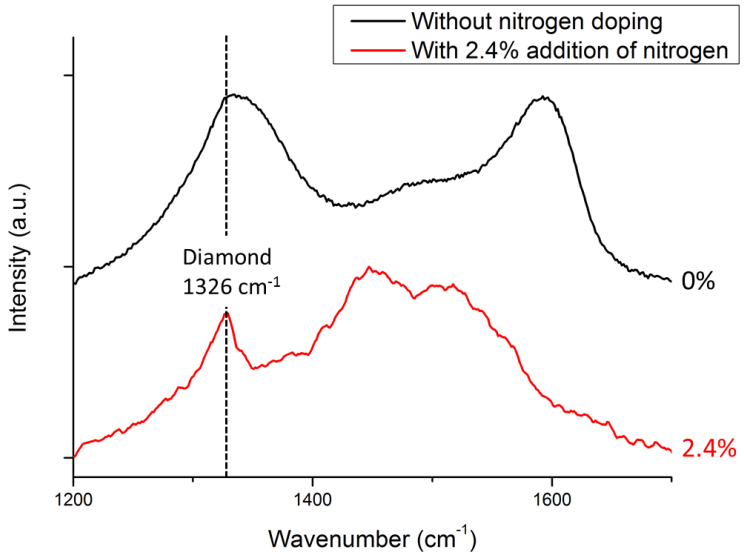

Figure 78. Raman spectra of the grown diamond thin films at 0 % and 2.4 % N_2 addition in a gas phase measured with excitation wavelength of 488 nm.

Conclusions

At low temperature of 250°C was observed significant improvement of the diamond film quality, i.e. sp^3/sp^2 ratio and well defined crystals with addition of nitrogen compared to layer deposited without nitrogen.

4.3 MW PE CVD homoepitaxial diamond growth

In the previous sub-chapters we studied boron and nitrogen doping in nanocrystalline diamond films to discover optimal growth conditions for fabrication of high quality diamond electrode and NV centres containing film. The best observed results were applied for construction of the homoepitaxial diamond biosensor device. Next two sub-chapters deal with synthesis of highly boron doped diamond layer with very flat surface and thin film with NV centres on top of it.

4.3.1 Highly boron doped single crystal diamond

This chapter deals with homoepitaxial highly boron doped growth leading to high B-doped diamond conductivity and ultra-flat surface, which is very important for the functionality of the biosensor.

Single crystals (100) oriented diamond from Sumitomo Electric Hartmetall GmbH were used as substrates. Figure 79a,b shows a surface morphology of a received (100) oriented Sumitomo substrate.

Both optical microscopy (by Marie Krečmarová) and optical profiler (by Dr. Ladislav Fekete) show large polishing lines on the surface formed during fabrication process which are inappropriate for very smooth diamond growth. Therefore the substrates were re-polished by using better quality of polishing by the Optima Diamant, spol. s.r.o. in Ostrava, Czech Republic. First were polished with using scaifes (30 cm in diameter, spinning at 3000 rpm). The substrates had their first 10 µm of surface removed by polishing to eliminate any damages caused by previous processes. After this removal the surfaces were "zoeted" (the sample is moved in a quick lateral movement across the scaife). The obtained re-polished crystals are very smooth (R_{RMS} < 1nm as measured by optical profiler) and do not show any visible polishing lines under optical microscope (Figure 79c).

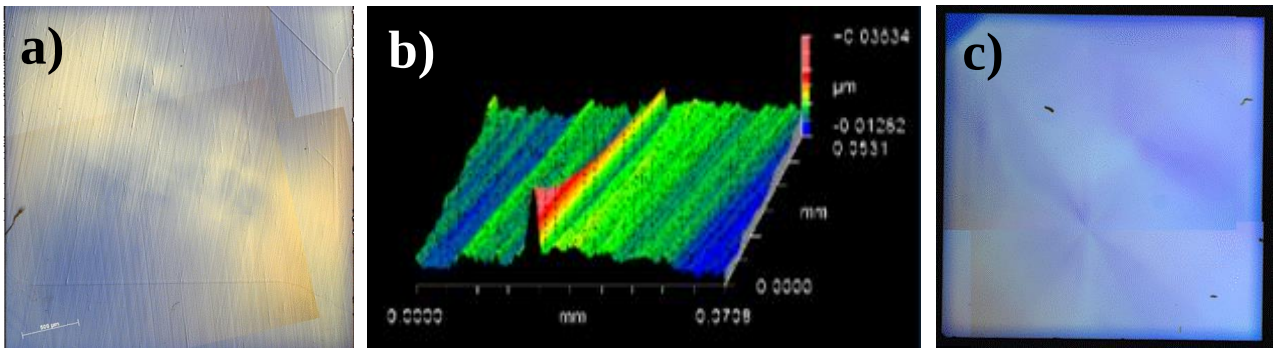

Figure 79. Optical microscopy picture of as received Sumitomo Electric Hartmetall GmbH (100) oriented crystals (a) and oblique plot of the surface measured by optical profiler (b); optical microscopy image of re-polished crystal in Optima Diamant (c).

Re-polished substrates were then cleaned 10 min in boiling H_2SO_4 + KNO_3, following by ultrasonic baths in hot deionized water, acetone and hot isopropyl alcohol (10 mins for each solution) (by Marie Krečmarová). The substrates were then 10 minutes plasma etched before growth in H_2 (98 %) and O_2 (2 %) plasma using 100 mbar working pressure and 500 W microwave power (by Marie Krečmarová) using Seki Technotron AX5010 CVD system (Figure 51) it he IoP ASCR. The highly boron doped homoepitaxial layer was grown in the same reactor (by Marie Krečmarová) in hydrogen rich gasses including 1 % CH_4 and 6000 ppm concentration of TMB precursor. Microwave power was 550 W, working pressure 100 mbar, substrate temperature 1100 °C and growth duration 9 h.

Figure 80a shows the optical image (by Marie Krečmarová) of the grown layer for sample 164. The sample's surface is highly defective, densely covered with pyramidal hillocks. There are few large pyramidal hillocks (Figure 80b) with the height of approximately 10 µm and higher thickness of the film on the edges (~12 µm) as measured by the Optical profiler (by Anderew Taylor). It´s surface

roughness is high R_{RMS} = 1.245 µm. The thickness of the grown layer calculated from a weight is 19.334 µm.

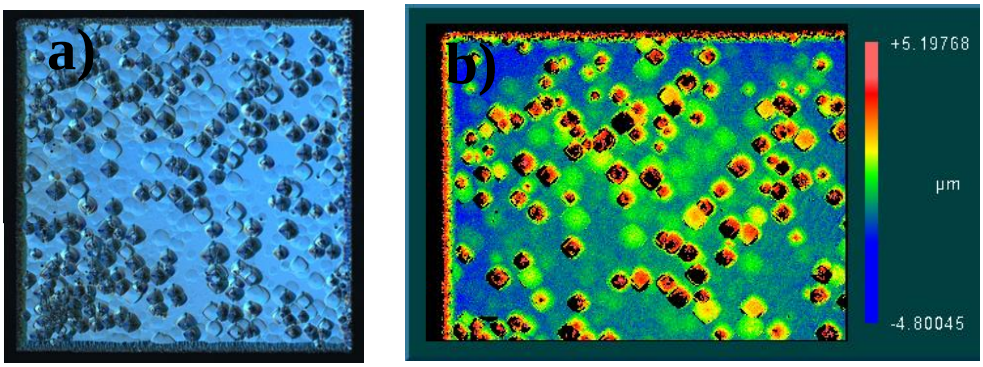

Figure 80. Optical microscope (a) and optical profiler (b) surface morphology images of the grown homoepitaxial layer (sample 164).

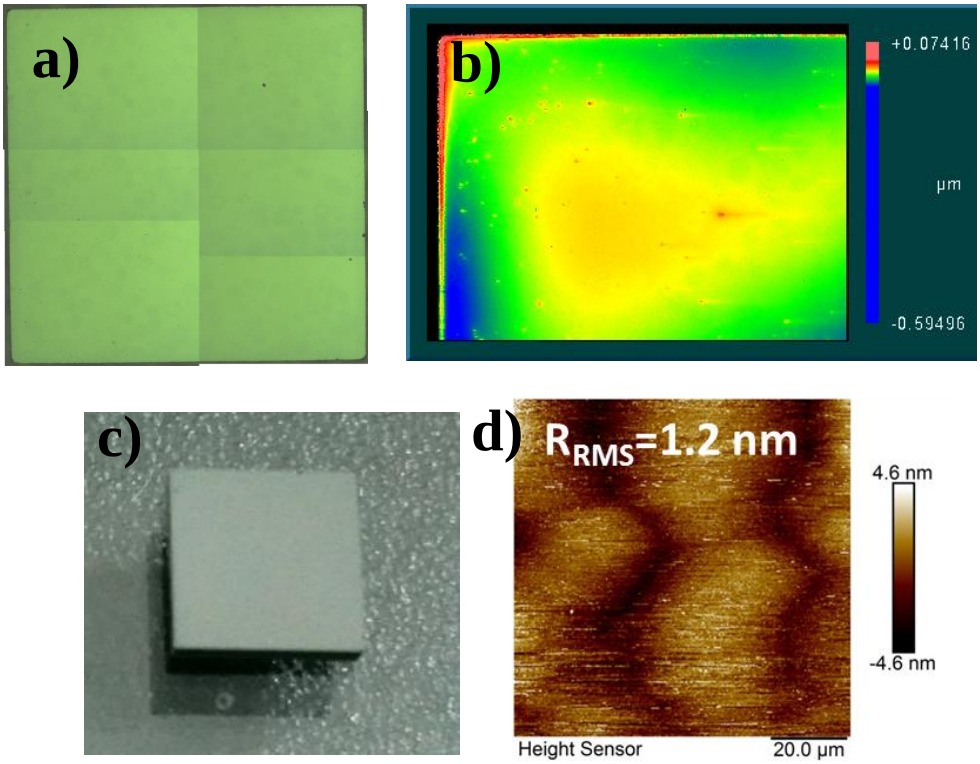

Figure 81. Optical microscope (a), optical profiler (b), photograph (c) and AFM (d) surface morphology images of the grown and polished highly boron doped homoepitaxial layer (sample 164).

Due to the many surface hillocks defects the grown layer was again re-polished by the Optima Diamant to obtain an ultra-flat surface. The thickness of the polished boron doped layer is 15.078 µm as obtained by weight measurement (sample 164). Approximately 0.15 mg of the layer was removed by polishing. The surface of the polished film is without any visible pyramidal hillocks defects. Figure

81c shows the photograph of the polished layer and figure 81a the optical image of the surface (by Marie Krečmarová). The surface of the layer is very smooth, the surface roughness obtained by optical profiler (by Andrew Taylor) is R_{RMS} = 10 nm (Figure 81b). The surface roughness measured (by Dr. Ladislav Fekete, see Chapter 4.1.1) with AFM (Figure 81d) is very low R_{RMS} = 1.2 nm.

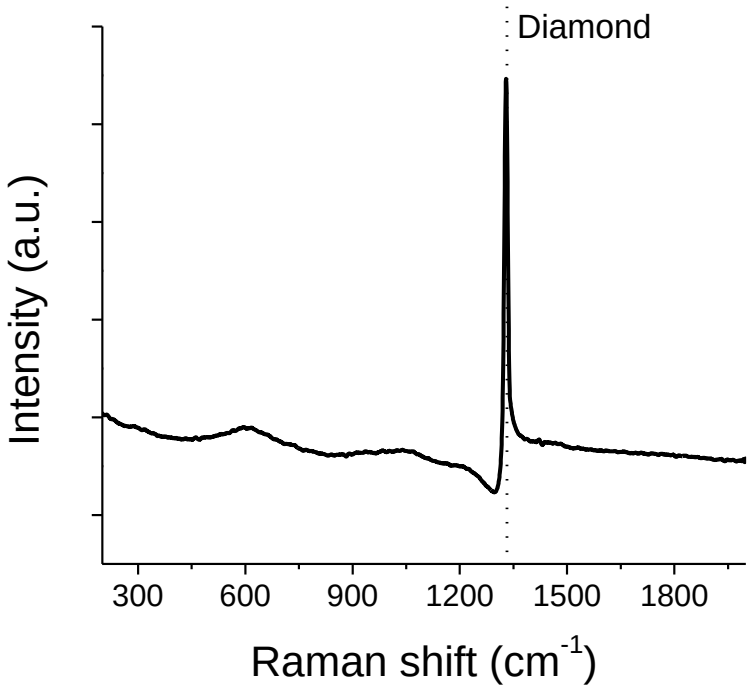

Figure 82 Raman spectra of the boron doped homoepitaxial films with excitation wavelength of 488nm.

Figure 82 shows the Raman spectra, measured (by Marie Krečmarová) with the Horiba Jobin Yvon T64000 Raman spectrometer equipped with a BXFM Olympus 9/128 microscope and a Horiba JY Symphony CCD detector at the IMO-IMOMEC with excitation power of 488 nm. The diamond peak at 1329 cm^{-1} is shifted due to the boron doping. Peaks observed at 604, 1039 and 1218 cm^{-1} could be related to the boron atoms in the diamond [120] [121] [126] The electrical properties measured by Van der Pauw method (see chapter 4.1.1) at the IoP ASCR (by Dr. Pavel Hubík) of the deposited films shows conductivity of 333 S/cm, carrier concentration of $1.1 \cdot 10^{21}$ cm^{-3} and mobility of 1.9 $cm^2/V \cdot s$.

4.3.2 Thin single crystal film with NV centres

In the previous chapter were fabricated highly boron doped single crystal diamond films with a very flat surface serving as an electrode for the diamond biosensing device. Following step for the biosensor functionality is deposition of a thin NV centre containing film on the highly boron doped electrode. Because Boron shifts Fermi level in diamond, we had to verify a fundamental question if B-

doped films and till which B-concentration can exhibit NV^- related luminescence. For this purpose the Boron doped films with N addition were deposited.

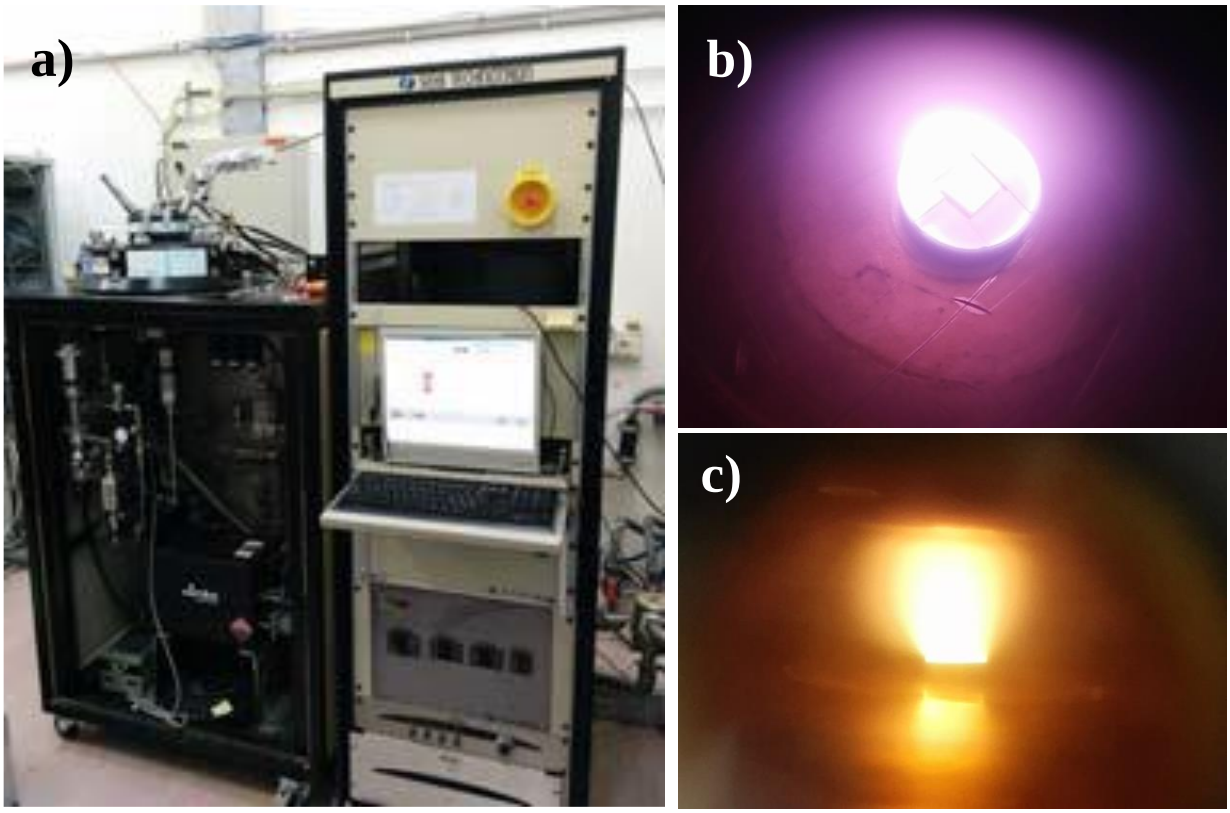

Figure 83. Astex AX6500 system (a) and MW PE CVD homoepitaxial diamond growth in the plasma reactor from top view (b) and side view (c) at the IMO-IMOMEC.

The highly boron doped (6000 ppm) single crystal (100) oriented layers with very flat surface (~ 1 nm) (see chapter 4.3.1) prepared at the IoP ASCR were used as substrates. The substrates were cleaned (Marie Krečmarová) 10 min in boiling H_2SO_4 + KNO_3, following by ultrasonic baths in hot deionized water, acetone and hot isopropyl alcohol (10 mins for each solution). Five samples were first protected against growth (by Marie Krečmarová) by thin titanium layer in two areas representing working and source electrodes (see Figure 7 or 105). Then the highly boron doped layer was overgrown with/without low boron doped and thin nitrogen doped film in the reactor the Astex AX6500 (Figure 83) at the IMO-IMOMEC (by Marie Krečmarová). The growth conditions for all samples are shown in Table 1. The sample thickness measured by profilometer (on a step prepared by etching of Ti protection layer) are plotted in Table 2 (by Marie Krečmarová).

Table 2. PE CVD growth conditions.

Sample	CH_4 (%)	N_2 (%)	B	MW power (W)	Working pressure (Torr)	Temperature (°C)	Duration (min)
164	0.4	Back-ground	0	900	70	940	15
165	2	0.1	Background	750	70	788	10 (B) + 1 (N_2)
166	2	0.1	Background	750	70	799	15 (B) + 1 (N_2)
167	2	0.1	Background	750	70	891	6 (B) + 1 (N_2)
168	4	0.1	Background	750	70	815	80 (B) + 5 (N_2)

Table 3. Thickness of grown diamond layers measured by profilometer.

Sample	Highly B (6000 ppm) doped diamond (μm)	Low B doped (1 ppm) diamond (nm)	Undoped/nitrogen doped diamond (nm)
164	~20	0	~15
165	~15	~250	~20
166	~15	~400	~20
167	~15	~100	~20
168	~15	~1900	~400

Sample 164 represents 15 nm very smooth thin film deposited on highly boron doped electrode. Nitrogen was incorporated from the residual nitrogen chamber background, no nitrogen was added into the gas mixture.

Sample 165 – 168 were grown first with a low boron doped interlayer (1 ppm). Note, that boron was incorporated into the interlayer from a residual chamber background. And after that overgrown with ~20 nm (samples 165 – 167) and ~400 nm (sample 198) nitrogen doped thin film.

Characterization of the fabricated samples is described in the chapter 4.6

Conclusions

The epitaxial highly (6000 ppm) boron doped diamond layers with high electrical conductivity of ~333 S/cm was deposited with approximately thickness of ~15 μm. After re-polishing surface is very smooth with surface RMS roughness of 1.2 nm. The low surface RMS roughness and a good electrical conductivity of the layer are good properties for the diamond electrode. Then the highly B doped layers were overgrown with or without low B doped (1 ppm) interlayer and a thin (~20 nm) NV centre containing diamond film on top as the NV centre charge state biosensing active film. Activity of the

NV centres depending on a diamond surface termination is investigated in the Chapter 4.7. Electrical manipulation of NV centre charge states by a transversal voltage bias is described in the Chapter 4.8.

4.4 NV photoluminescence study in nanocrystalline diamond films

4.4.1 Effect of electron irradiation on NV centres in NCD films

It is assumed that more incorporated nitrogen atoms are in substitutional position [91] and don't form NV centres, therefore it is certainly possible to increase the density of photoluminescent NV centres by irradiation (electrons, protons, neutron or alpha particles) of diamond layers to generate vacancies in the crystal and by a subsequent annealing at high temperature to move vacancies and react with substitutional nitrogen atoms and form new NV centres.

Experimental details

Nanocrystalline diamond samples deposited on silicon substrates (5 × 5 mm) and (1 × 1 mm) at the IoP ASCR using the Seki Technotron AX5010 cavity based MW PE CVD deposition system (by Marie Krečmarová) was chosen for the electron irradiation tests. These samples were synthetized with 0.07 % nitrogen and 1 % methane concentration in hydrogen rich gas mixtures, 1 kW of microwave power, 50 mbar of working pressure. Thickness of the NCD film for sample 1 is 1000 nm and 2400 nm for sample 2. A MT 25 microtron at the Nuclear Physics Institute of the ASCR, v. v. i. (by Dr. David Chvátil) with working energy of 16.6 MeV and electron current of 20 μA was used as high energy electrons source. Minimum electron energy of 6 MeV can be obtained with this system. Two experiments were carried out, investigation of electron trajectory configuration and dependency of irradiation time on NV centres activity.

For the first experiment was used sample 1 (5 × 5 mm), which was mounted such that the entire sample is irradiated for duration of 2 hours. The different configurations for the electron beam trajectory including combinations of clear passage of electrons (only primary electrons emission), collimator (secondary electrons emission from collimator) and water cooling (back scattered electrons emission from water cooling) have been tested to investigate the effect of different electrons energy. The different configurations are shown in Figure 84. The energies of back scattered and secondary electrons are in the order of few keV´s in comparison of the incident beam with MeV energy.

For the second experiment, configuration including water cooling and collimator was used. Sample 2 (1 × 1 mm) was irradiated in three different areas for followed durations: 6 hours (fluence $4.06 \cdot 10^{18}$

electrons/cm^2), 9 hours (fluence 6.09·10^{18} electrons/cm^2) and 12 hours (fluence 8.11·10^{18} electrons/cm^2).

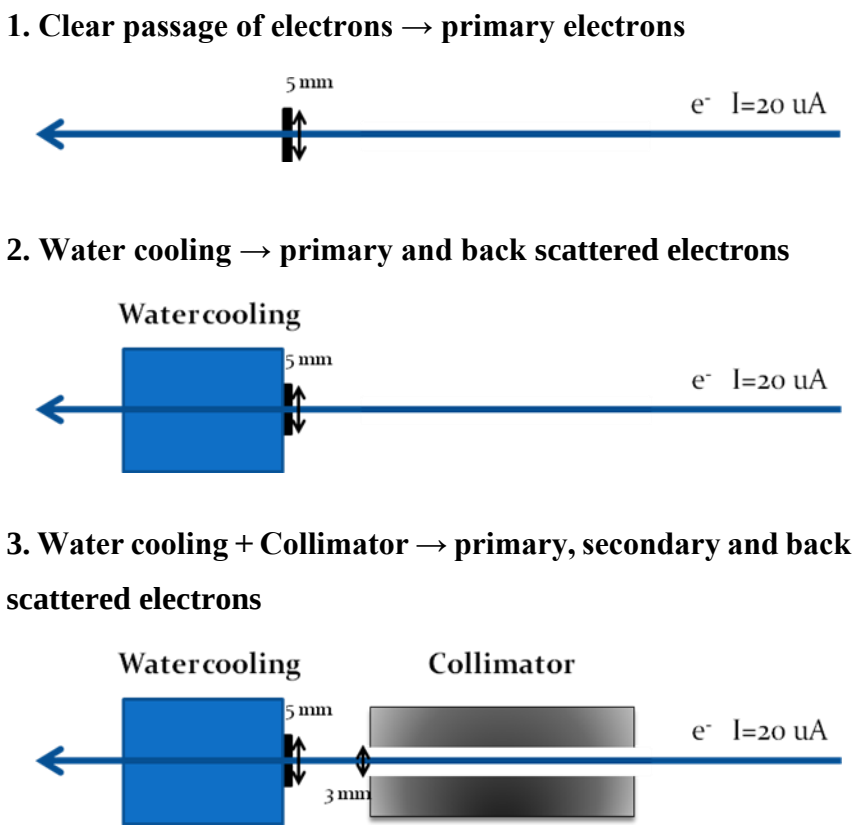

Figure 84. Three configurations for electron irradiations of the nitrogen doped NCD diamond samples using collimator and water cooling combinations or clear passage of electrons.

The annealing was performed at the IoP ASCR (by Marie Krečmarová) at low pressure of 5 mbar with Ar flow, temperature 700 °C for duration of 1 hour. Photoluminescence maps of NV centres were investigated before and after the irradiation and annealing processes at same points (by Marie Krečmarová) using a Renishaw InVia Raman Microscope at the IoP AS CR, with a 514 nm excitation laser and 5x objective at room temperature by scanning setup as following: at whole area for sample (5 × 5 mm - 36 measured points) and for sample 2 at three irradiated areas with different duration time (each area of ~7 mm^2 - 12 measured points). PL spectra are presented as an average of measured NV PL points normalised to sp^3 diamond peak.

Results and discussions

Figure 85 represents measured PL spectra before and after the electron irradiation for different electron trajectory. Electron irradiation of the sample irradiated only with primary electrons (16.6 MeV)

without a collimator and water cooling leads to an increase of the NV PL intensity approximately of 4 %. Using of the water cooling (primary and back scattered electrons) brings even more enhancement of the NV PL with an increase of NV PL intensity (~5 %). The Best improvement of the NV PL was achieved with placement of the collimator to the electron beam with used the water cooling (primary, secondary and back scattered electrons). With this electron irradiation arrangement was obtained NV PL intensity increase of (~10 %).

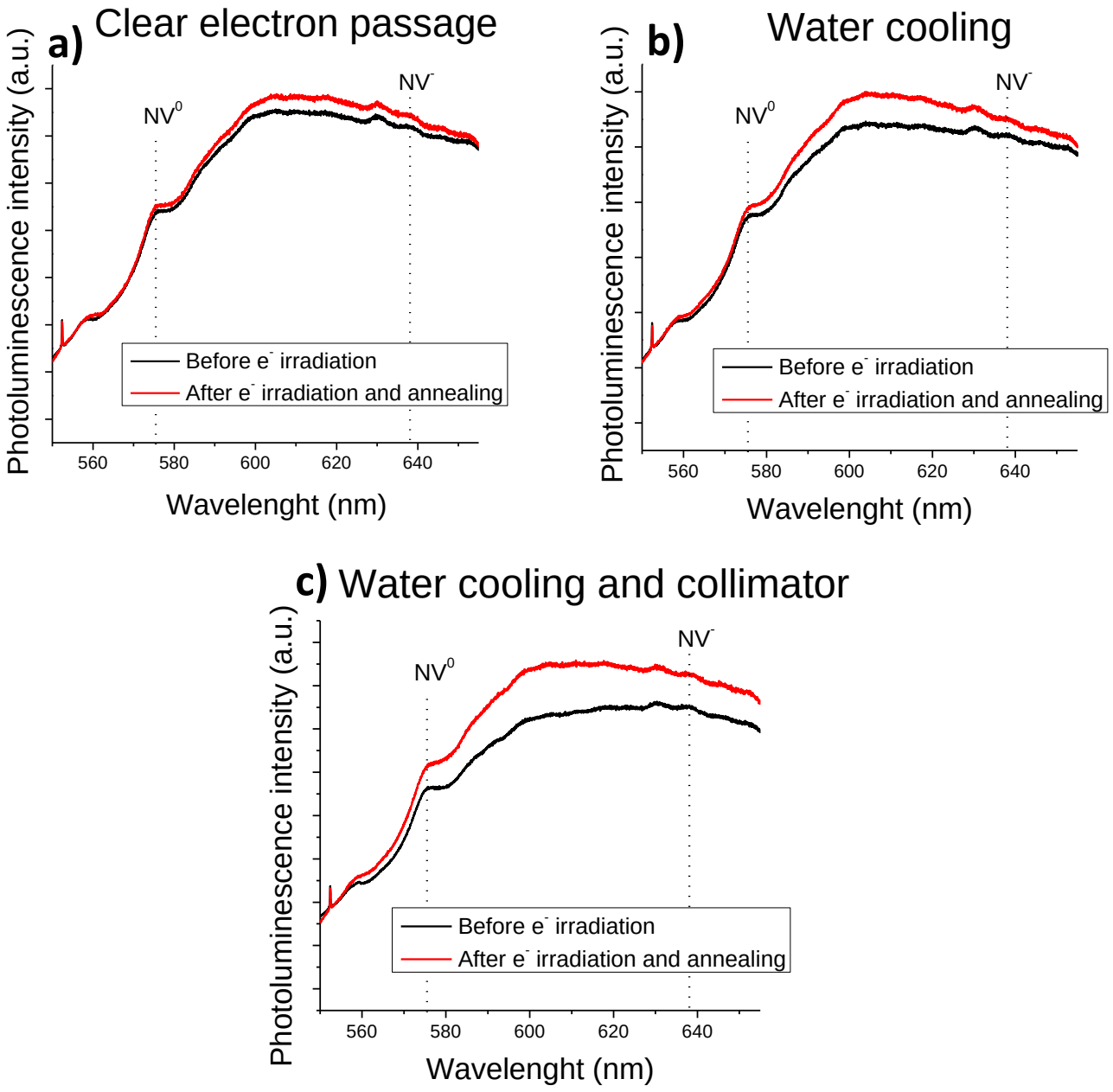

Figure 85. Photoluminescence maps of irradiated sample 1 before and after an electron irradiation, depending of an irradiating setup.

The most efficient electron beam trajectory for the enhancement of NV centre PL (collimator + water cooling) was used for the second experiment with different irradiation time. PL spectra before and after electron irradiation with different irradiation time are shown in Figure 86. NV PL intensity increases with duration of electron irradiation time. Irradiation time of 6 hours results in NV PL enhancement for ~6 %, 9 hours for ~9 % and 12 hours for ~39 % in comparison to non-irradiated sample.

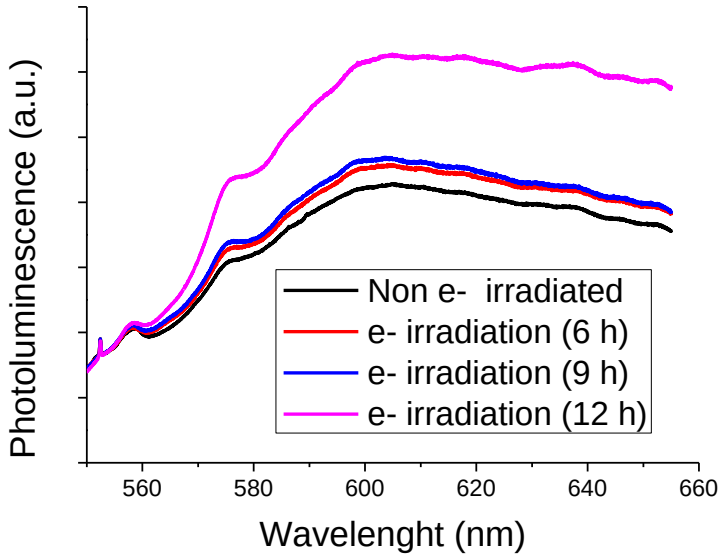

Figure 86. Photoluminescence maps of irradiated sample 2 before and after an electron irradiation, depending of irradiation time.

Conclusions

Enhancement of the NV PL was achieved with using all electron irradiation setup arrangements. Clear electron passage only with primary electrons (16.6 MeV) leads to the increase of the NV PL intensity of ~4 %. Using of the water cooling (primary and back scattered electrons) brings even enhancement of the NV PL with the NV PL intensity increase of ~5 %. The Best improvement of the NV PL up to ~10 % was achieved with placement of the collimator to the electron beam and with used the water cooling (primary, secondary and back scattered electrons). Enhancement of NV PL was observed also by longer irradiation time. The biggest improvement of NV emission was observed with electron irradiation for 12 hours with ~39 % increase of PL in comparison to non-irradiated sample.

4.4.2 NV photoluminescence study as function of thickness of NCD films

For functionality of the diamond biosensor, which consists of thin sensing diamond film with NV centres deposited on boron doped diamond electrode, NV PL was studied in nanocrystalline diamond as function of its thickness, and thus crystals size and various amount of sp^2 carbon phase on grain boundaries, which affects the NV photoluminescence.

Experimental details

The diamond films were grown on (100) oriented crystalline silicon substrates at the IoP ASCR (by Marie Krečmarová) using the Seki Technotron AX5010 cavity based MW PE CVD deposition system. The diamond layers were deposited in two steps: first was deposited a thicker undoped layer and then thin nitrogen doped nanocrystalline diamond film on top. Growth conditions were the following: 1 kW microwave power, 50 mbar working pressure, and average substrate temperature is 700 °C. The gas phase compositions during depositions were 1% CH_4 and 0.07 % N_2 in H_2.

Table 4. Thicknesses of the multilayer consist of an intrinsic and nitrogen doped NCD diamond thin film on top. The thicknesses of the nitrogen doped films are estimated from gases flows and deposition time.

Sample ID	Total thickness (nm)	Thickness of i-film (nm)	Thickness of N-doped film (nm)
1	1800	1500	300
2	912	903	9
3	335	330	5
4	74	69	5
5	19	16	3

The estimated thicknesses from the growth rate of intrinsic and nitrogen doped films of all diamond deposited films are reported in Table 4. Photoluminescence maps of NV centres were investigated using a confocal microscope (FBMI) with a 532 nm excitation laser at room temperature (by Dr. Michal Gulka). Surface morphology was measured using AFM in semi contact mode NTEGRA-Prima at the IoP AS CR (by Dr. Ladislav Fekete).

Results and discussions

Figure 87 shows AFM filtered (local contrast) surface images of deposited films together with their surface roughness. There is a good diamond coverage without any holes for all sample thicknesses

from 1800 to 19 nm. All images show increasing grain sizes and RMS roughness with diamond film thickness.

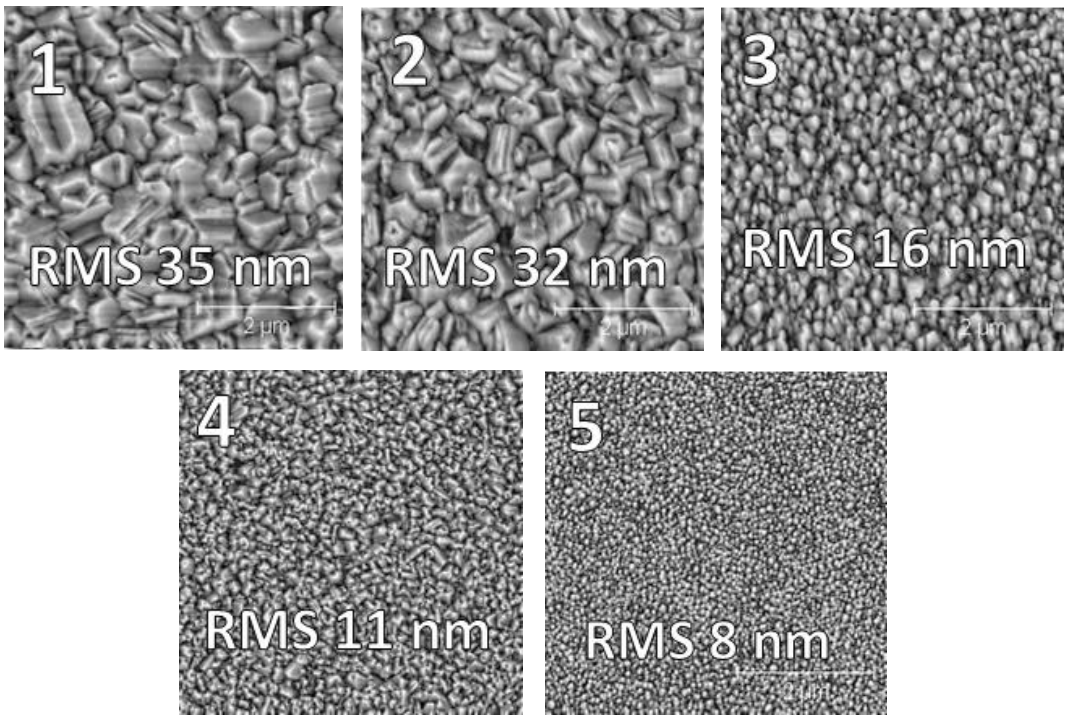

Figure 87. Local contrast AFM images of surface morphology of all deposited multilayer.

Figure 88 shows confocal microscopy photoluminescence measured with 532 nm excitation wavelength. In addition to substrate Si peak at 547 nm, NV^0 zero phonon line at 575 nm, NV^- zero phonon line at 637 nm and also silicone vacancy (Si-V) peak at 736.5 nm are observed. Si-V colour centre is incorporated during the CVD growth. This Si-V peak is characterized by photoluminescence intensity rising with the film thickness (Figure 88b).

NV photoluminescence intensity increases with film thickness, predicting, that some NV centres were formed also in the undoped film. Intrinsic and nitrogen doped films contain unwanted boron atoms with estimated concentration of ~10^{17} cm^{-3}, which were incorporated during the growth from chamber residual background. The presenting boron atoms decrease the NV^- photoluminescence intensity [90], nevertheless the NV centres are active in those boron concentration. Another factor which quenches NV photoluminescence is sp^2 bonded carbon, which is surrounded in higher amount around smaller crystal grains. NV centre can exhibit in very thin sample thickness of 19 nm (3nm N_2 doped film and 16 nm undoped film) and thus in very small crystal grains. Figure 88c shows its photoluminescence spectra with presenting larger NV^0 and negligible NV^- peak.

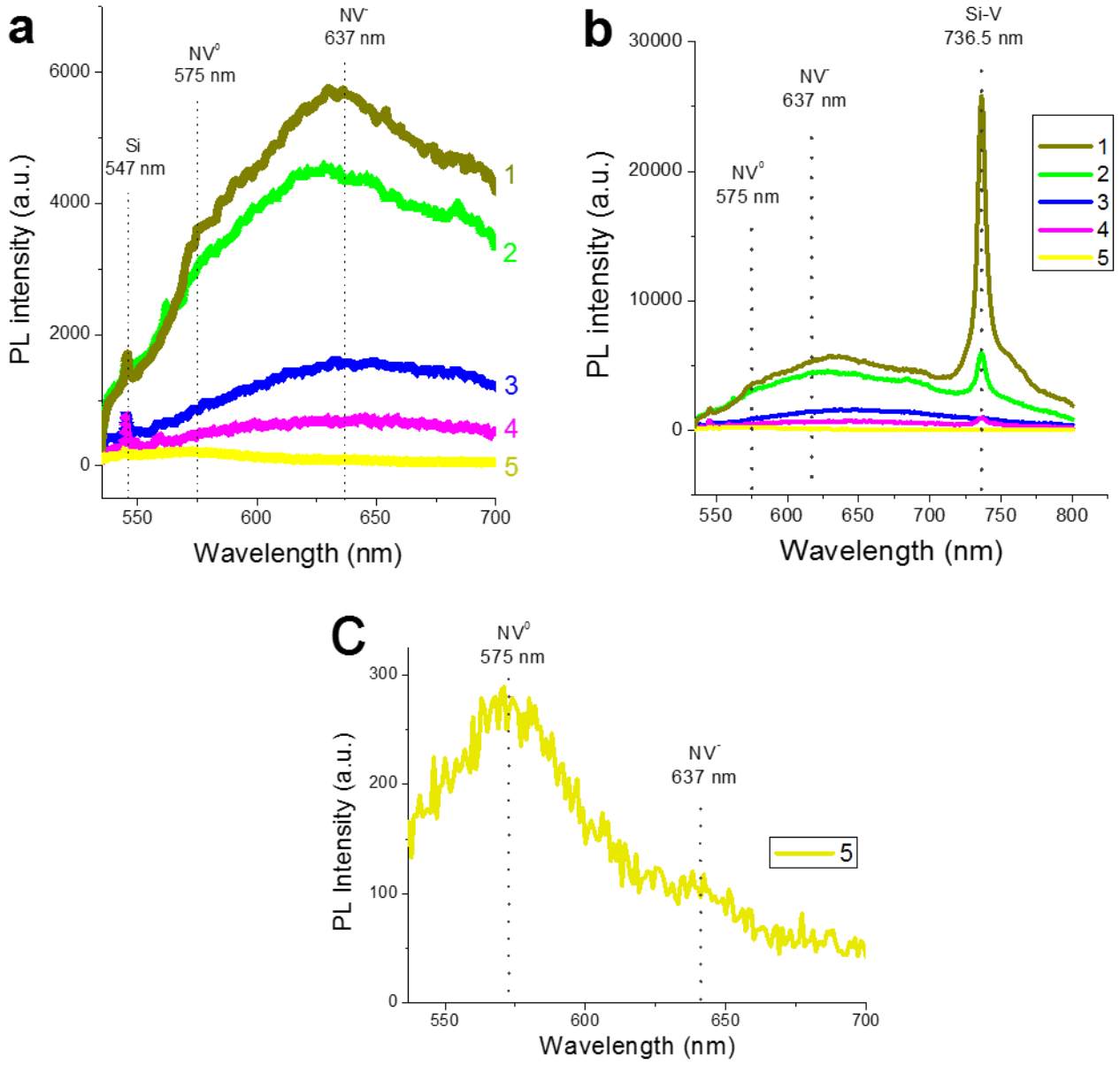

Figure 88. Photoluminescence measured using confocal microscope with excitation wavelength of 532 nm: photoluminescence for all samples showing NV PL (a), NV and Si-V e for all samples with high intensity of the Si-V compared to NV (b), and NV photoluminescence of sample 5 (3 nm N-doped on 16 nm undoped diamond) with higher occupation of the NV^0 centre.

Conclusions

We studied the NV photoluminescence in the nanocrystalline diamond thin films. NV photoluminescence intensity rises with sample thickness. Minimum thickness presenting NV centres was found in the film consist of 3 nm nitrogen doped film grown on 16 nm undoped film with higher photoluminescence intensity for NV^0 centre. All samples exhibit also Si-V colour centre, which were created during the growth by a diffusion from Si substrate.

4.4.3 NV photoluminescence study as function of boron acceptors concentration in the NCD film

Because the final device consists of a heterostructure of boron doped electrode and thin NV centres containing layer on top, investigations about B acceptor influence on NV PL had to be carried out. Boron acceptor atoms influence the Fermi level position of NV^- centre and could lead to quenching of NV PL at its higher concentrations, and thus study of an effect of boron acceptors incorporated at different concentrations in the diamond layers containing NV centres was required.

Experimental details

The low nitrogen doped nanocrystalline diamond films were grown on silicon substrates with different boron concentration at the IoP ASCR (by Marie Krečmarová) using the Seki Technotron AX5010 cavity based MW PE CVD deposition system. Growth conditions were 1 kW microwave power, 50 mbar working pressure, 0.07 - 0.17 % nitrogen and 1 % methane concentration in total hydrogen rich gas mixtures, 700 °C average substrate temperature and 4 - 5 hours deposition time. No TMB was added into the deposition gas. The boron was incorporated into the layers just from a different level of the residual chamber boron background. The chamber boron background increased with the boron doping level. Thus this experiment followed the boron doping study. To estimate the actual boron background level, intrinsic nanocrystalline films were grown on corning glass substrates for Hall electrical properties investigation before each nitrogen doped depositions. Table 5 summarizes deposited nitrogen doped nanocrystalline diamond samples with the estimated concentration of the incorporated boron atoms.

Table 5. Grown low nitrogen doped NCD films with increasing chamber boron background.

Sample ID	N_2 concentration in gas phase (%)	B concentration (cm^{-3})
1	0.07	$4 \cdot 10^{17}$
2	0.17	$5 \cdot 10^{18}$
3	0.07	$2 \cdot 10^{19}$
4	0.07	$8 \cdot 10^{19}$
5	0.07	$1 \cdot 10^{20}$
6	0.07	$2 \cdot 10^{20}$

AFM surface morphology was performed using the NTEGRA-Prima microscope in semi contact mode at the IoP AS CR (by Dr. Ladislav Fekete). Raman spectroscopy was measured using the Renishaw

InVia system (by Marie Krečmarová) in IoP ASCR with excitation wavelengths of 488 nm at room temperature. The NV centre photoluminescence was measured using the Renishaw InVia Raman Microscope at the IoP ASCR (by Marie Krečmarová), with a 514 nm excitation laser and laser power of 25 mW at room temperature.

Results and discussions

Reduction of the growth rate was observed at a higher boron background starting from 2e19 cm^{-3}. Local contrast AFM surface morphology of samples 1 and 4 is shown in Figure 89. The samples show clear crystalline facets and coverage without any holes. Crystalline facets of sample 4 grown with higher chamber boron background have sharper edges than sample 1.

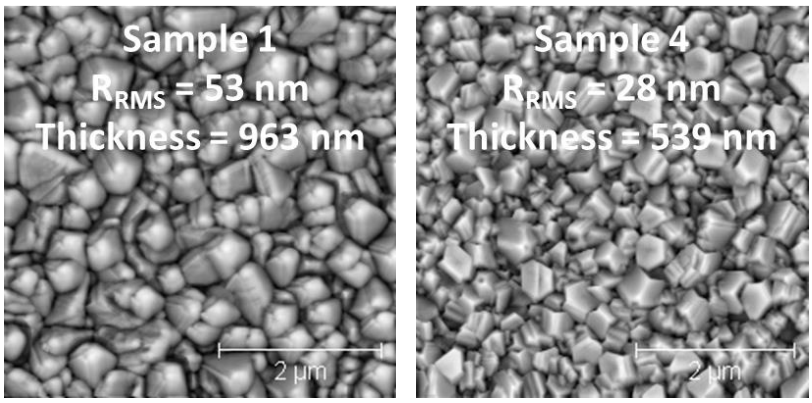

Figure 89. AFM local contrast surface morphology images of samples 1 and 4.

The Raman spectra of all deposited nitrogen doped nanocrystalline diamond layers (Figure 90) shows a diamond band at 1333 cm^{-1}, and transpolyacetylene related peaks [117] at 1140 cm^{-1} and 1488 cm^{-1}. The sample 1 and 2 deposited with lower boron background shows a disordered D band at 1366 cm^{-1} and graphitic G band at 1561 cm^{-1}. On the contrary, D and G bands are absent in samples 3 – 6 which were grown at a higher boron background. The high chamber boron background results in better diamond quality of low nitrogen doped films.

Photoluminescence spectra of the deposited nanocrystalline diamond layers are plotted in Figure 91. NV photoluminescence was observed only in layers with small concentration of boron for sample 1 and 2. Chamber boron background at 2e19 cm^{-3} and higher leads to NV centre photoluminescence quenching.

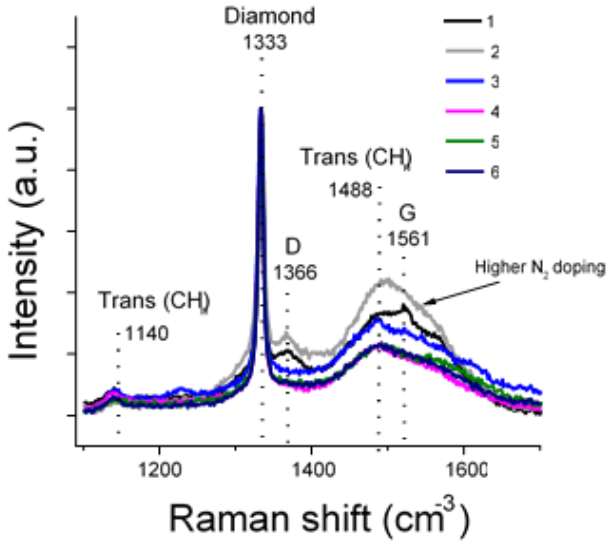

Figure 90. Raman spectra of nanocrystalline diamond layers grown with a different chamber boron background concentration measured with 488 nm excitation wavelength.

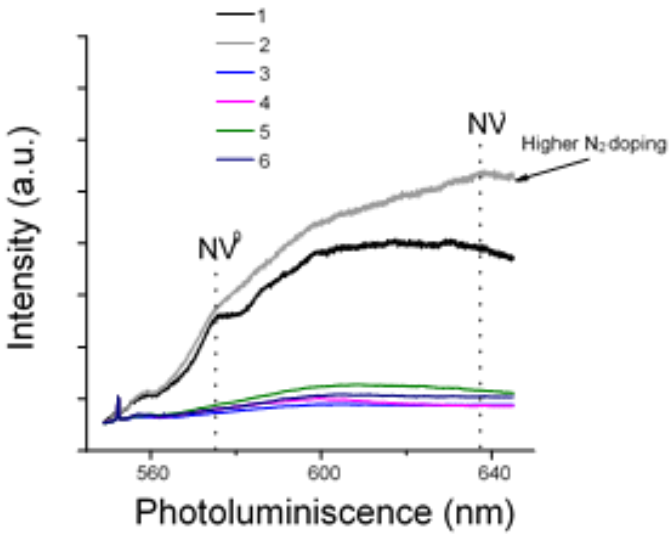

Figure 91. Photoluminescence spectra of nanocrystalline diamond layers with a different chamber boron background concentration measured with 514 nm excitation wavelength.

Conclusions

The low nitrogen doped nanocrystalline diamond films were deposited with different concentration of residual chamber boron background and therefore also incorporated boron acceptors into the layers. The High level of boron concentration improves the diamond quality during the low nitrogen doped growth as shown by the Raman spectroscopy. Quenching of NV centre photoluminescence was observed from an estimated boron concentration in the NCD film starting at 2e19 cm^{-3} and higher.

4.5 Electrochemical impedance spectroscopy study of BNCD/NCD electrodes

4.5.1 Influence of the thickness of NCD film on electrochemical properties

The purpose of the experiment is gaining knowledge of an influence of electrical resistive NV centres containing NCD films deposited on the top of boron doped electrode on electrochemical performance of the sensor. The sensor is composed of boron doped diamond electrode deposided on the p- type conductivity silicon substrate and with undoped diamond film on top.

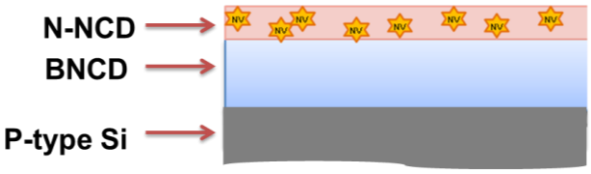

Figure 92. Scheme of the sensor.

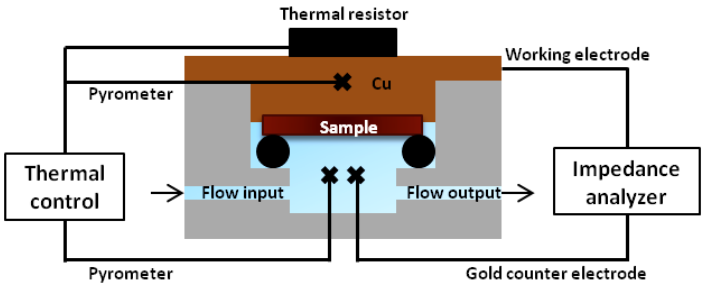

Figure 93. Scheme of the flow cell.

Experimental details

The nanocrystalline diamond films were grown in the CVD systems Astex AX6500 (with and without boron background - Figure 83) at IMO-IMOMEC (by Marie Krečmarová). First BNCD was grown on p-type conductive (100) silicon substrate followed by an undoped NV centre containing (N-NCD) thin film on top of BNCD (Figure 92). Growth conditions for boron doped film were 3 kW, 70 Torr, substrate temperature ~ 800 °C, gas compositions 0.5 % CH_4 and 5000 ppm TMB. Further on, N-NCD was deposited on top of BNCD in boron clean reactor NV centres were generated in the NCD film from N adsorbed in chamber walls or present as a background in the gas phase. The conditions were 1 % CH_4 in H_2, 3 kW microwave power, 70 Torr chamber pressure and substrate temperature ~800 °C. Photoluminescence measurements confirmed the NV centres in all deposited undoped N-NCD films. The thickness of BNCD is 200 nm and the thickness off overgrown undoped film varying from 0 to 168 nm.

The electrochemical impedance spectroscopy was measured using a Hewlett Packard 4248 Precision LCR meter at IMO-IMOMEC (by Marie Krečmarová). For the measurements we designed of a flow cell shown in Figure 93. The impedance was measured with 10 mV of AC voltages applied to the flow cell at 37°C. As an electrolyte we used BupH^{TM} phosphate buffered saline (PBS) with pH 7.2. The impedance was measured for 31 frequencies in a range from 100 Hz to 100 kHz. The electrical circuit parameters were determined by fitting the impedance data to the equivalent circuit (Figure 94) over the total frequency range from 100 Hz to 100 kHz using the ZSimpWin V3.60 software from EChem Software.

Results and discussions

The electrochemical response in the flow cell was fitted by an equivalent circuit (shown in Figure 94) which consists of the solution resistance R_s, between the gold counter electrode and the N-NCD surface, in series with the parallel combination of the double layer constant phase element (no prefect capacitor) Q_{dl} and resistance R_{dl} and in series with another circuit which represents parallel combination of charge space region constant phase element Q_{scr} and resistance $R_{scr.}$ The used equivalent circuit the best fitted for the experimental data.

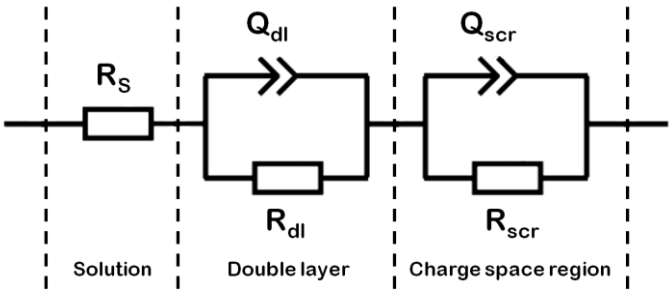

Figure 94. Equivalent circuit used for fitting of the impedance data.

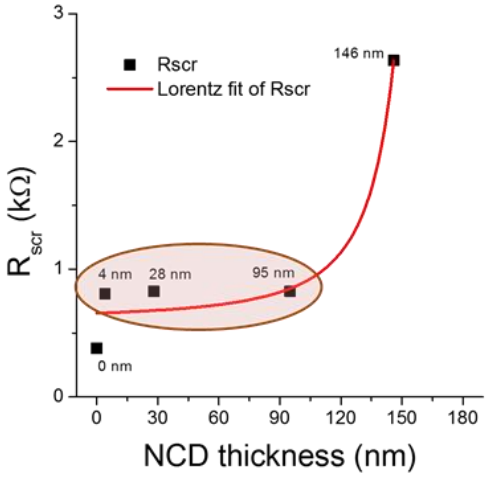

Figure 95. Charge transfer resistance R_{ct} as function of a different thickness of N-NCD film.

The fitted values of the equivalent circuit elements for a different thickness of N-NCD films deposited on top of boron doped NCD layers are shown in Table 6. Concerning to the fitted values, it was found, that the charge transfer resistance is similar for N-NCD thickness between 4 nm and 95 nm (Figure 95). Figure 96 represents Bode plot of the phase angle and the impedance in the complex form as function of the frequency. The thickest electrode with 146 nm of N-NCD film shows as expected the maximum value of impedance.

The Nyquist plot of the electrochemical impedance spectra with different thickness of undoped N-NCD film (not shown) exhibits not circular shape of curves, but rather straight, probably due to the high resistances. The curves are tilted down with increasing thickness of undoped N-NCD film. Fitted data shows similar charge space region and double layer resistances and capacitances for N-NCD thickness between 4 and 95 nm (Table 6).

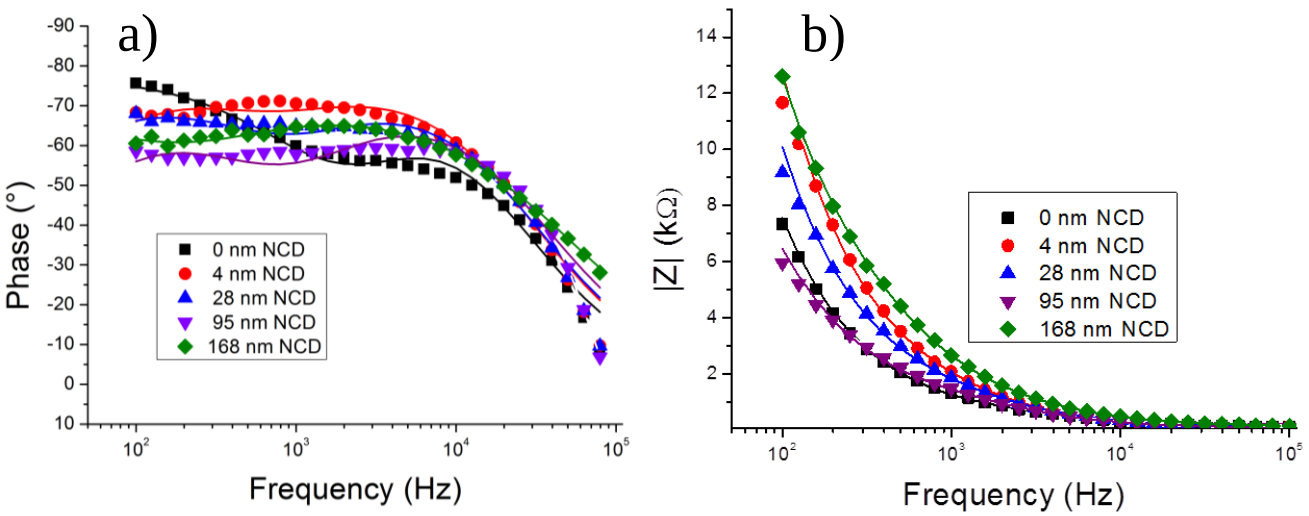

Figure 96. Bode plot of the phase angle (a) and the complex impedance (b) as function of the frequency of electrodes with different thickness of undoped N-NCD film. The symbols represent the measured data and the solid lines the fitted data.

Table 6. Fitted electronical elements to the equivalent circuit.

Circuit parameters	**N-NCD thickness**				
	0 nm	**4 nm**	**28 nm**	**95 nm**	**146 nm**
R_s **(Ω)**	108	105	102	81	114
Q_{dl} **(μ·S·s^n)**	15	22	32	57	61
n_{dl}	0.99	0.91	0.89	0.87	0.78
R_{dl} **(kΩ)**	Undef.	57	61	22	Undef.
Q_{scr} **(μ·S·s^n)**	48	47	33	30	68
n_{scr}	0.88	0.91	0.92	0.91	0.85
R_{scr} **(kΩ)**	380	807	825	827	2636
χ^2	$6.6\cdot10^{-3}$	$5.0\cdot10^{-3}$	$5.6\cdot10^{-3}$	$1.1\cdot10^{-2}$	$4.7\cdot10^{-4}$

Conclusions

By the electrochemical impedance spectroscopy it was found by numerical fitting that the thickness of N-NCD film between 4 and 95 nm shows similar charge space region capacitances. The electrochemical parameters started to change at higher thickness of N-NCD than 95 nm.

4.6 Fabrication of the label free microfluidic diamond biosensor with electrochemical and NV centre optical readout

The Combination of the sensitivity of the near surface NV centre charge state on surface functionalization with electrochemical microfluidic device brings possibilities for the construction of a new sensitive biosensor with an electrochemical and an optical detection of charged biomolecules. A design of the biosensor with described working principle and fabrication process is reported in next chapters.

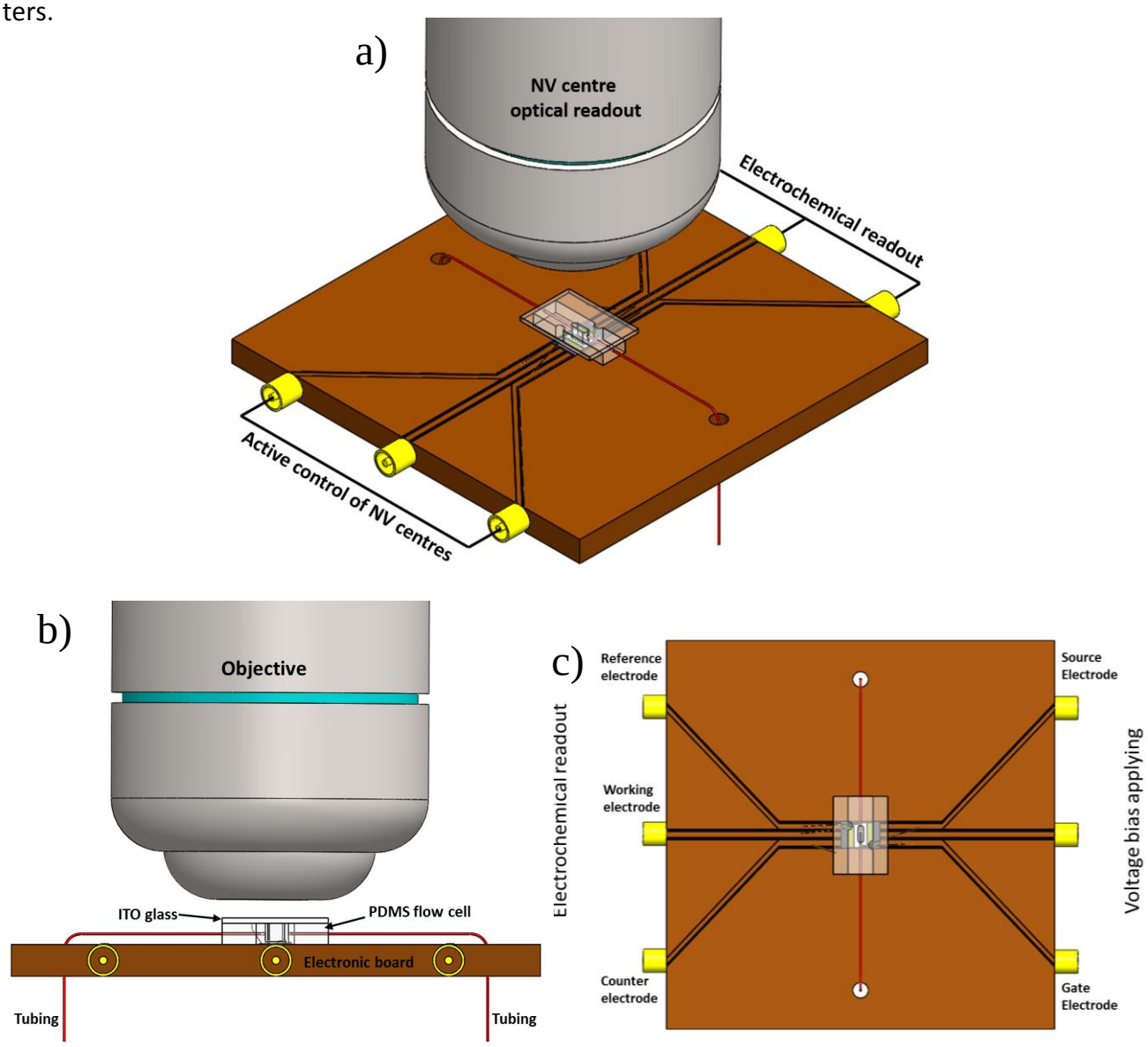

Figure 97. The design of the biosensor including the diamond device, microfluidic cell covered by ITO glass and tubing, electronic board and objective: 3D view (a) and side view (b); top view of the biosensor device with shown electrical connections for electrochemical readout (working, reference and counter electrode) and application of the gate voltage bias (c).

4.6.1 Design and working principle of the biosensor

The design of the microfluidic biosensor is represented in Figure 97. The drawings were made using the Solidworks software (by Marie Krečmarová). The biosensor consists of a diamond device and a polydimethylsiloxane (PDMS) microfluidic flow cell covered by indium tin oxide (ITO) coated glass sheet, which are connected to the electronic board. All the parts are described in more detail in the next chapters.

The biosensor has two electrically controlled functions: an electrochemical readout and an active control of the NV centre charge state by a gate voltage (Figure 97c and 98a,d). For the charge state control of the NV centres we used a source electrode on boron doped diamond and a gate electrode on nitrogen doped diamond with NV centres (Figure 105). The active manipulation of the NV centre charge state is presented in the chapter 4.8.

The NV photoluminescence is detected by confocal microscopy through transparent ITO glass in the microfluidic channel and through micro fabricated holes in the gate electrode located on the nitrogen doped diamond (Figure 107 and 108). The electrochemical readout can be used for the control of a biochemical reaction in the electrochemical microfluidic channel. The working electrode is located directly on the boron doped diamond film. The reference electrode is placed on the nitrogen doped diamond film. Counter electrode represents optically transparent conductive ITO coated glass which covers the microfluidic PDMS flow cell.

Figure 98 shows the drawing of the microfluidic PDMS/ITO structure covering the diamond device and partially also the diamond board for a better mechanical stability. The total thickness of the PDMS/ITO structure is 2.5 mm, which is lower than the working distance of the used objective. The volume of the PDMS flow cell is 34 µl. The PDMS structure has 2 gaps for wire bonding of 4 electrodes on the corners of the diamond device. Figure 98 represents the side and top view of the biosensor, for better illustration with and without ITO coated glass and PDMS flow cell, with 5 wire bonded contacts (4 on the diamond device and 1 on the ITO coated glass).

Figure 99 shows the photograph of the constructed biosensor device. The diamond device with 4 electrodes is embedded in the electronic board gap at the same surface height level, which leads to good mechanical cohesion of the PDMS structure with the flow cell. On the photograph there are 2 gaps visible in the PDMS structure allowing electrical wire bond connections for 4 electrodes at 2

corners on the diamond device. Finally the PDMS is covered by ITO coated glass and taped to the electronic board (Figure 99e).

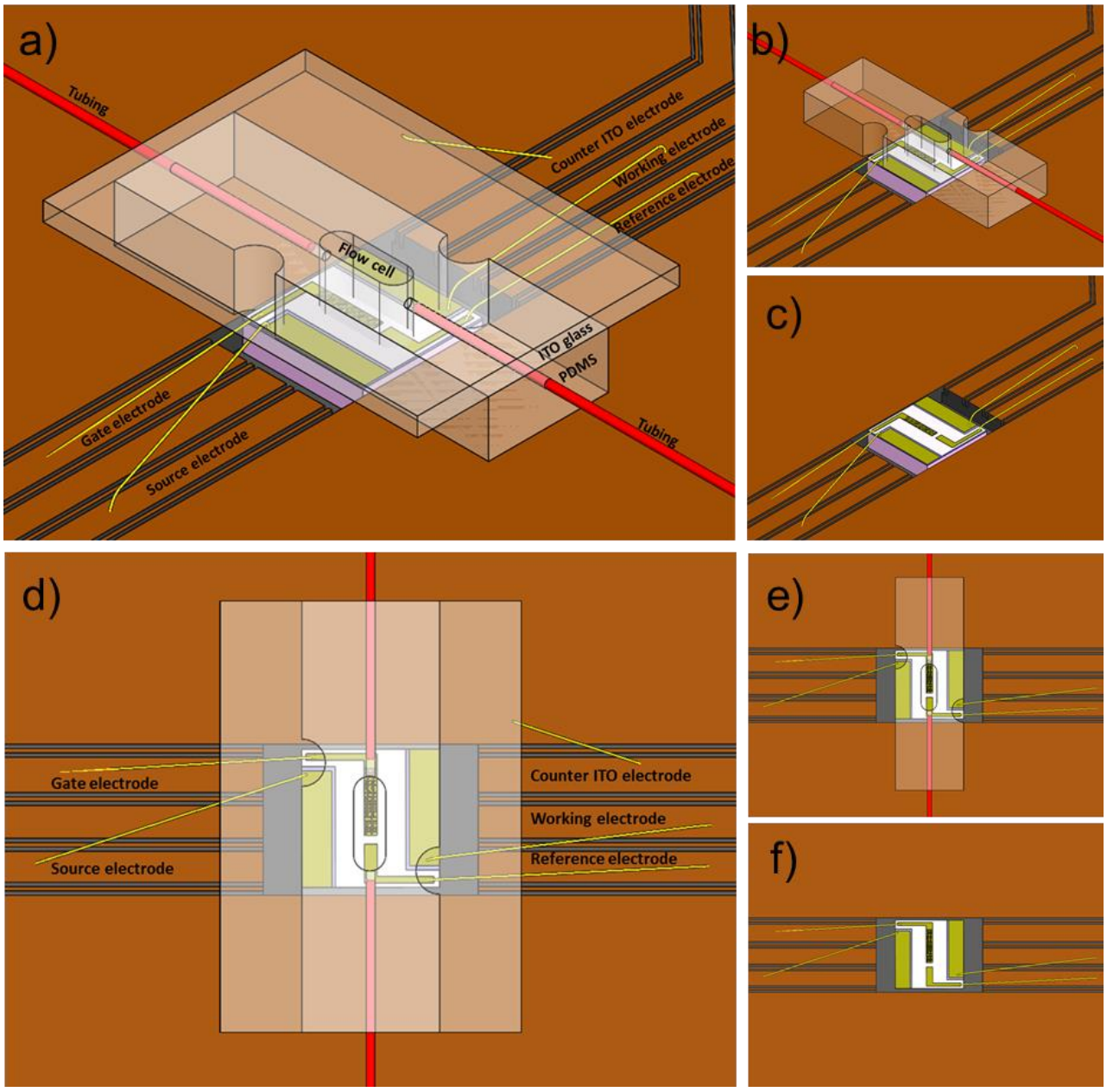

Figure 98. The scheme of the biosensor consisting of the diamond device, the PDMS microfluidic flow cell with tubing covered by ITO glass and wire bonded electrode contacts on the electronic board: side view of the complete device (a), device without ITO glass (b), device without microfluidic cell and ITO glass (c) and top view of the complete device (d), device without ITO glass (e), device without microfluidic cell and ITO glass (f).

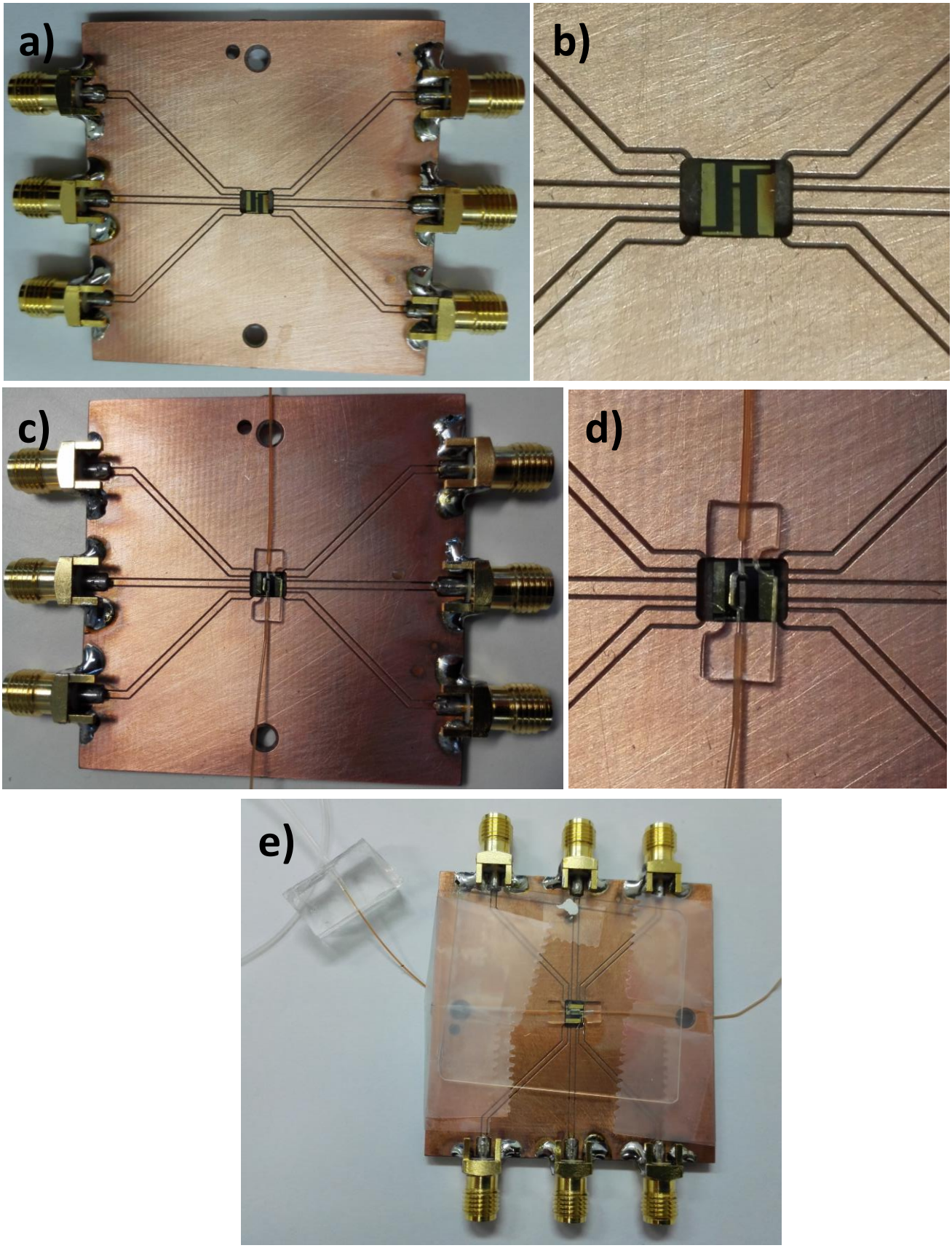

Figure 99. Photograph of the biosensor including the electronic board with embedded diamond device (a,b), PDMS flow cell with tubing (c,d) covered with ITO coated glass (e). Diamond device was further connected to the electronic board as described in the Figure 98.

Conclusion

The novel biosensor for label free detection of charged molecules as for instance DNA or polymers was fabricated. The detection principle is based on the NV centre charge state optical detection combined with electrochemical readout in the microfluidic channel.

4.6.2 Fabrication of the PDMS microfluidic cell

The scheme of the PDMS flow cell is shown in Figure 100. Figure 101 represents the scheme of the PDMS flow cell covered by the ITO coated glass slide. The drawings (Figure 100 and 101) were made by using the Solidworks software (by Marie Krečmarová) and the dimensions are given in mm scale. The optical image (by Marie Krečmarová) of the PDMS flow cell is shown in Figure 102.

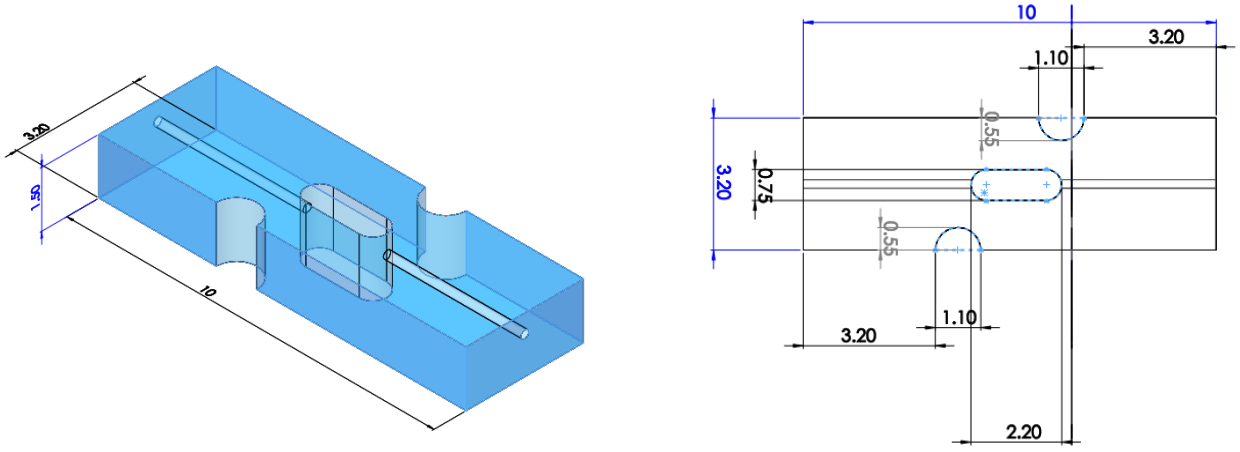

Figure 100. 3D view (left) and top view (right) design of the PDMS flow cell (dimensions are in mm scale).

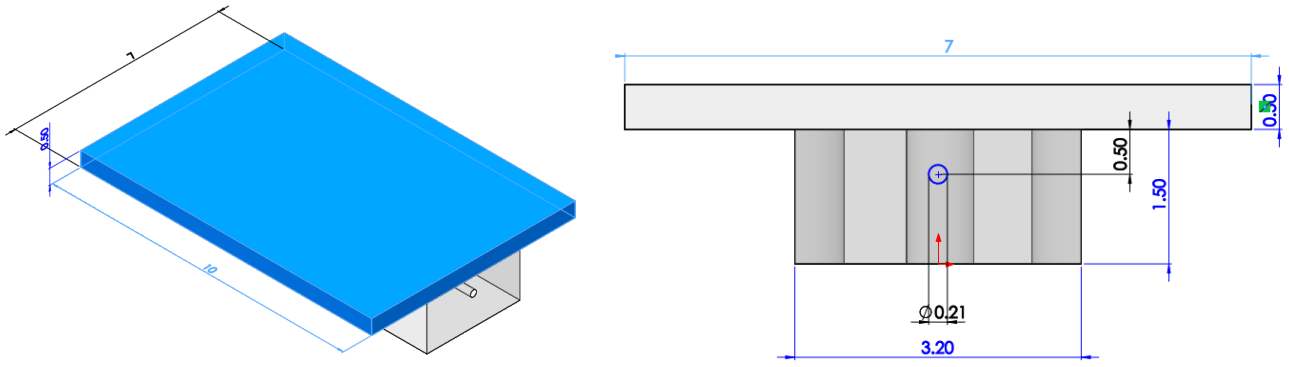

Figure 101. 3D view (left) and top view (right) design of the PDMS flow cell covered with ITO coated glass slide (dimensions are in mm scale).

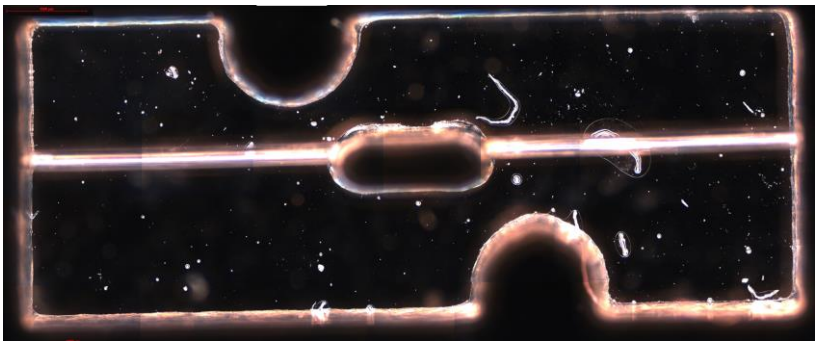

Figure 102. Optical image of the PDMS flow cell before cleaning.

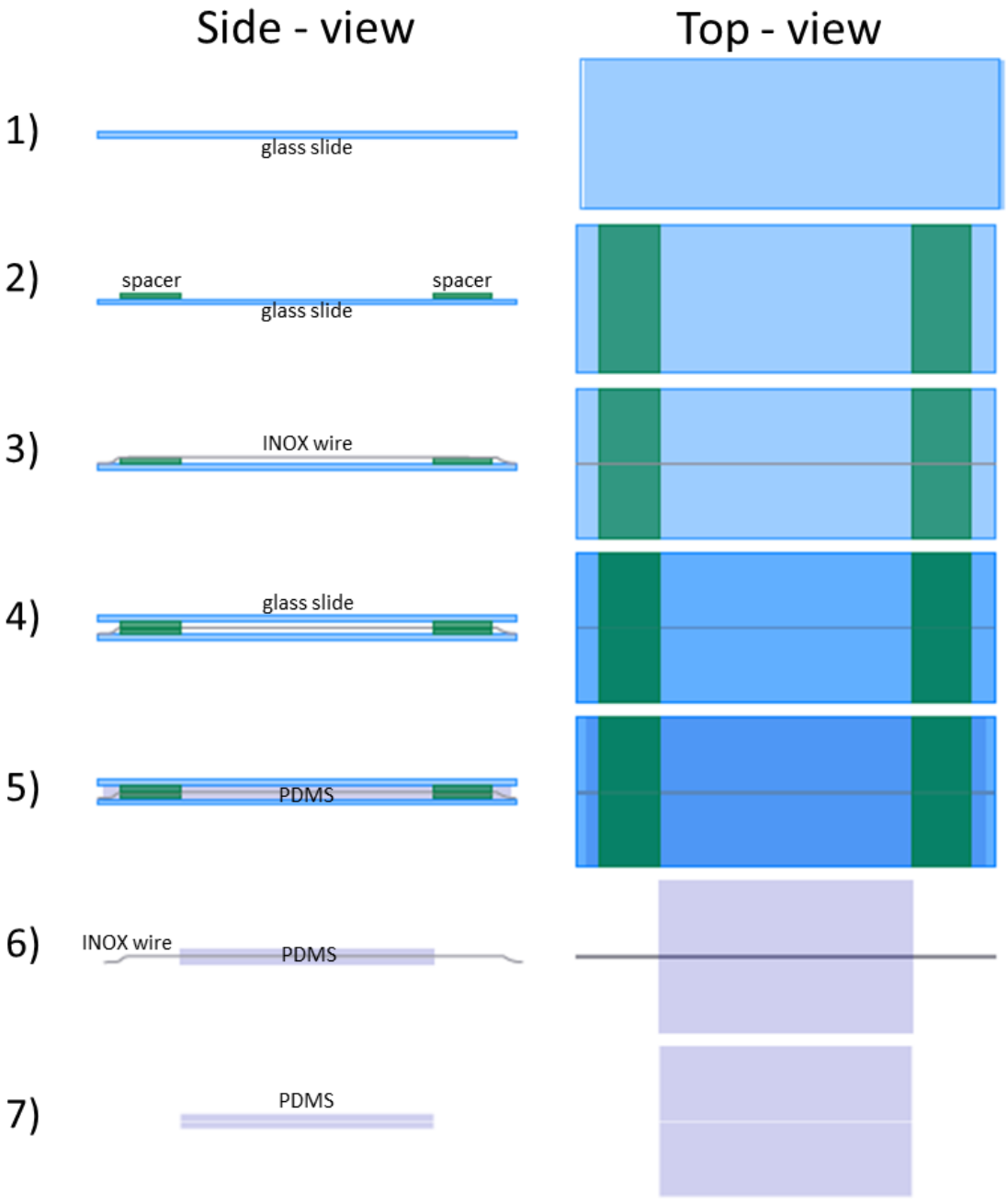

Figure 103. Fabrication of the microchannel in a PDMS film.

The PDMS flow cell was fabricated at the Hasselt University (by Dr. Thijs Vandenryt). In Figure 103, the fabrication process of the microchannel in a PDMS film is shown. On the clean microscope glass slides (1) were two spacers placed of half the desired thickness (1 mm) of the flow cell (2) and an INOX wire (0.2mm) was suspend (3). On the spacers and wire were added another two spacers and glass slide creating a cavity of the desired thickness (2 mm) of the flow cell with a wire in the middle (4). The cavity was filled with PDMS (Sylgard 184, 10:1 mixing ratio) and cured for at least 30 min at 70°C (5). Then the glass slides and spacers were removed and only PDMS with Wire embedded remained (6). Finally trimmed edges of the wire were gently pulled out of the PDMS (7).

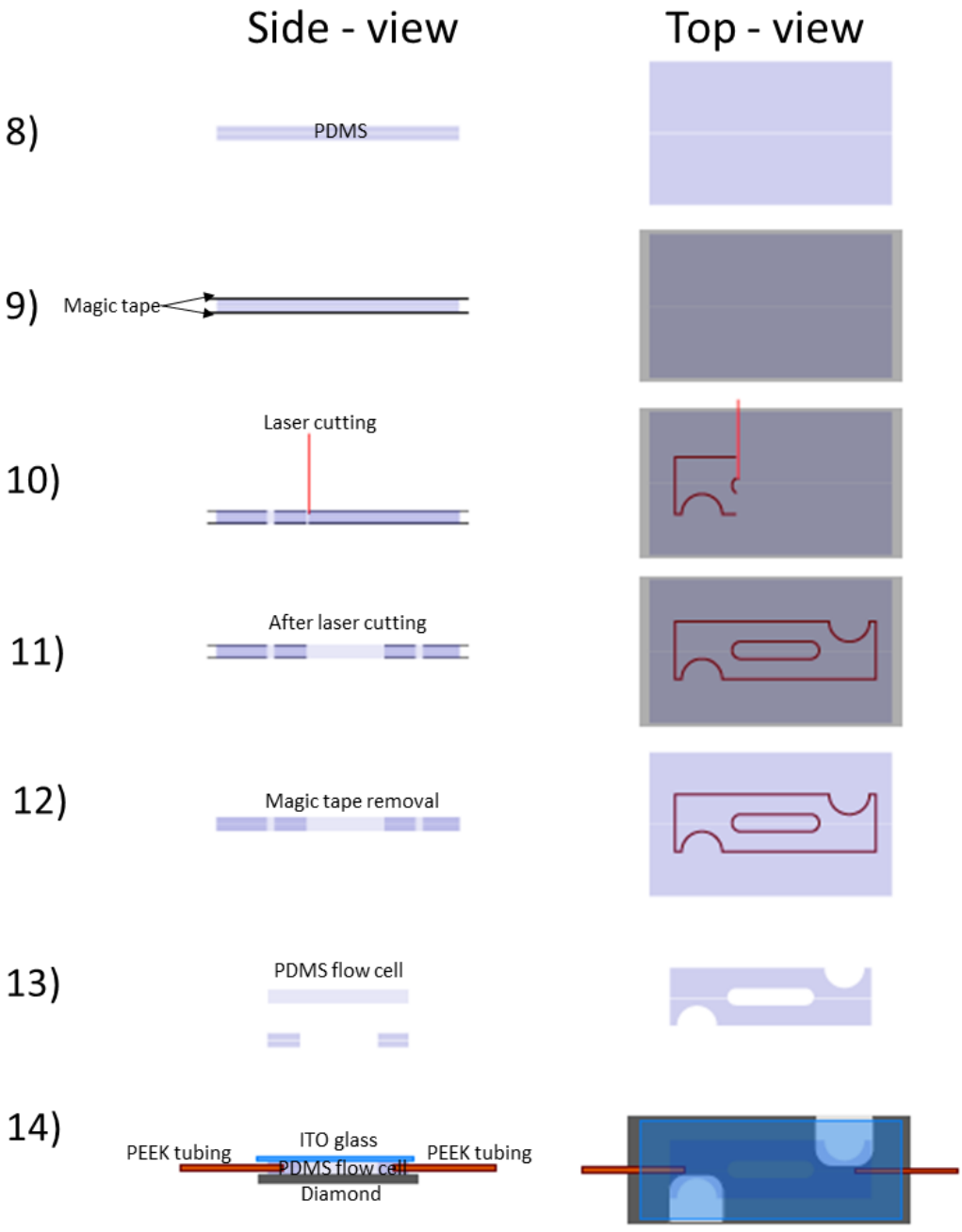

Figure 104. Fabrication of the PDMS flow cell.

Figure 104 shows the fabrication process of the flow cell. The fabricated PDMS slab (8) was cleaned by DI water and IPA and taped on top and bottom by Scotch Magic tape (9). The PDMS slab was cut by laser (Trotec Speedy 100R, settings: Power 60%, Speed 8%, 2 passes) into the desired design (10). The flow cell was then cleaned with DI water and IPA (11) and tapes were removed (12). After further cleaning there was only PDMS flow cell remaining (13). Then it was inserted into the PDMS flow cell tubing (PEEK 360 µm OD x 50 µm ID), the flow cell was placed on diamond substrate and covered by ITO coated glass slide as top electrode.

Conclusion

The PDMS flow cell was fabricated by creation of a microchannel in a PDMS film followed by laser cutting of the cell to the desired design. The PDMS flow cell is placed on the diamond substrate and covered by ITO coated glass as a counter electrode.

4.6.3 Fabrication and characterization of the homoepitaxial diamond device

Fabrication process

The scheme of the diamond device represents Figure 105. Figure 106 shows the photograph of the fabricated diamond device. The device consists of (6000 ppm) boron doped diamond electrode and N-doped film with NV centres, which are deposited on (100) oriented homoepitaxial diamond substrate. The diamond is equipped with 4 Ti/Au electrodes placed on boron and nitrogen doped diamond film. As described in the previous chapter the device is electrically controlled and has two functions: an active control of the NV centre charge state by applying gate voltage and electrochemical readout or setting up the voltage to specific reference voltage. The design includes a working electrode on the diamond surface (counter electrode represents ITO coated glass sheet). The change of NV PL is monitored as response to charged molecules attracted on the diamond surface. The PL is measured by a confocal microscope through microfabricated holes in the gate electrode. Figure 107 shows the photograph of the gate electrode with the fabricated micro holes (diameter ~5 µm).

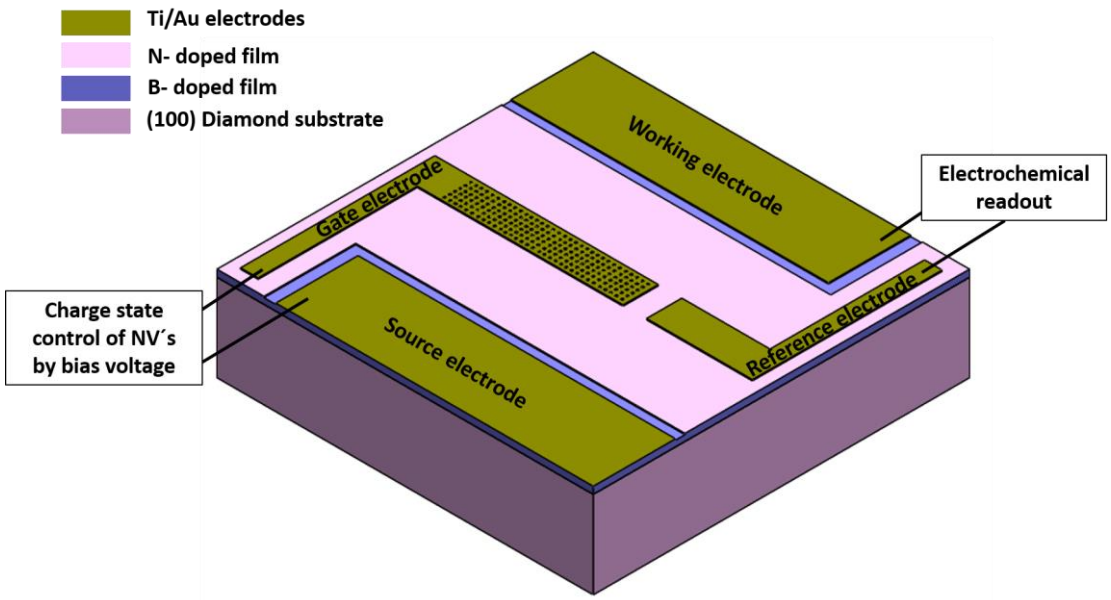

Figure 105. The design of the diamond device with electronically controlled functions: a charge state modulation of the NV centre charge state and an electrochemical readout. The diamond device consist of highly boron doped ultra-flat diamond film and nitrogen doped diamond NV centre containing film on top and 4 Ti/Au electrodes.

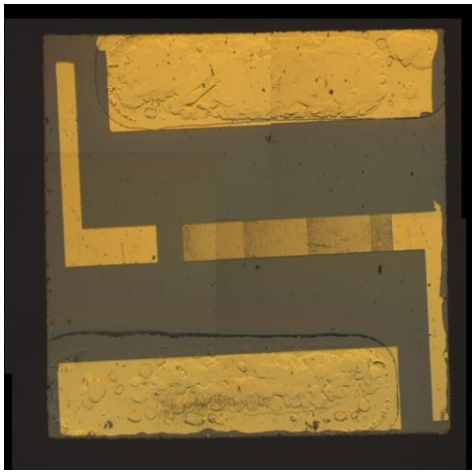

Figure 106. Photograph of the diamond sample 165 with fabricated electrodes.

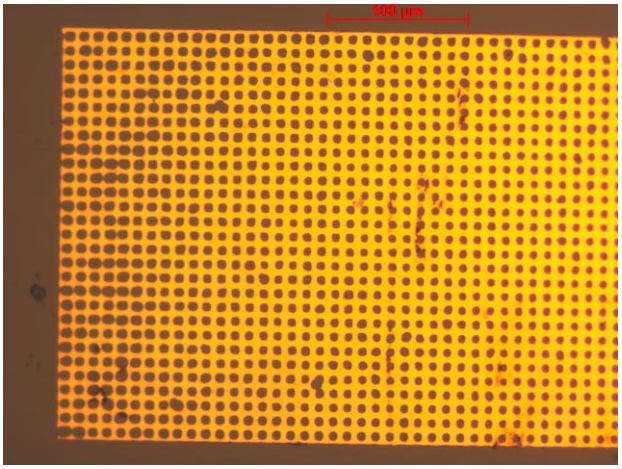

Figure 107. Optical microscopy image of the diamond sample 165: zoom on the sensing gate electrode with micro holes.

First a highly conductive boron doped layer with a very flat surface was fabricated at the IoP ASCR (by Dr. Vincent Mortet and Marie Krečmarová). The details of the layer fabrication process is described in in chapter 4.3.1. Before further diamond growth, a thin titanium film was sputtered (by Marie Krečmarová) on the boron doped diamond surface in areas representing working and source

electrodes (see Figure 105) at the IMO-IMOMEC. The highly boron doped (6000 ppm) film was overgrown (by Marie Krečmarová) firstly with and without low boron doped (1 ppm) interlayer and after that by N-doped thin films with NV centres (Table 2 and 3) at the IMO-IMOMEC (chapter 4.3.2). Finally ohmic titanium/gold (Ti/Au = 20/80 nm) contacts were fabricated by classical photolithography, metal evaporation, etching and annealing (by Dr. Vincent Mortet) at the IoP ASCR (Figure 106); and contacts (for preliminary samples) titanium/aluminium (Ti/Al = 30/150 nm) by classical photolithography, metal sputtering, etching and annealing at the IMO-IMOMEC (by Marie Krečmarová). The detail of the gate electrode microstructures is shown in the Figure 107 (optical microscopy image) and in the Figure 108 (PL map).

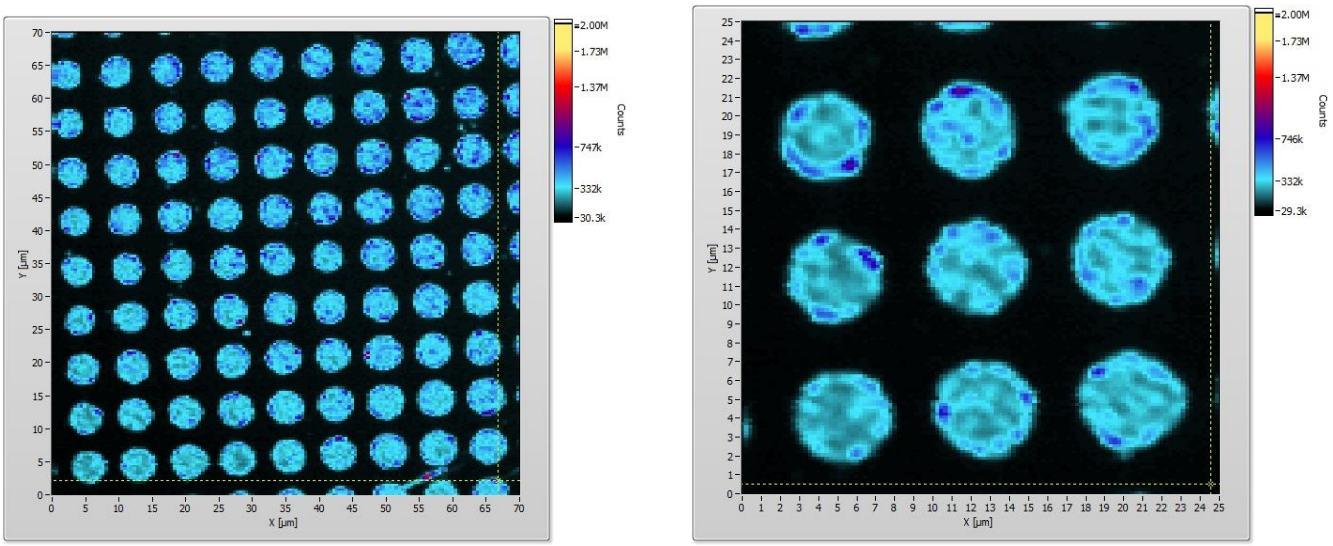

Figure 108. PL maps of gate microstructures on sample 164 (excitation laser power of 8mW).

NV PL characterization

The NV photoluminescence was measured (by Marie Krečmarová) close to the gate electrode with microstructures (Figure 107 and 108) by the home built confocal microscope at the IMO-IMOMEC. PL was excited by the 500 mW Gem laser from Laser Quantum producing 532 nm CW excitation, directed by Gaussian beam optics to 100x magnification Long Working Distance M Plan Semi-Apochromat – LMPLFLN objective with N.A. of 0.8 and WD of 3.4 mm. The PL counts were detected using Excelitas single photon counter after a dichroic mirror and a 650 nm long pass filter, filtering out green laser. Optically detected magnetic resonance (ODMR) technique, which is described in the Chapter 2.6.2, was carried out to detect NV^- centres, using the same laser setup (by Marie Krečmarová). A copper wire (20 µm) was placed over the diamond sample and laser was focused

close to the wire and gate electrode. For the detection was used 8 mW laser power and 1.8 W microwave power without an applied external magnetic field. The voltage for the NV centre active control was applied on the gate electrode based on estimate band bending, modelled using the AMPS-1D software (Analysis of Microelectronic and Photonic Structures) by numerical calculations of the Poisson's and the continuity equation (by Marie Krečmarová). The calculation methods are explained more detail in the AMPS-1D user manual [127].

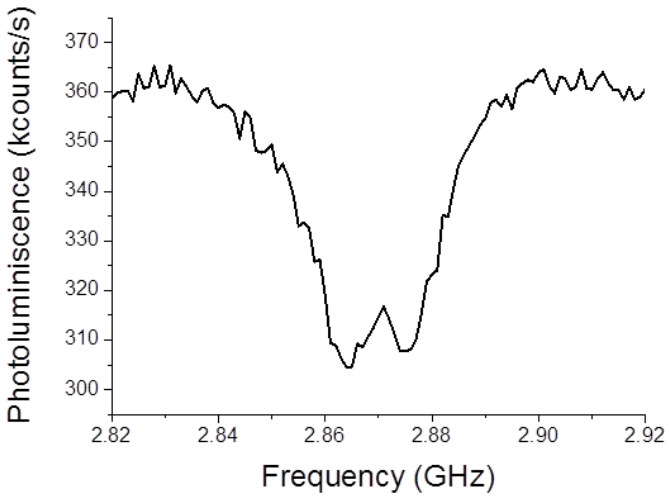

Figure 109. ODMR spectra of a NV^- centres cluster in the O-terminated diamond sample 164 (a).

NV PL spectra of all deposited films (see Table 2 and 3) with O- surface termination are shown in Figure 110a. The PL spectra were normalised to NV^0 ZPL line. The maximum amount of the NV centres was observed in the sample 168 with the highest thickness of N-doped film (400 nm), however the deep located NV centres are not sensitive on the diamond surface charge and thus this sample was not appropriate. Therefore another samples were grown with 15-20 nm thin N-doped film with NV centres and with/without a low boron doped interlayer (1 ppm) on the highly boron doped layer (6000 ppm).

The Sample 164 consists of single NV´s and NV centre clusters (Figure 117). The concentration of nitrogen vacancy centres in the produced sample was estimated from confocal PL measurements to be of a concentration ~10 NV centres/um^2. Even after oxygen termination the NV centres were mainly in NV^0 charge state due to the underlying highly boron doped layer, which tunes the Fermi level position below defect level of NV^- centre (see band bending model in the Figure 111a). Nevertheless,

some of the NV centres can exhibit also in NV^- charge state by O-termination, as it was confirmed by ODMR spectroscopy (Figure 109).

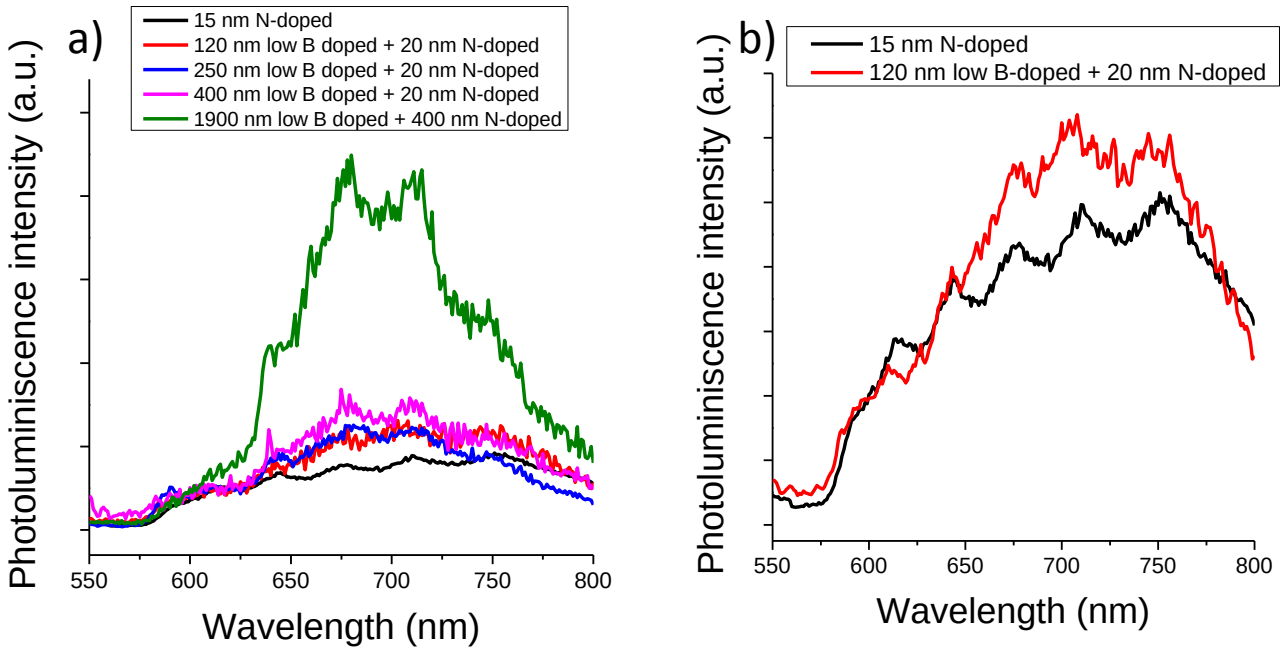

Figure 110. PL spectra of all grown O-terminated samples (a) and comparison of the O-terminated sample 164 and 167 (b) showing a higher occupation of NV^0 PL for sample 164 grown directly on highly B doped layer (6000 ppm) and on the other hand showing higher occupation of NV^- PL for sample 167 grown with the low B doped (1 ppm) interlayer.

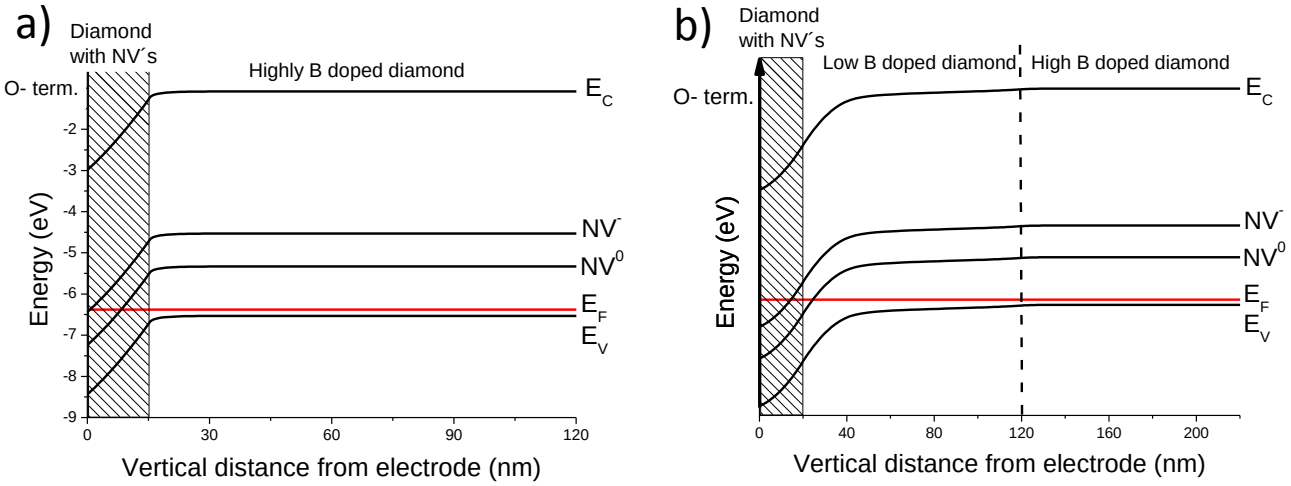

Figure 111. Band bending of the sample 164 (a) and sample 167 (b) with O- surface termination. The Fermi level is positioned below the defect level of NV^- centre and NV centres are mostly in NV^0 or NV^+ charge state for sample 164 lacking the low B doped (1ppm) interlayer (a). On the contrary the Fermi level is positioned above the NV^- defect level for sample 167 grown with the low B doped interlayer and thus NV centres are mostly in NV^- charge state.

For a purpose of tuning the Fermi level position above the NV^- defect level, the samples 165 – 168 were grown with a low boron doped (1ppm) interlayer. Figure 111b represents the band bending model of the oxygen terminated sample 167 consisting of a 100 nm thin low boron doped interlayer (1 ppm) with 20 nm diamond thin film with NV centres on top, grown on a highly boron doped (6000 ppm) single crystal diamond electrode. Figure 110b shows comparison of NV PL of the sample 167 and 164. NV centres of the sample 167 are in NV^- charge state with higher intensity of PL, whereas NV centres of the sample 164 lacking the low B doped interlayer are mostly in NV^0 charge with lower PL intensity. Those two samples were used for further characterisations and the DNA sensing.

Conclusions

In conclusion, the device for biosensing applications consisting of an ultra-flat highly boron doped (6000 ppm) diamond electrode, with/without a low B doped (1 ppm) interlayer and a thin (15 – 20 nm) NV centre containing the diamond film on top was developed. The device is equipped with planar titanium/gold electrodes for the charge state control of the NV centres and the electrochemical readout which are located on boron and N- doped films. The surface of the N- doped film is oxygen terminated predicting the close surface NV centres charge state be preferably in NV^-. However, the underlying B doped layer has also influence on the Fermi level position of N-doped layer and thus the NV centre charge state. In case of absence of the low B doped interlayer, the highly B doped layer tunes the NV centres to NV^0 charge state. Contrary the low B doped interlayer sets the NV centres to NV^- charge state with higher intensity of PL. To verify inter conversion of NV^0 and NV^- charge state is essential for the biosensor functionality.

4.7 Control of the NV centre charge state by surface functionalization

The sensing principle of the biosensor is based on the close surface sensitivity of NV centres on a diamond surface termination for detection of charged molecules as DNA or polymers. To demonstrate the function of sensor we investigated first a passive charge control of NV centres by diamond surface termination.

As was discussed in the previous chapter, the underlying boron doped layer shifts the Fermi level position close to the valence band and also affects the Fermi level position of N- doped film. Concentration of boron acceptor atoms in the underlying layer (1 ppm and 6000 ppm doped) tunes the NV centre charge state (see Figure 111). The NV centre charge state depends also on surface termination

of the N- doped film. Oxygen termination shifts the Fermi level position upwards to the conduction band predicting the NV^- charge state. Contrary hydrogen and polyethyleneimine (PEI) termination shifts the Fermi level position downwards to the valence band with more preferable charge state of NV^0 and NV^+. In this chapter we investigate activity of the NV centres related to the surface termination of the N- doped film.

4.7.1 Oxygen and Hydrogen terminated surface

The effect of surface hydrogen and oxygen termination is investigated on sample 164 (Table 2 and 3) representing a very smooth 15 nm intrinsic film with single NV centres and NV centre clusters deposited on a highly boron doped (6000 ppm) electrode without a low boron doped interlayer. The oxygen and the hydrogen terminated surface was created by exposure to oxygen, respectively to hydrogen plasma (by Marie Krečmarová). The NV photoluminescence was measured (by Marie Krečmarová) at the IMO-IMOMEC with the home built microscope (more details in the chapter 4.6.3) without using of the microfluidic cell. This work is submitted to the IFMBE conference proceeding.

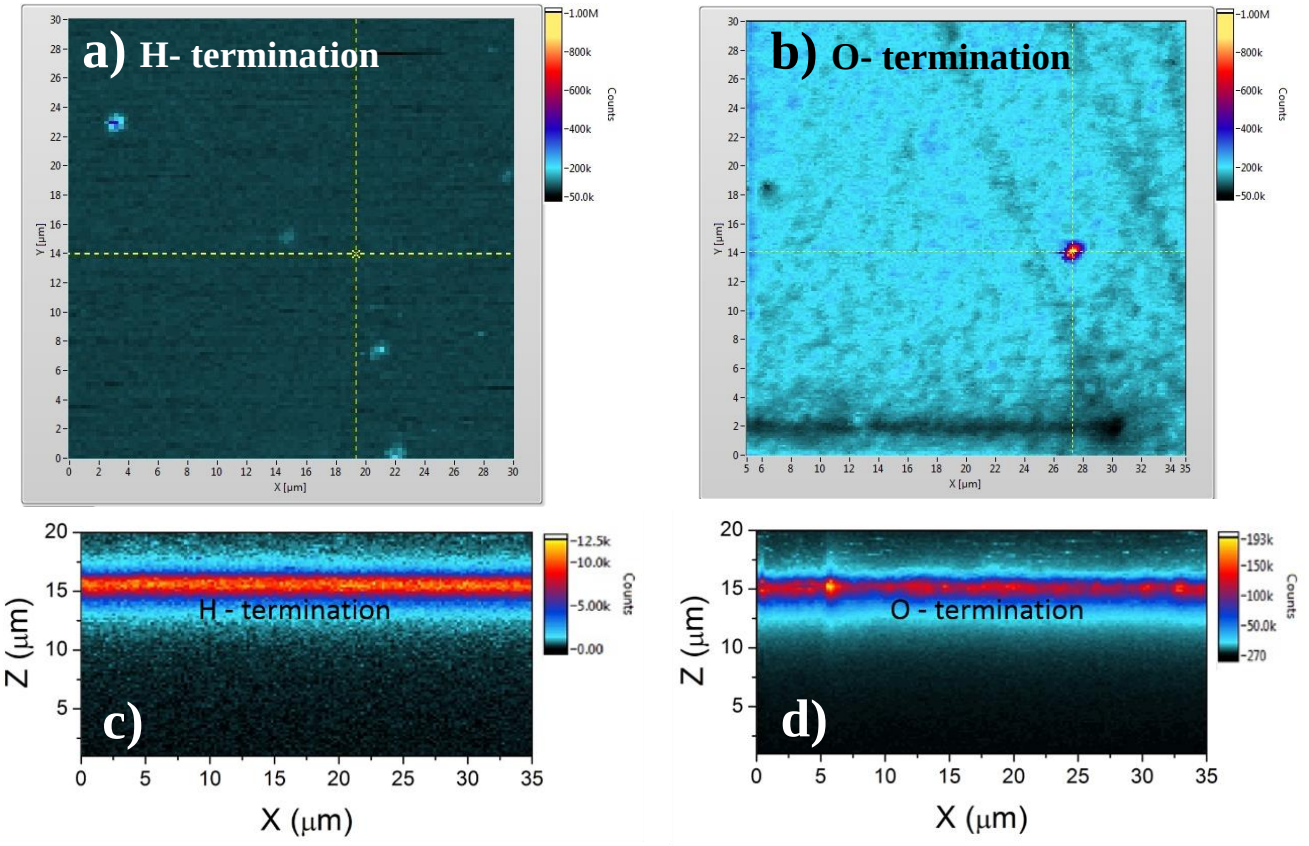

Figure 112. PL intensity surface and cross section maps (532 nm excitation wavelength, 650 LP filter, 50 uW laser power) showing app. 15 times higher intensity for oxygen terminated diamond surface (b, d) then hydrogen terminated diamond surface (a, c) of sample 164. (a)

Figure 112 shows PL surface and cross section PL maps with the use of 50 uW laser power for both (H and O) surface terminations. Very low photon counts can be established from hydrogen terminated surface, suggesting that the NV-layer is partially depleted by band bending from B-doped side and/or as well by an upwards bending close at the diamond surface. In case of oxygen terminated surface PL counts increased dramatically more than order of magnitude (15 times higher) than for the hydrogen terminated surface, suggesting the restoration of flat bands at the surface. This change is a dramatic improvement compared to previous research where the changes were ~ 10 – 20 % [24]. PL spectroscopy shows predominantly NV^0 charge state with O- termination, which is quenched by H- termination to more preferably non-PL NV^+ state (Figure 113).

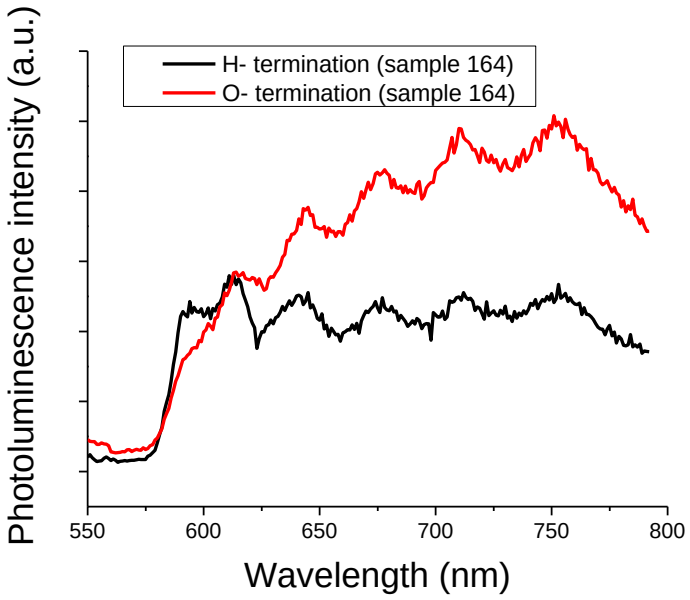

Figure 113. Normalised PL spectra showing a higher NV^0 peak for H- termination and a higher PL intensity of NV^- and its side bands for O- termination (sample 164).

4.7.2 Polyethylenimine terminated surface

This chapter deals with NV centre charge state manipulation by a surface functionalization with a strongly cationic polyethylenimine (PEI) polymer. For the experiment a sample 167 (Table 2 and 3) was used, which consists of 100 nm thin low boron doped (1 ppm) interlayer deposited on highly boron doped (6000 ppm) diamond and 20 nm thin nitrogen doped film with NV centres on top of it.

Before PEI attachment the diamond surface was first exposed to oxygen plasma (by Marie Krečmarová) for it to obtain a very clean and negatively charged surface. PEI molecules are then electrostatically attracted (by Marie Krečmarová) on negative oxygen's terminated surface. The solution of PEI

50 % w/v in H_2O has been purchased from Sigma-Aldrich, it was first diluted with milli Q water to the final concentration of 0.2 % w/v and then ultrasonicated for 30 minutes. The sample 167 was immersed into the solution for 8 hours and then rinsed with milli Q water and dried with a nitrogen gun. For better adhesion of PEI molecules, the sample was baked at 90 °C. After the baking, the sample was exposed for 2 minutes in a low power (50 W) oxygen plasma (by Marie Krečmarová) so that only a thin mono layer of PEI molecules would remain on the surface.

The NV photoluminescence was measured (by Marie Krečmarová) at the IMO-IMOMEC with the home built microscope (more details in the chapter 4.6.3) without using of the microfluidic cell.

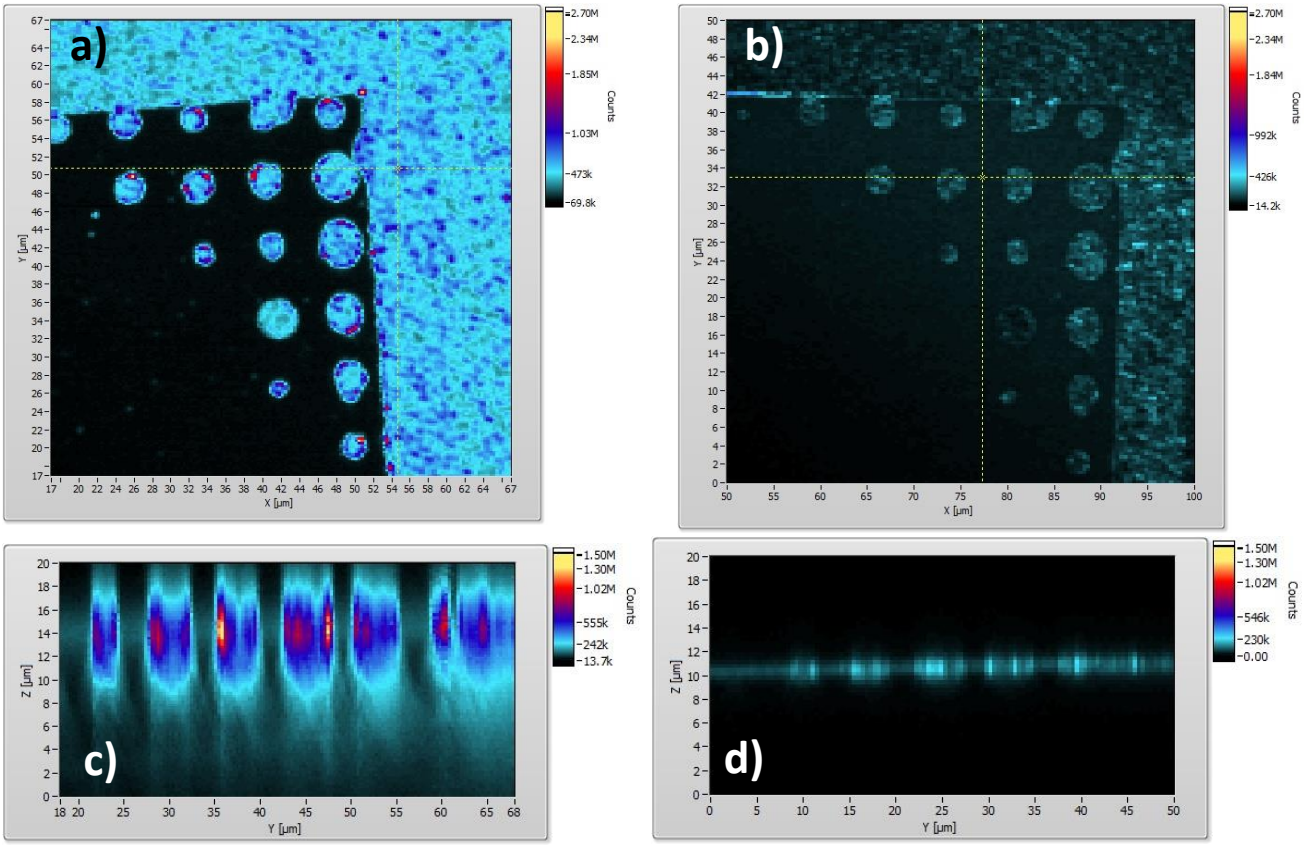

Figure 114. PL intensity XY maps with oxygen termination (a) and PEI termination (b) surface, PL intensity YZ maps with oxygen termination (c) and PEI termination (d) surface.

The XY surface and YZ cross section NV PL maps of O- and PEI functionalization are shown in Figure 114. As was discussed previously, presence of the underlying low B doped diamond film (1 ppm) and diamond sensor surface O- termination result in NV^- preferable charge state (see Figure 111b). PL spectra measurements (Figure 115) shows higher occupation of NV^- charge state for O- termination, which is consistent with the band bending modelling. Figure 114 shows a rapid decrease of PL counts

after PEI functionalization. The NV PL spectra shows an even more drastic quenching effect than for H- termination (Figure 115). The PEI termination tunes the NV centres into a mostly non-PL NV^+ state. Note that the PL intensity spectra for the PEI functionalization presents a fake peak located around 750 nm, which is related to the monochromator grating.

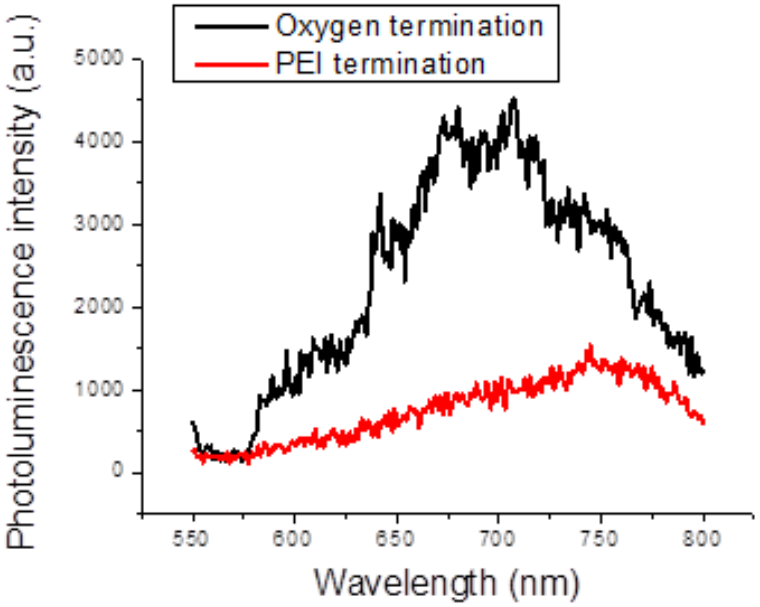

Figure 115. PL spectra with oxygen and PEI surface termination (e) measured with 532 nm excitation wavelength, 650 LP filter and 8mW laser power).

Conclusions

The inter conversion of NV^0 and NV^- charge state was verified by a diamond surface termination. The positive surface termination (H, PEI) results in a preferable NV centre charge state of NV^0 or non-PL NV^+, whereas negative surface termination (O) leads to NV^- charge state. The switching of the NV centre charge state as a response of diamond surface termination is a crucial tool for the sensitive sensing of charged molecules with the diamond device.

4.8 Active control of the NV centre charge state by voltage bias

To demonstrate the sensor function we manipulated with the band bending by the application of bias voltage from -3 V to +3 V on the gate electrode. Figure 116 shows the concept of the sensing system including confocal microscope, electronic board and diamond device (by Marie Krečmarová). The PL was detected close to the gate electrode with an 8 mW laser power and a 650 nm long pass

filter (by Marie Krečmarová). A band bending under a different applied voltage on the device was simulated (by Marie Krečmarová) by using the AMPS-1D [127]. This work is planned to be submitted to a journal such as Scientific Reports and Nanoscale.

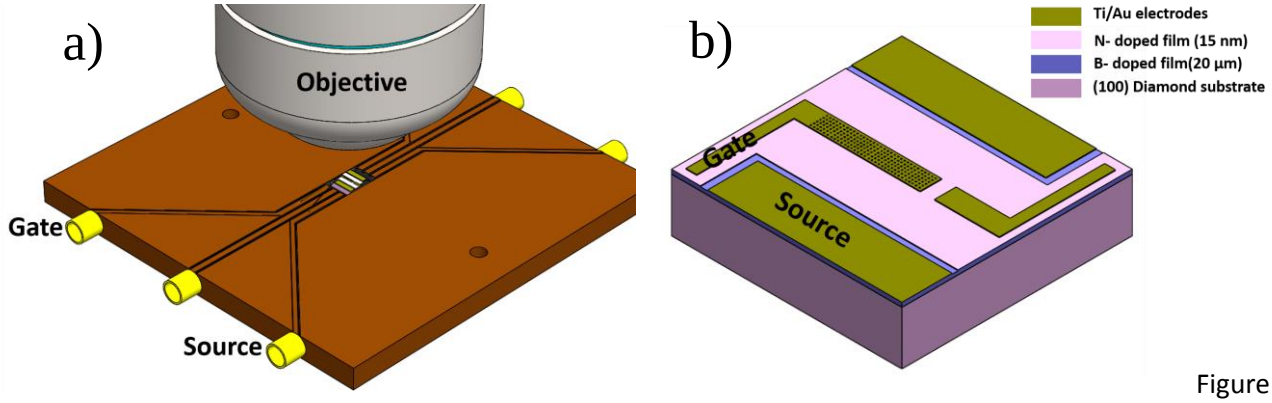

Figure 116. Scheme of the sensing system consisting of diamond sample wire bonded on electronic board and confocal microscope readout (a), scheme of the diamond device (b).

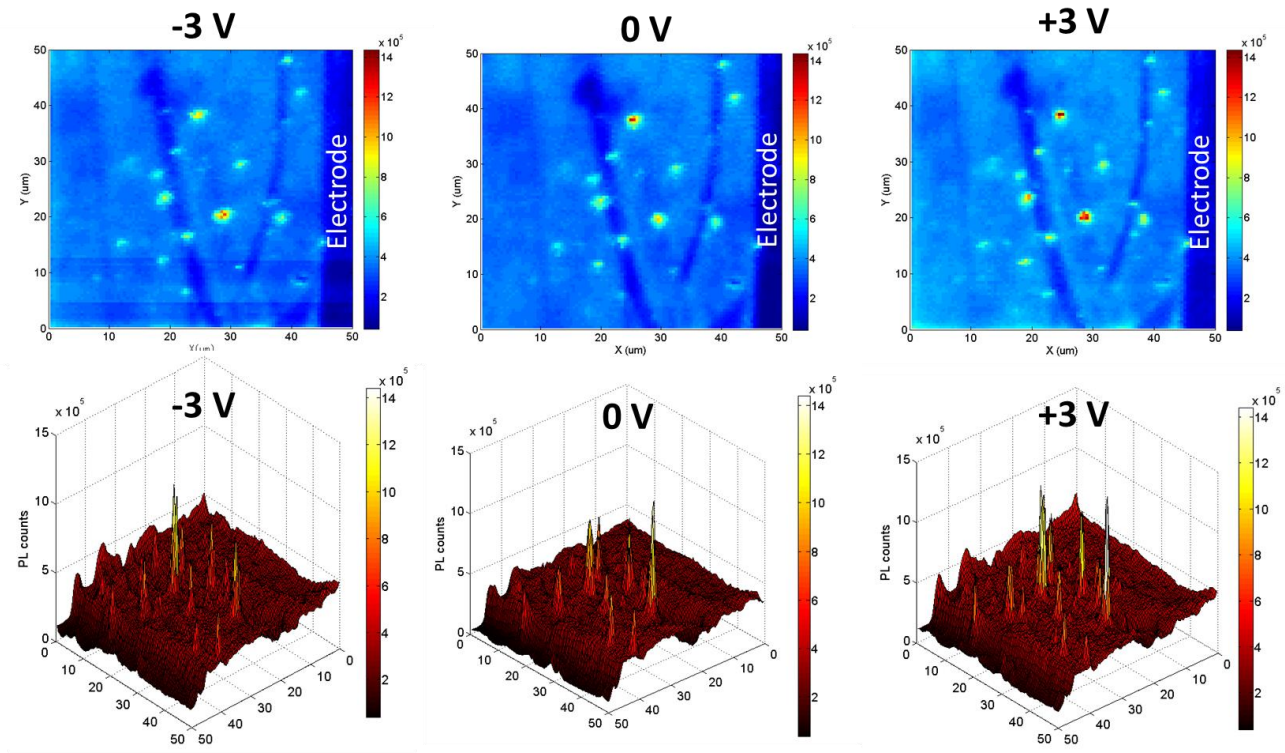

Figure 117. PL intensity 2D maps (up) and 3d maps (down) of the sample 1 under -3 V, 0 V and +3V gate voltage, showing higher electron occupation of NV^- centres at positive voltage.

The diamond device consists of metallically B doped (6000 ppm) diamond layer and 15 nm thin NV centre containing film on top of it (without lightly B doped interlayer). Band bending profile of NV^-

centre level under gate voltage is simulated in Figure 118b. Modelling gives value of the electric field of $2.7 \cdot 10^6$ V/cm. PL was detected close to the gate electrode with 8 mW laser power as function of a gate voltage. Single NV centre has typical PL counts of 45 kcount/sec, what was calculated by geometry of the objective and the index of refraction of diamond.

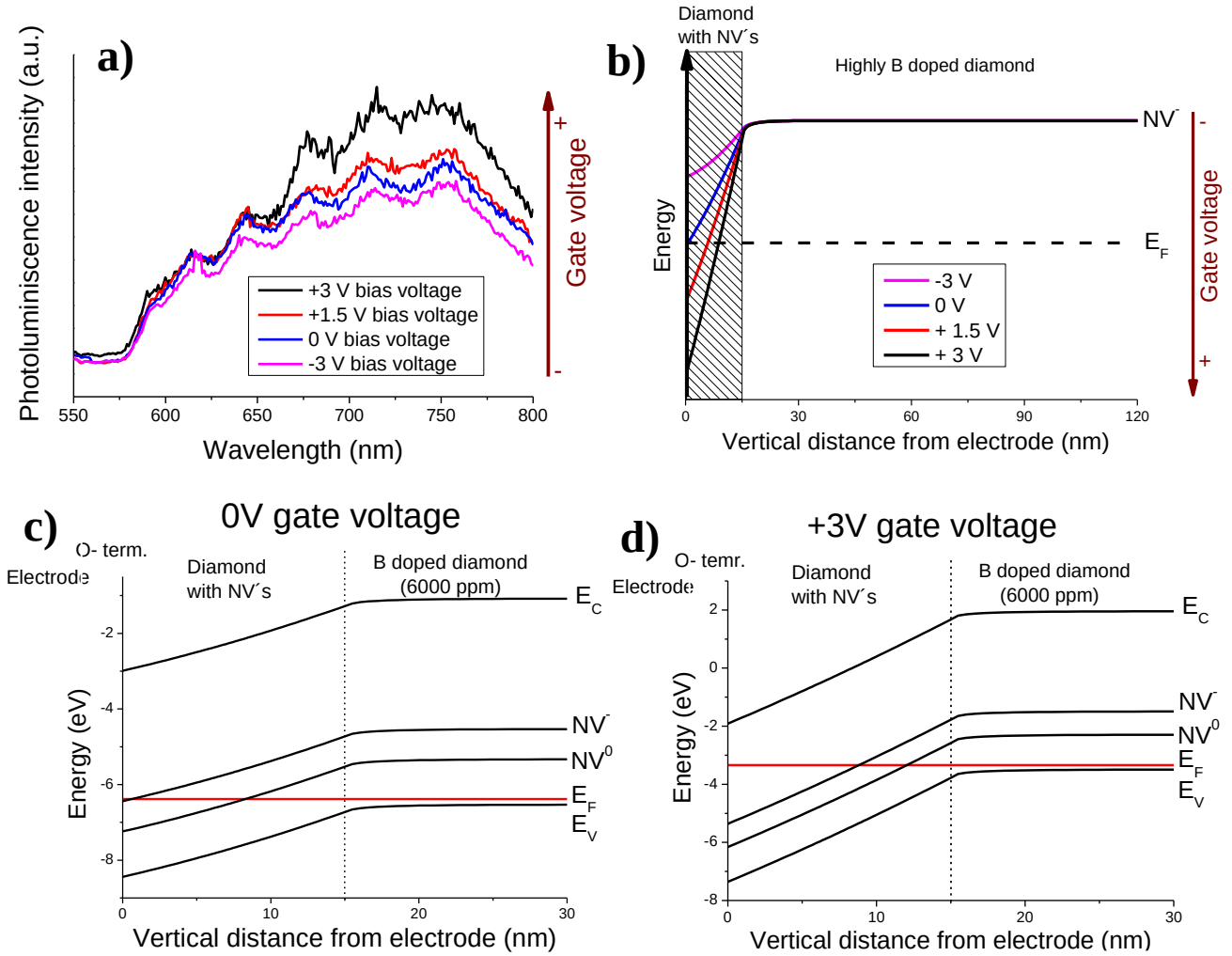

Figure 118. PL intensity spectra (8 mW laser power) at gate voltages (sample 1) from -3 V to + 3 V showing increase of the NV- centre occupation with positive gate voltage (a), NV^- centre energy level simulation by applying of gate voltage from -3 V to +3 V (b), detail of the band bending modelling under an applied gate voltage of 0 V (c) and +3 V (d).

Figure 117 shows PL intensity on the 2D and 3D maps of single NV and NV centre clusters for bias voltage of -3 V, 0 V and +3 V located close to the gate electrode. Some NV centre clusters became brighter by the application of +3 V voltage, which means that more NV centres are swapped to a NV^- charge state. When a negative voltage of -3 V was applied, the same spots became darker, consistent

with the band bending modelling (Figure 118b). The switching of NV^-/NV^0 charge state occupation was repeated by cycling the device between +3 V and -3 V with no hysteresis.

Figure 118a shows PL intensity spectra for the NV centre cluster occurring close to the gate electrode. By increasing positive voltage, the occupation of NV^- increases with higher PL intensity. On the other hand, the application of a -3 V negative voltage leads to the increase of NV^0 peak and decrease of NV^- PL intensity. The data are consistent with band bending modelling (Figure 118b-d). The NV centres are mostly in NV^0 charge state with applied negative gate voltage of -3 V or 0 V. The Fermi level is positioned above the NV^- centre level with positive gate voltage of +1.5 V and +3 V.

Conclusions

In conclusion, active manipulation of the NV centre charge state was demonstrated by applying the bias voltage. Gate voltage between +3 V and -3 V was applied and PL intensity of the NV centres were monitored close to the gate electrode on the oxygen terminated surface. NV centre occurs more preferably in the NV^- charge state by the application of the +3 V on the gate electrode, and conversely in the NV^0 charge state by applying the -3 V. The simulations of the device band bending confirmed shifting of the Fermi level above the NV^- centre transition level for applied positive gate voltage starting from +1.5 V and vice versa below the NV^- centre transition level in case of 0 V and -3 V gate voltage. The functionality of the diamond device was verified before its implementation with the electrochemical flow cell.

4.9 Label free electrochemical DNA detection

Electrochemical impedance spectroscopy was carried out to monitor the biochemical reaction of the DNA attachment on the PEI terminated diamond biosensor surface at the IMO-IMOMEC. Firstly it is discussed and solved problem with filling the flow cell by PBS electrolyte solution without bubbles. Secondly the ssDNA immobilization by the electrochemical impedance spectroscopy is verified.

Experimental details

We used the sample 167 (see Table 2 and 3) consisting of 100 nm low B doped (1 ppm) interlayer between the highly boron doped (6000 ppm) diamond layer and the 20 nm thin nitrogen doped film with NV centres on top as the diamond device. For detection we have used NH_2 terminated DNA

Oligo molecules with 23 Bases 5´-/5AmMC6/TTT TTA ATT AAA GCT CGC CAT CA purchased from Integrated DNA technologies, BVBA. The dry DNA molecules were dispersed in the Milli-Q water up to concentration of 100 pmol/µl (by Marie Krečmarová). For filing the flow cell we have used the IsmatecIPC peristaltic dispensing pump (Figure 120). The flow cell was filled by the DNA solution and kept there for 1 hour (by Marie Krečmarová). Before EIS measurement the flow cell was firstly pumped with PBS electrolyte to remove not superficial non-attached DNA molecules.

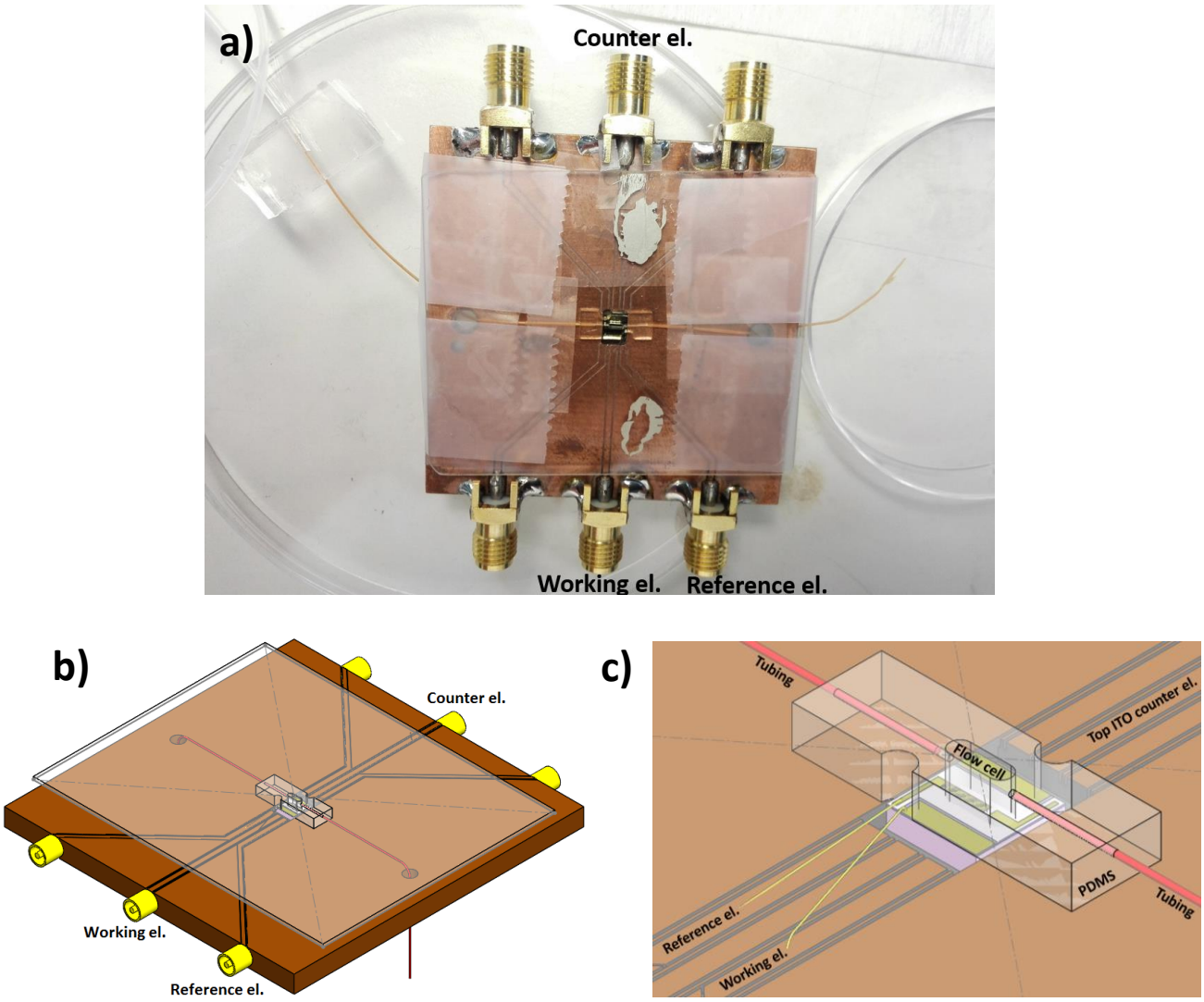

Figure 119. Photograph (a) and schemes (b,c) of the microfluidic diamond device.

Photograph and scheme of the microfluidic diamond device is shown in the Figure 119. For the EIS measurement only two electrodes were used – working electrode connected on the boron doped diamond and counter electrode connected on the ITO coated conductive glass, which was covering the PDMS flow cell. The ITO coated glass has a larger planar dimensions of 4·5 cm for better adhesion

of a PDMS structure. The volume of a microfluidic cell is ~34 µl. The electrochemical impedance spectroscopy was measured (by Marie Krečmarová) using the Hewlett Packard 4248 Precision LCR meter at the IMO-IMOMEC. The impedance was measured with 10 mV AC voltages applied to the flow cell at the room temperature. As an electrolyte we used BupH^{TM} phosphate PBS with pH 7.2. The PBS was ultrasonicated for 5 minutes to remove any bubbles before filling the flow cell. The impedance was measured for 31 frequencies in a range from 100 Hz to 100 kHz. The electrical circuit parameters were determined by fitting the impedance data to the equivalent circuit (Figure 125) over the total frequency range from 100 Hz to 100 kHz using Zview software from Scribner Associates (by Marie Krečmarová).

Filling the flow cell

Figure 120 shows the setup used for the filing of the flow cell with the pump. The peristaltic pump allows flow up to 2 µl/min, which is very suitable for the microfluidic application. The precise filling of the flow cell was monitored by the USB microscope. The flow cell was first cleaned by a flow of the isopropanol and Mili-Q water and then was filled with PBS solution (with air access between alternating the solutions). Figure 121 shows picture of the flow cell filled with PBS before and after EIS measurement. Before the EIS measurement, the flow cell wasn't filled completely and a bubble, visible by the microscope, was present near the tubing. After the EIS measurement (>200 min) the bubble became even larger.

Figure 120. Setup for the filing of the flow cell.

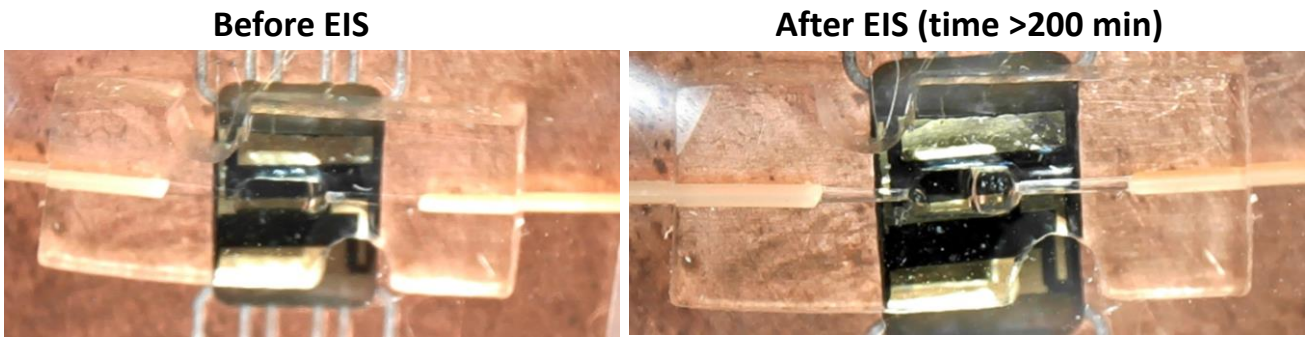

Figure 121. The flow cell filled with the PBS electrolyte before EIS measurement (left) and after EIS measurement (right).

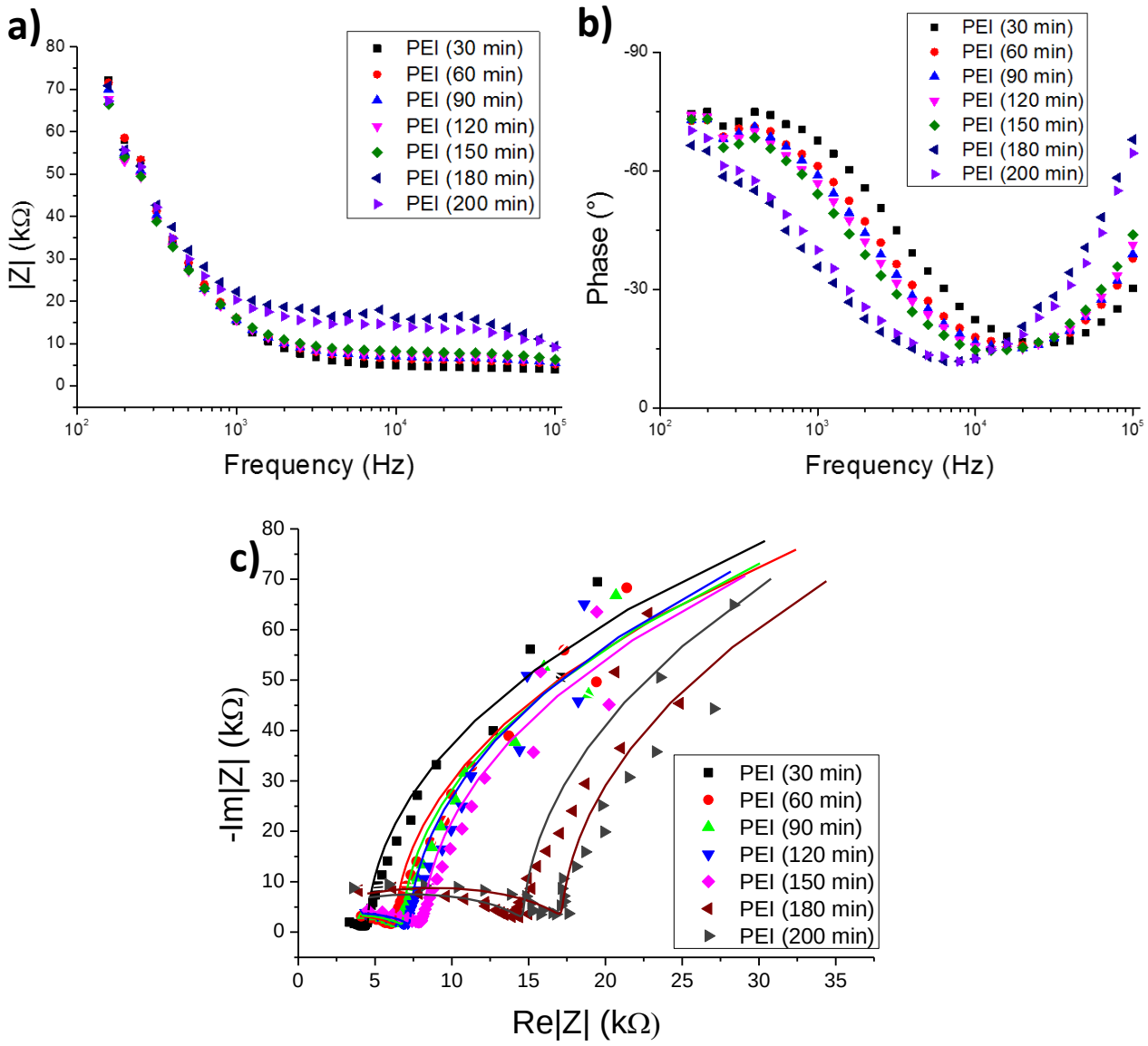

Figure 122. Bode plot shows the complex impedance (a) and of the phase angle (b) as function of the frequency; and Nyquist plot (c) of the PEI functionalized diamond electrode measured for 200 minutes (symbols represent measured data and curves fitted data to the equivalent circuit).

Table 7. Electronical elements fitted to the equivalent circuit for PEI terminated diamond surface showing changing of the parameters with time and bubble evolution.

Fitted parameters	PEI (30 min)	PEI (60 min)	PEI (90 min)	PEI (120 min)	PEI (150 min)	PEI (180 min)	PEI (200 min)
R_s (Ω)	1275	738	635	403	354	N.A.	N.A.
C_{dl} (nF)	11.7	11.9	12.5	13.0	13.1	13.7	13.7
R_{dl} (kΩ)	272.1	267.3	273.2	284.1	277.8	362.2	315.0
C_{scr} (pF)	41.1	24.3	22.5	20.3	19.3	15.8	15.5
R_{scr} (kΩ)	3.27	5.65	6.21	6.88	7.82	14.79	17.20
χ^2 (10^{-3})	9.78	9.36	7.72	9.19	8.90	10.30	5.72

Due to the bubble progression the electrochemical properties of the flow cell, with PEI terminated diamond, were changed. Figure 122 shows Bode plots and Nyquist plot of the microfluidic device as function of time. Impedance increases at higher frequencies with time (Figure 122a). Phase decreases at lower frequencies and increases at higher frequencies with time (Figure 122b). The Nyquist plot of the impedance spectra is shifted on the real impedance axes with time. The measured data were fitted to the equivalent circuit (Figure 125). Table 7 shows that charge space region resistance increases with time and charge space capacitance decreases with time.

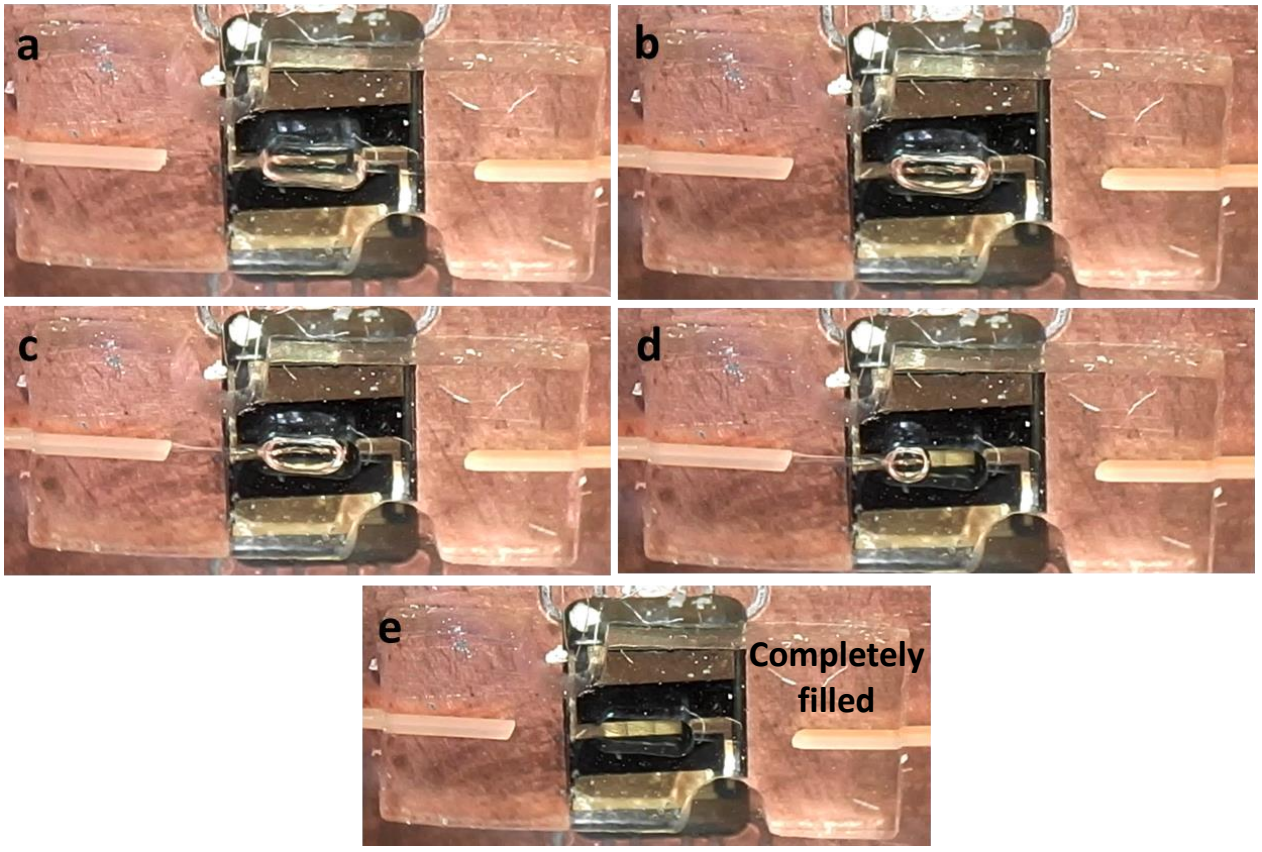

Figure 123. Microscope images of the flow cell filling by isopropanol. The air in the flow cell is being reduced with the flowing isopropanol (a – d) until the flow cell is completely filled (e).

Because the EIS measurement was affected by the bubble evolution, it was not fully stable, therefore it was important to fill the flow cell completely without any bubbles. Fully filled flow cell was achieved only with isopropanol. And thus, the flow cell was firstly completely filled with isopropanol, after that flow was carefully changed for PBS to avoid air access in the microfluidic tubing and flow cell. Figure 123 shows optical microscopy images, recorded during the flow cell filling by isopropanol with flow rate of 50 µl/min.

Label free electrochemical DNA detection

The electrochemical impedance spectroscopy was used for verification of the DNA immobilization on the PEI terminated diamond surface. This work is planned to be submitted to a journal such as Scientific Reports and Nanoscale. For the measurement, the flow cell was completely filled with PBS electrolyte without any visible bubbles (Figure 124), by pre-filling the flow cell with isopropanol.

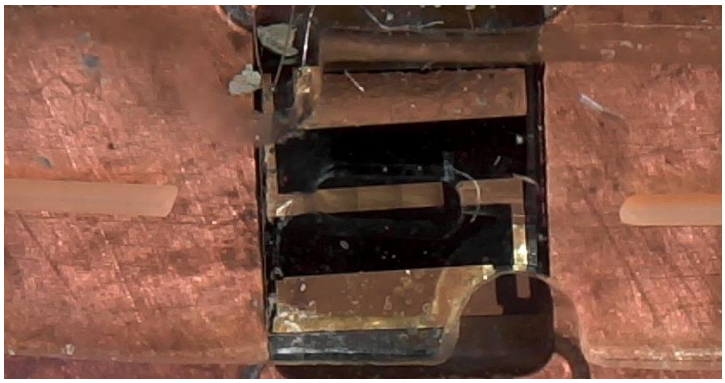

Figure 124. Microscope image of the completely filled flow cell with PBS electrolyte.

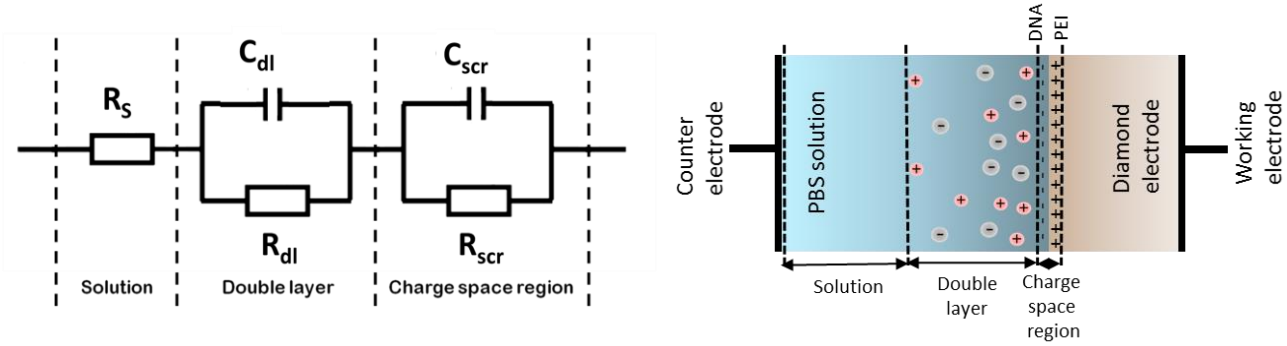

Figure 125. Equivalent electrical circuit used for the measured electrochemical data (left) and scheme of the electrochemical system (right).

The EIS measurements were carried out for duration of 120 minutes. Because the flow cell is lacking air bubbles, the EIS measurements were stable. Figure 126a shows Bode plot of the electrochemical

impedance in complex form and the phase shift as function of frequency for PEI and PEI-DNA functionalized diamond surfaces. Difference plots of the impedance in complex form and the phase shifts for the PEI and PEI-DNA diamond surface functionalization are shown on Figure 126b,c. After the DNA immobilization a higher difference of complex impedance at low frequencies and a higher difference of phase at higher frequencies are visible. The experimental data were fitted to the equivalent circuit (Figure 125), they are plotted in the Table 8. Double layer capacitance and resistance as well as charge space region resistance increases with the DNA immobilization.

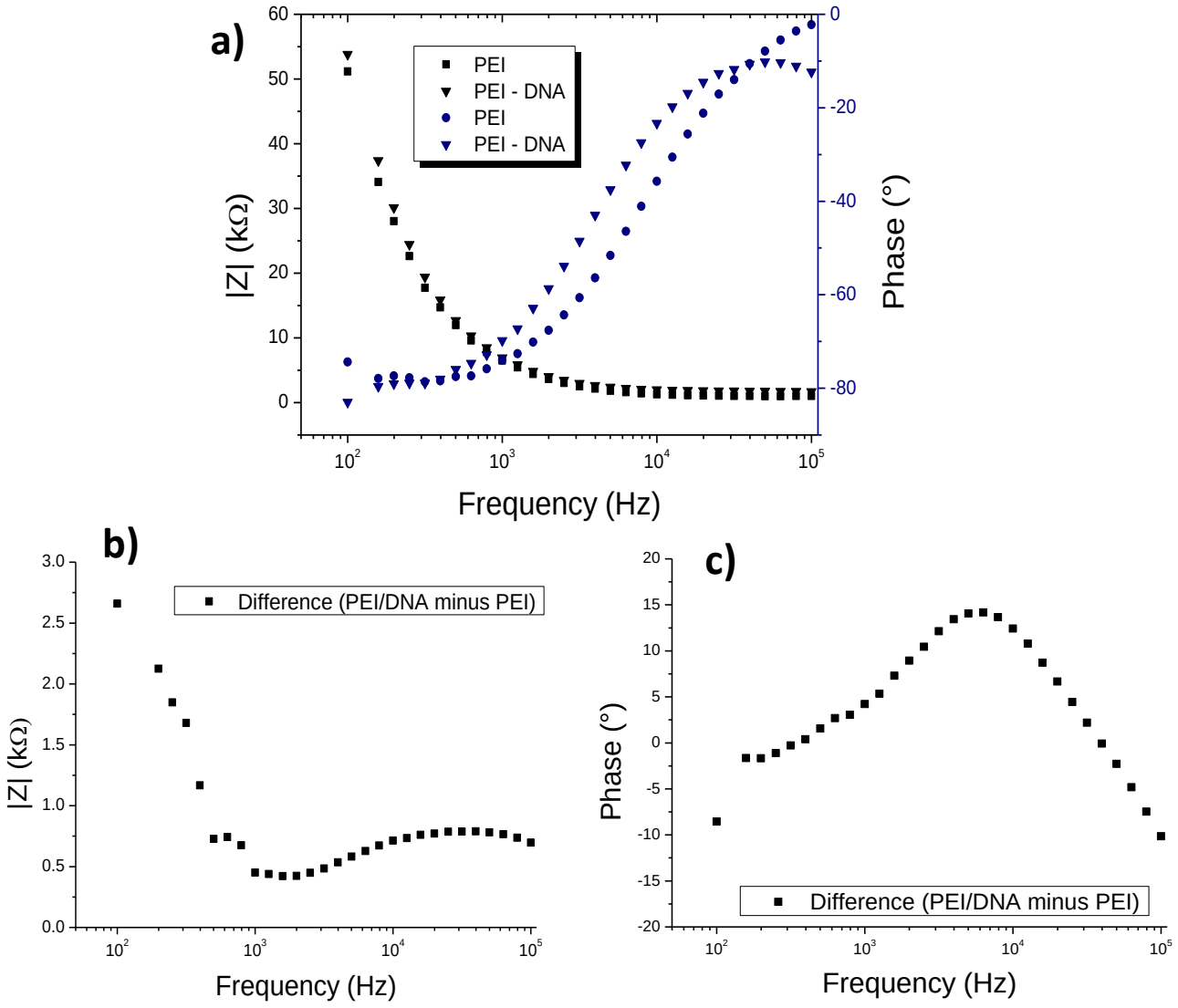

Figure 126. Bode plot of the complex impedance and phase for PEI and PEI-DNA terminated surface (a), difference plots of the complex impedance (b) and phase (c) for PEI and PEI-DNA terminated surface.

Table 8. Electronical elements fitted to the equivalent circuit for PEI and PEI-DNA functionalized diamond surface.

Fitted parameters	PEI	PEI-DNA
R_s (kΩ)	1.0	1.8
C_{dl} (nF)	88	93
R_{dl} (kΩ)	1.4	1.8
C_{scr} (nF)	29	28
R_{scr} (kΩ)	22.5	86.2
χ^2 (10^{-3})	2.0	9.2

Conclusions

We have verified electrochemical functionality of the biosensor and diamond surface bio-functionalization. The label free DNA detection was performed by the EIS. The diamond surface is functionalized by strongly cationic polymer PEI. As a target molecules are used ssDNA by electrostatic attraction on the positive PEI monolayer. The measured EIS data fitted to an equivalent electrical circuit shows that double layer capacitance and resistance as well as charge space region resistance increased after the DNA immobilization.

4.10 Label free NV centre charge state DNA detection

The NV centres close to the diamond surface are sensitive on the diamond surface functionalization. If the surface is (O- terminated), the NV centre is mostly in NV^- charge state. On the other hand, positive surface charge (H- and PEI- termination) switch NV photoluminescence to the NV^0 or not photoluminescent NV^+ charge state. This effect was used for the label free NV centre charge state control DNA detection. NV PL is quenched by positive PEI surface functionalization and it can be reversed to negative NV^- charge state by captured electron from an immobilized negative DNA molecule. This work is planned to be submitted to a journal such as Scientific Reports and Nanoscale.

For the experiment we used sample 167 (see Table 2 and 3) with 100 nm low B doped (1 ppm) interlayer between highly boron doped (6000 ppm) diamond layer and 20 nm thin nitrogen doped film with NV centres on top. Oxygen terminated clean diamond surface was covered with 0.3 % v/w PEI

by technique described in the Chapter 4.7.2 (by Marie Krečmarová). For detection was used 100 nmole NH_2 terminated DNA Oligo molecules 23 Bases 5´-/5AmMC6/TTT TTA ATT AAA GCT CGC CAT CA purchased from Integrated DNA technologies, BVBA. The sample with PEI monolayer was then dipped for 1 hour into the negatively charged ssDNA solution with concentration of 100 pmol/µl and un-immobilized ssDNA molecules were removed by the PBS flow (by Marie Krečmarová). The negative ssDNA molecules were electrostatically attracted to the positive PEI monolayer. NV photoluminescence was detected (by Marie Krečmarová) through the gate electrode microstructures without the microfluidic device, using home build confocal microscope (more specified in chapter 4.3) with using 8 mW laser power and 650 nm long pass filter. A band bending under a different voltage applied was simulated (by Marie Krečmarová) by using the AMPS-1D [127].

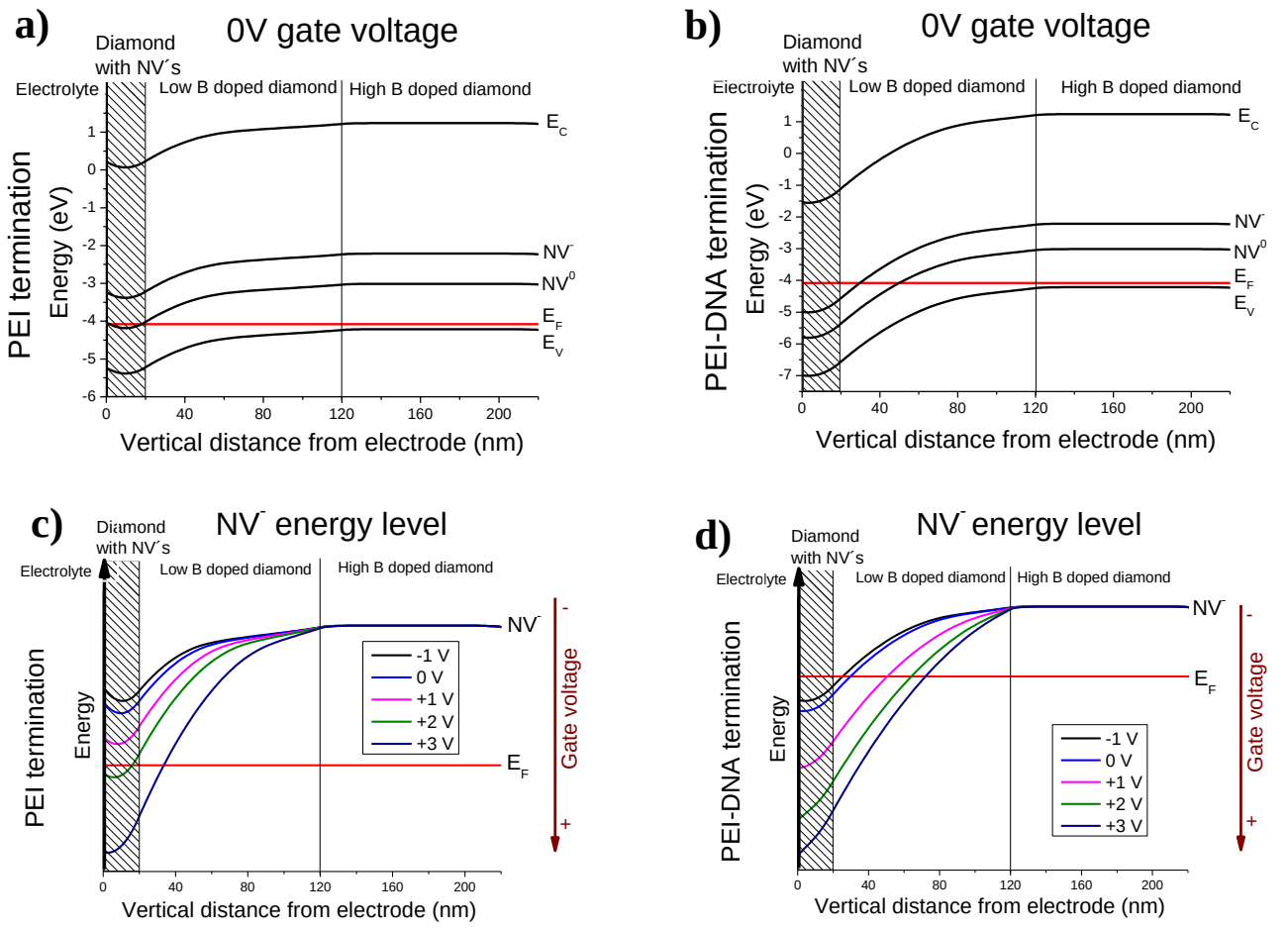

Figure 127. Band bending simulation (sample 2) for PEI (a) and PEI-DNA (b) surface termination at 0 V gate voltage, NV^- centre energy levels for PEI (c) and PEI-DNA (d) surface termination at gate voltage from -1 V to +3 V, and NV^- centre energy level at 0 V gate voltage for PEI and PEI-DNA surface termination (e) showing Fermi level energy positioned about both states.

The biosensor DNA detection principle is based on switching the NV centre charge state as a reaction on diamond surface termination by positive PEI and negative DNA molecules. To demonstrate the charge state manipulation band bending modelling was performed. PEI termination strongly affects the NV centres, the Fermi level energy is below the NV^- centre transition level with applied lower gate voltage than +2 V (Figure 127a,c). The NV centres are recovered to NV^- centre state after the DNA attachment with all simulated gate voltages from -1 V to +3 V (Figure 127b,d). Gate voltage was set as 0 V corresponding to Fermi level position between NV^- centre energy levels states of PEI and PEI-DNA surface termination (Figure 129b). This enable effective switching of the NV PL from $NV^{0/+}$ (PEI) to NV^- (PEI-DNA) for the sensitive DNA detection.

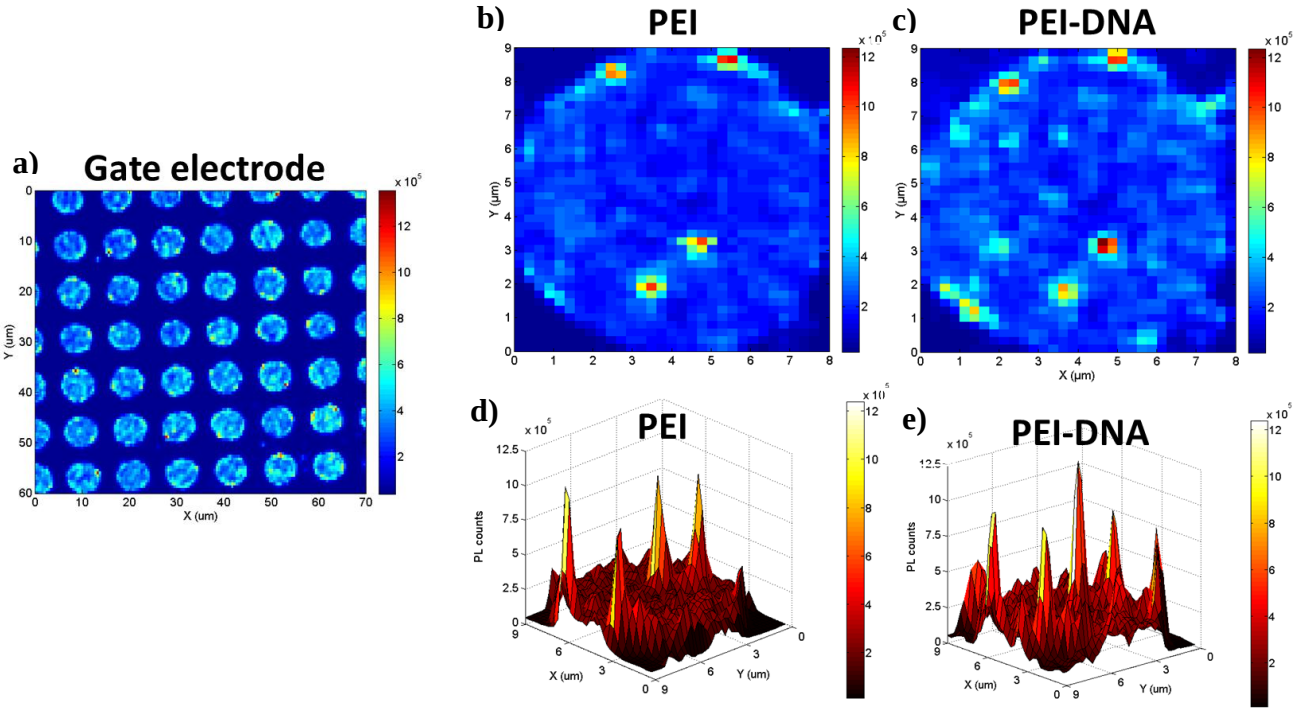

Figure 128. PL intensity maps (sample 2, 8 mW laser power): 2D maps of micro fabricated holes in the gate electrode (a), 2D PL maps of PEI (b) and PEI-DNA (c) terminated diamond surface and 3D PL maps of PEI (d) and PEI-DNA (e) terminated diamond surface.

PL was detected through micro holes in the gate electrode (Figure 128a) with 8 mW laser power. In Figure 129, PL intensity 2D and 3D maps are shown. Laser is focused on one micro hole with PEI termination (128b,d) and PEI-DNA termination (128c,e). When negative DNA molecules are attracted on the positive PEI terminated diamond surface, some NV centres localised close to the surface became brighter. PL spectra of the NV centre clusters, measured at same point for PEI and PEI-DNA termination with 8 mW laser power are shown in Figure 129a. PEI termination tunes NV centres to

NV^0 and NV^+ charge and low intensity of predominantly NV^0 photoluminescence is detected. When negative DNA molecules are electrostatically attracted on the positive PEI molecules, NV photoluminescence increases approximately two times and NV centres are switched to NV^- charge state. The experimental results are consistent with band bending modelling (105).

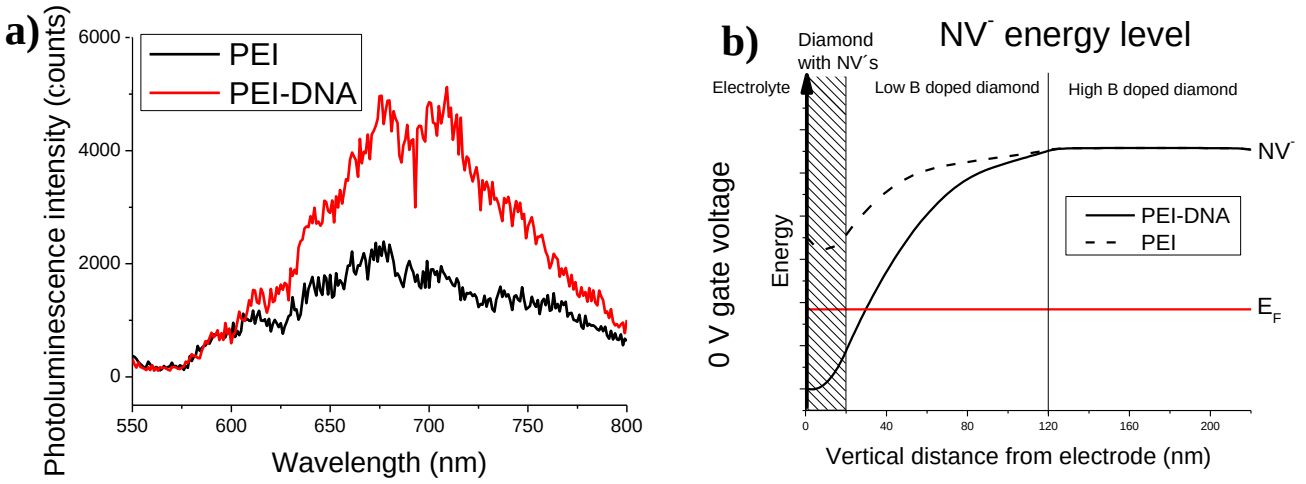

Figure 129. PL intensity spectra (sample 2, 8 mW laser power) for PEI and PEI-DNA diamond surface termination (a), and band bending simulation of NV^-centre energy level at 0 V gate voltage for PEI and PEI-DNA surface termination showing Fermi level energy positioned around half of both states value (b).

Conclusions

The label free DNA NV centre charge state sensor, based on switching of NV photoluminescence detection principle, was fabricated. The sensor operate at 0 V gate voltage, corresponding to the Fermi level position between NV^- centre energy levels states of PEI and PEI-DNA surface termination, which allows effective switching of the NV centre charge state ($NV^{0/+}$/NV^-) for sensitive DNA detection. The near surface NV centres react on the diamond surface charge. Positive surface charge with PEI molecules tunes the NV centres to NV^0 and NV^+ charge and low intensity of predominantly NV^0 photoluminescence is detected. When negative DNA molecules are electrostatically attracted on the positive PEI molecules, NV photoluminescence increases approximately two times and NV centres are being switched to NV^- charge state.

5 Conclusions

The main goal of my PhD work was to design and realize the principle of label free detection of DNA molecules using NV centre in diamond nanosensor, combined with electrochemical detection. The main idea for this biosensor is the combination of an electrochemical device with sensing using NV quantum colour centre. The principle of the NV centre charge state detection of charged biomolecules as DNA or polymers, is based on switching of the close surface NV PL (NV^0/NV^-) as a response on the diamond surface termination [35].

The label free microfluidic diamond biosensor was designed and fabricated. The diamond device consists of highly boron doped (6000 ppm) homoepitaxial (100) diamond electrode capped with a thin low boron doped (1 ppm) interlayer (100 nm) and a NV centres containing diamond layer (~20 nm) on top. The biosensor consists of the single crystal diamond device mounted onto an electronic board and covered with PDMS flow cell and ITO glass. The biosensor has two electrically controlled functions: active control of the NV centre charge state by applying a bias voltage between the gate and source electrodes and electrochemical readout. NV photoluminescence is detected by confocal microscopy on the gate electrode through fabricated micro holes. The biochemical reactions in the microfluidic channel are controlled by the electrochemical impedance spectroscopy.

The work presents the whole fabrication process of the biosensor. It starts with a study of MW PE CVD diamond growth to acquire best growth condition for fabrication of the high quality diamond electrode and NV centre containing diamond films. Further on, we investigated the NV centre charge state by studying the passive (by surface termination and diamond impurities) and active (by electric field) NV charge state manipulation. Based on these results we proceeded with fabrication of the label free DNA microfluidic biosensor and finally detection of DNA molecules by NV centre optical and electrochemical detection techniques based on PEI and PEI-DNA diamond surface bio-functionalization.

MW PE CVD nanocrystalline diamond growth

Boron doping

Chapter 4.1.3: The electrical, optical and characterisitcs properties of variously boron doped nanocrystalline diamond layers were studied. The higher methane concentration leads to improvement of growth rate, but also the presence of transpolyacetylene. The transpolyacetylene

Raman peaks desapeared with thermal annealing at 900°C. Higher concentrations of TMB result in the improvement of a growth rate and larger grain size. The presence of the incorporated boron atoms were confirmed using the FTIR and Raman spectroscopy by occurence of boron related phonon bands at measured spectas. The nanocrystalline diamond layers were deposited with various boron concentrations from semiconducting to metallic conduction regions. The boron doping of 160 ppm of TMB and higher reaches the semiconductive/metallic transition region with Hall holes mobility higher than 1e20 cm^{-3}. Resistivity and Hall mobility decreases with boron doping. The higher boron doping than 1000 ppm does not induce any improvement of conductivity. Higher boron doping (250 - 1000 ppm of TMB) shows stable electrical properties with temperature. Low boron doping (133 ppm of TMB) leads to a change of electrical properties with temperature.

Nitrogen doping

The morphological, structural and optical properties of the deposited nanocrystalline diamond films were studied as function of nitrogen doping using conventional MW resonance cavity and large area linear antenna MW PE CVD systems.

Chapter 4.1.4: In the conventional MW resonance cavity MW PE CVD deposition system the diamond growth rate increases with nitrogen concentration and working pressure. At high nitrogen concentrations, the surface morphology of deposited thin films changes dramatically due to re-nucleation and results in a production of small crystals together with high sp^2 bonded carbon fraction that results into the quenching of photoluminescence. The optimal deposition conditions for creation of NV centres have been found with using the lowest nitrogen concentration (0.07 %) in the gas phase.

Chapter 4.2.2: The study of the nanocrystalline diamond growth using the low pressure large area linear antenna MW PE CVD system confirmed, that a small addition of nitrogen improves the growth rate and dramatically changes surface morphology from well facetted diamond crystals to UNCD like morphology. In contrary to UNCD prepared from Ar rich plasmas, Raman spectra exhibits clear diamond peaks and the layers are very resistive. The TEM characterizations show large and randomly oriented elongated diamond aggregates with a large proportion of planar defects and the presence of 5 nm grains nearby the larger grains. Higher nitrogen addition leads to strong diamond etching, resulting in significant decrease of deposition rate, reduction of nucleation density, formation of isolated facetted diamond grains and NV luminescence. Using the large linear antenna a MW PE CVD system was investigated also a low pressure and a low temperature diamond growth at 250°C, which

is important for the diamond coating of the biomaterials that have a low melting point such as polymers, to increase its biocompatibility. By the addition of nitrogen we have observed a significant improvement of the diamond film quality, i.e. sp^3/sp^2 ratio and well-defined crystals in comparison to the layer deposited without nitrogen that show amorphous phase content.

In conclusion, the best condition for creation of NV centres were found by using the minimum nitrogen concentration (0.07 %) in the gas phase during the conventional MW resonance cavity MW PE CVD diamond growth.

MW PE CVD homoepitaxial diamond growth

Chapter 4.3.1: The epitaxial highly (6000 ppm) boron doped diamond layers with high electrical conductivity of ~333 S/cm were deposited with approximate thickness of ~15 μm. After re-polishing the surface is very smooth with surface RMS roughness of 1.2 nm. The low surface RMS roughness and a good electrical conductivity of the layer are good properties for the diamond electrode.

Chapter 4.3.2: Then the highly B doped layers were overgrown with or without low B doped (1 ppm) interlayer and a thin (~20 nm) NV centre containing diamond film on top as the NV centre charge state biosensing active film. The single crystal diamond device characterization is described in the Chapter 4.6.3.

NV photoluminescence study in nanocrystalline diamond films

4.4.1 Effect of electron irradiation on NV centres in NCD films: We studied a possibility to increase the density of photoluminescent NV centres by electron irradiation. Enhancement of the NV PL was achieved with using all electron irradiation setup arrangements. The Best improvement of the NV PL up to ~10 % was achieved with placement of the collimator onto the electron beam using the water cooling (primary, secondary and back scattered electrons). Enhancement of NV PL was observed also by longer irradiation time. The biggest improvement of NV emission was observed with electron irradiation for 12 hours with ~39 % increase of PL in comparison to non-irradiated sample.

The results were used for design of the diamond biosensor, which consists of thin sensing diamond film with NV centres deposited on boron doped diamond electrode, PL was studied as function of the different NCD film thickness and different concentration of boron acceptors incorporated in the NCD films.

4.4.2 NV photoluminescence study as function of thickness of NCD films: NV photoluminescence intensity rises with the sample's thickness. Minimum thickness presenting NV centres were found in the film consisting of 3 nm nitrogen doped film, grown on 16 nm undoped film with higher photoluminescence intensity for NV^0 centre. All samples exhibit also Si-V colour centres, probably created during the growth by a diffusion from the Si substrate.

4.4.3 NV photoluminescence study as function of boron acceptors concentration in the NCD film: Boron acceptor atoms influence the Fermi level position of NV^- centre and could lead to quenching of NV PL at its higher concentrations, and thus study of an effect of boron acceptors incorporated at different concentrations, in the diamond layers containing NV centres, was performed. The low nitrogen doped nanocrystalline diamond films (0.07 %) were deposited at different concentrations of residual chamber boron background. The boron background level corresponds to the increasing boron doping (during the B doping study) in the diamond growth. An estimated amount of acceptor atoms incorporated into the diamond layers were acquired by the Hall measurements. Quenching of NV centre photoluminescence was observed from an estimated boron concentration in the NCD film starting at 2e19 cm^{-3} and higher.

The label free microfluidic diamond biosensor with electrochemical and NV centre optical readout

The label free microfluidic diamond biosensor is composed of single crystal diamond sensing device, microfluidic flow cell with ITO coated glass and electronic board. DNA detection principle of the biosensor is based on NV centre charge state optical detection combined with electrochemical readout in microfluidic channel. Firstly, we manipulated with NV centre charge state occupation (NV^- /NV^0/NV^+) passively by surface functionalization (O, H, PEI) and actively by voltage bias (-3 V to +3 V). The label free DNA detection benefits from the NV centre charge state sensitivity on diamond surface functionalization. NV PL is quenched by positive PEI surface functionalization and it can be reversed to negative NV^- charge state by captured electron from an immobilized negative DNA molecule.

4.7 Control of the NV centre charge state by surface functionalization: The inter conversion of NV^0 and NV^- charge state by diamond surface termination was verified. PL intensity decreases approximately 15 times with positive H- termination in comparison to negative O- termination. Rapid decrease of PL intensity was also observed by cationic polymer PEI termination. Positive surface termination (H, PEI) results in a preferable NV centre charge state of NV^0 or non-PL NV^+, whereas negative

surface termination (O) leads to NV^- charge state. The switching of the NV centre charge state as a response, on diamond surface termination, is crucial tool for the sensitive charged molecules sensing with the diamond device.

4.8 Active control of the NV centre charge state by voltage bias: The NV centre charge state was also controlled actively by applying the bias voltage (from +3 V to -3 V) between gate and source electrodes on the diamond device. The diamond surface was oxygen terminated and photoluminescence was detected close to the gate electrode. Applying of the +3 V positive voltage results in a more preferable charge state of NV^- (higher ratio of NV^-/NV^0), whereas NV centres are more likely in NV^0 (lower ratio of NV^-/NV^0) with the application of the -3 V negative voltage. The band bending modelling confirmed shifting of the Fermi level above the NV^- centre transition level for applied positive bias voltage higher than +1.5 V and shift of the Fermi level below the NV^- centre transition level in case of applied voltage of 0 V and -3 V. In conclusion, active manipulation of the NV centre charge state was demonstrated by applying the bias voltage. The functionality of the diamond device was verified before its implementation with the electrochemical flow cell.

4.9 Label free electrochemical DNA detection: We verified the electrochemical functionality of the biosensor and diamond surface bio-functionalization. The label free DNA detection was performed by the EIS. The diamond surface is functionalized by a cationic polymer PEI. As a target molecule ssDNA is used, immobilised by electrostatic attraction on the positive PEI monolayer. The measured EIS data fitted to an equivalent electrical circuit shows that double layer capacitance and resistance as well as charge space region resistance, increases after the DNA immobilization.

4.10 Label free NV centre charge state DNA detection: For effective switching of the NV centre charge state ($NV^{0/+}/NV^-$), the sensor operates at 0 V gate voltage, corresponding to the Fermi level position between NV^- centre energy levels states of PEI and PEI-DNA surface termination for sensitive DNA detection. The near surface NV centres react on the diamond surface charge. Positive surface charge with PEI molecules tunes the NV centres to NV^0 and NV^+ charge and low intensity of predominantly NV^0 photoluminescence is detected. When negative DNA molecules are electrostatically attracted on the positive PEI molecules, NV photoluminescence approximately two times increases and NV centres are switched to NV^- charge state.

Author's contribution

Author's contribution of Marie Krečmarová was as follow:

Diamond growth (Chapter 4.1 – 4.5): Nanocrystalline and single crystal homoepitaxial diamond growth at different deposition parameters (gas composition, working pressure, microwave power, substrate temperature…) using microwave resonant cavity and linear antenna microwave plasma enhanced chemical vapour deposition systems (Chapter 4.1 – 4.5).

Diamond film characterizations (Chapter 4.1 – 4.5): Diamond film thickness measurements by optical reflectance interferometry assuming the index of refraction of the layers and profilometry; Optical microscopy characterizations; Raman spectroscopy characterizations of diamond film quality (sp^3/sp^2 carbon phase ratio) at two different excitation wavelengths (325 nm and 488 nm); calculation of diamond grain size by fitting of the Raman peak at two different wavelengths (325 nm and 488 nm); Fourier transform infrared spectroscopy transmittance measurements of boron doped diamond films in the mid infrared region; NV photoluminescence measurements of nitrogen doped diamond films with 514 nm excitation wavelength at room and liquid nitrogen temperature; four probe boron doped diamond films resistivity measurements by van der Pauw method; electrochemical impedance spectroscopy characterizations of nanocrystalline diamond electrodes (Chapter 4.5).

Diamond electrochemical NV centre charge state biosensor (Chapter 4.6 – 4.10): Design of the biosensor using the Solidworks software; fabrication of the diamond device and electrodes (diamond deposition – boron and nitrogen doped double layer, photolithography - metal sputtering, wet etching and thermal annealing); assembly of the whole biosensor (diamond device, microfluidic flow cell and electronic board); optical microscopy of the diamond device and polydimethylsiloxane flow cell; NV photoluminescence and Optically detected magnetic resonance measurements by confocal microscopy at 532 nm wavelength; applying a voltage bias on gate electrode for active control of NV centres; diamond device surface termination by oxygen and hydrogen plasma for passive control of NV centres; band bending modelling of the diamond device under a bias voltage and different surface functionalization; bio-functionalization of the diamond device (ssDNA attachment on polyethylenimine terminated surface); filling the microfluidic flow cell and electrochemical impedance spectroscopy measurements.

Furthermore, the contribution was processing of the all measured data and figures and writing of the dissertation thesis.

6 References

1. McNaught A. D., Wilkinson A. IUPAC. Compendium of Chemical Terminology, 2nd ed. (the “Gold Book”). Oxford: Blackwell Scientific Publications (1997).

2. Dorothee Grieshaber, Robert MacKenzie, Janos Vörös and Erik Reimhult. Electrochemical Biosensors - Sensor Principles and Architectures. *Sensors* 8 (2008) 1400-1458.

3. Rastislav Monošíka, Miroslav Streďanský, Ernest Šturdíka. Biosensors - classification, characterization and new trends. *Acta Chimica Slovaca.*5(1) (2012) 109-120.

4. Kashif Riaz, Siu-Fung Leung, Zhiyong Fan, Yi-Kuen Lee. Low-Cost Energy-Efficient 3-D Nano-Spikes-Based Electric Cell Lysis Chips. *Microelectromechanical Systems Journal* 26 (2017) 910-920.

5. Micro Nano Tech Conference 2011. What are biomems? Available online [November 2017] at http://scme-nm.org/files/SCME_MNT_BioMEMS_Workshop.pdf.

6. Satoshi Koizumi, Christoph Nebel, and Milos Nesladek. *Physics and Applications of CVD Diamond.* Weinheim: s.n., (2008).

7. Cyril Popov, Wilhelm Kulisch. Nanocrystalline Diamond Films for Biosensor Applications. In J.P. Reithmaier et al. (eds.), Nanotechnological Basis for Advanced Sensors, NATO Science for Peace and Security Series B: *Physics and Biophysics* (2011), DOI 10.1007/978-94-007-0903-4_47.

8. Affymetrix GeneChip arrays. Available online [November 2017] at https://www.thermofisher.com/.

9. Nsofor, Chijioke A. DNA microarrays and their applications in medical microbiology, *Academic Journals*, 9(1) (2014) 1-11.

10. A. Hadidi, H. Czosnek and M. Barba. Dna microarrays and their potential applications for the detection of plant viruses, viroids, and phytoplasmas, *Journal of Plant Pathology* 86 (2) (2004) 97-104.

11. Seokheun Choi, Michael Goryll, Lai Yi Mandy Sin, Pak Kin Wong, Junseok Chae. Microfluidic-based biosensors toward point-of-care detection of nucleic acids and proteins. *Microfluid Nanofluid.* 10 (2011) 231–247.

12. Hadar Ben-Yoav, Peter H. Dykstra, Tanya Gordonov, William E. Bentley, Reza Ghodssi. A Microfluidic-based Electrochemical Biochip for Label-free DNA. *J. Vis. Exp.* 91 (2014).

13. Dongneng Jiang, Guiming Xiang, Chang Liu , Juanchun Yu, Linlin Liu, Xiaoyun Pu. Development of a Cyclic Voltammetry Method for DNA Electrochemical Detection on Microfluidic Gene Chip. *Int. J. Electrochem. Sci.* 7 (2012) 10607 - 10619.

14. Randeep Kaur, Ildiko Badea. Nanodiamonds as novel nanomaterials for biomedical applications: drug delivery and imaging systems, *International Journal of Nanomedicine* 8 (2013) 203–220.

15. Veronique Vermeeren, Sylvia Wenmackers, Patrick Wagner and Luc Michiels. DNA Sensors with Diamond as a Promising Alternative Transducer Material. *Sensors* 9 (2009) 5600-5636; doi:10.3390/s90705600. 2009.

16. Dai KATO, Osamu NIWA. Carbon-based Electrode Materials for DNA Electroanalysis, *Analytical Sciences* 29 (2013).

17. Atomchip Group. Available online [November 2017] at http://atomchip.org/diamonds/.

18. Ariful Haque and Sharaf Sumaiya. An Overview on the Formation and Processing of Nitrogen-Vacancy Photonic Centers in Diamond by Ion Implantation. *J. Manuf. Mater. Process.* 1(6) 2017; doi:10.3390/jmmp1010006.

19. J. O. Orwa, A. D. Greentree, I. Aharonovich, A. D. C. Alves, J. VanDonkelaar, A. Stacey, S. Prawer. Fabrication of single optical centres in diamond—a review, *Journal of Luminescence* 130 (2010) 1646–1654.

20. Andrew D. Greentree, Barbara A. Fairchild, Faruque M. Hossain, and Steven Prawer. Diamond integrated quantum photonics, *materialstoday* 11(9) (2008).

21. C. Schreyvogel, V. Polyakov, R. Wunderlich, J. Meijer and C. E. Nebel. Active charge state control of single NV centres in diamond by in-plane Al-Schottky junctions. *Scientific Reports* 5 (2015) 12160.

22. Romana Schirhagl, Kevin Chang, Michael Loretz, and Christian L. Degen. Nitrogen-Vacancy Centers in Diamond: Nanoscale Sensors for Physics and Biology Annu. *Rev. Phys. Chem*. 65 (2014) 83-105.

23. Maria Simanovskaia, Kasper Jensen, Andrey Jarmola, Kurt Aulenbacher, Neil Manson,and Dmitry Budker. Sidebands in optically detected magnetic resonance signals of nitrogen vacancy centers in diamond, *Physical Review B* 87, 224106 (2013).

24. Vladimíra Petráková, Miloš Nesládek, Andrew Taylor, František Fendrych, Petr Cígler, Miroslav Ledvina, Jiří Vacík, Jan Štursa, and Jan Kučka. Luminescence properties of engineered nitrogen vacancy centers in a close surface proximity, *Phys. Status Solidi* 208(9) (2011) 2051–2056.

25. J. Havlik, H. Raabova , M. Gulka, V. Petrakova, M. Krecmarova, V. Masek, P. Lousa, J. Stursa , H.-G. Boyen, M. Nesladek and P. Cigler. Benchtop Fluorination of Fluorescent Nanodiamonds on a Preparative Scale: Toward Unusually Hydrophilic Bright Particles. *Adv. Funct. Mater.* 26 (2016) 4134–4142.

26. X. Chen, Ch. Zou, Z. Gong, Ch. Dong, G. Guo and F. Sun. Subdiffraction optical manipulation of the charge state of nitrogen vacancy center in diamond. *Light: Science and Applications* 4(1) (2015) e230.

27. X.-D. Chen, C.-L. Zou, F.-W. Sun, G.-C. Guo. Optical manipulation of the charge state of nitrogen-vacancy center in diamond. *Applied Physics Letters* 103(1) (2013) 013112.

28. B. Grotz, M.V. Hauf, M. Danker, B. Naydenov, S. Pezzagna, J. Meijer, F. Jelezko, J. Wrachtrup, M. Stutzmann, F. Reinhard and J. A. Garrido. Charge state manipulation of qubits in diamond. *Nature Communications* 3 (2012) 1729.

29. Ch. Schreyvogel, M. Wolfer, H. Kato, M. Schreck and Chr. E. Nebel. Tuned NV emission by in-plane Al-Schottky junctions on hydrogen terminated diamond. *Scientific Reports* 4 (2014) 3634.

30. M. V. Hauf, P. Simon, N. Aslam, M. Pfender, P. Neumann, S. Pezzagna, J. Meijer, J. Wrachtrup, M. Stutzmann, F. Reinhard and J. A. Garrido. Addressing Single Nitrogen-Vacancy Centers in Diamond with Transparent in-Plane Gate Structures. *Nano Lett.* 14 (2014) 2359−2364,.

31. S. Karavelia, O. Gaathona, A. Wolcotta, R. Sakakibaraa, O. A. Shemeshe, D. S. Peterkag, Edward S. Boydene, J. S. Owend, R. Yusteg and Dirk Englund. Modulation of nitrogen vacancy charge state and fluorescence in nanodiamonds using electrochemical potential. Proceedings of the National Academy of Sciences of the United States of America 113(15) (2016) 3938-3943.

32. K. Ohashi, T. Rosskopf, H. Watanabe, M. Loretz, Y. Tao, R. Hauert, S. Tomizawa, T. Ishikawa,J. Ishi-Hayase, S. Shikata, C. L. Degen, and K. M. Itoh. Negatively Charged Nitrogen-Vacancy Centers in a 5 nm Thin 12C Diamond Film, *Nano Lett.* 13 (2013) 4733−4738.

33. Tobias Nobauer, Kathrin Buczak, Andreas Angerer, Stefan Putz, Georg Steinhauser, Johanna Akbarzadeh, Herwig Peterlik, Johannes Majer, Jörg Schmiedmayer and Michael Trupke. Creation of ensembles of nitrogen-vacancy centers in diamond by neutron and electron irradiation (2013), available online [November 2017] at: http://arxiv.org/pdf/1309.0453.pdf.

34. R. Schirhagl, K. Chang, M. Loretz, and Ch. L. Degen. Nitrogen-Vacancy Centers in Diamond: Nanoscale Sensors for Physics and Biology. *Annu. Rev. Phys. Chem.* 65 (2014) 83-105.

35. F.F. De Oliveira, S. A. Momenzadeh, D. Antonov, J. Scharpf, C. Osterkamp, B. Naydenov, F. Jelezko, A. Denisenko, J. Wrachtrup. Toward Optimized Surface δ-Profiles of Nitrogen-Vacancy Centers Activated by Helium Irradiation in Diamond*. Nano Letters* 16(4) (2016) 2228-2233.

36. V. Petrakova, V. Benson, M. Buncek,A. Fiserova, M. Ledvina, J. Stursa, P. Cigler and M. Nesladek. Imaging of transfection and intracellular release of intact, non-labeled DNA using fluorescent nanodiamonds. *Nanoscale* 8 (2016) 12002–12012.

37. J. D. Watson, et al. Molecular Biology of the Gene, 5th ed., Chapter 6: The Structures of DNA and RNA (2004), ISBN-13 978-0-8053-4635-0, available online [March 2017] at http://biology.kenyon.edu/courses/biol63/watson_06.pdf.

38. Sternberg, James A. Shapiro and Richard von. Why repetitive DNA is essential to genome function. *Biol. Rev.* 80 (2005) 1–24.

39. Ronald R Breaker, Gerald F Joyce. A DNA enzyme that cleaves RNA, *Chemistry & Biology* 1 (1994) 223-229.

40. Kumar, Ajay. In situ Hybridization, *International Journal of Applied Biology and Pharmaceutical Technology* I(2) (2010), ISSN 0976-4550.

41. Engineering, The Royal Academy of. Synthetic Biology: scope, applications and implications (2009), ISBN: 1-903496-44-6, available [November 2017] at: http://www.raeng.org.uk/publications/reports/synthetic-biology-report.

42. Vilda, Raul Măluţan and Pedro Gómez. In Thermodynamics - Fundamentals and Its Application in Science, Thermodynamics of Microarray Hybridization (18) (2012), ISBN 978-953-51-0779-8. Available online [November 2017] at: http://www.intechopen.com/books/thermodynamics-fundamentals-and-its-application-in-science/thermodynamics-of-microarray-hybridization.

43. Sabine Szunerits, Rabah Boukherroub. Different strategies for functionalization of diamond surfaces, *J Solid State Electrochem* 12 (2008) 1205–1218

44. Integrated DNA Technologies. Strategies for Attaching Oligonucleotides to Solid Supports. 2014(v6). Available online [November 2017] at https://www.idtdna.com/.

45. Sabine Szunerits, Rabah Boukherroub. Different strategies for functionalization of diamond surfaces, *J Solid State Electrochem* 12 (2008) 1205–1218

46. Oliver A Williams, Richard B Jackman. Surface conductivity on hydrogen terminated diamond. *Semicond. Sci. Technol.* 18 (2003) S34–S40.

47. Anke Krueger, Daniel Lang. Functionality is Key: Recent Progress in the Surface Modification of Nanodiamond, *Adv. Funct. Mater* 22 (2012) 890–906.

48. P.W. May, J.C. Stone, M. N. R. Ashfold, K. R. Hallam,W. N. Wang, N. A. Fox. The effect of diamond surface termination species upon field emission properties, *Diamond and Related Material*s 7 (1998) 671-676.

49. Mei Wang, Manash R. Das, Vera G. Praig, Francois LeNormand, Musen Li, Rabah Boukherroub and Sabine Szunerits. Wet-chemical approach for the halogenation of hydrogenated boron-doped diamond electrodes, *Chem. Commun.* (2008) 6294-6296.

50. Matthew R. Lockett, Lloyd M. Smith. Halogenation of Carbon Substrates for Increased Reactivity with Alkenes, *Langmuir* 26(22) (2010) 16642–16646.

51. Y. Ikeda, T. Saito, K. Kusakabe, S. Morooka, H. Maeda, Y. Taniguchi, and Y. Fujiwara. Halogenation and butylation of diamond surfaces by reactions in organic solvents, *Diam. Relat. Mater.* 7 (1998) 830-834.

52. Vijayalakshmi Velusamy, Khalil Arshak, Catherine F. Yang, Lei Yu, Olga Korostynska, Catherine Adley. Comparison Between DNA Immobilization Techniques on a Redox Polymer Matrix, *American Journal of Analytical Chemistry* 2 (2011) 392-400.

53. T. Gregory Drummond, Michael G. Hill and Jacqueline K. Barton. Electrochemical DNA sensors, *Nature Biotechnology* 21 (2003) 1192-1199.

54. Fang Wei, Peter B. Lillehoj, And Chih-Ming Ho. DNA Diagnostics: Nanotechnology-Enhanced Electrochemical Detection of Nucleic Acids, *Pediatric research* 67(5) (2010) 458–468.

55. Harvey, David. Analytical Chemistry 2.0 Chapter 11: Electrochemical Methods, available online [November 2017] at: http://www.asdlib.org/onlineArticles/ecourseware/Analytical%20Chemistry%202.0/Text_Files.html.

56. Christopher M. A. Brett, Ana Maria Oliveira Brett. Electrochemistry Principles, Methods, and Applications, Oxford University Press Inc., New York 1994, ISBN 0 19 855388 9 (Pbk).

57. Martin Bartosika, Roman Hrstka, Emil Palecek, Borivoj Vojteseka. Magnetic bead-based hybridization assay for electrochemical detection of microRNA, *Analytica Chimica Acta* 813 (2014) 35–40.

58. M. H. Abouzar, A. Poghossiana, A. Razavi, O. A. Williams, N. Bijnens, P. Wagner, M. J. Schöninga. Characterisation of capacitive field-effect sensors with a nanocrystalline-diamond film as transducer material for multi-parameter sensing, *Biosensors and Bioelectronics* 24 (2009) 1298–1304.

59. Antoine Blin, Ismaïl Cissé and Ulrich Bockelmann. Electronic hybridization detection in microarray format and DNA genotyping, *Sci. Rep.* 4 (2014) 4194.

60. Ying Ma, Changqun Cai, Huimin Yang, Lin Luo, and Xiaoming Chen. The Amplified Resonance Light Scattering Signal Detection of DNA Hybridization Using Polycyclic Aromatic Hydrocarbons as a Probe, *Spectroscopy Letters*, 47 (2014) 184–191.

61. O. A. Williams. Nanocrystalline diamond, *Diam. Relat. Mater.* 20 (2011) 621–640.

62. Vadym N. Mochalin, Olga Shenderova, Dean Ho and Yury Gogotsi. The properties and applications of nanodiamonds, *NATURE NANOTECHNOLOGY* 7 (2012) 11-23.

63. V. Kočka, T. Jirásek, A. Taylor, F. Fendrych, B. Rezek, Z. Šimůnková, I. Mrázová, P. Toušek, J. Mistrík, V. Mandys, M. Nesládek. Novel Nanocrystalline Diamond Coating of Coronary Stents Reduces Neointimal Hyperplasia in Pig Model Experimental & Clinical Cardiology 20 (2014) 65-76.

64. Chavin Jongwannasiri, Nutthanun Moolsradoo, Anak Khantachawana, Pongpan Kaewtatip, and Shuichi Watanabe. The Comparison of Biocompatibility Properties between Ti Alloys and Fluorinated Diamond-Like Carbon Films, 2012 (2012) 724126, available online [November 2017] at: http://dx.doi.org/10.1155/2012/724126.

65. Dr. Michael Rowe. Interventional Cardiologist. Coronary Stenting. Available online [November 2017] at http://www.michaelrowecardiologist.com.au/coronary-stenting-michael-rowe.html.

66. Jr., Robert A. Freitas. Nanomedicine, volume IIA: Biocompatibility (2003), ISBN: 1-57059-700-6.

67. W. Okrój, M. Kamińska, L. Klimek, W. Szymański, B. Walkowiak. Blood platelets in contact with nanocrystalline diamond surfaces, *Diamond & Related Materials* 15 (2006) 1535–1539.

68. Andrew Taylor, František Fendrych, Ladislav Fekete, Jan Vlček, Vladimíra Řezáčová, Václav Petrák, Jaroslav Krucký, Miloš Nesládek, Michael Liehr. Novel high frequency pulsed MW-linear antenna plasma-chemistry: Routes towards large area, low pressure nanodiamond growth. *Diamond & Related Materials* 20 (2011) 613–615.

69. FND BIOTECH. Available online [November 2017] at http://www.fndbiotech.net/.

70. Christopher M. Breeding, James E. Shigley,. The “type” classification system of diamonds and its importance in gemology, *GEMS & GEMOLOGY* 45 (2) (2009) 96–111.

71. R. A. Khmelnitskiy. Prospects for the synthesis of large single-crystal diamonds. Physics Uspekhi 58(2) (2015) 134-149.

72. Antwerp diamond research. Available online [November 2017] at http://www.wtocd.be/en/Fundamental/Fundamental_research.html.

73. A. P. Bolshakova, V. G. Ralchenkoa, A. V. Polskiya, V. I. Konova, E. E. Ashkinazia, A. A. Khomicha, G. V. Sharonovb, R. A. Khmelnitskyc, E. V. Zavedeeva, A. V. Khomichd, and D. N. Sovyk. Growth of Single Crystal Diamonds in Microwave Plasma, *PLASMA PHYSICS REPORTS* 38(13) (2012) 1113-1118.

74. A. Tallaire, A.T. Collins, D. Charles, J. Achard, R. Sussmann, A. Gicquel, M.E. Newton c, A.M. Edmonds c, R.J. Cruddace. Characterisation of high-quality thick single-crystal diamond grown by CVD with a low nitrogen addition, *Diamond & Related Materials* 15 (2006) 1700–1707.

75. Six, Element. Single crystal synthetic diamond, available online at [November 2017]: http://www.e6.com/wps/wcm/connect/E6_Content_EN/Home/Materials+and+products/Single+crystal+synthetic+diamond/.

76. O. S. Alexander Vul'. Detonation Nanodiamonds: Science and Applications. ISBN 9789814411271 - CAT# N10815.

77. David Amans, Anne-Claire Chenus, Gilles Ledoux, Christophe Dujardin, Cécile Reynaud, Olivier Sublemontier, Karine Masenelli-Varlot, Olivier Guillois. Nanodiamond synthesis by pulsed laser ablation in liquids. Diamond and Related Materials 18(2-3) (2009) 177-180.

78. G Ali Mansoori, Patricia Lopes Barros de Araujo, Elmo Silvano de Araujo. Diamondoid Molecules. With Applications in Biomedicine, Materials Science, Nanotechnology & Petroleum Science. ISBN: 978-981-4291-60-6.

79. Oliver A. Williams, Miloš Nesládek. Growth and properties of nanocrystalline diamond films, *phys. stat. sol. (a)* 203(13) (2006) 3375–3386.

80. Tokuda, Norio. Homoepitaxial Diamond Growth. In Novel Aspects of Diamond, N. Yang (ed.), Topics in Applied Physics 121 (2015).

81. J. Isberg, J. Hammersberg, E. Johansson, Tobias Wikström, Daniel J. Twitchen, Andrew J. Whitehead, Steven E. Coe, Geoffrey A. Scarsbrook. High Carrier Mobility in Single-Crystal Plasma-Deposited Diamond, *Science* 297(5587) (2002) 1670.

82. The element SIX CVD diamond handbook. Available online [November 2017] at https://e6cvd.com/media/wysiwyg/pdf/E6_CVD_Diamond_Handbook_A5_v10X.pdf.

83. M. Werner, R. Locher, W. Kohly, D.S. Holmes, S. Klose, H.J. Fecht. The diamond Irvin curve, *Diamond and Related Materials* 6 (1997) 308.

84. W. Gajewski, P. Achatz, O. A. Williams, K. Haenen, E. Bustarret, M. Stutzmann, and J. A. Garrido. Electronic and optical properties of boron-doped nanocrystalline diamond films, *Physical Review* B 79 (2009) 045206.

85. Victor Acosta and Philip Hemmer, Guest Editors. Nitrogen-vacancy centers: Physics and Applications, *MRS BULLETIN* 38 (2013) 127-130.

86. Murphy, Damien M. EPR (Electron Paramagnetic Resonance) Spectroscopy of Polycrystalline Oxide Systems, In Metal Oxide Catalysis 25 (2009) 1-50.

87. Marcus W. Doherty, Neil B. Manson, Paul Delaney, Fedor Jelezko, Jörg Wrachtrupe and Lloyd C.L. Hollenberga. The nitrogen-vacancy colour centre in diamond (2013), available online [November 2017] at http://arxiv.org/pdf/1302.3288.pdf.

88. Takayuki Iwasaki, Wataru Naruki, Kosuke Tahara, Toshiharu Makino, Hiromitsu Kato, Masahiko Ogura, Daisuke Takeuchi, Satoshi Yamasaki, and Mutsuko Hatano. Direct Nanoscale Sensing of the Internal Electric Field in Operating Semiconductor Devices Using Single Electron Spins. ACS Nano1 (2) (2017) 1238–1245.

89. Vladimíra Petráková, Andrew Taylor, Irena Kratochvílová, František Fendrych, Jiří Vacík, Jan Kučka, Jan Štursa, Petr Cígler, Miroslav Ledvina, Anna Fišerová, Peter Kneppo, and Miloš Nesládek. Luminescence of Nanodiamond Driven by Atomic Functionalization: Towards Novel Detection Principles, *Adv. Funct. Mater.* 22 (2012) 812–819.

90. Y. Doi, T. Makino, H. Kato, D. Takeuchi, M. Ogura, H. Okushi, H. Morishita, T. Tashima, S. Miwa, S. Yamasaki, P. Neumann, J. Wrachtrup, Y. Suzuki, and N. Mizuochi. Deterministic electrical charge state initialization of single nitrogen-vacancy center in diamond. Physical Review X. 4 (2014) 011057. Available online [November 2017] at http://mizuochilab.kuicr.kyoto-u.ac.jp/publicationsE.html.

91. K. Groot-Berning, N. Raatz, I. Dobrinets, M. Lesik, P.Spinicelli, A. Tallaire, J. Achard, V. Jacques, J.-F. Roch, A. M. Zaitsev, J. Meijer and S. Pezzagna. Passive charge state control of nitrogen-vacancy centres in diamond using phosphorous and boron doping. *Phys. Status Solidi A* 211(10) (2014) 2268–2273.

92. A. M. Edmonds, U. F. S. D'Haenens-Johansson, R. J. Cruddace, and M. E. Newton. Production of oriented nitrogen-vacancy color centers in synthetic diamond, *PHYSICAL REVIEW* B 86 (2012) 035201.

93. M. Shimizu, T. Makino, T. Iwasaki, J. Hasegawa, K. Tahara, W. Naruki, H. Katoc, S. Yamasaki, M. Hatano. Charge state modulation of nitrogen vacancy centers in diamond by applying a forward voltage across a p–i–n junction. *Diamond & Related Materials* 63 (2016) 192–196.

94. A. Stacey, T. J. Karle, L. P. McGuinness, B. C. Gibson, K. Ganesan, S. TomljenovicHanic, A. D.) Greentree, A. Hoffman, R. G. Beausoleil, and S. Prawer. Depletion of nitrogen vacancy color centers in diamond via hydrogen passivation, *Applied Physics Letters* 100 (2012) 071902.

95. Claire Glover, M. E. Newton. Hydrogen Incorporation in Diamond: TheVacancy-Hydrogen Complex, *Physical Review Letters* 92(13) (2004) 135502.

96. R. U. AKhan, P. M. Martineau, B. L. Cann, M. E. Newton, and D. J. Twitchen. Charge transfer effects, thermo and photochromism in single crystal CVD synthetic diamond, J. Phys.: *Condens. Matt*er 21 (2009) 364214.

97. James E. Butler, Anirudha V. Sumant. The CVD of Nanodiamond Materials, *Chem. Vap. Deposition* 14 (2008) 145–160.

98. Bristol, CVD group of University of. Modelling diamond growth, available online [November 2017] at http://www.chm.bris.ac.uk/pt/diamond/growthmodel.htm.

99. F. Piazza, F. Solá, O. Resto, L.F. Fonseca, G. Morell. Synthesis of diamond nanocrystals on polyimide film, *Diamond & Related Materials* 18 (2009) 113–116.

100. Robert A. Wilson, Heather A. Bullen. Introduction to Scanning Probe Microscopy (SPM), Basic Theory, Atomic Force Microscopy (AFM). Department of Chemistry, Northern Kentucky University, Highland Heights, KY 41099. Available online [November 2017]: http://asdlib.org/onlineArticles/ecourseware/Bullen/SPMModule_BasicTheoryAFM.pdf.

101. E. Meyer. Atomic force microscopy. *Progress in Surface Science* 41 (1992) 3-49.

102. My Scope training for advanced research. Scanning Electron Microscope Training module Available online [November 2017] at: http://www.ammrf.org.au/myscope/pdfs/sem.pdf.

103. Ltd., JEOL. Scanning electron microscope A to Z, Basic knowledge for using the SEM. Available online [November 2017] at: http://www.jeol.co.jp/en/applications/pdf/sm/sem_atoz_all.pdf.

104. Nixon, W. C. The General Principles of Scanning Electron Microscopy. Philosophical Transactions of the Royal Society of London. Series B, Biological Sciences, Vol.261, No. 837, A Discussion on New Developments in Electron Microscopy with . *Emphasis on their Application in Biology.* (1971) 45-50. Available online [November 2017] at: http://links.jstor.org/sici?sici=0080-4622%2819710527%29261%3A837%3C45%3ATGPOSE%3E2.0.CO%3B2-Z.

105. Instruments, Princeton. Raman Spectroscopy Basics. Available online [November 2017] at: http://web.pdx.edu/~larosaa/Applied_Optics_464-564/Projects_Optics/Raman_Spectrocopy/Raman_Spectroscopy_Basics_PRINCETON-INSTRUMENTS.pdf.

106. University, Åbo Akademi. Raman Spectroscopy. Available online [November 2017] at: http://users.abo.fi/mhotokka/mhotokka/lecturenotes/ms04.d/ms04-raman-eng.pdf.

107. Scientific, Thermo. Introduction to Raman Spectroscopy. Available online [November 2017] at: http://www.biotechprofiles.com/companyfiles/madisonnetwork/5bdd0a9f37694d6c9fb6e62db5049477.pdf

108. Nathan S. Claxton, Thomas J. Fellers, and Michael W. Davidson. LASER SCANNING CONFOCAL MICROSCOPY. Department of Optical Microscopy and Digital Imaging, National High Magnetic Field Laboratory,The Florida State University. Available online [November 2017] at: http://www.olympusconfocal.com/theory/LSCMIntro.pdf.

109. Denis Semwogerere, Eric R. Weeks. Confocal Microscopy. Emory University, Atlanta, Georgia, U.S.A. Available online [November 2017] at: http://www.physics.emory.edu/faculty/weeks//lab/papers/ebbe05.pdf.

110. Vineeta Rai, Nrisingha Dey. The Basics of Confocal Microscopy. Institute of Life Sciences, Laboratory of Plant Biotechnology, Dept. of Gene Function & Regulation, Bhubaneswar (Orissa), India. Available online [November 2017] at: http://cdn.intechopen.com/pdfs-wm/15801.pdf.

111. Kasper A. Borup, Eric S. Toberer, Leslie D. Zoltan, George Nakatsukasa, Michael Errico, Jean-Pierre Fleurial, Bo B. Iversen, and G. Jeffrey Snyder. Measurement of the electrical resistivity and Hall coefficient at high temperatures. *REVIEW OF SCIENTIFIC INSTRUMENTS* 83 (2012) 123902.

112. Manual, Lake Shore 7500/9500 Series Hall System User''s. APPENDIX A, HALL EFFECT MEASUREMENTS. Available online [November 2017] at: http://physics.oregonstate.edu/~tate/TateLabWiki/lib/exe/fetch.php?media=hall:manual_app_a_hallmeasurementsystem.pdf

113. Toru Matsumura, Yuichi Sato. A Theoretical Study on Van Der Pauw Measurement Values of Inhomogeneous Compound Semiconductor Thin Films. *J. Mod. Phys*. 1 (2010) 340-347.

114. Associates, Scribner. Scribner Associates - Tutorial, Scribner Associates Inc. 150 E. Connecticut Ave, Southern Pines, North Carolina 28387 USA. Scribner Associates. Available online [November 2017] at: http://www.scribner.com/.

115. Byoung-Yong Chang, Su-Moon Park. Electrochemical Impedance Spectroscopy. *Annu. Rev. Anal. Chem.* 3 (2010) 207–29.

116. Su-Moon Park, Jung-Suk Yoo. Electrochemical impedance spectroscopy for better electrochemical measurements. *Anal. Chem.* 75 (2003) 455A-461A.

117. R. Pfeiffer, H. Kuzmany, P. Knoll, S. Bokova, N. Salk, B. Günther. Evidence for trans-polyacetylene in nano-crystalline diamond films. *Diamond and Related Materials* 12 (2003) 268–271.

118. H. Sternschulte, T. Bauer, M. Schreck, B. Stritzker. Comparison of MWPCVD diamond growth at low and high process gas pressures. *Diamond & Related Materials* 15 (2006) 542–547.

119. Kevin E. Bennet, Kendall H. Lee, James N. Kruchowski, Su-Youne Chang, Michael P. Marsh, Alexander A. Van Orsow, Aurelio Paez and Felicia S. Manciu. Development of Conductive Boron-Doped Diamond Electrode: A microscopic, Spectroscopic, and Voltammetric Study. *Materials* 6 (2013) 5726-5741.

120. Li Niu, Jia-Qi Zhu, Xiao Han, Man-Lin Tan, Wei Gao, Shan-Yi Du. First principles study of structural, electronic and vibrational properties of heavily boron-doped diamond. *Physics Letters A* 373 (2009) 2494–2500.

121. V. D. Blank, V. N. Denisov, A. N. Kirichenko, M. S. Kuznetsov, B. N. Mavrin, S. A. Nosukhin, S. A. Terentiev. Raman scattering by defect-induced excitations in boron-doped diamond single crystals. *Diamond & Related Materials* 17 (2008) 1840–1843.

122. Marie (Jakl) Krečmarová, Michal Gulka, Ladislav Fekete, Zdeněk Remeš, Vladimíra Petráková, Vincent Mortet and Miloš Nesládek. Production of nitrogen vacancy centers in nanocrystalline diamond thin film for quantum biosensing applications. Proceeding Instruments and methods for biology and medicine 2014, (2014) 23-25, ISBN 978-80-01-05636-3.

123. Marie (Jakl) Krečmarová, Václav Petrák, Andrew Taylor, Kamatchi Jothiramalingam Sankaran, I-Nan Lin, Aleš Jäger, Viera Gärtnerová, Ladislav Fekete, Jan Drahokoupil, František Laufek, Jiří Va-cík, Pavel Hubík, Vincent Mortet and Miloš Nesládek. Change of diamond film structure and morphology with N2 addition in MW PECVD apparatus with linear antenna delivery system. Physica Status Solidi A, 211 (2014) 10, 2296–2301 (2014).

124. L Fekete, K Kůsová, V Petrák, I Kratochvílová. AFM topographies of densely packed nanoparticles: a quick way to determine the lateral size distribution by autocorrelation function analysis. *Journal of Nanoparticle Research* 14 (8) (2012 1062.

125. V. Hnatowicz, J. Vacik, D. Fink, Deconvolution of charged particle spectra from neutron depth profiling using Simplex method. *Review of Scientific Instruments* 81 (2010) 0739061-0739067.

126. Sunil K. Karna, Yogesh. K. Vohra, Samuel T. Weir. Optical and Electrical Characterization of Boron-Doped Diamond. arXiv:1210.7846v2.“.

127. AMPS-1D software (Analysis of Microelectronic and Photonic Structures). Available online [November 2017] at: http://www.ampsmodeling.org/.

7 Abbreviations used in the work

AFM - Atomic force microscopy

BNCD – boron doped nanocrystalline diamond

CCD - charge-coupled device

CV - Cyclic voltammetry

CVD – chemical vapour deposition

DNA - deoxyribonucleic acid

DPV - differential pulse voltammetry

dsDNA - double stranded DNA

EDC - 1-ethyl-3-(3-dimethylaminopropyl)-carbodiimide

EDIS - Electrolyte-diamond-insulator-semiconductor

EIS – electrochemical impedance spectroscopy

EPR - electron paramagnetic resonance

FA – fatty acids

FBMI CTU - Faculty of Biomedical Engineering of Czech Technical University in Kladno

FET - Electrolyte-gated field effect transistors

FTIR - fourier transform infrared spectroscopy

HOMO - highest occupied molecular orbital

HPHT – high pressure high temperature

IMO-IMOMEC - Hasselt University's Institute for Materials Research

IoP ASCR - Institute of physic Academy of science in Prague, Czech Republic

IR - infrared

ITO - indium tin oxide

LUMO - lowest unoccupied molecular orbital

mRMA - messenger RNA

MW PE CVD – Microwave plasma-enhanced chemical vapour deposition

NCD - nanocrystalline diamond

NV - nitrogen vacancy

ODMR - optically detected magnetic resonance

PCD - polycrystalline diamond

PCR - Polymerase chain reaction

PDMS – polydimethylsiloxane

PE CVD - Plasma-enhanced chemical vapor deposition

PEI – polyethylenimine

PL – photoluminescence

PMT - Photomultiplier tubes

RNA - ribonucleic acid

rRNA - ribosomal RNA

SEM - Scanning electron microscopy

Si-V - silicone vacancy

sscDNA - single stranded complimentary RNA

ssDNA - single stranded DNA

SSMCC - (sulfo-succinimidyl 4-(N-maleimidomethyl) cyclohexan-1-carboxylate)

TMB – trimethylboron

TNT – trinitrotoluene

tRNA - transfer RNA

UA - 10-undecenoic acid

UNCD - ultra-nanocrystalline diamond

UV - ultraviolet

Appendix I: Author's publications

Publications related to the topic of doctoral thesis:

- J. Havlik, H. Raabova, M. Gulka, V. Petrakova, M. Krecmarova, V. Masek, P. Lousa, J. Stursa, H.-G. Boyen, M. Nesladek, P. Cigler. Benchtop Fluorination of Fluorescent Nanodiamonds on a Preparative Scale: Toward Unusually Hydrophilic Bright Particles. Advanced Functional Materials 26 (2016) 23, 4134-4142 (IF = 11.38). Citations (11/2017): 6.
- M. J. Krečmarová, V. Petrák, A. Taylor, K. J. Sankaran, I-N. Lin, A. Jäger, V. Gärtnerová, L. Fekete, J. Drahokoupil, F. Laufek, J. Vacík, P. Hubík, V. Mortet and M. Nesládek. Change of diamond film structure and morphology with N2 addition in MW PECVD apparatus with linear antenna delivery system. Physica Status Solidi A, 211 (2014) 10, 2296–2301 (2014) (IF = 1.53). Citations (11/2017): 2.
- M. J. Krečmarová, M. Gulka, L. Fekete, Z. Remeš, V. Petráková, V. Mortet and M. Nesládek. Production of nitrogen vacancy centers in nanocrystalline diamond thin film for quantum biosensing applications. Proceeding Instruments and methods for biology and medicine 2014, (2014) 23-25, ISBN 978-80-01-05636-3.
- M. Vlčková (Krečmarová), M. Stefanovič, V. Petrák, F. Fendrych, A. Taylor, L. Fekete and M. Nesládek. Nanodiamond seeding of rough substrates. Proceeding Instruments and methods for biology and medicine 2011, (2011) 11-15, ISBN 978-80-01-04915-0.
- M. Krečmarová, T. Vandenryt, M. Gulka, E. Bourgeois, L. Fekete, R. Thoelen, V. Mortet and M. Nesládek. Microfluidic diamond biosensor using NV centre charge state detection. This work is submitted (February 2018) to the IFMBE conference proceeding.
- M. Krečmarová, M. Gulka, T. Vandenryt, E. Bourgeois, J. Hrubý, R. Thoelen, V. Mortet and M. Nesládek. Diamond electrochemical sensor based on NV centre charge state control. This work is planned to be submitted (March 2018) to a journal such as Scientific Reports and Nanoscale.

Other publications:

- A. Talbi, A. Soltani, A. Rumeau, A. Taylor, L. Drbohlavová, L Klimša, J. Kopeček, L. Fekete, M. Krečmarová, V. Mortet. Simulations, fabrication and characterisations of diamond coated Love wave surface acoustic wave sensors. Physica Status Solidi A, 212 (2015) 11, 2606-2010 (IF = 1.53). Citations (11/2017): 3.
- V. Petrák, J. Krucký and M. Vlčková (Krečmarová). Boron Doped Nanocrystalline Diamond Films for Biosensing Applications. Acta Polytechnica. 51 (2011) 5. Citation (11/2017): 1.
- L. Drbohlavova, J. Bulir, V. Valeš, M. J. Krecmarova, A. Taylor, A. Talbi, A. Soltani, V. Mortet. Fabrication methods of diamond coated Love wave SAW biosensors for bacterial detection applications. Instruments and methods for biology and medicine 2015. Praha: CTU, (2015) 11-14, ISBN 978-80-01-05851-0.

Appendix II: Conference participations

- Oral presentation: World Congress on Medical Physics and Biomedical Engineering 2018, 3. – 8. June 2018, Prague, Czech Republic. Topic: „DNA microfluidic biosensor using NV centre charge state detection in diamond".
- Oral presentation and Symposium assistant: 2017 E-MRS Fall Meeting and Exhibit, 18. – 21. September 2017, Warsaw, Poland. Topic: „DNA biosensor based on charge state of NV centres in diamond combined with microfluidic device".
- Poster presentation: Hasselt Diamond Workshop 2017, SBDD XXII, 9. - 11. March 2017, Hasselt, Belgium. Topic: „Label free microfluidic DNA biosensor with electrochemical and NV centre optical readout".
- Poster presentation: Hasselt Diamond Workshop 2016, SBDD XXI, 9. - 11. March 2016, Hasselt, Belgium. Topic: „Charge state control of NV centres in intrinsic - highly boron doped diamond nanostructures for biosensing applications".
- Poster presentation: Hasselt Diamond Workshop 2015, SBDD XX, 25. - 27. February 2015, Hasselt, Belgium. Topic: „Novel concept NV centre - electrochemical diamond trace element chemosensors".
- Invited oral presentation: Summer school Nanoscale diagnostic methods in biology and medicine, Faculty of Biomedical Engineering, Czech Technical University, September 18. - 21. 2014, Lázně Poděbrady, Hotel Zámeček, Czech Republic. Topic: „Label free diamond based diagnostic methods for detection of oligonucleotides hybridization".
- Poster presentation: International Conference on Diamond and Carbon Materials, 7. – 11. September 2014, Melia Castilla, Madrid, Spain. Topic: „Linear antenna microwave plasma CVD diamond deposition: effect of nitrogen addition into the gas phase".
- Award for the best oral presentation: Instruments and Methods for Biology and Medicine 2014, 2nd of June 2014, CTU FBME, Kladno, Czech Republic. Topic „Production of nitrogen vacancy centers in nanocrystalline diamond thin film for quantum biosensing applications".
- Poster presentation: Hasselt Diamond Workshop 2014, SBDD XIX, 19. - 21. February 2014, Hasselt, Belgium. Topic: „Effect of plasma chemistry on diamond growth in MW PECVD apparatus with linear antenna delivery system at low pressure and low temperature".
- Poster presentation: Hasselt Diamond Workshop 2012, SBDD XVII 14. - 16. March 2012, Hasselt, Belgium. Topic: „Plasma treated and untreated nanodiamond seeding of polymers".
- Oral presentation: Instruments and Methods for Biology and Medicine 2011, 2nd of June 2011, CTU FBME, Kladno, Czech Republic. Topic: „Nanodiamond seeding of rough substrates".